Large Stand-off Magnetometry for Non-invasive Pipeline Inspection

Christopher Lee Cookson

School of Electronic and Electrical Engineering

University of Leeds

Submitted in accordance with the requirements for the degree of

Doctor of Philosophy

October 2018

The candidate confirms that the work submitted is their own and that appropriate credit has been given where reference has been made to the work of others.

This thesis is dedicated to my family.

Acknowledgements

I would like to thank my PhD supervisors at the University of Leeds: Prof. Steven Freear for his guidance and constant encouragement, Dr David Cowell for his insightful questions and comments during this work and Dr Chau Vo for his input into the project from his expertise in the area.

I give thanks to the many people from industry who I have worked with in the process of this work especially Peter Martin from National Grid for regularly making time to discuss the project direction. I thank National Grid for funding the project, allowing me to undertake this research. I also thank Speir Hunter Ltd. for the use of their IP in further developing their patented survey tools.

I would like to thank the members of the Ultrasound group at the University of Leeds including Dr Stephen Staples for his patience in helping me get up to speed with the project when I started and his helpful insights and Chris Adams for giving a helpful outside perspective as a sounding board throughout the project. I thank Louise Coffey and Anna de Jong for their secretarial support during the project.

I am especially grateful to my endlessly supportive family especially my nan Marlene Cookson for giving me endless support and for making the best cups of tea, my granddad David Cookson for constant encouragement to pursue my interests in science and engineering, my mum Suzanne Ray for her infinite patience and care throughout my life, my step-dad William Ray for his generous support of my activities, my uncle Stephen Cookson for encouraging my eccentric schemes and of course my fiancèe Sara Carlsson for constant love and support, for putting up with me during the long hours working on this project and for baking the best cinnamon buns.

Abstract

This research sought to answer the question what improvements can be made to the magnetometry survey tool developed at the University of Leeds in collaboration with Speir Hunter to increase the detection and location of features on steel natural gas pipelines.

Natural gas is a major component of the UK's energy usage and the pipeline network which transports this gas is vital to the UK's energy infrastructure. The predominant risk to the supply of gas is from infrastructure failure, the largest primary cause of these failures on the aging pipeline network is corrosion of the pipe wall. This corrosion develops over time, early detection and repair of these features can prevent these pipeline incidents. Pipeline incidents have many consequences such as loss of life, interruption of gas supply, property damage, regulator fines and reputational damage to the pipeline operator. Current inspection techniques are not available for all pipelines therefore complimentary inspection techniques are required. One such technique is large stand-off magnetometry.

To answer the primary research question this was broken down into three further specific questions. These were: how can the survey data best be presented to maximise anomaly identification, how does the magnetometer separation in the array effect the sensitivity of the array to anomalies in the magnetic gradient field, and, how does the location of the anomaly in the magnetic field relate to the location of the feature on the pipeline. Laboratory experiments were conducted using $1/2''$, $3/4''$, $1''$ and $1\,1/2''$ diameter steel conduits, AlNiCo magnets and magnetised short sections of $1''$ diameter conduit to conduct small scale experiments on known simulants.

Linear integral convolutions were found to be the best way to present the data from magnetometry scans for the easy identification of anomalies in the magnetic field by the user. A peak angular magnetometer separation at the conduit centreline of 32° at a height of 50 mm and 23° at 300 mm were found, the relationship between this peak and the height above the centreline of the conduit becomes steady at 23°. The anomaly location in the magnetic field was found to deflect from the pipe feature along the conduit, this showed an average deflection of 16° which was linear with increasing height above the conduit.

These findings give recommendations for the development of the large stand-off magnetometry survey array to increase the number of magnetometers in the array to five, to increase the separation between the centre and outermost magnetometers to 0.75 m and to add an additional magnetometry array layer. These will allow the data to be presented in a way which makes anomaly identification easier, increase the amplitude of anomalies by approximately 20% in the magnetic field increasing the sensitivity of the array and allow the angular deflection along the pipe to be determined to increase the locational accuracy of the feature by approximately 1 – 2.5 m.

Contents

List of Figures

List of Tables

Chapter 1

Introduction

1.1 Rationale for pipeline inspection

This project was undertaken to explore the use of large stand-off magnetometry for non-invasive pipeline inspection, the research focussed on the survey array tool used to conduct these inspections.

The network of pipelines that transport natural gas are a vital part of the UK's energy infrastructure [18]. Incidents on these pipelines that lead to an uncontrolled release of gas have potentially catastrophic consequences to the public, operating companies and the environment [19]. Inspections are carried out on pipelines to detect stress concentration zones, which can be caused by cracks or corrosion. These inspections inform on the need for action to prevent an incident caused by these defects.

The most common technique for performing these inspections is using a tool known as a pig (pipeline inspection gauge) to perform in-line inspection (ILI) of the pipe. This is performed by propelling the pig through the pipeline using a differential in the pressure of the gas. The pig is propelled between specially constructed stations for inserting and removing the pig [20], this is colloquially known as "pigging". Not all pipelines are suitable for pigging due to changes in pipe diameter or tight bends in the pipeline. In the pipelines that are suitable for pigging the act of sending an object down the centre of the pipe carries risks to the pipeline.

Complimentary inspection techniques are therefore required to inspect pipelines which cannot be pigged or to supplement the data from a pig. Large stand-off magnetometry is a technique for non-invasive inspection of pipelines, this has been developed at the University of Leeds in collaboration with Speir Hunter [21][22].

1.1.1 National grid gas network

The UK gas pipeline network comprises approximately 284,000 km of pipelines, including the transmission network of high pressure pipelines 7,600 km in length [23]. These pipelines deliver 995 TWh of energy to 17.7 million customers annually [24], this compares to 307 TWh of electricity used in the UK annually [25].

In 2017 approximately 40.5% of this electricity generated in the UK was generated from natural gas fired power stations [26]. Heating and hot water generation makes up approximately 40% of the UK's total energy consumption, 85% of UK homes use natural gas for this [27]. The demand for natural gas peaks in the winter months when heating is required the most, this has to be delivered through the existing pipeline network. The peak recorded daily winter demand for gas occurred in January 2010 at 465 mcm/d[1], the maximum currently deliverable is 618 mcm/d [29].

The predominant threat to the supply of gas is pipeline and terminal failures [30], these interruptions to the supply are on the order of weeks to months [31]. These interruptions leave potentially vulnerable domestic users without gas to heat their homes or industry without gas to run their plants.

The national transmission system (NTS) of pipelines for natural gas was constructed in the 1960s over a 10 year period [32] in response to the discovery of large quantities of natural gas in the north sea and the subsequent conversion from town gas [33]. While the NTS has an expected life of 80 years [34] the condition of the aging pipelines require inspection to ensure an uninterrupted and safe operation [25]. National Grid must be able to deal with supply interruptions and take reasonable action to anticipate and prevent factors that could lead to these interruptions [35].

A pipeline incident leading to a loss of supply of natural gas can have many consequences [36], these include:

- the human consequences such as loss of life or injuries from an incident or the loss of domestic heating in the winter months,
- the property damage caused by any sudden release of pressure from the pipline,
- the financial consequences such any penalties imposed by the courts, and
- the consequences to the company such as reputational damage.

---

[1] The unit mcm is million standard cubic meters, the industry standard for measuring gas volume. A standard cubic meter is the volume of gas which occupies 1 m^3 at 15°C and 1.013 bar. mcm/d is the flow rate of the gas and signifies million standard cubic meters per day [28].

A more detailed analysis of four pipeline incidents and their consequences are given in section 1.1.3.

1.1.2 Pipeline network incident data

Natural gas can be transported by pipeline, rail and truck. These transport methods had an average incident rate of 0.12×10^{-4}, 1.5×10^{-4} and 0.14×10^{-4} per km.yr respectively in America for the period 2005 – 2009 [37]. Whilst the pipeline and truck rates are similar there is an under reporting of truck road accidents as minor incidents do not trigger further investigations unlike pipeline and rail incidents [38]. The fatality rate associated with pipelines, rail and truck transport of hazardous materials in America in the same period was 1, 2.4 and 10.2 per year respectively. This data shows that pipelines are the safest way of transporting natural gas over large distances [39]. However given the effects of a pipeline incident regular inspection and preventative measures are still required.

The European gas pipeline incident data group (EGIG) aggregates a register of gas transmission pipeline incidents since 1970 in Europe. An incident is defined as any event that leads to an unplanned release of gas from a pipeline. The pipelines for which this data is gathered are steel, onshore pipelines outside of the fence line of gas installations operating at a pressure greater than 15 bar. The EGIG gathers data on 142,794 km of pipeline and has a total database exposure of 4.41 million km.yr of pipelines, there are 1,366 recorded incidents in the database [1]. The length of the pipelines versus the nominal diameter of the pipes in the EGIG data base is shown in figure 1.1.

Figure 1.2 shows the primary causes of pipeline incidents for the year 1974 – 2016, these are grouped into:

- Corrosion, these incidents are caused primarily by pipeline failures due to the corrosion in the pipe wall.

- External interference, these incidents are primarily caused by the pipeline being damaged by an external event such as it being struck and damaged by agricultural or excavation machinery.

- Construction defect, these incidents are primarily caused by failures due to a defect in the original construction of the pipe such as an insufficiently penetrated seam weld.
- Other, these incidents are caused by events not included in the above categories, these include erroneous hot taps and ground movement such as landslides and sinkholes.

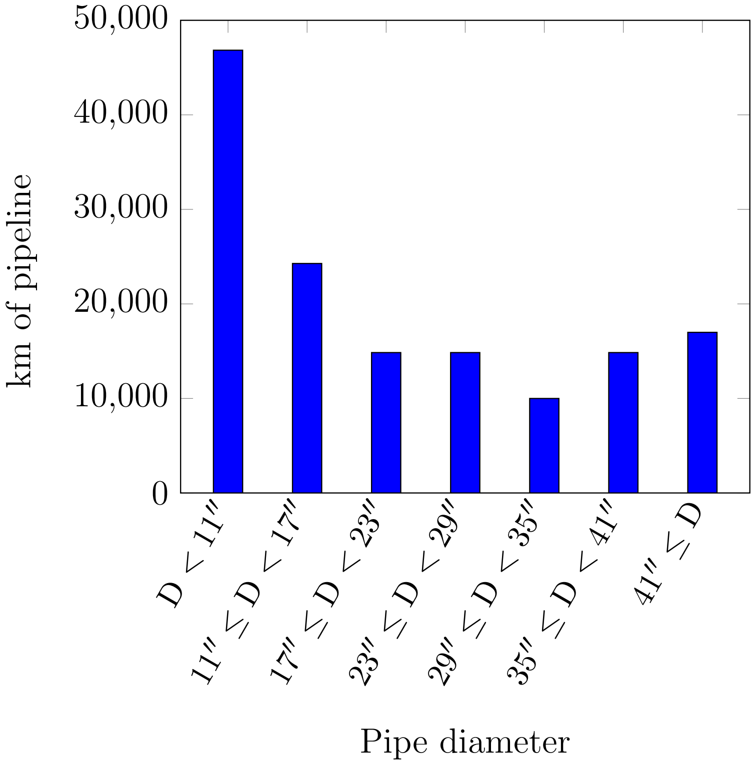

Figure 1.1: Bar chart showing the length of steel onshore gas pipelines operating with a pressure ≥ 15 bar in Europe in 2016 for each nominal diameter range.

The Alberta Energy and Utilities Board (EUB) maintains a register of pipeline incidents in the province of Alberta, Canada from 1980 to 2016 for pipelines with an operating pressure greater than 7 bar [2][3][4]. In December 2012 the total pipeline length for natural gas pipelines in Alberta was 238,500 km, of which 88.9% were constructed of steel. The length of the pipelines versus the nominal diameter of the pipes in the EGIG data base is shown in figure 1.3. The primary

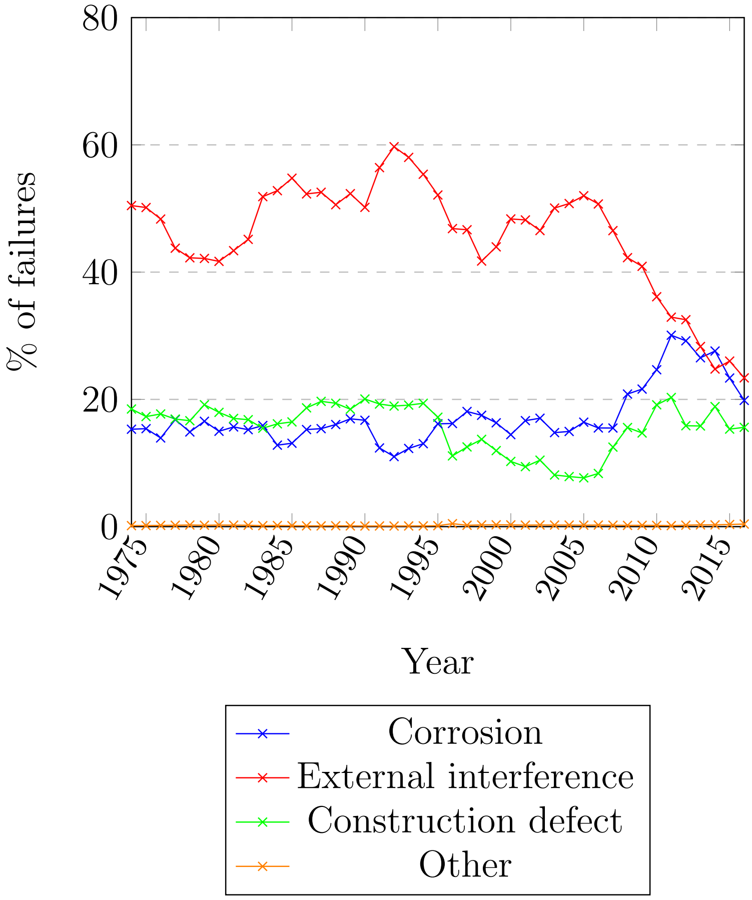

Figure 1.2: Plot showing the percentage of unplanned releases of gas from a pipeline in Europe for each type of primary failure cause for the years 1974 – 2016. [1]

causes of pipeline incidents for the year 1980 – 2012 are shown in figure 1.4, these are grouped into corrosion, external interference and other.

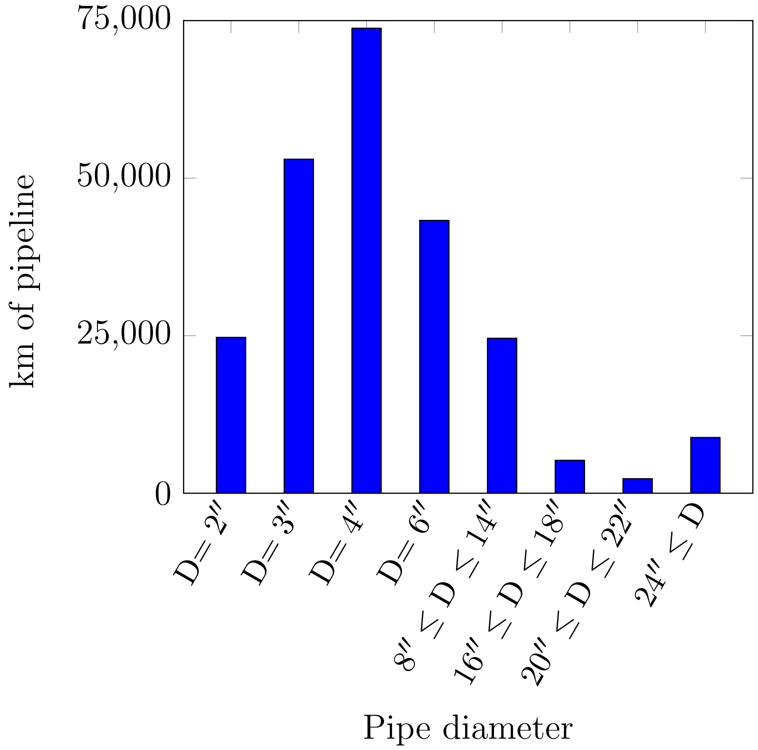

Figure 1.3: Bar chart showing the length of steel onshore gas pipelines operating with a pressure ≥ 7 bar in Alberta, Canada in 2016 against the nominal diameter.

Figure 1.2 shows that as the pipeline networks have aged corrosion and weakening in the pipeline due to construction defects have increased to become the dominant causes of pipeline incidents. Figure 1.4 shows that the primary cause of pipeline failures in the network are failures due to corrosion. Corrosion develops over time until the pipeline no longer has the strength to resist the pressure from the gas within. Construction defects cause the stress in the pipe wall to concentrate in that area that over time weaken the pipe wall until the pipeline fails. Both of these causes can be detected early through regular inspection and corrective action taken before they reach this state. This highlights the need

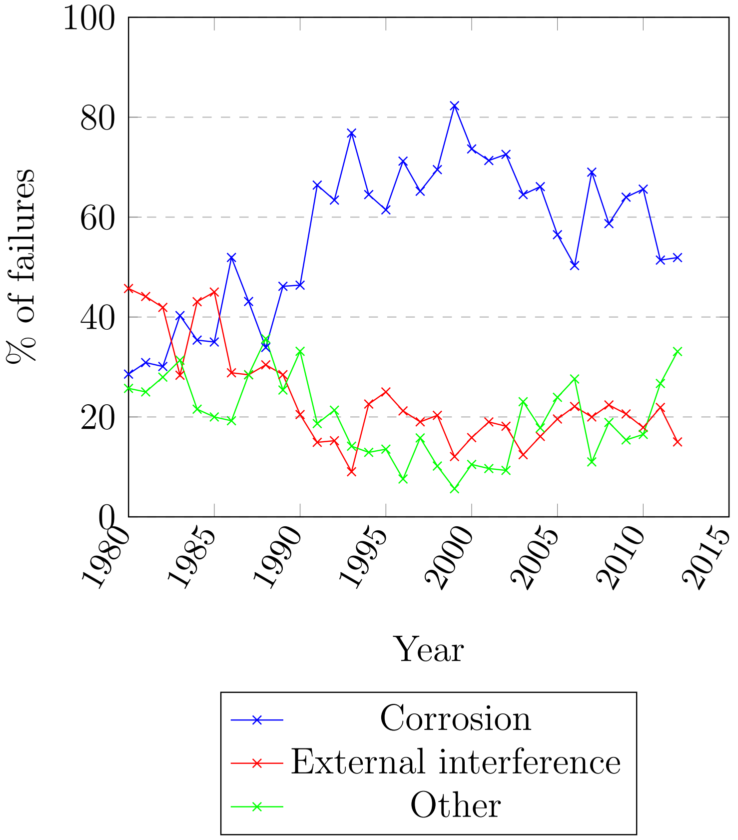

Figure 1.4: Plot showing the percentage of unplanned releases of gas from a pipeline in Alberta, Canada for each type of primary failure cause for the years 1980 – 2016. [2][3][4]

for inspection techniques for pipelines to prevent these incidents from occurring. The other major cause of failures in both registers is external interference, this can be due to deficiency in the location and depth information for the pipeline preventing appropriate steps being taken to avoid the pipeline. This highlights the need for accurate positions and depths of the pipelines.

1.1.3 Significant pipeline incidents

To demonstrate the causes and consequences of steel gas transmission pipeline failures four incidents are presented in this section, one from Belgium and three from America. In all four cases investigators have identified integrity management issues which have failed to detect the problem before the incident has occurred.

1.1.3.1 Ghislenghien pipeline explosion

On the morning of the 30th July 2014 an explosion occurred on an industrial site near to Ath, Belgium due to gas leaking from an underground pipeline [40]. The explosion caused 24 fatalities and a further 132 severe injuries. The incident was found to have been caused by an excavator striking the pipeline during construction work on the 24th June 2004 weakening the pipe wall, the damage was reported but not followed up on.

On the 30th July 2014 at 6:30 am a gas leak was reported to the Belgian natural gas transmission system operator, Fluxys. The leak was reported to the fire service at 8:15 am, who arrived at the scene at 8:30 am. An audible hissing sound from the leak was reported to have been heard, the leak also produced a condensation trail around 15 m high due to the rapid reduction in pressure of the gas leaking from the pipe. At 9:00 am the gas ignited causing an explosion, this created a fireball approximately 150 – 200 m high with a temperature of 3000°C at the centre. In the explosion an 11 m section of pipeline was ejected a distance of 150 m. The pipeline was isolated from the gas network two minutes later, the flare from the pipeline rupture continued to burn for a further 20 minutes. Army units had to be called in to help co-ordinate the response and help transport victims to hospitals and specialist burn units. A motorway was closed and local residents displaced while the incident was dealt with and the area made safe.

Figure 1.5: Photograph showing the approximately 150 m high flare resulting from the ignition of the gas leaking from the Ghislenghien pipeline rupture at approximately 9 am on 30th July 2014. The incident resulted in 24 fatalities, 132 serious injuries and significant property damage in the vicinity. Image courtesy of Belga Image.

The pipeline was 1 m diameter steel pipe operating at a pressure of 80 bar with a depth of coverage of 1.1 m and a wall thickness of 13 mm. The pipeline ran from the port of Zeebrugger to France [41].

Figure 1.6: Photograph showing the crater resulting from the explosion of the gas leaking from the Ghislenghien pipeline rupture on 30th July 2014. The ends either side of the 11 m section which was ejected in the ignition are visible, as is the damage to surrounding buildings and the rubble created. Image courtesy of Associated Press.

The incident had many consequences that can be separated into four categories: the human consequence, property damage, economic consequences and reputation loss. The human cost of the incident was 24 fatalities which included: five fire-fighters, one police officer and five employees making it the most deadly industrial accident in Belgium since 1956. 132 people suffered physical injuries, predominantly burns. Assessment of the impact of the incident on survivors [42] showed that 42.2 % of the 33 survivor sample size had not returned to work due to the psychological effects 12 months after the incident. The study also found PTSD symptoms in those surveyed did not significantly reduce in the two year period immediately after the disaster. The property damage was total destruction of the industrial site within a radius of 200 m from the leak, rooves and cars were damaged or destroyed within a 1200 m radius of the incident. The property damage was estimated in October 2004 to be €100 million. 14 companies and individuals were charged by Belgian state prosecutors with causing unintentional injuries and manslaughter in relation to the explosion, Fluxys was the main defendant in the proceedings. On the 22nd February 2010 Fluxys was acquitted while three other defendants were found guilty. This decision was appealed by the public prosecutor and on 28th June 2011 Fluxys was found jointly responsible for the incident [43].

1.1.3.2 Carlsbad pipeline explosion

On the morning of the 19th August 2000 an explosion occurred near to the Pecos river crossing near to Carlsbad in New Mexico, America due to a steel gas transmission pipe rupture [44]. The explosion resulted in 12 fatalities, three cars being destroyed and two pipeline suspension bridges being badly damaged. An investigation found the incident to have been caused by extensive wall loss due to corrosion of the interior of the pipeline. An image of the site can be seen in figure 1.7 showing the rupture site and the area in which the victims were camping and the pipeline river crossing. The fire from the ruptured pipeline is shown in figure 1.8.

On 19th August 2000 at 5:26 am an alarm triggered at the gas control centre in El Paso showing a rapid loss of pressure on the pipeline into the Pecos River compressor station. The controller contacted the Pecos River district lead operations specialist and requested someone to go to the compressor station. At 5.35 am the pipeline rupture was detected due to the fire. The pipeline was shut-off using the valves and the fire burned out at 6:21 am. A 14 m length of the pipeline was ejected approximately 88 m from the rupture by the explosion [5]. The explosion caused a 15.5 m by 34.5 m crater, this is shown in figure 1.9.

The investigation into the failure discovered severe internal corrosion along the bottom of the inside wall of the pipe with no evidence of corrosion along the top half or on the exterior of the pipe, this corrosion extended for 6.5 m along the pipe wall. The metal loss in the corrosion was approximately 72 % of the wall thickness, this loss of wall thickness led to overstress of the pipe wall causing

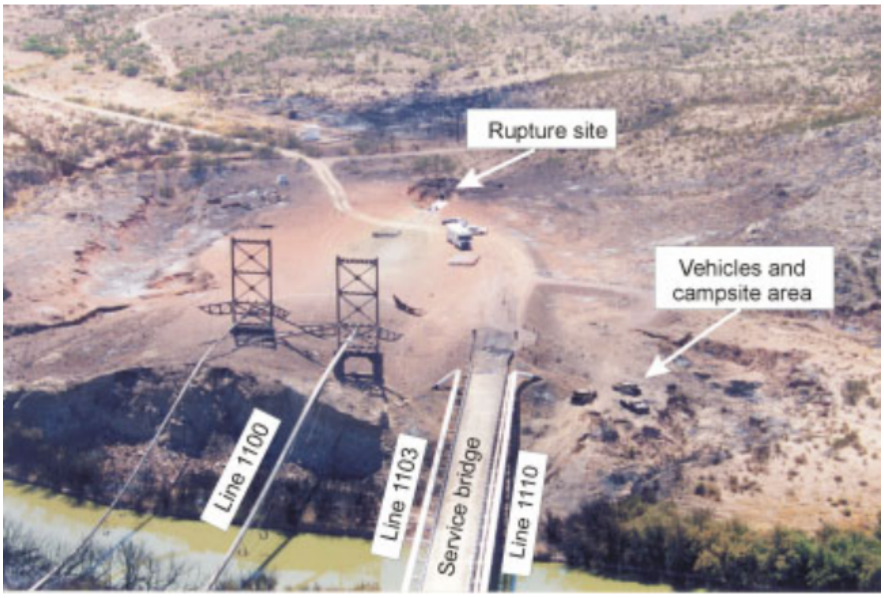

Figure 1.7: Photograph showing the site of the pipeline rupture in Carlsbad, New Mexico on 30th August 2000. The site of the rupture, the area in which the victims were camping and the pipeline river crossing can be seen. On the image various pipelines are shown, line 1103 was the line which ruptured. [5].

Figure 1.8: Photograph showing fire due to ignition of gas leaking from a pipeline rupture in Carlsbad, New Mexico on 19th August 2000. The pipeline river crossing suspension supports can be seen in the foreground. The ignition resulted in 12 fatalities and approximately $1 million in property damage. [5].

Figure 1.9: Photograph showing the crater from the ignition of the gas from a pipeline rupture in Carlsbad, New Mexico in 30th August 2000. The crater is approximately 15.5 m by 34.5 m in size and the ends of the pipe left when a 14 m length was ejected by the ignition are indicated by the black arrows. The pipeline river crossing suspension supports can be seen in the background[5].

the failure. The pipeline was 30″ diameter steel pipe operating at a pressure of 46 bar and a wall thickness of 8.5 mm. The pipeline was regularly pigged for cleaning and in-line inspection however due to a reduced port valve the section where the rupture occurred could not be pigged. A 33 mile length of the piggable section of the line was inspected in February 2000, this showed no regions of internal corrosion of concern. The section that failed had not been inspected internally since its construction in 1950 due to it being unpiggable. Routine visual inspection had not found any traces of corrosion as this only showed the external surface of the pipe [5].

The incident resulted in the fatalities of a group of 12 camping approximately 200 m away from the site of the rupture. The operating company received a \$15.5 million fine and the court mandated \$86 million improvements to corrosion controls and pipeline modification due to the incident. The total property damage caused by the incident was approximately \$1 million [45].

1.1.3.3 San Bruno pipeline explosion

On the evening of the 9th September 2010 an explosion occurred in a residential area of San Bruno in California, America due to an underground steel pipeline rupturing. The explosion killed eight people, severely injured 10 more and caused minor injuries to a further 48. The investigation into the incident found that it was caused by over pressure stressing a defect in a longitudinal seam of a short section of pipe [46]. The resulting flare from the ignition is shown in figure 1.10.

On the 9th September 2010 scheduled engineering work was being conducted at the Milpitas gas control terminal, this work caused multiple brief interruptions in the live pipeline data. During the work the valves were kept open manually to prevent fail closed states due to interruptions in electrical supply. At 4:38 pm the electrical work was completed and the valves returned to automatic operation. Operators at the terminal depowered the circuits that had been replaced, this inadvertently cut the power to a control panel causing erratic voltages on the valve controls causing all valves to fully open, when the power was restored they remained fully open. At 5:22 pm 60 alarms were displayed on the console including controller error and high pressure alerts. When the alarms occurred,

Figure 1.10: Photograph showing the fire resulting from the ignition of gas leaking from a pipeline rupture in a residential area of San Bruno, California on 7th September 2010. The ignition resulted in eight fatalities, 10 severe injuries and approximately $13.5 million of property damage. Image courtesy of Associated Press.

the pressure in the pipeline was reading 25 bar, this increased to 28.8 bar by 5:25 pm and to 34.5 bar at 5:52 pm. The pipeline was returned to its normal operating pressure at 6:02 pm. The line ruptured at 6:11 pm, this was detected at 6:15 pm when the pressure dropped to 10 bar. The pipe was a 30″ diameter steel pipe with a wall thickness of 9.5 mm and a maximum allowable operating pressure of 27.5 bar [6].

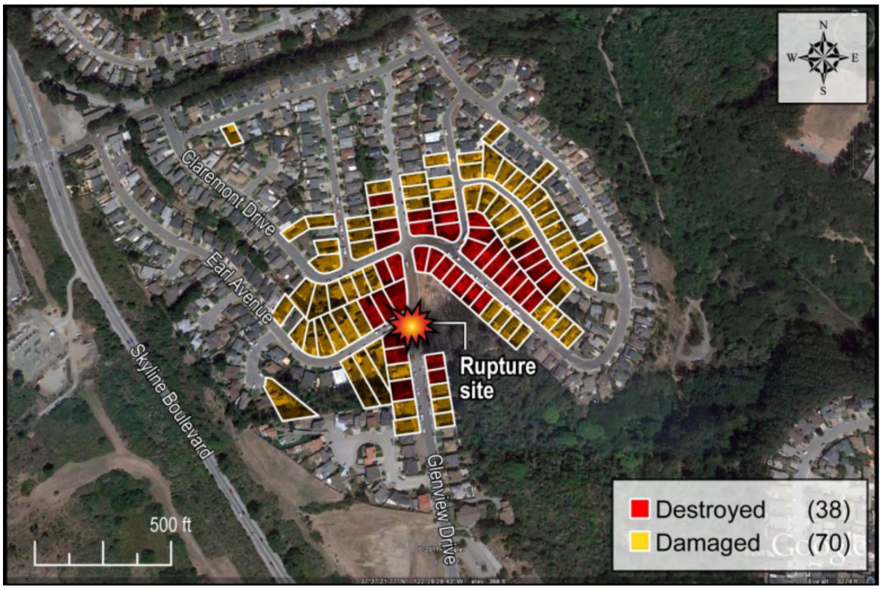

Figure 1.11: Map showing the location of the fire resulting from the ignition of gas leaking from a pipeline rupture in a residential area of San Bruno, California on 7th September 2010 and the houses which were either damaged or destroyed [6].

The investigation found that the seam weld of the pipe that failed had not fully penetrated when the pipe was constructed, this was not discovered when the pipe was being laid in 1956. The weld defect grew in size along the seam weld over time becoming a fatigue fracture which ruptured through the increased pressure during the work on the terminal. On analysis of the pipe the fracture feature was consistent with a rupture of a pre-existing 61 mm long crack. The pipeline was unpiggable due to different diameter pipe sections in the pipeline and no adequate examination methodology was put in place to detect the defect in the pipe wall [6][47].

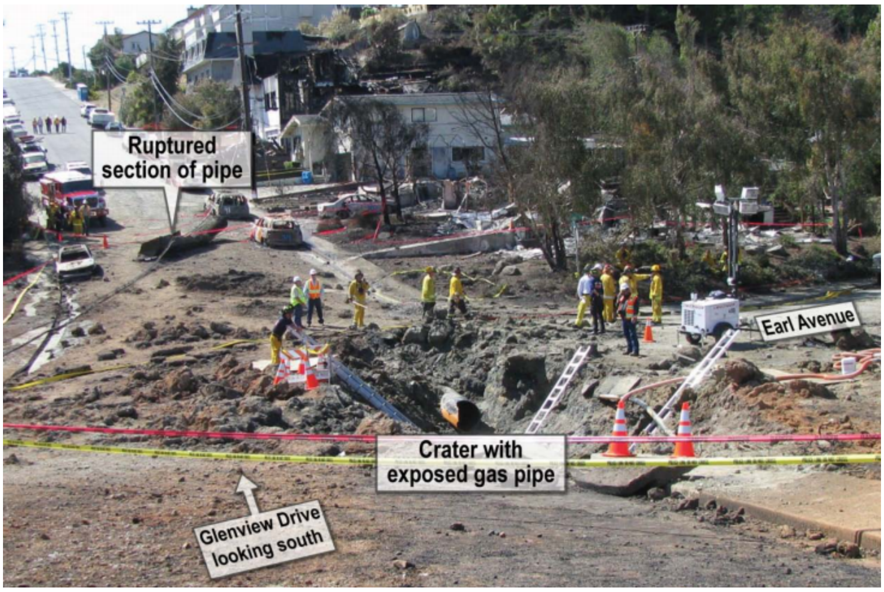

Figure 1.12: Photograph showing the crater created by the ignition of gas leaking from a pipeline rupture in a residential area of San Bruno, California on the 7th September 2010, the crater was approximately 22 m by 8 m. The 8.5 m section of pipe can be seen in the image approximately 30 m away from the crater [6].

Figure 1.13: Photograph showing the damage to houses in the aftermath of ignition of gas leaking from a pipeline rupture in a residential area of San Bruno, California on 7th September 2010. Houses can be seen to have been completely destroyed. Image courtesy of Associated Press.

When the pipe ruptured an estimated 1.4 mcm of gas was released, when the gas ignited the explosion resulted in eight fatalities, 10 people seriously injured and 48 people with minor injuries. The resulting fire destroyed 38 homes, caused severe damage to 17 and minor damage to 53; 74 cars were damaged or destroyed. A play park and a woodlands were also damaged by the fire. The accident response involved 600 fire-fighters and 325 law enforcement personnel, the fires burned for 50 hours after the initial ignition and 300 houses were evacuated. The damage to the neighbourhood following the event is shown in figures 1.13 and 1.14. The initial ignition left a 22 m by 8 m crater and ejected an 8.5 m section of pipe 30 m.

The operating company for the pipeline was fined $1.6 billion by the state regulators for the incident and prosecuted for 11 counts of violating the pipeline safety act. The company was found guilty of five counts and were given a $3 million fine, ordered to perform 10,000 hours community service and ordered to spend $3 million to publicise its criminal conduct [48]. The operator also paid over $560 million in compensation to the victims and city, the cost of repairs to the pipeline was $13.5 million and the value of the lost gas was estimated at

$263,000.

Figure 1.14: Photograph showing the destroyed houses and a burnt out car in the aftermath of ignition of gas leaking from a pipeline rupture in a residential area of San Bruno, California on 7th September 2010 [6].

1.1.3.4 Sissonville pipeline rupture

On the afternoon of the 11th December 2012 an underground gas pipe ruptured close to the I-77 interstate highway near to Sissonville in West Virginia, America. The leaking gas ignited causing the destruction of three houses and 250 m of the highway. The investigation into the incident found that the cause of the rupture was corrosion leading to extensive metal loss of the pipe wall [7]. An aerial image showing the flare from the ignited gas is shown in figure 1.15, a view from the highway of the flare is shown in figure 1.16.

At 12:41 pm on the 11th December 2012 a rupture occurred in the pipe, this ignited causing a flare to burn towards the highway. The pipe was a 20″ diameter steel pipe with a wall thickness of 7.1 mm operating at 64 bar. The rupture was determined to be due to pipe wall metal loss from external corrosion of the pipe. The corrosion was a section 1.8 m longitudinal to the pipe by 0.6m on the external surface on the bottom of the pipe, this caused approximately 63% metal

Figure 1.15: Aerial photograph showing the flare due to the ignition of gas leaking from a ruptured gas pipeline in Sissonville, West Virginia on 11th December 2012. The ignition destroyed three houses and the surface of the I-77 highway resulting in a prolonged closure for repairs. Image courtesy of West Virginia state police.

Figure 1.16: Photograph showing the flare due to the ignition of gas leaking from a ruptured gas pipeline in Sissonville, West Virginia on 11th December 2012. The ignition destroyed three houses and the surface of the I-77 highway resulting in a prolonged closure for repairs. Image courtesy of West Virginia state police.

loss in this region, weakening the pipe wall. The pipe fractured longitudinally creating a 6.2 m long tear in the pipe wall. The corrosion resulted from the protective coating being scraped away by rocks when the trench was backfilled during construction, which had not been detected due to the pipeline being unpiggable.

The fire caused by the ignition of the leak left three houses destroyed. 250 m of the highway surface was damaged by the heat, requiring a 19 hour closure for resurfacing. The cost of the repair to the pipeline was $2.9 million, the upgrades to the system to better accommodate pigging cost $5.5 million and the value of the gas lost in the fire was $285,000.

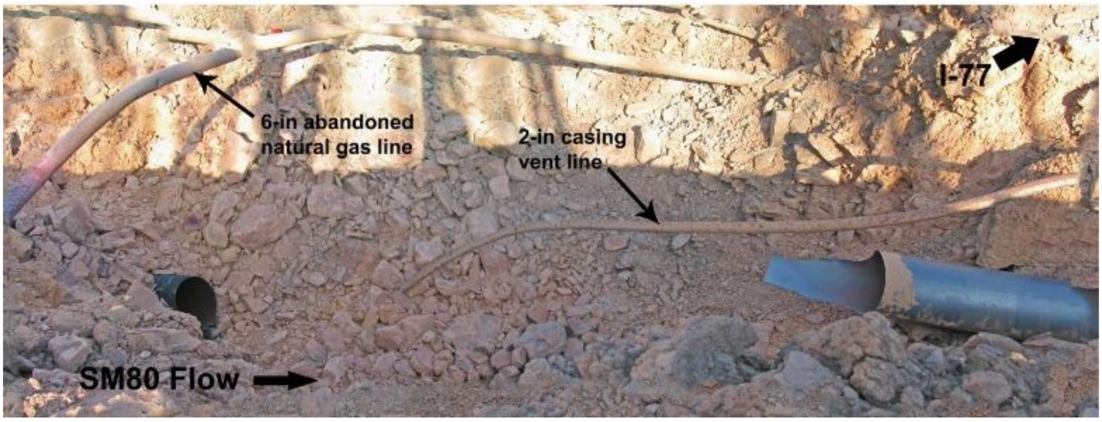

Figure 1.17: Photograph showing the crater caused by the ignition of gas leaking from a ruptured gas pipeline in Sissonville, West Virginia on 11th December 2012 [7].

1.1.4 Rationale discussion

Natural gas is a major component of the UK's energy consumption, this is delivered throughout the country by a network of steel pipelines called the national transmission system (NTS) which was constructed starting in the 1960s. The greatest threat to the supply of natural gas is infrastructure failure, the loss of gas supply can have severe consequences, especially during winter when demand is at its peak due to heating requirements.

European and Canadian incident data for gas pipelines show that corrosion has become the predominant primary cause of unplanned releases of gas from pipelines, this has increased with the age of the pipelines. Corrosion develops over time and so these incidents are preventable through early detection and corrective action. Accidental damage caused to the pipelines through external events such as being struck by an excavator is also a major cause of pipeline incidents, these can be reduced through accurate mapping of the pipelines and inspection in case of a strike.

Currently in-line inspection (ILI), in which a tool called a pig is propelled down the inside of the pipe is the major inspection technique. This carries a risk to the pipe due to the need to open the pipelines to insert and remove the pig as well as the risk of sending a large mass down the centre of the pipe. Pipelines must be designed to accommodate an ILI pig as narrowing in the pipe, valves and tight bends can render the pipe unpiggable.

Four incidents have been presented:

- The incident at Ghislenghien was due to an excavator striking the pipe during construction work, this was a piggable pipe but was not pigged after the strike was reported. A need exists for a fast and easily deployable inspection technique to inspect the pipeline after reported accidental strikes to assess the need for immediate action to prevent an incident.

- The incident at Carlsbad was due to corrosion that had not been detected due to the pipe being unpiggable and no alternative inspection techniques put in place.

- The incident in San Bruno was due to a construction defect that failed due to operator error causing an overpressure in the pipeline. The pipeline was unpiggable due to the different diameters of pipe sections in the pipeline, this prevented the defect from being detected and corrective action taken.

- The incident in Sissionville was due to external corrosion from damage to the pipeline protective coating. The pipeline was unpiggable and so this corrosion had not been detected prior to the incident.

These incidents demonstrate a need for a complimentary inspection technique to ILI pigging to detect defects in unpiggable pipelines, to increase the positional accuracy of pipeline maps and to allow a fast response to reports of accidental strikes on pipelines due to the ease of deployment versus pigging. Large stand-off magnetometry has the potential to compliment ILI inspections by allowing coverage of unpiggable pipelines and be deployed rapidly to assess pipelines following an incident such as an accidental strike or to allow inspection of a pipeline involved in a land slip where the angle and diameter of the pipe following the incident are not known and so cannot be safely pigged.

1.2 Project objectives

The objective of this research was to investigate ways of improving the detection of pipeline features and locational accuracy of detected features of the large stand-off magnetometry survey array developed at the University of Leeds in co-operation with Speir Hunter.

This overall objective was broken into research objectives which could be investigated in the laboratory to improve the sensitivity and accuracy of the survey array. These were:

1 To investigate the presentation of the magnetometry survey data to improve anomaly location by a user.

2 To investigate if there is an optimum magnetometer separation in the survey array and determine the anomaly to separation relationship.

3 To investigate the locational relationship between the magnetic anomalies and pipeline features and how this affects the accuracy of feature location.

4 To use the data gathered in the laboratory to provide recommendations for future development on the large stand-off magnetometry survey array.

1.3 Contribution

This thesis contains the following chapters:

- Chapter 2

Gives a brief history of magnetometry in geophysical surveys including its expansion into pipeline surveying including the patented survey equipment designed at the University of Leeds and deployed by Speir Hunter Ltd, the patent holders. This chapter shows that the detection of anomalies using magnetometry has been used extensively in geophysics and archaeology and that this has been extended to pipeline inspection. This has been further developed with the design and construction of a survey array for inspections of pipelines.

This chapter presents a model for the magnetisation of a hollow cylinder which has been expanded to consider a pipe section. A model for the magnetic field from a defect in two dimensions has been considered and expanded to give magnetic data at three-dimensional positions to allow the gradient field to be calculated for the defects in this model.

- Chapter 3

Gives details of the laboratory set-up used for the experiments carried out in later chapters to investigate the survey array. This chapter also details the repeatability of the data gathered in the laboratory to give statistical validity to the results in the experiments presented later in this thesis.

- Chapter 4

Gives details of techniques considered for the analysis and presentation of the laboratory and survey data gathered in large stand-off magnetometry. This includes the use of linear integral convolution (LIC) to represent this data, a technique that has not previously been demonstrated in literature for magnetometry geophysics or NDT.

This chapter suggests that adding two magnetometers in line in the magnetometry survey array would allow linear integral convolutions to be generated from the survey data giving a texture representing the magnetic vector field from the pipeline to be produced for a strip above the pipe, potentially allowing additional anomalies to be picked out by an end user.

- Chapter 5

Gives details of investigations carried out in the laboratory into the optimum angle between the inner and outer magnetometers in the magnetometry array in the large stand-off survey system to give the best sensitivity to magnetic anomalies. This has not previously been considered for the survey system that is currently deployed for magnetometry surveys of pipelines for NDT.

This chapter details laboratory investigations on conduits with a discontinuity in the material magnetic susceptibility caused by cutting the conduit with a pipe cutter. The anomaly in the magnetic gradient field was measured and the amplitude of the anomalies investigated for different magnetometer separations. This chapter provides experimental evidence of the existence of an optimum angle between the magnetometers and suggests optimising the surveying the magnetometry array to the survey being completed.

- Chapter 6

Gives details of investigations carried out in the laboratory into the effects of distance from the pipeline on the magnetic anomalies used to determine pipeline feature locations. This has not previously been investigated in large stand-off magnetometry for pipeline inspection.

This chapter details laboratory investigations of simulant pipelines constructed from dipole pipe sections, this investigation looked into the anomaly position in the magnetic field for heights above the pipeline. Both AlNiCo magnets and short magnetised conduit sections were used as simulants for pipe sections.

This chapter provides experimental evidence of an offset in the position of detected anomalies along the pipeline centreline generated by the surrounding pipe sections, this suggests adding additional layers of magnetometer to the survey equipment would improve locational accuracy of the pipeline features.

This research has contributed to the following:

- Speir Hunter LTD (2018) World Patent Publication No WO/2018/046947 “Pipeline mapping system”.
- S. G. H. Staples, B. T. H. Varcoe, C. Vo, D. Cowell, C. Cookson, S. Freear. “Bar magnet model for large stand-off magnetometry”, Unpublished manuscript, 2016.

Chapter 2

Background of magnetic non-invasive inspection for pipelines

2.1 History of large stand-off magnetometry

2.1.1 Large strand-off magnetometry in exploration geophysics

Magnetic survey methods use the induced and remnant magnetic fields in materials, these are a function of the susceptibility of the material and the magnetising field. Large stand-off magnetometry surveying techniques are passive techniques in which the local geomagnetic field is used as the magnetising field, rather than an active technique which uses an imposed field to which the reaction of the survey area to the field is measured [49].

The first recorded observation of the effects of the geomagnetic field was approximately 200 BC when it was noticed that a naturally magnetised piece of magnetite, known as a lodestone [50], would return to face in the same direction each time if suspended from a piece of silk fibre, though the reason for this was not known at the time [51]. The magnetisation of iron in the geomagnetic field was first reported in 1040 AD [52] when it was observed that a thin piece of iron heated to red-hot then placed on a line running north-south and allowed to cool would return to pointing north-south when floating in a bowl of water [53]. This was adopted for navigation [54]. This effect occurred because the iron was heated to above its Curie temperature, the point which a material above this temperature loses its permanent magnetic property. As the iron cooled below this point the domains aligned to the geomagnetic field leaving the iron with a permanent magnetisation along its axis. This magnetised iron strip would then point to the north as it aligned with the geomagnetic field when allowed to rotate freely such as when floating in a bowl of water.

The first reported successful use of passive magnetometry for magnetic exploration was in 1688 for locating iron ore for mine locating [55]. This iron ore was a magnetite vein which exhibits a natural magnetisation due to the geomagnetic field [56]. This survey was completed with a sun compass where the shadow from a pole cast by the sun is used to determine geographic north and the variation of a compass from this noted. With the invention of more advanced magnetometers magnetometry became a major survey technique. During World War II the Allies experimented with using the newly invented fluxgate magnetometer mounted to aircraft to locate the distortion of the geomagnetic field caused by submerged Axis submarines [49].

More recently magnetometry survey techniques have been used for locating mineshafts, which give a different signal to natural caves [57], locating illegally buried toxic or hazardous waste [58] and in locating unexploded ordnance in which the shock of the impact of the ordnance removes its magnetic history [59].

Passive magnetometry is the most frequently used survey technique in archaeology [60], this was first used in 1959 to locate the site of Romano-British pottery kilns in a four acre area in a short period of time before construction was to be carried out on the site [61]. The location of fires can be detected as these convert non-magnetic hematite in the soil into its magnetic form magnetite which has a much greater susceptibility [62].

2.1.2 Large stand-off magnetometry of pipelines

It was found that when a geophysical magnetic survey was carried out in an area where a pipeline was present [63], the magnetic fields from the pipe was periodic along the pipe with a period approximately the same length as the length of a pipe section in the pipeline [8]. As a result of this observation surveys were carried out on three pipelines with known positions and section lengths.

One of these surveys was carried out on a 450 mm diameter pipe constructed from ductile iron with pipe section lengths of 5.5 m, at a depth of 2 m using two fluxgate magnetometers to calculate the vertical magnetic gradient from the pipe. This was done to negate the need for corrections for variation in the geomagnetic field. The results from the survey show peaks in the gradient of the magnetic field of 0.5 μT/m with the peaks occurring at regular periods. It was found that the location of these peaks coincided with the locations of the joints between the pipe sections [64]. Figure 2.1 shows the contour of the magnetic field gathered in these surveys, reproduced from Sowerbutts' work [8].

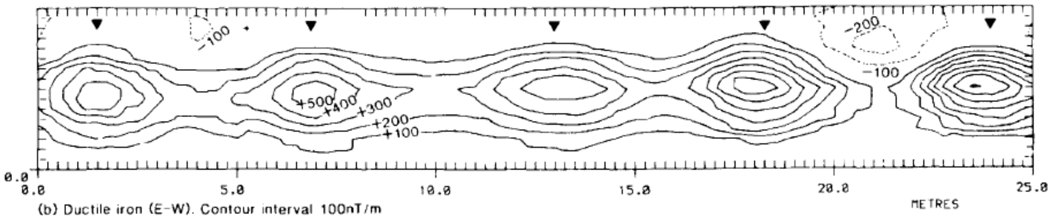

Figure 2.1: Magnetic contour plot of a ductile iron pipeline with a diameter of 450 mm and a section length of 5.5 m at a depth of 2 m. The position of joints between the pipes is marked on the plot and shows that the peaks in the magnetic gradient field are approximately at the position of these joints. Reproduced from Sowerbutts' work [8].

This result and other results presented in the same work on similar pipelines show that the positions of the joints between these sections can be predicted to within 1 m using these peaks. These results suggest that the individual pipe sections have a remnant magnetisation from manufacture and other effects such as current from cathodic protection [65] which form a single magnetic dipole in the pipe section.

2.2 The Villari effect

Magnetisation in ferromagnetic materials can be explained in terms of domains [66]. A domain is a microscopic volume in the material in which the atomic spins are aligned, this produces a region in the material with a saturation magnetisation. In an unmagnetised material these domains are randomly aligned with respect to each other, when a force is applied which causes these domains to align with each other a net magnetisation is produced in the material [67].

When a material is subjected to a magnetising field the length of the material changes [68], this effect is known as magnetostriction. This is due to the domains in the material rotating in response to the magnetising field increasing the magnetostatic energy in the material. The system reacts to reduce this energy by expanding the material [69]. These changes are small, typically in the order $^{\Delta l}/_{l} \sim 10^{-5}$ where l is the length of the material before magnetisation and Δl is the change in length of the material at saturation magnetisation, this is known as the co-efficient of linear magnetostriction, λ_s [70].

The inverse of magnetostriction, known as the Villari effect has also been observed [71]. In the Villari effect altering the stress in the material changes the material's magnetisation. The Villari effect is due to the response of the magnetic susceptibility of the material to the change in the stress of the material [72]. This change in susceptibility changes the magnetisation of the material due to the reliance of the magnetisation on the magnetic susceptibility shown in equation 2.1 [73].

$$M = \chi_M H \tag{2.1}$$

Where

M is the magnetostriction for the material at magnetic saturation,

H is the magnetising field, and

χ_M is the magnetic susceptibility of the material.

Ferromagnetic materials have a hysteretic magnetisation relationship with the magnetising force [74]. As the domains are aligned by the magnetising force the magnetisation of the material is increased, if this force is removed the domains relax but retain some of the direction imposed on them by the force as energy is required to rotate domain walls. This leaves the material in a magnetised state after the magnetising force has stopped acting upon it, this magnetisation is known as remnant magnetisation [75]. An example magnetic hysteresis curve is shown in figure 2.2.

In materials with a positive magnetostriction co-efficient such as iron and steel, compressive stress tends to decrease the magnetisation in the material while tensile stress tends to increase the magnetisation in the material. This change in the magnetisation for the same magnetising field due to the stress has the effect of rotating the hysteresis curve, this is shown for compressive and tensile stress in figure 2.3 [10].

This magnetic hysteresis means that when a material is magnetised by the change in stress, an amount of the magnetisation induced remains when the

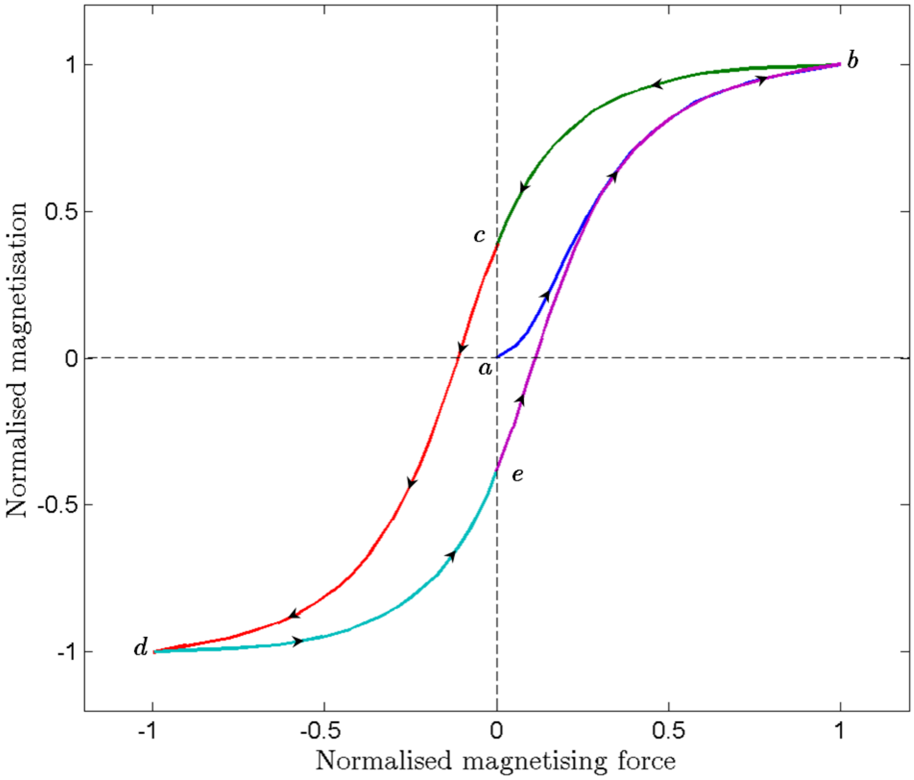

Figure 2.2: Magnetic hysteresis curve of the magnetisation of a sample versus the magnetising force acting upon it. When a material with no magnetisation, at point **a**, experiences a magnetising force its magnetisation increases until saturation, point **b**. When the magnetising force is removed the material does not return to an unmagnetised state due to the energy required to relax the domains, this magnetisation is the remnant magnetisation shown at point **c**. When the material is subject to a magnetising force in the opposite direction to the material magnetisation, the magnetisation reduces and aligns to the magnetising force giving the opposite saturation, at point **d**. When this force is removed the material returns to the remnant magnetisation in that direction, point **e**. This magnetisation continues around the hysteresis loop with changes in the magnetising force [9].

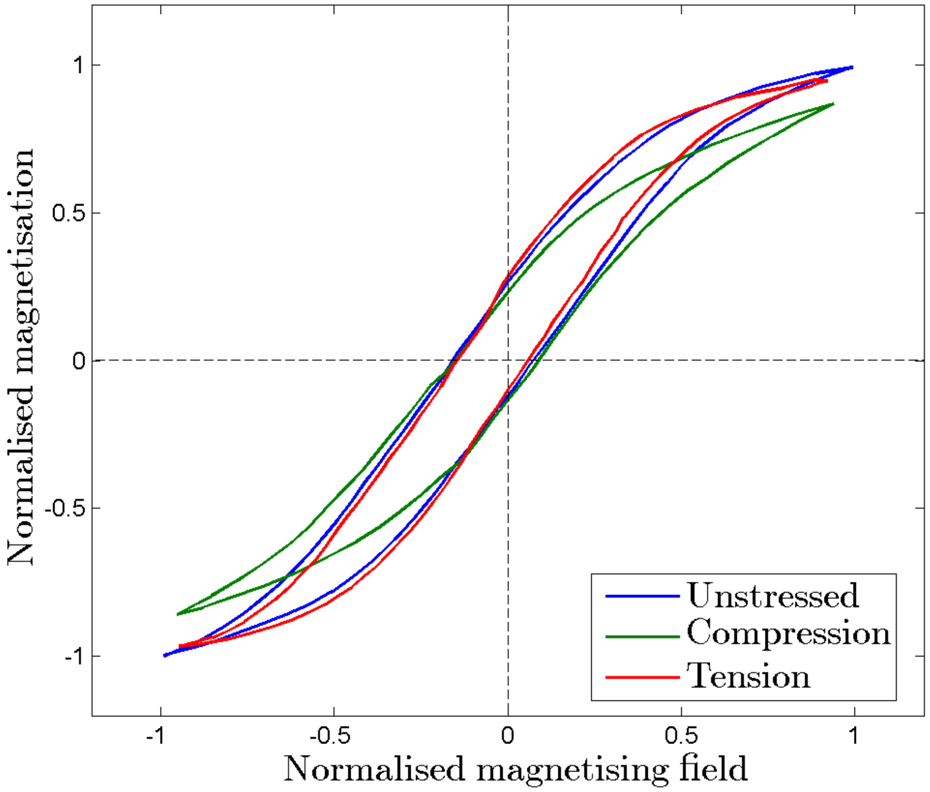

Figure 2.3: Plot showing the magnetic hysteresis loop for a material with a positive magnetostriction co-efficient under stress. Compressive stress tends to decrease the magnetisation at a given magnetising field, while tensile stress tends to increase the magnetisation at a given magnetising field [10].

stress is relaxed [76]. If the material is subjected to stress cycling the first stress gives rise to the greatest increase in magnetisation, when this stress is relaxed the material returns to its remnant magnetisation [77]. When the material is stressed again it starts from this remnant magnetisation, increases to a peak magnetisation with the stress. When the stress is relaxed again the material returns to a greater remnant field than the first cycle. With repeated cycling this magnetisation tends towards a reversible, anhysteretic magnetisation stress relationship [78]. In this anhysteretic state the material will reversibly alternate between a remnant and magnetised state with stress.

The stress induced magnetisation due to the Villari effect was proposed as a magnetometry inspection technique in ferromagnetic structures to detect the flux leakage from high stress regions. The Villari effect can be used to locate stress concentrations zone is in buried gas pipelines that could be indicative of a defect at that location [79][80].

2.3 Magnet model of pipe sections

2.3.1 The pipe section dipole model

When a pipe is manufactured it retains a magnetisation due to the geomagnetic field. A long thin cylinder has a preferential direction of magnetisation parallel to the centreline of the cylinder [81]. This allows individual pipe sections to be thought of as a single dipole with an axial magnetisation when viewed at a sufficient distance from the pipe. This dipole approximation gives rise to the pipe section dipole model which treats each pipe section in the pipeline as an axially magnetised dipole which are randomly aligned or antialigned with respect to each other [82]. A model for the magnetic field from an axially magnetised pipe section is analysed in section 2.3.2.

2.3.2 Magnetic model of an axially magnetised cylinder

Only a uniformly magnetised sphere will produce a perfect magnetic dipole, other magnetic material geometries can be approximated as a dipole field at large distances [83]. First a solid axially magnetised cylindrical permanent magnet is considered. The magnetisation inside a permanent magnet, $\vec{M}$, is given by equation 2.2 [84][85].

$$\vec{M} = \begin{bmatrix} \frac{1}{1+\chi N_1} & 0 & 0 \\ 0 & \frac{1}{1+\chi N_2} & 0 \\ 0 & 0 & \frac{1}{1+\chi N_3} \end{bmatrix} \left(\chi \vec{H}_a + \vec{H}_r\right) \tag{2.2}$$

Where

$\vec{M}$ is the magnetisation inside a permanent magnet,

χ is the susceptibility of the material,

N_1, N_2, N_3 are the shape demagnetisation factors along the principal axes of the magnet, these are shape dependant and $\sum_{i=1}^{3} N_i = 1$ [86][87],

$\vec{H}_a$ is the applied field, and

$\vec{H}_r$ is the magnetic remanence of the material.

To take into account the shape a dimensional ratio must be defined, in the case of a cylinder this is the diameter to length ratio, this is defined as β in equation 2.3.

$$\beta = \frac{D}{L} \tag{2.3}$$

Where

β is the material shape parameter, in the case of a cylinder its diameter to length ratio,

D is the outer diameter of the cylinder, and

L is the length of the cylinder.

In order to calculate the magnetisation $\vec{M}$ from equation 2.2 it is necessary to calculate the shape demagnetisation factors for the cylinder. The demagnetisation factors can only be calculated exactly for an ellipsoid, for other geometries the factors are an approximation [84][88]. These factors for a cylinder can be found in look up tables [86], in the case of a cylinder the radial demagnetisation factor,

N_r, is given and the axial demagnetisation factor, N_a, can be calculated as $N_a = 1-2N_r$ [89]. Values for the radial demagnetisation factor of a cylinder for different diameter to length ratios are shown in table 2.1 [13].

β	N_r
0.01	0.00105
0.05	0.00617
0.1	0.0172
0.125	0.02
0.2	0.04
1	0.27

Table 2.1: Table of the values of the radial demagnetisation factor, N_r, for given diameter to length ratios, β [13].

The values of the demagnetisation factor versus the diameter to length radius for the cylinders are shown by red markers on a logarithmic plot in figure 2.4. The calculated line of best fit for these values is also shown, this will be used to calculate the values for the demagnetisation factors for this section.

The line of best fit shown in figure 2.4 taken from values of the radial demagnetisation factor for given ratios of diameter to length is given by equation 2.4.

$$N_r = \beta^{1.2286} e^{-1.3022} \tag{2.4}$$

For a permanent magnet with no external fields the magnetic field can be calculated from a scalar potential field Φ using equations 2.5 [90].

$$\vec{H} = -\nabla\Phi \qquad \nabla^2\Phi = \nabla \cdot \vec{M} \tag{2.5}$$

Where

$\vec{H}$ is the magnetic field,

Φ is the magnetic scalar potential, and all other terms are defined above.

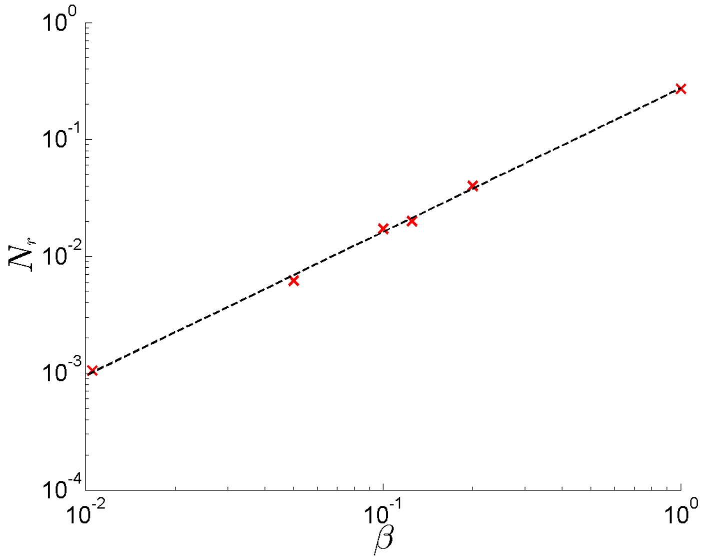

Figure 2.4: Logarithmic plot showing the radial demagnetisation factors, N_r, versus the given diameter to length ratio, β, from table 2.1 marked in red. The calculated line of best fit given by equation 2.4 is shown by the dashed black line.

These can be solved by direct integration shown in equation 2.6 [91].

$$\Phi\left(\vec{P}\right) = \frac{1}{4\pi}\left(\int_v \frac{\nabla \cdot \vec{M}}{\mid \vec{P} - \vec{\rho} \mid} dv + \oint_S \frac{\hat{n} \cdot \vec{M}}{\mid \vec{P} - \vec{\rho} \mid}\right) da \tag{2.6}$$

Where

$\hat{n}$ is the normal unit vector pointing out of the surface of the magnetic material,

$\vec{P}$ is the vector from the centre of the magnetic material to the point of interest,

$\vec{\rho}$ is the vector from the centre of the magnetic material to the point of integration, and all other terms are defined above.

For a material with a constant susceptibility and uniform magnetisation through the volume $\nabla \cdot \vec{M} = 0$, therefore equation 2.6 becomes equation 2.7.

$$\Phi\left(\vec{P}\right) = \frac{1}{4\pi}\left(\oint_S \frac{\hat{n} \cdot \vec{M}}{\mid \vec{P} - \vec{\rho} \mid} da\right) \tag{2.7}$$

This can be expanded using a Taylor series to give equation 2.8 [92].

$$\Phi\left(\vec{P}\right) = \frac{1}{4\pi}\sum_{n=0}^{\infty} \frac{1}{P^{n+1}} \oint_S \rho^n P_n\left(\hat{P} \cdot \hat{\rho}\right)\left(\hat{n} \cdot \vec{M}\right) da \tag{2.8}$$

Where

P_n are the Legendre polynomials. [93],

$\hat{P}$ is the unit vector in the $\vec{P}$ direction,

$\hat{\rho}$ is the unit vector in the $\vec{\rho}$ direction, and all other terms are defined above.

Due to the definition of $\hat{n}$ and the identity $\vec{a} \cdot \vec{b} = \mid a \mid\mid b \mid \cos\theta$, where $\vec{a}$ and $\vec{b}$ are vectors, $\mid a \mid$ and $\mid b \mid$ are the vector magnitudes and θ is the angle between $\vec{a}$ and $\vec{b}$, the values for $\hat{n} \cdot \vec{M}$ for an axially magnetised cylinder are given in equation 2.9.

$$\hat{n} \cdot \vec{M} = \begin{cases} \mid M \mid & \text{For the top surface of the cylinder} \\ - \mid M \mid & \text{For the bottom surface of the cylinder} \\ 0 & \text{Radially from the cylinder} \end{cases} \tag{2.9}$$

A spherical coordinate system as shown in figure 2.5 is defined for determination of the terms in equation 2.8.

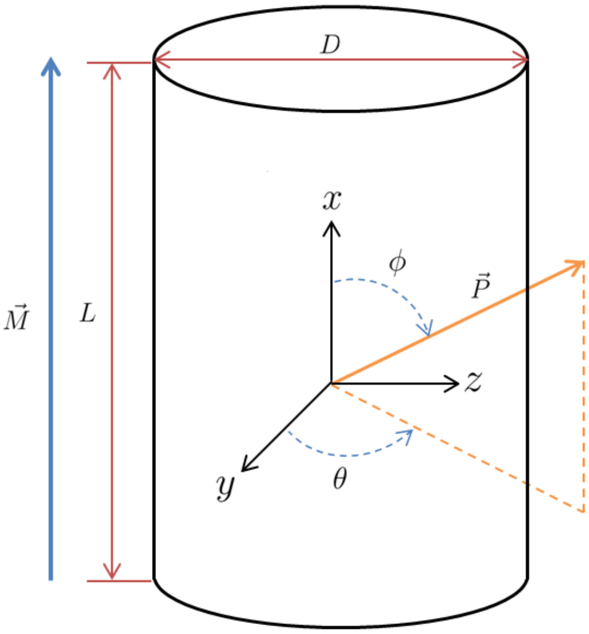

Figure 2.5: Spherical and cartesian co-ordinate systems for an axially magnetised cylinder of length L and diameter D, showing the vector $\vec{P}$ from the centre of the cylinder to the point of interest.

In figure 2.5 $\hat{r}$ is the unit vector pointing in the $\vec{P}$ direction, $\hat{\theta}$ is the unit vector in the positive $\vec{\theta}$ direction, and $\hat{\phi}$ is the unit vector in the positive $\vec{\phi}$ direction.

A second co-ordinate set for integration purposes is also defined relative to the magnetisation, $\vec{M}$, these are $\hat{\rho}'$ the unit vector in the $\vec{\rho}'$ direction where $\vec{\rho}'$ is the vector from the centre of the material to the point of integration, $\hat{\theta}'$ is the unit vector in the positive θ' direction where θ' is taken from the magnet axis, and $\hat{\phi}'$ is the unit vector in the positive ϕ' direction where ϕ' is taken from an axis orthogonal to the magnet axis.

Converting to spherical co-ordinates and substituting equation 2.9, equation

2.8 becomes equation 2.10.

$$\Phi\left(P,\beta\right)=\frac{M}{4\pi}\sum_{n=0}^{\infty}\frac{\left({}^{L}\!/\!{}_{2}\right)^{n+2}}{P^{n+1}}D_n\left(P,\beta\right) \tag{2.10}$$

Where

$$\begin{aligned} D_n\left(P,\beta\right)=&\int_0^{2\pi}\int_0^{\tan^{-1}(\beta)}\frac{P_n\left(\hat{P}\cdot\hat{\rho}\,'\right)\sin\theta'}{\left(\cos\theta'\right)^{n+3}}d\theta' d\phi' \\ &-\left(-1\right)^n\int_0^{2\pi}\int_{\pi-\tan^{-1}(\beta)}^{\pi}\frac{P_n\left(\hat{P}\cdot\hat{\rho}\,'\right)\sin\theta'}{\left(\cos\theta'\right)^{n+3}}d\theta' d\phi' \end{aligned} \tag{2.11}$$

By definition $\vec{B}=\mu\vec{H}$ and from Maxwell's laws $\nabla\cdot\vec{B}=0$ [94] this means only odd n terms in the Taylor expansion of D_n are non-zero, this is shown in equation 2.12. The first non-zero term B_1 is the dipole term and is geometry independent, all higher are dependent on magnetic material geometry.

$$D_n\left(P,\beta\right)=\begin{cases}2\displaystyle\int_{(1+\beta)^{-\frac{1}{2}}}^{1}\int_0^{2\pi}\frac{P_n\left(\hat{P}\cdot\hat{\rho}\right)}{z^{n+3}}d\phi' dz & n \text{ odd.}\\ 0 & n \text{ even.}\end{cases} \tag{2.12}$$

In cylindrical geometry, in a spherical co-ordinates system $\hat{P}\cdot\hat{\rho}\,'$ becomes equation 2.13.

$$\hat{P}\cdot\hat{\rho}\,'=\sqrt{\left(1-z^2\right)}\sin\theta\left(\sin\phi\sin\phi'+\cos\phi\cos\phi'\right)+z\cos\theta \tag{2.13}$$

The magnetic field for an axially magnetised cylinder is therefore given in equation 2.14.

$$\vec{B}(\vec{P}) = \frac{\mu_0}{4\pi}\frac{m}{V}\sum_{n\ odd}\frac{\left(L/2\right)^{n=2}}{p^{n+2}}\left(\left(n+1\right)D_n\hat{r} - \frac{dD_n}{d\theta}\hat{\theta}\right) \tag{2.14}$$

Where

m is the magnitude of the dipole moment,

p is the magnitude of the displacement vector from the centre of the cylinder, and all other terms are defined above.

Given that $m\cos\theta\hat{r} = \hat{P}\hat{P}^T\vec{m}$ and $m\sin\theta\hat{\theta} = \left(\hat{P}\hat{P}^T - \mathbf{I}\right)\vec{m}$ where $\vec{m}$ is the dipole moment of the cylinder and $\mathbf{I}$ is the identity matrix, equation 2.14 can be rewritten into a co-ordinate system free form. The first term is the dipole term, this is given by equation 2.15.

$$B_1 = \frac{\mu_0}{4\pi}\frac{1}{p^3}\left(3\hat{P}\hat{P}^T - \mathbf{I}\right)\vec{m} \tag{2.15}$$

This gives a dipole field which has a dependence on the cylinder aspect ratio as the $\vec{m}$ term has a dependence on this as shown in equation 2.4. To consider a pipe this model must be expanded to include the fact a pipe is not a solid cylinder but is a hollow cylinder. A pipe can be thought of as a cylinder of magnetic material with a co-centred cylinder of the same length and a diameter given by equation 2.16 with the opposite magnetisation to the main cylinder.

$$D_2 = D_1 - 2t \tag{2.16}$$

Where

D_2 is the inner diameter of the pipe, in this model the diameter of the inner cylinder,

D_1 is the outer diameter of the pipe, in this model the diameter of the outer cylinder, and

t is the wall thickness of the pipe being considered.

In this system it is necessary to define β for each cylinder. These are $\beta_1 = {}^{D_1}/_{L}$ and $\beta_2 = {}^{D_2}/_{L}$ for the outer and inner cylinders respectively. The contribution to the magnetic field from each cylinder is scaled by the cylinder volume and summed, this is given by equation 2.18. The volume for each cylinder can be calculated in terms of β, this gives equation 2.17. Since the inner cylinder will always have a smaller outer diameter than the outer and both have the same length $\beta_1 > \beta_2$.

$$V_i = \frac{\pi}{4} L^3 \beta_i^2 \tag{2.17}$$

Where

V_i is the volume of cylinder i,

β_i is the ratio of diameter to length for cylinder i, and all other terms are defined above.

$$B = \sum_{i=1}^{2} V_i B_i \tag{2.18}$$

Where

B is the total magnetic field from the pipe,

V_i is the volume of cylinder, and

B_i is the dipole magnetic field strength calculated from equation B_1 for cylinder i.

The field from a 12 m long 36″ outer diameter pipe with a wall thickness of ${}^{3}/_{8}$″, a common dimension for buried pipe sections [95], in an axial magnetising field for a height above the pipe of 6 m was calculated from equation 2.18.

The calculated magnetic field was taken for the position of three magnetometers with a lateral separation orthogonal to the pipe centreline of 0.5 m. These were used to calculate the gradient field along the pipe length from equations 2.30 and 2.31, the same as for the magnetometry survey array detailed in section 2.5. The data from the three magnetometers in the array is used to calculate the three components of the gradient field, $\Delta\Delta B$, from the magnetic field strength measurements. This is calculated using equations 2.19 and 2.20.

$$\Delta\vec{B}_{12} = \frac{\left(\vec{B}_1 - \vec{B}_2\right)}{S} \qquad \Delta\vec{B}_{23} = \frac{\left(\vec{B}_2 - \vec{B}_3\right)}{S} \tag{2.19}$$

$$\Delta\Delta\vec{B} = \Delta\vec{B}_{12} - \Delta\vec{B}_{23} \tag{2.20}$$

Where:

$\vec{B}_1$**,** $\vec{B}_2$ **and** $\vec{B}_3$ are the three-dimensional magnetic field strengths from the magnetometers,

S is the separation between the magnetometers,

$\Delta\vec{B}_{12}$ **and** $\Delta\vec{B}_{23}$ are the three-dimensional gradients across the two magnetometers indicated by the subscripts and,

$\Delta\Delta\vec{B}$ is the three-dimensional gradient field used in the survey analysis.

The axial ($\Delta\Delta B_x$) and radial ($\Delta\Delta B_z$) component of the magnetic gradient field are shown in figure 2.6.

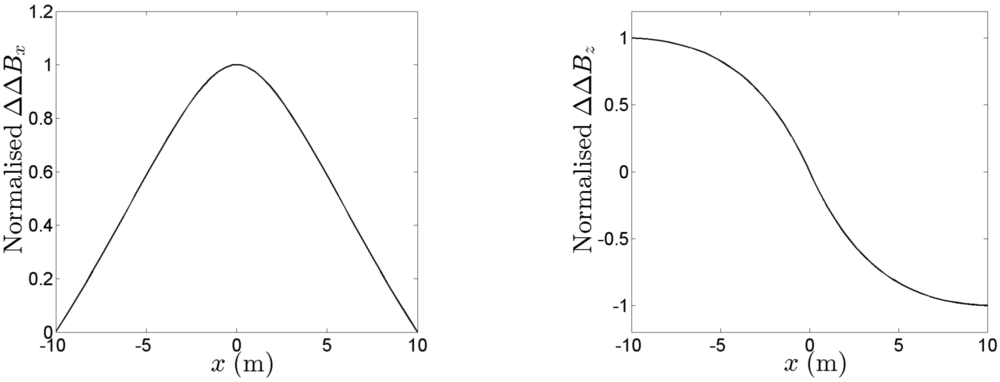

(a) Normalised $\Delta\Delta B_x$ component of the gradient field from the dipole field of a 36″ pipe with a wall thickness of ³⁄₈″ and length of 12 m at a height above the pipe of 6 m.

(b) Normalised $\Delta\Delta B_z$ component of the gradient field from the dipole field of a 36″ pipe with a wall thickness of ³⁄₈″ and length of 12 m at a height above the pipe of 6 m.

Figure 2.6: Normalised $\Delta\Delta B_x$ and $\Delta\Delta B_z$ components of the gradient field from the dipole magnetic field from a 36″ pipe with a wall thickness of ³⁄₈″ and length of 12 m at a height above the pipe of 6 m.

2.4 Magnetic flux leakage

2.4.1 Self magnetic flux leakage

Magnetic flux leakage (MFL) techniques are non-destructive testing (NDT) methods that detect the magnetic flux leaving the surface of the material due to the change in susceptibility from defects in the material [96][79]. This effect is shown in figure 2.7.

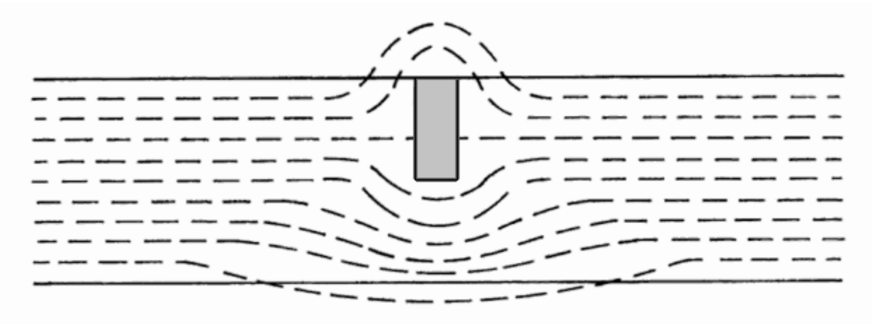

Figure 2.7: Diagram showing the magnetic flux in the material and the magnetic flux leakage from a material with a rectangular defect shown in grey [11].

MFL techniques use a strong magnetic field to induce magnetisation into the material being tested to detect the flux leaking from the surface of the material [80]. This is the case with pigging where strong permanent magnets are used to induce a field in the pipe walls [97][20]. Reviews of the flux leakage from a defect for an ellipsoidal defect region were undertaken and yielded equation 2.21 for the magnetising field [98][99].

$$H_i = \frac{\mu_M}{\mu_M + N_d \left(\mu_{\text{defect}} + \mu_M\right)} H_a \tag{2.21}$$

Where

H_i is the internal field of the defect,

H_a is the applied magnetic field,

μ_M is the permeability of the material,

$\mu_{\mathbf{defect}}$ is the permeability of the defect, and

N_d is the demagnetising factor which depends on the shape of the defect.

The MFL from a two-dimensional defect with a rectangular cross-section has been modelled as a magnetic dipole [100]. This was expanded to a modelled three-dimensional ellipsoid defect which also shows a magnetic dipole field [101], and has been experimentally confirmed [102].

The MFL theory has been expanded to use the material magnetisation due to the geomagnetic field as the applied magnetic field, this is known as the self magnetic flux leakage (SMFL) [103]. This is used in NDE techniques which do not require an additional magnetic field such as the metal magnetic memory method [104] and large stand-off magnetometry [105].

2.4.2 In-line inspection

In-line inspection (ILI) is an MFL technique for detecting defects in pipelines. ILI used a tool known as a pig (pipe inspection gauge) which is propelled through the pipe using a pressure differential in the gas, a pig used for ILI is shown in figure 2.8.

The pig uses MFL for defect detection, this is done by positioning strong permanent magnets around the circumference of the pig which travel close to the pipe wall. This magnet causes the pipe wall to saturate, when the magnet passes a defect zone some of the flux leaks out of the pipe wall, this is then detected by magnetometer arrays also positioned on the pig [106]. A schematic diagram of the magnet, magnetometer and a pipe wall with a defect is shown in figure 2.9.

The information that a defect zone was detected by the pig is useless if there is no information where the defect was detected along the pipeline. To measure the position of the detected magnetic anomalies the pig has odometer wheels, gyroscopes and accelerometers. The positional data can become inaccurate with distance from the launcher as factors such as wheel slip on the pipe wall introduce odometer errors [20]. The positional accuracy is improved through the use of tie points, these are GPS control points along the pipeline which the location data from the pig are linked to convert the pig locational data into a GPS location

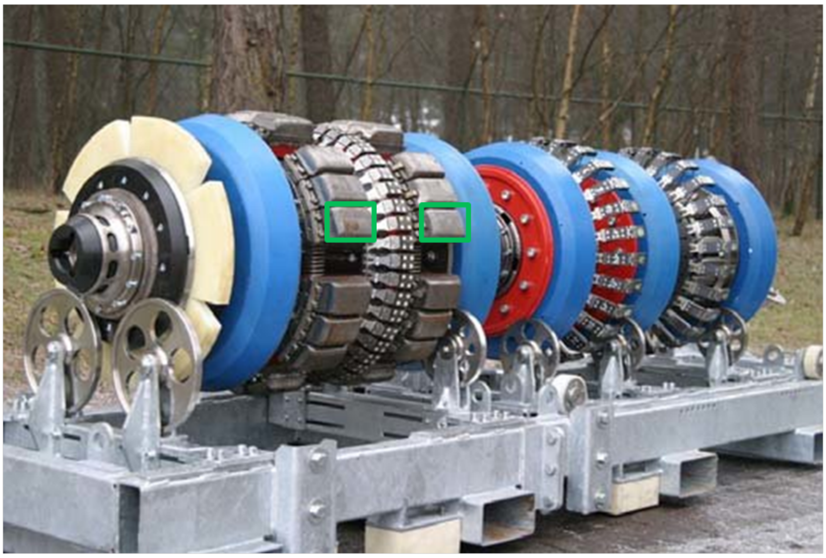

Figure 2.8: A pig used for in-line inspection of a pipeline using magnetic flux leakage (MFL) to locate defects in the pipeline wall, a pair of magnet poles are shown with green rectangles. The pig is propelled through the pipeline using a gas pressure differential. Image reproduced from [12].

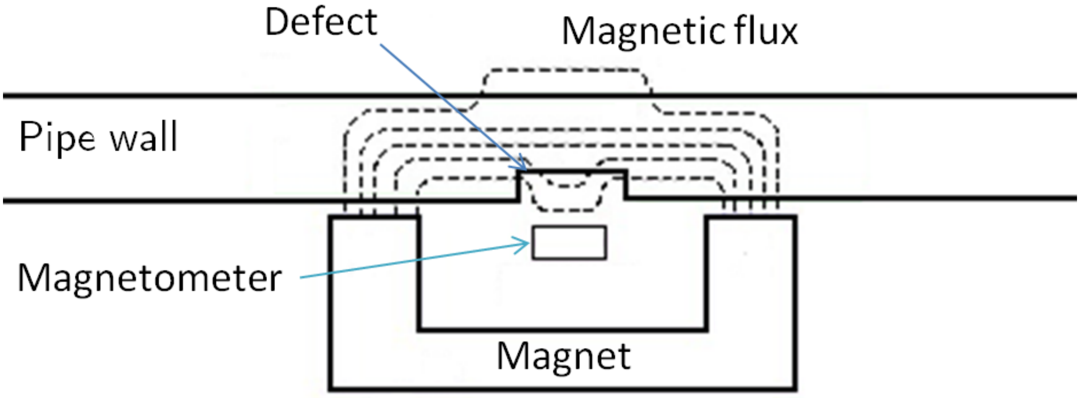

Figure 2.9: Schematic of a permanent magnet from a pig. These are arranged around the circumference of the pig and travel close to the pipe wall to saturate it, producing a magnetic flux leakage in the defect areas which is detected by the magnetometer. Two such magnet faces are indicated in figure 2.8 above with green rectangles.

[107]. The interval for which 80% of defects detected will be from the actual defect location are shown versus the pig velocity and tie point distance are shown in table 2.2[14].

80% confidence interval (m)		Tie point distance (km)				
		1	2	4	10	25
Pig velocity (m/s)	0.5	1.0	1.5	8.0	-	-
	1.0	0.7	1.0	3.0	25.0	-
	3.0	0.7	1.0	2.0	10.0	70.0

Table 2.2: Table showing the interval for which a detected defect will be within for 80% of detected defects versus the pig velocity through the pipe and distance between the tie points for a precision pig. [14]

Pigging poses risks to the pipeline such as:

- a pig getting stuck inside the pipe reducing or blocking the flow necessitating an expensive excavation to remove it [108],
- a magnet coming loose from the pig and attaching to the pipe wall which, the location of which cannot be determined from the ground above the pipe rendering the pipeline unpiggable until this is removed,
- the vibration associated with the movement of the pig through the pipe causing cracks to propagate further into the wall.

There are risks to the operator involved in pigging, for example when opening the pipeline to launch and receive the pig. A major accident associated with pigging operations occurred in Germany around 2004 when an operator was opening the receiver to retrieve a pair of pigs. The operator was stood in front of the receiver unbolting the cover when the cover snapped out driven by the two pigs being ejected from the pipe. The operator was struck by the first pig weighing 150 kg at a velocity of approximately 220 km/h throwing them 27 m from the receiver, the operator died at the scene due to blunt force trauma from the pig. The accident was deemed to have been caused by the second pig becoming temporarily stuck in the pipe until pressure built up and fired it forwards into the first pig and then both out of the receiver [109].

2.4.3 Metal magnetic memory

The metal magnetic memory (MMM) method is a technique for finding stress regions in ferromagnetic structures using the SMFL from the remnant magnetisation of a material due to the stress in the defect zone [110]. This technique has an approved ISO standard [111]. The MMM method uses magnetometry close to the surface of the material to detect the SMFL from the stress zone created by a defect [112].

In the MMM method stress regions are indicated by a zero-crossing in the magnetic field normal to the surface of the material and a peak in the magnetic field parallel to the surface of the material [113]. This is consistent with opposite poles forming at each side of the stress region [105]. The MMM method has been shown to be capable of locating cracks in rotor blades due to the stress from the defect [114] and welds in pipes due to the residual stress from the welding [115].

A model for the signal from defect regions in the MMM method was developed using the theory of magnetic charges being concentrated in the defect zone due to the dislocation caused by the deformation [116][117], this is shown and expanded on for predicting the gradient field from a defect in section 2.4.4.

2.4.4 The Wang defect model

In this section a two-dimensional rectangular defect zone of width $2b$ mm and depth d mm is considered in a ferromagnetic material as shown in figure 2.10 [116].

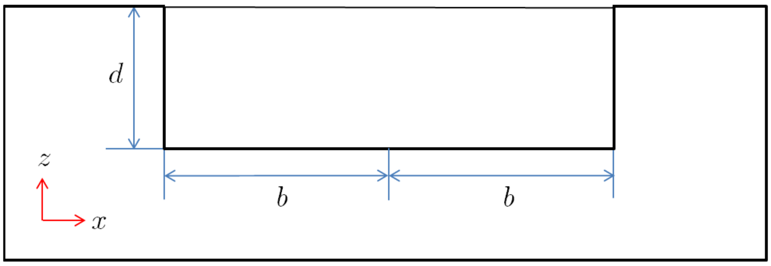

Figure 2.10: Diagram showing a rectangular defect zone in a ferromagnetic material of width $2b$ mm and depth d mm.

In this defect the plastic deformation will be at a maximum at the centre of the defect and reduce linearly to zero at the edges of the defect. If we use the idea of a theoretical magnetic charge which is analogous to an electric charge [118], a linear relationship between the plastic deformation and the charge density can be assumed. Thus the magnetic charge density in the defect region can be described by equation 2.22. The magnetic charge density in x for the defect is shown in firgue 2.11.

$$\rho_x = \begin{cases} \left(\dfrac{x+b}{b}\right)\rho_{\max} & x \in [-b, 0],\ z \in [0, -d] \\ -\left(\dfrac{b-x}{b}\right)\rho_{\max} & x \in [0, b],\ z \in [0, -d] \\ 0 & x \in [-\infty, -b] \text{ or } x \in [b, +\infty] \text{ or } z \in [-d, -\infty] \end{cases} \tag{2.22}$$

Where

$\boldsymbol{\rho_{\max}}$ is the maximum magnetic charge density in the defect zone, and all other terms are defined above.

To calculate the magnetic components at a point the sum of magnetic contributions from area elements in the defect zone must be calculated. This is shown in figure 2.12.

The contribution to the magnetic field at point $P(x_0, z_0)$ in the x direction is given by equation 2.23 and the z direction by equation 2.24.

$$dB_x = \begin{cases} \dfrac{\chi_M \rho_{\max}\left(\frac{x+b}{b}\right)dxdz}{2\pi\bar{\mu}\left[(x-x_0)^2+(z-z_0)^2\right]}(x_0 - x) & x \in [-b, 0],\ z \in [0, -d] \\ -\dfrac{\chi_M \rho_{\max}\left(\frac{b-x}{b}\right)dxdz}{2\pi\bar{\mu}\left[(x-x_0)^2+(z-z_0)^2\right]}(x_0 - x) & x \in [0, b],\ z \in [0, -d] \end{cases} \tag{2.23}$$

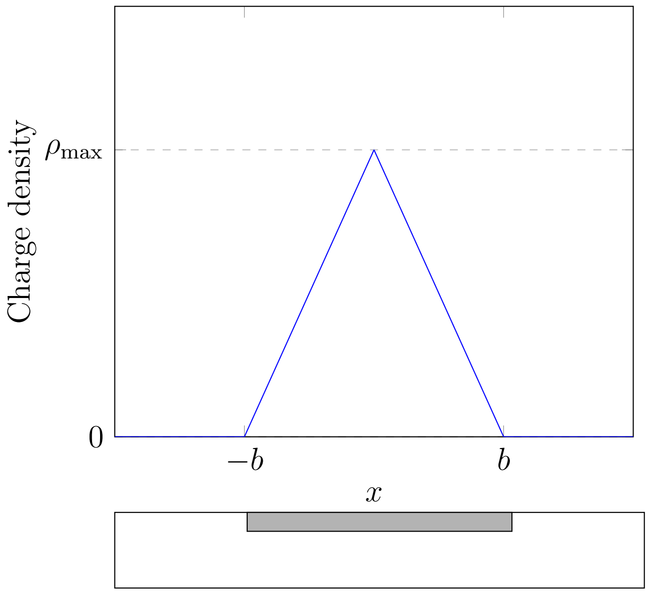

Figure 2.11: Graph of the magnetic charge density in a ferromagnetic material, shown by the white rectangle, with a defect zone shown by the grey rectangle. From equation 2.22.

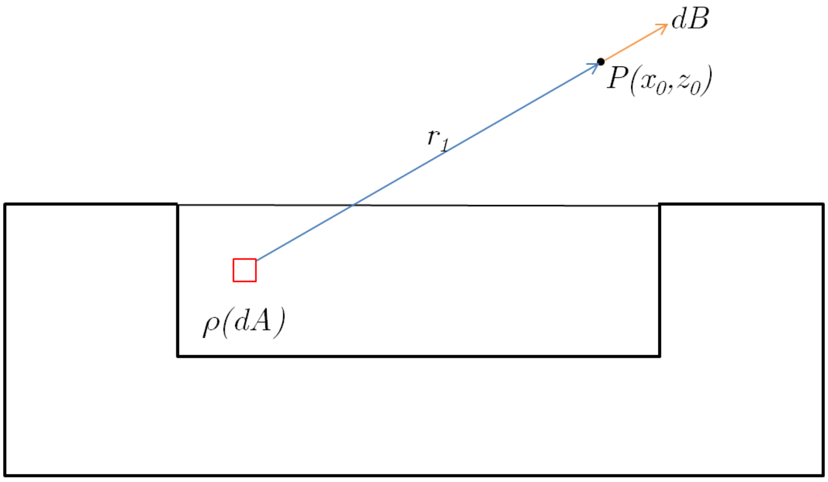

Figure 2.12: Diagram showing the area element in the defect zone contribution, dB to the total field at point $P(x_0, z_0)$.

$$dB_r = \begin{cases} \dfrac{\chi_M \rho_{\max} \left(\frac{x+b}{b}\right) dxdz}{2\pi\bar{\mu}\left[(x-x_0)^2+(z-z_0)^2\right]}(z_0-z) & x\in[-b,0],\ z\in[0,-d] \\ -\dfrac{\chi_M \rho_{\max} \left(\frac{b-x}{b}\right) dxdz}{2\pi\bar{\mu}\left[(x-x_0)^2+(z-z_0)^2\right]}(z_0-z) & x\in[0,b],\ z\in[0,-d] \end{cases} \tag{2.24}$$

Where

χ_M is the susceptibility of the material with the defect,

dB_x is the x component of the magnetic field at point $P(x_0, z_0)$ due to the area segment in the defect zone,

dB_z is the z component of the magnetic field at point $P(x_0, z_0)$ due to the area segment in the defect zone,

$\bar{\mu}$ is the effective magnetic permeability, and all other terms are defined above.

To find the magnetic field strength at point $P(x_0, z_0)$ equations 2.23 and 2.24 must be calculated for all area elements in the defect zone, this gives equations 2.25 and 2.26 [117].

$$\begin{aligned} B_{p(x_0)} = A\Bigg(&\int_{-b}^{0}\int_{-d}^{0} \frac{\left(\frac{x+b}{b}\right)(x_0-x)}{\left[(x-x_0)^2+(z-z_0)^2\right]}\frac{z_0}{(z_0-z)}dxdz \\ &-\int_{0}^{b}\int_{-d}^{0} \frac{\left(\frac{b-x}{b}\right)(x_0-x)}{\left[(x-x_0)^2+(z-z_0)^2\right]}\frac{z_0}{(z_0-z)}dxdz\Bigg) \end{aligned} \tag{2.25}$$

$$\begin{aligned} B_{p(z_0)} = A\Bigg(&\int_{-b}^{0}\int_{-d}^{0} \frac{\left(\frac{x+b}{b}\right)z_0}{\left[(x-x_0)^2+(z-z_0)^2\right]}dxdz \\ &-\int_{0}^{b}\int_{-d}^{0} \frac{\left(\frac{b-x}{b}\right)z_0}{\left[(x-x_0)^2+(z-z_0)^2\right]}dxdz\Bigg) \end{aligned} \tag{2.26}$$

Where

$$A = \frac{\chi_M \rho_{\max}}{2\pi\mu_0},$$

$B_{p(x_0)}$ is the x component of the magnetic field at point $P(x_0, z_0)$ from the defect area,

$B_{p(z_0)}$ is the radial component of the magnetic field at point $P(x_0, z_0)$ from the defect area, and

all other terms are defined above.

The x and z component of the magnetic field from a defect 40 mm wide with a depth of 10 mm positioned at (0,0) at a height above the defect of 2 m versus the x position are shown in figure 2.13.

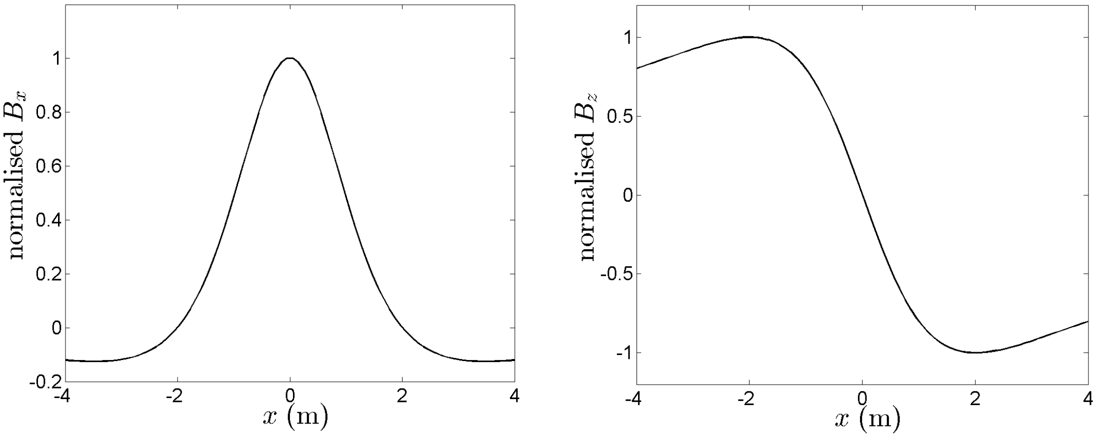

(a) Normalised B_x component of the magnetic field from a defect centred at $(0, 0)$ that is 40 mm wide with a depth of 10 mm at a height above the defect of 2 m.

(b) Normalised B_z component of the magnetic field from a defect centred at $(0, 0)$ that is 40 mm wide with a depth of 10 mm at a height above the defect of 2 m.

Figure 2.13: Normalised B_x and B_z components of the magnetic field from a defect centred at $(0, 0)$ that is 40 mm wide with a depth of 10 mm at a height above the defect of 2 m.

To expand this model to be able to calculate the gradient field the way it is in the field survey array, this was done by considering a defect on a pipe with the array above. Equations 2.25 and 2.26 were modified by altering the point distance component $\left[(x-x_0)^2+(z-z_0)^2\right]$ to $\left[(x-x_0)^2+(y-y_0)^2+(z-z_0)^2\right]$ to give equations 2.27 and 2.28 to account for the addition of the y component. Equation 2.25 gives the longitudinal component of the magnetic field at the measurement point and so needs no alteration for the angle while equation 2.26 gives the radial component of the magnetic field and so the angle must be resolved into the co-ordinate system used in the survey array. This is shown in figure 2.14, the radial field was resolved into the survey array co-ordinate system using equation 2.29.

$$\begin{aligned} B_{p(x_0)} = A\Bigg(& \int_{-b}^{0}\int_{-d}^{0} \frac{\left(\frac{x+b}{b}\right)(x_0-x)}{\left[(x-x_0)^2+(y-y_0)^2+(z-z_0)^2\right]} \frac{z_0}{(z_0-z)} dxdz \\ & - \int_{0}^{b}\int_{-d}^{0} \frac{\left(\frac{b-x}{b}\right)(x_0-x)}{\left[(x-x_0)^2++(y-y_0)^2(z-z_0)^2\right]} \frac{z_0}{(z_0-z)} dxdz \Bigg) \end{aligned} \tag{2.27}$$

$$\begin{aligned} B_{p(z_0)} = A\Bigg(& \int_{-b}^{0}\int_{-d}^{0} \frac{\left(\frac{x+b}{b}\right)z_0}{\left[(x-x_0)^2+(y-y_0)^2+(z-z_0)^2\right]} dxdz \\ & - \int_{0}^{b}\int_{-d}^{0} \frac{\left(\frac{b-x}{b}\right)z_0}{\left[(x-x_0)^2+(y-y_0)^2+(z-z_0)^2\right]} dxdz \Bigg) \end{aligned} \tag{2.28}$$

Where all terms are defined above.

$$B_z = B_r \cos(\phi) = B_r \cos\left(\tan^{-1}\left(\frac{S}{z}\right)\right) \tag{2.29}$$

The B_x and B_z components were calculated above the defect for the three magnetometry positions, using these values the gradient field was calculated and plotted. These are shown in figure 2.15.

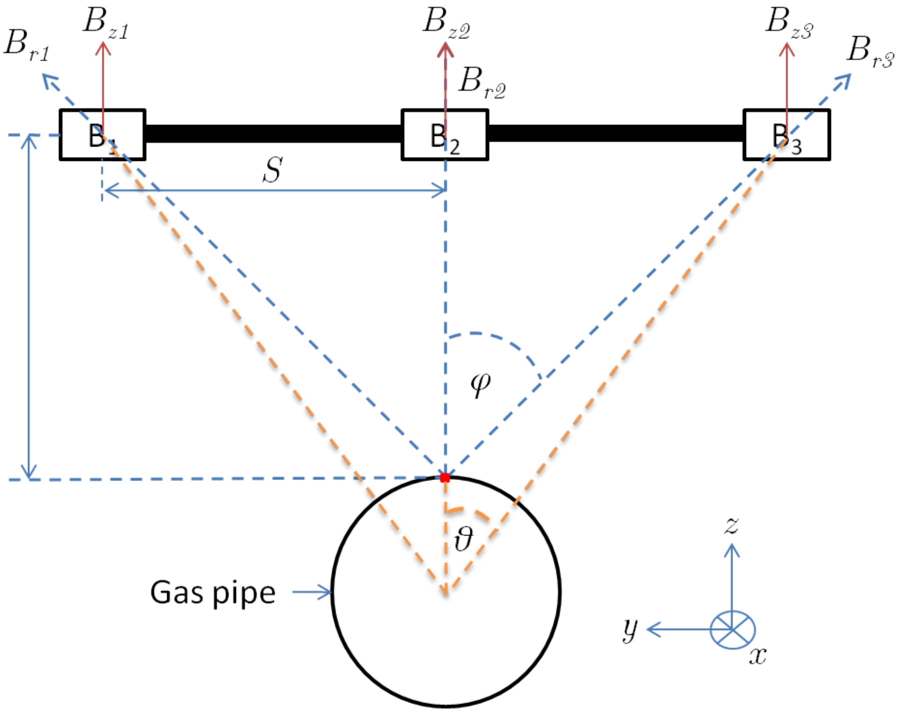

Figure 2.14: Diagram of the magnetometry array above a defect in the pipe wall, shown in red. The angle at the defect, ϕ is shown by blue dashed lines while the angle at the centreline, θ is shown by orange dashed lines.

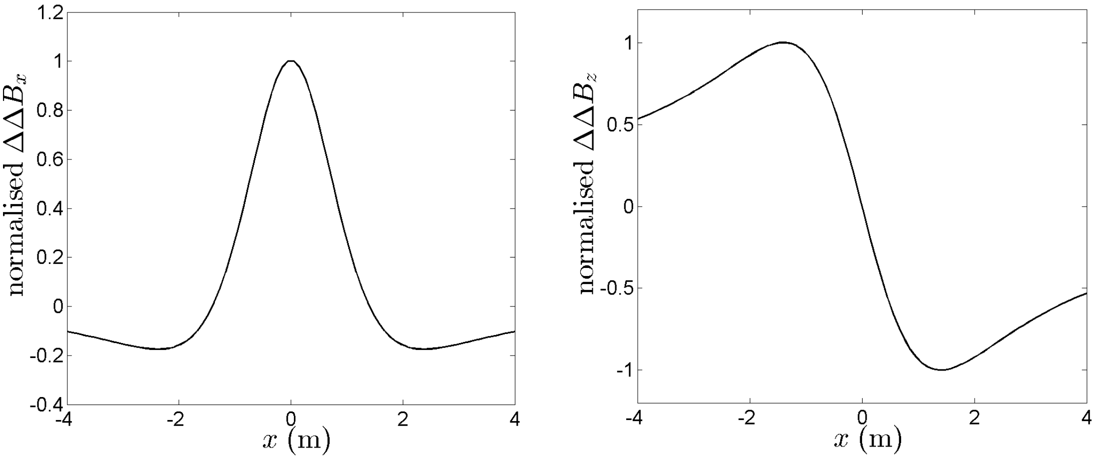

(a) Normalised $\Delta\Delta B_x$ component of the magnetic gradient field from a defect centred at $(0, 0)$ that is 40 mm wide with a depth of 10 mm at a height above the defect of 2 m, calculated with a magnetometer separation of 0.5 m.

(b) Normalised $\Delta\Delta B_z$ component of the magnetic gradient field from a defect centred at $(0, 0)$ that is 40 mm wide with a depth of 10 mm at a height above the defect of 2 m, calculated with a magnetometer separation of 0.5 m.

Figure 2.15: Normalised $\Delta\Delta B_x$ and $\Delta\Delta B_z$ components of the magnetic gradient field from a defect centred at $(0, 0)$ that is 40 mm wide with a depth of 10 mm at a height above the defect of 2 m, calculated with a magnetometer separation of 0.5 m.

2.5 Large stand-off magnetometry equipment for use in non-invasive pipeline inspection

The magnetometry survey system for conducting non-invasive inspection of buried pipelines comprises:

- an array of three magnetometers,
- Two Topcon GNSS receivers, and
- an FPGA and flash memory.

This system was developed at the University of Leeds and has been used in surveys of gas pipelines since 2012 by the intellectual property owners, Speir Hunter [21][22]. A block diagram of these subsystems to make up the full system is shown in figure 2.19. A photograph of the full system with the above subsystems labelled is shown in figure 2.17.

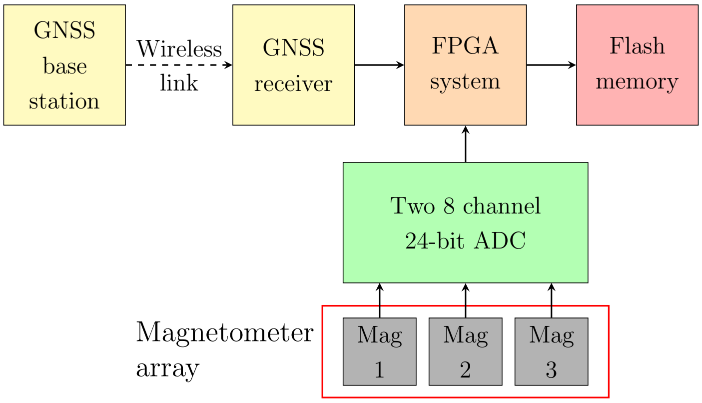

Figure 2.16: Block diagram of the large stand-off magnetometry array system.

The magnetometry survey of the pipeline is carried out by locating the centreline of the pipe using a pipeline locator. The position on the ground above the centreline is marked out with survey flags, for the operator to follow keeping the centre magnetometer above the centreline of the pipe with the outer magnetometers either side of the centreline. The location for the magnetic field strength measured is taken using a Topcon GR-5 GNSS receiver with a Topcon GR-5 base

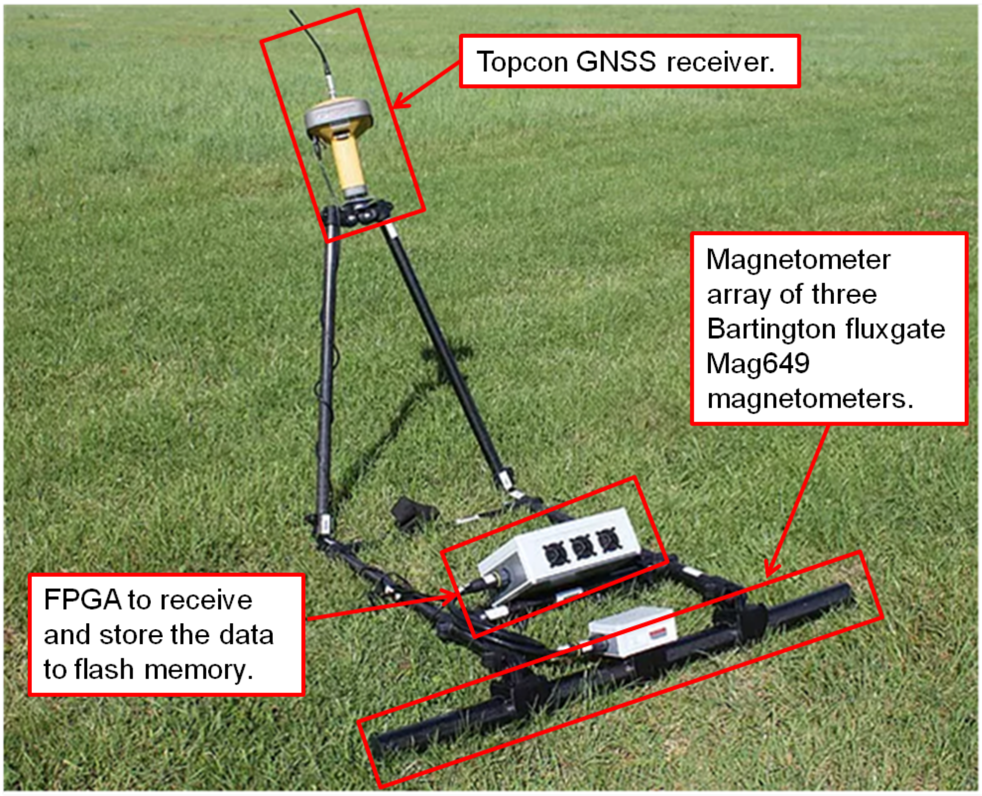

Figure 2.17: Field survey system for non-invasive magnetic inspection of gas pipelines. Labelled in the image are the three major systems: the magnetometer array of three Bartington Mag649 magnetometers, Topcon GNSS receiver and FPGA/flash memory control and data storage system.

station at a known location to increase locational accuracy. Pictures taken of the survey procedure are shown in figure 2.18, an operator using the pipeline locator to locate the pipe is shown in figure 2.18a, the survey flags in position in figure 2.18b, the operator carrying the array above the flags in figure 2.18c and the Topcon base station in position in figure 2.18d.

The magnetometry array is an array of three Bartington Mag649 fluxgate magnetometers, these are arranged in a line with a separation of 0.5 m between them. The centre magnetometer is positioned to trace out the centreline of the pipe with the outer magnetometers either side of the pipe. A schematic of the magnetometer array, with its co-ordinate system is shown aligned with a pipeline in figure 2.19. The data from the magnetometers is sent to an ADC, the data is then sent to the FPGA for storage into the flash memory.

The data from the three magnetometers is used to calculate the three components of the gradient field, $\Delta\Delta B$, from the magnetic field strength measurements. This is calculated using equations 2.30 and 2.31.

$$\Delta\vec{B}_{12} = \frac{\left(\vec{B}_1 - \vec{B}_2\right)}{0.5} \qquad \Delta\vec{B}_{23} = \frac{\left(\vec{B}_2 - \vec{B}_3\right)}{0.5} \tag{2.30}$$

$$\Delta\Delta\vec{B} = \Delta\vec{B}_{12} - \Delta\vec{B}_{23} \tag{2.31}$$

Where:

$\vec{B}_1$, $\vec{B}_2$ and $\vec{B}_3$ are the three-dimensional magnetic field strengths from the magnetometers as numbered in figure 2.19,

$\Delta\vec{B}_{12}$ and $\Delta\vec{B}_{23}$ are the three-dimensional gradients across the two magnetometers indicated by the subscripts and,

$\Delta\Delta\vec{B}$ is the three-dimensional gradient field used in the survey analysis.

The location of the magnetic data points gathered is taken from a pair of Topcon GR-5 GNSS receivers in Real Time Kinematic mode (RTK). One of the receivers is attached to the survey array and connected to the FPGA to index the magnetic field data to the location it was gathered, the other is used as a stationary base station to increase the accuracy of the survey receiver. Positional

(a) Photograph of an operator using a pipe locator to place survey flags along the ground in the position abover the centreline of the pipe.

(b) Photograph of the survey flags used to mark out the position above the centreline of the burried pipeline for the operator to follow.

(c) Photograph of an operator using the magnetometer survey array to measure the magnetic field from the pipeline.

(d) Photograph of Topconbase station positioned on a tripod.

Figure 2.18: Photographs from field surveys of live buried pipelines using the magnetometry survey system. Subfigure a shows an operator using a pipe locator to map out the position above the centreline of the pipe with flags. Subfigure b showing the flags marking out the position above the centreline of the pipeline for the operator to follow. Subfigure c shows an operator carrying the survey system along the flags marking out the position above the centreline of the pipe. The photographs shown in subfigures a and c were taken by Stephen Staples at surveys I was present at and are reproduced with permission.

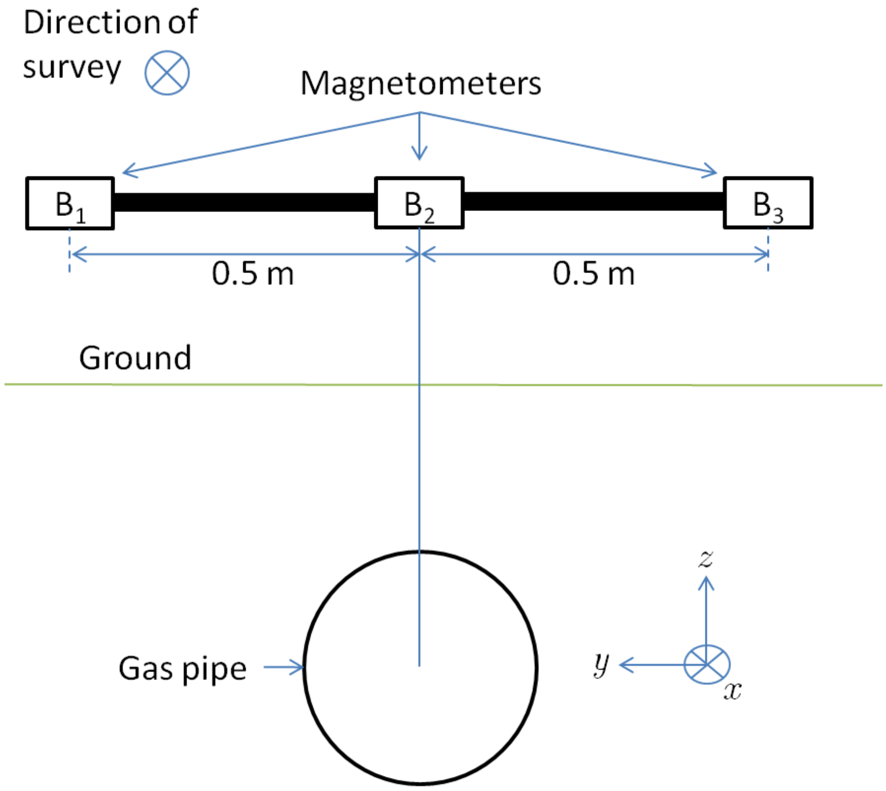

Figure 2.19: Cross section schematic of the configuration of the magnetometers in the field survey array, showing the magnetometers, pipeline and co-ordinate system. The magnetometers are Bartington Mag649 fluxgate magnetometers that measure the magnetic field strength in the three dimensions defined by the axes. The centre magnetometer is designated magnetometer 2 while those either side of the pipe are designated 1 and 3, these give the magnetic field strengths B_2, B_1 and B_3 respectively.

data gathered by the system has an accuracy of ± 15 mm at a range of 5 - 10 km from the base station depending on obstructions [119].

The system uses an FPGA base unit that takes the three-dimensional data from the magnetometer array, which is converted by two eight channel 24-bit ADCs. The magnetic data is then indexed using the location data from the Topcon GNSS receiver. The data is saved to a flash memory drive to be downloaded to a computer and analysed.

2.6 Conclusion

Large stand-off magnetometry has been used extensively in exploration geophysics and in archaeology to detect features of interest. It was discovered that the magnetic field from a pipeline in a field gave a repeating pattern of peaks which coincided with the weld location between the pipe sections.

This change in magnetic field is thought to be due to the Villari effect, in which a ferromagnetic material stressed within a magnetic field becomes magnetised, however other material changes could also be responsible. This is due to the stress allowing the domains to rotate easier to align to the magnetising field, this can be measured as a change in the susceptibility of the material. Magnetisation follows a hysteresis curve as the domains do not fully relax to the unmagnetised state when the magnetising field is removed. This leads to stress causing a magnetisation in the material that remains once the stress has stopped.

A magnetic model for gas pipelines is to treat each pipe section as an individual dipole running along the centreline of the pipe, this leads to a model for a hollow cylindrical permanent magnet being considered. This model shows a dependence of the magnetisation on the ratio of the diameter to the length for the pipes, it also shows a peak and zero-crossing associated with each pipe section.

Magnetic flux leakage (MFL) is the effect in a magnetised material due to a change in susceptibility of the material, this causes magnetic flux to leave the surface of the material and link to the other side of the change in susceptibility. This allows the defect to be detected by the change in the magnetic field in these regions.

Pipeline inspections are carried out using a tool known as a pig that is propelled through the centre of the pipe using a differential in the gas pressure. The pig carries strong magnets to magnetise the pipe wall and a magnetometer to detect any flux leakage from this magnetisation. The pig indexes these defects with the location in the pipe using odometer wheels, gyroscopes and accelerometers. These can achieve an 80% interval of detection of ± 0.7 m.

MFL can also be used in a system where the material is magnetised by the geomagnetic field and no additional magnetic fields, this is known as self magnetic flux leakage (SMFL). A technique known as metal magnetic memory (MMM) utilises SMFL to locate defect zones in pipe walls by passing a magnetometer close to the surface of the pipe to detect the flux leakage.

The SMFL signal from a defect can be characterised by considering the defect to be made up of magnetic point charges due to the dislocation from the defect zone. This model can be adapted to allow for a magnetic gradient field from the defect to be calculated, this model predicts a peak and zero-crossing in the longitudinal and radial gradient fields respectively.

The equipment for use in non-invasive pipeline inspection uses a magnetometry array of three fluxgate magnetometers, a GNSS receiver and FPGA to process and record the data from the survey. This allows for magnetic surveys of pipelines to be conducted and the gradient field for the pipeline to be calculated to negate variations in the background field. The system has been used for large stand-off magnetic surveys of pipelines and is subject to patents for its design and operation.

To investigate the design of the magnetometry equipment used in surveys of buried gas pipelines, magnetic data must be gathered for known pipes. To control the environment for this and to allow for full three-dimensional magnetic data to be measured laboratory experiments have been conducted.

As shown in section 2.3.2, the diameter to length ratio affects the magnetic field from a pipe. A full-sized pipe section is too large for the laboratory and would create a difficulty in measuring the full field data, a short section of field pipe section however would change this ratio and so affect the magnetisation. Therefore in the laboratory small diameter conduits have been used which allow this ratio to be maintained and for the full three-dimensional magnetic field to be measured.

Chapter 3

Laboratory magnetometry set-up and repeatability

3.1 Introduction

To allow scans on known pipes in three-dimensional space it was necessary to conduct experiments in the laboratory. The simulants used in the laboratory to simulate pipe sections were mild steel conduits, these are described together with the laboratory experimental set-up in section 3.2 in this chapter.

The repeatability of the data gathered using this laboratory set-up on a test conduit was investigated in section 3.3 to give statistical validity to the results gathered with this set-up on these conduits in the laboratory experiments. This is required to give confidence that the data gathered in the laboratory experiments is valid.

3.2 Experimental set-up

To gather magnetic field data in three-dimensional space from a known sample at a known position in a repeatable way experiments were conducted in the laboratory. This allowed for higher data densities with greater control over the sample orientation and state. Further the experiments in the laboratory allowed for samples to be swapped in the same position and orientation to account for environmental effects. Due to the weight and size of pipe sections it was impractical to use full-sized pipe sections in the laboratory, therefore simulants were used in place of gas pipe sections to investigate how the magnetic field varies in space and with different simulants.

Magnetometry has been used to measure the magnetic field from stressed steel bars [105] and for hydrostatically stressed gas pipes in the laboratory by others at the University of Leeds prior to this work [120]. The magnetometry array has also been used in field trials to gather data from buried pipelines [121]. Laboratory experiments have been carried out on pipes and pipe simulants for the purposes of magnetic NDT by other groups [122][123].

The conduit pipes used as pipe simulants were chosen as these are long enough to allow a centre section away from any end effects to be scanned, while maintaining a high length to diameter ratio of the pipe to maintain the magnetic profile of the cylinder. The experimental set-up designed to facilitate this use of conduits as pipe simulants in these laboratory experiments is described in this section. The properties of the conduits used as simulants are also described in this section.

3.2.1 Magnetometry scanning rig for laboratory testing

To scan the samples in the laboratory the magnetometer was connected to a scanning arm which the magnetometer can be moved along using a stepper motor to move the magnetometer in one dimension. This arm was moved in an orthogonal dimension using a second stepper motor. Together these stepper motors move the magnetometer in a programmed two-dimensional cartesian grid with the steps defined in multiples of 1 mm. The magnetometer measures the magnetic field strength in the three components at each of these points which is then recorded. The magnetometer was mounted onto the scanning arm in a way which allows it be manually moved in the third dimension to allow multiple plane of scans to taken, giving a full three-dimensional magnetic field around the sample.

This scanning system was mounted onto an aluminium frame connected with stainless steel fasteners to support it in place. The frame was constructed of aluminium to prevent it causing any extraneous magnetic fields. The sample being scanned was held in place on an aluminium stand that was constructed, this was attached to the magnetometer stand to hold it stationary relative to the magnetometer reference position. A three-dimensional render of the stand constructed from aluminium to hold the sample without introducing extraneous magnetic fields is shown in figure 3.1. A labelled photograph of the laboratory set-up showing the sample being scanned, the magnetometer, stepper motors and stands is shown in figure 3.2.

3.2.2 Laboratory magnetometer system

The magnetometer used to measure the magnetic field in the laboratory was the same magnetometer as is used on the field magnetometry survey array. This is the Bartington Mag649 fluxgate magnetometer which measures the magnetic field strength in three dimensions, with a range of $\pm 100\mu$T and a resolution of $\pm 0.1\mu$T [124]. The magnetometer was mounted on to the scanning arm on the

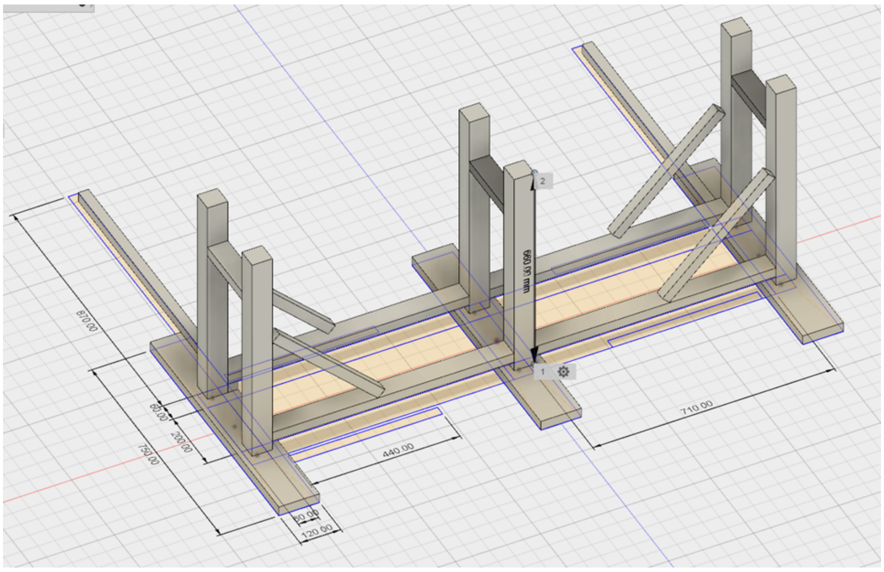

Figure 3.1: Three-dimensional render of the aluminium frame with dimensions used to support the sample being scanned. This was designed and built during this work to support samples being scanned without introducing extraneous magnetic fields.

laboratory scanning rig described in subsection 3.2.1 using nylon fittings. The magnetometer is shown attached to the scanning arm in figure 3.2. An image of the magnetometer is shown in figure 3.3

3.2.3 Properties of the conduit pipes used in experimental measurements

The simulants that were chosen to simulate pipelines in the laboratory were galvanised mild steel conduits, with a range of outer diameters and wall thicknesses. These are the correct geometry, are seam welded as in the field pipe sections and are readily available from multiple suppliers. The material properties of the conduits and the pipelines used in the field are given in table 3.1.

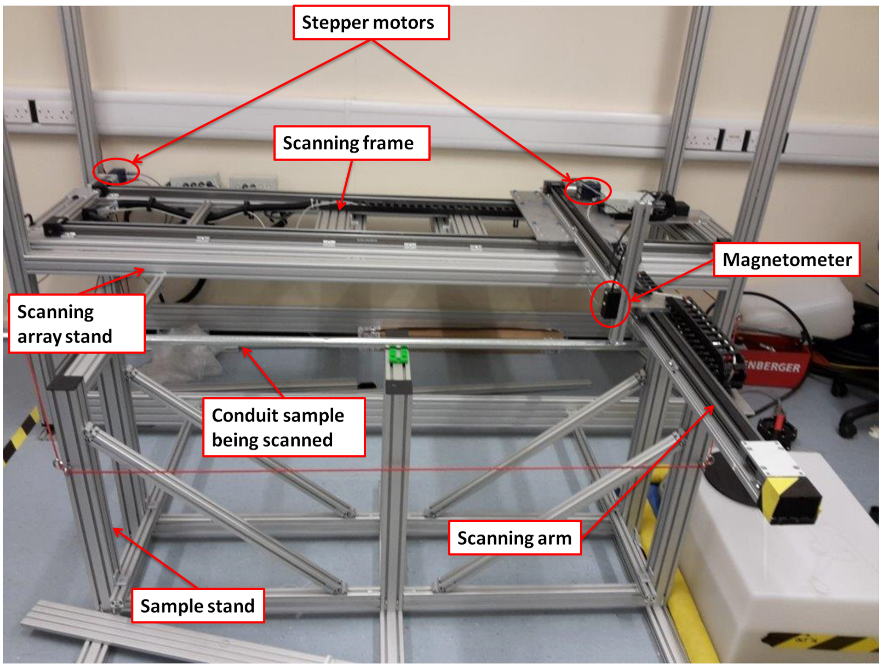

Figure 3.2: Photograph of the laboratory magnetometer scanning set-up used for the laboratory experiments in this work. Labelled in the photo are the conduit being scanned in position, the magnetometer, stepper motors and stands constructed from aluminium.

Figure 3.3: Image of the Bartington Mag649 three axis fluxgate magnetometer used to gather the magnetic field strength data in the laboratory experiments.

Steel Grade	Chemical Composition				Mechanical Properties		
Steel number	C max	Mn max	P max	S max	Yield Strength (MPa)	Tensile Strength (MPa)	Young's modulus (GPa)
S 195T	0.20	1.40	0.035	0.030	195	320 - 520	268
X42	0.22	1.30	0.030	0.030	290	414	290

Table 3.1: Table of material properties of the conduits, constructed from S 195T, used as pipe simulants in the laboratory and in pipeline sections, constructed from X42, in the field [15][16].

The nominal diameters for the conduits used as pipe simulants in the laboratory experiments were $^1/_2''$, $^3/_4''$,$1''$ and $1^1/_2''$, a photo of the four sizes are shown size by side in figure 3.4.

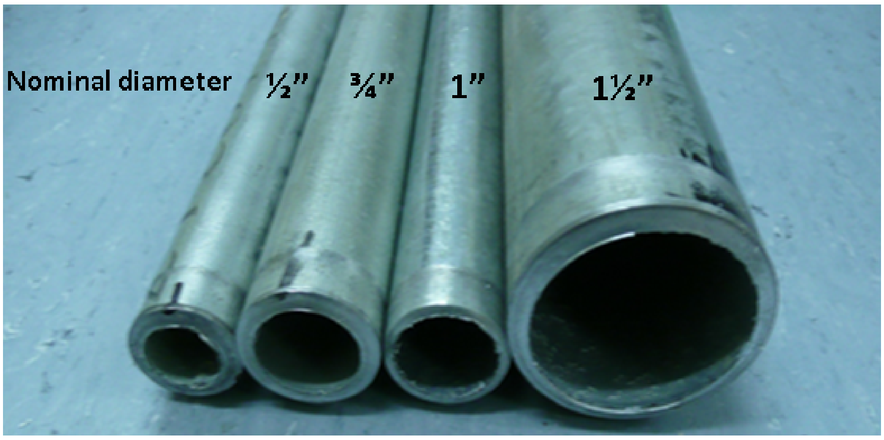

Figure 3.4: Photograph of the four conduit sizes in the laboratory, from left to right nominal diameter $^1/_2''$, $^3/_4''$, $1''$ and $1^1/_2''$.

The $1''$ nominal diameter conduit is designed to meet BS 4568 [125], these were supplied in 3.75 m lengths. The $^1/_2''$, $^3/_4''$ and $1^1/_2''$ nominal diameter conduits were designed to meet the medium grade standards of BS EN 10255:2004 [15], these were supplied in 3.2 m lengths. To relate the magnetic measurements to the physical size of the conduits the physical dimensions of the conduits had to be measured. The dimensions measured are shown in figure 3.5 and the measured dimensions are given in table 3.2.

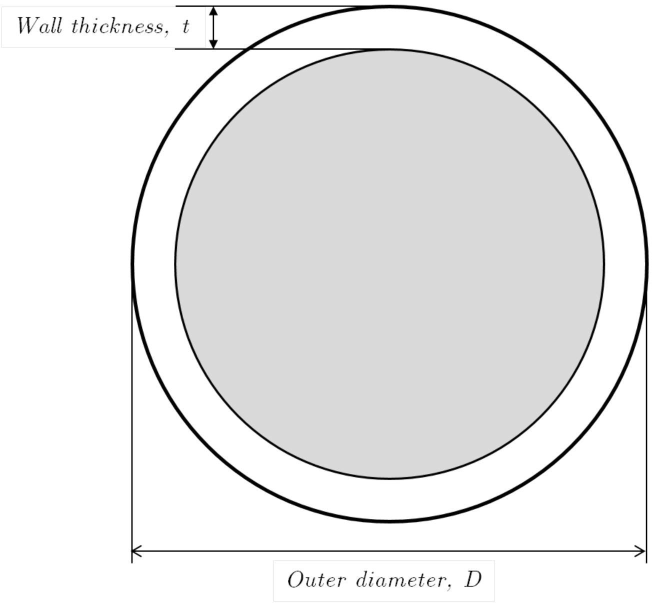

Figure 3.5: Diagram of the cross section of the conduits showing the actual outer diameter, D, and the conduit wall thickness, t.

To measure the actual dimensions of the conduits 30 measurements were taken for the outer diameter of each nominal diameter, D, and the wall thickness, t. These were taken using callipers on three different conduits for each size taking 10 from each. These measurements were taken at different rotations around the conduit and at different cuts to account for any non-uniformity of the conduit cross section. The mean and standard deviation of the measurements were calculated. The standard deviation was multiplied by 1.96 in order to find the bounds for which 95% of the measurements fall [126]. These are shown in table 3.2.

Nominal Pipe Diameter (″)	Mean Outer Diameter (mm)	Mean Wall Thickness (mm)
$^{1}/_{2}$	21.5 ± 0.3	3.2 ± 0.3
$^{3}/_{4}$	27.0 ± 0.3	3.2 ± 0.2
1	25.0 ± 0.5	1.6 ± 0.2
$1^{1}/_{2}$	48.3 ± 0.5	3.2 ± 0.2

Table 3.2: Table of the mean and bounds for which 95% of the data falls for the measured outer diameter and conduit wall thickness dimensions for each of the given nominal diameters of the conduits $^{1}/_{2}$″, $^{3}/_{4}$″, 1″ and $1^{1}/_{2}$″.

These conduits make suitable laboratory simulants for the pipe sections used in the field as they have the correct geometry, a seam weld and are constructed of materials with a similar Young's modulus. The stress magnetisation relationship of a material is dependent on its Young's modulus [121], there is a difference of only 7.6% between the Young's moduli of the materials.

These conduits were easily cut using a standard pipe cutter, shown in figure 3.6 and easily positioned and manipulated by hand in the laboratory environment. The thick-walled conduits required a pipe vice to hold them while they were cut with the pipe cutter, this is shown in figure 3.7.

The cutter is used to cut conduits by tightening it around the conduit and rotating it around to run the blade over the surface. This is tightened as the conduit is cut to cut further and further through the wall until the cut goes through the wall. This cutting creates a burr on the interior of the conduit wall, this burr was removed by running a blunt blade around the interior wall. To cut the thick-walled conduit with the cutter the conduit had to be clamped into a pipe vice to stop it rotating with the cutting blade. The vice uses a chain to hold the conduit in position, the vice is designed to not distort the pipe wall when tightened around it.

Figure 3.6: Pipe cutter used to cut the conduit into required sizes. This is done by running a cutting blade over the surface of the pipe as it is rotated around the pipe, the cutter is progressively tightened as the blade cuts further in until it has cut entirely through the pipe wall.

Figure 3.7: A short section of 1″ diameter conduit in the pipe vice used to hold the conduits for cutting. This holds the conduit in position using a chain that is tightened around it, this vice is designed to not distort the cross section of the pipeline.

The wall thickness to outer diameter ratio is greater for the laboratory conduits than for the field pipelines by up to a factor of five. The ratios for the conduits used in the laboratory as well as the ratios for 12″ and 30″ schedule 40 field pipes [17] are shown in table 3.3.

Pipe type	Nominal Pipe Diameter (″)	$^t/_D$
Laboratory conduits	$^1/_2$	0.15
	$^3/_4$	0.12
	1	0.06
	$1^1/_2$	0.07
Schedule 40 pipe	12	0.03
	36	0.03

Table 3.3: Table showing the pipe wall thickness to pipe outer diameter ratio for the conduits used as laboratory simulants and for 12″ and 30″ nominal diameter schedule 40 field pipe [17].

3.3 Repeatability of experimental data

Repeatability is the agreement of data gathered in the same laboratory, on the same test subject, in a short period of time, using the same equipment by the same operator [127]. The repeatability of the data can be stated as the bounds for which 95% of test data gathered under the conditions above is expected to be within [128], in this way smaller 95% bounds represent a greater repeatability of the experiment.

The repeatability is important to evaluate in order to gauge confidence in the gathered data. A high level of repeatability verifies the statistical validity of the results, a high level of confidence can therefore be attributed to data with a high level of repeatability.

The work in this section was carried out to characterise the experimental set-up and methodology. This was done to verify that the data gathered in the laboratory underpinning all of the experimental work undertaken can be given a high level of confidence.

Statistically analysing experimental data by calculating the repeatability is used as an indicator of agreement between data sets [128]. Repeatability is widely used in data analysis to give a prediction of the error in a data set where a "true value" cannot be directly measured [129].

The central limits theorem states that the distribution of independent unbiased random errors in gathered data will tend towards a normal distribution [130]. This means that if the errors do not show an unbiased normal distribution when sufficient data points are compared, that there are non-random or linked sources of errors which need to be identified to prevent biasing of the results.

The laboratory equipment has potential sources of error in the measurement system. All of the sources of error are not easily characterisable and random errors can occur in any data set. Therefore it is necessary to analyse gathered data to gauge the level confidence that can be attributed to the laboratory data. This has been carried out by scanning a cut $1''$ diameter steel conduit, repeating the scan 30 times. This number of scans were carried out to gather enough data points to account for a potential non-normal distribution in the errors when calculating the repeatability bounds.

In this section the repeatability of the laboratory set-up and methodology is assessed and the distribution of the errors evaluated to verify that these conform to the central limits theorem.

3.3.1 Repeatability methodology

The mean and bounds for which 95% of data falls within were calculated for the 30 magnetic field strength data points for each x co-ordinate. The mean of the data points was calculated using equation 3.1, the standard deviation for the data points was calculated using equation 3.2. The standard deviation is multiplied by a correction co-efficient, C_N, calculated using equation 3.3, this is to account for any underestimation of the error due to data set size [131]. The value of the correction co-efficient versus the sample size for sample sizes from $N = 2 - 30$ is shown in figure 3.9. The 95% interval is calculated by equation 3.4.

The 95% bounds equation 3.4 is valid only for cases where $N \geq 30$ or cases where $N < 30$ where the data is normally distributed around the mean [132]. As it is unknown if there is any bias in the laboratory set up which would cause a deviation from a normal distribution for the 95% bounds at least 30 data points must be taken to ensure that the 95% bounds are valid [133]. The gathered data can then be used to assess the distribution to give confidence in the validity of smaller data sets if the data has a normal distribution about the mean.

In order to measure the repeatability and error in the laboratory equipment a 200 mm section in a 3.75 m long 1″ diameter conduit, detailed in section 3.2.3, was scanned 30 times. The origin for the co-ordinate system was defined as the end of the conduit in the x direction, the centreline of the conduit in the y direction and the surface of the conduit in the z direction. The conduit was cut using the pipe cutter at $x = 1500$ mm. Each scan was taken in the region $x = 1400 - 1600$ mm, in x steps of 10 mm at a distance z of 50 mm above the outer surface of the conduit along the conduit centreline. The cut was created and scanned using the equipment shown in section 3.2.2. Between each scan the magnetometer was returned to $(0, 0, 0)$ then set back to the beginning of the scan, this was to include the error from the location system into the repeatability, however the height was not altered. Using the gathered magnetic field strengths the magnetic gradient for each point was calculated. The cut, scanning region and co-ordinate system is shown in figure 3.8.

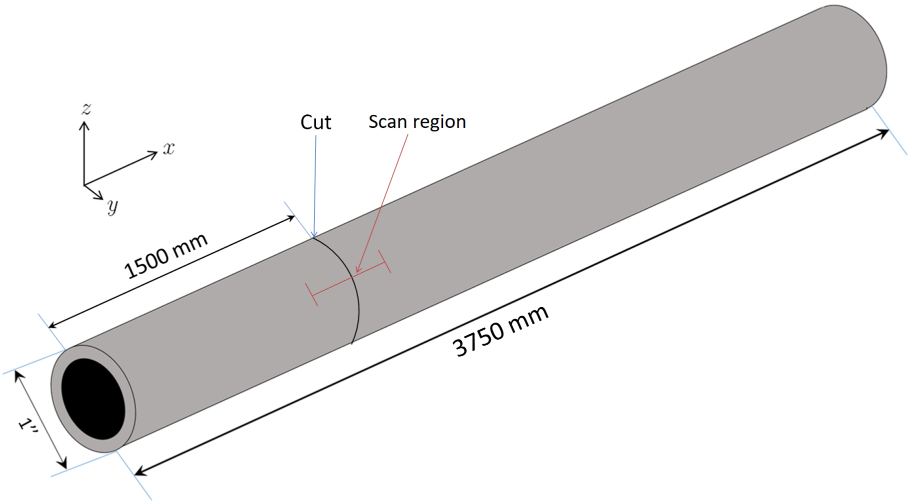

Figure 3.8: Diagram of a full 3.75 m length 1″ diameter conduit with cut, scanning region and co-ordinate system used in the repeatability scans shown.

Using the gathered magnetic field strengths, the magnetic gradient for each point was calculated.

$$\bar{B} = \frac{1}{N}\sum_{i=1}^{N} B_i \tag{3.1}$$

Where:

$\bar{B}$ is the mean of the data,

N is the number of data points and

B_i is the i_{th} data point.

$$\sigma = C_N\sqrt{\frac{\sum_{i=1}^{N}(B_i - \bar{B})}{(N-1)}} \tag{3.2}$$

Where:

σ is the standard deviation,

N is the number of data points,

B_i is the i_{th} data point,

$\bar{B}$ is the mean of the data points, and

C_N is the corrective constant given in equation 3.3.

$$C_N = \sqrt{(\frac{N-1}{2})\frac{\Gamma[(N-1)/2)]}{\Gamma(N/2)}} \tag{3.3}$$

Where:

C_N is the corrective co-efficient and

N is the number of data points.

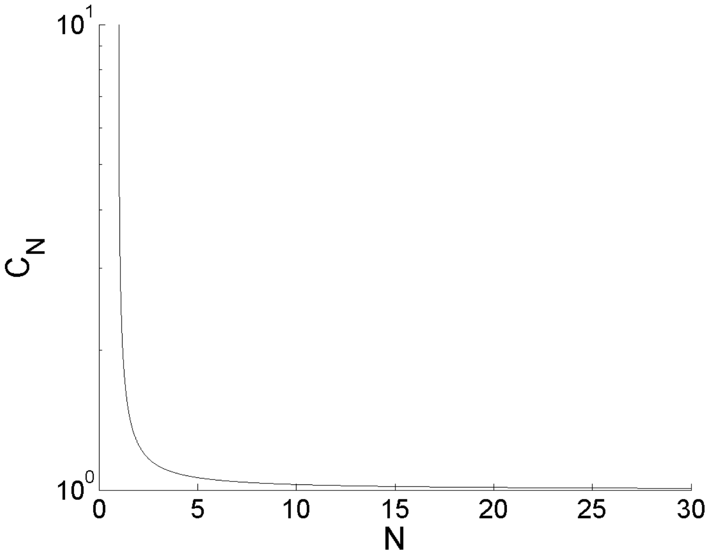

Figure 3.9: The value of the corrective co-efficient for standard deviation of small sample sizes, $N \leq 30$, to account for under estimation of the standard deviation in small sample sizes, C_N, calculated using equation 3.3, versus the data sample size, N, for $2 \leq N \leq 30$.

The range for which 95% of gathered data is expected to fall within was calculated using equation 3.4 [126].

$$B_{95} = \bar{B} \pm 1.96\sigma \tag{3.4}$$

Where:

B_{95} is the bounds for which 95% of gathered data falls,

$\bar{B}$ is the mean of the data points, and

σ is the standard deviation of the data.

As can be seen in figure 3.9 the value of C_N decreases with increasing sample size tending towards 1. With a sample size of 2 the corrective co-efficient increases the calculated standard deviation by approximately 25%, while at a sample size of 30 this reduces to <1%. These corrective factors are required as the standard deviation tends to produce lower than expected errors for small sample sizes.

3.3.2 Repeatability results

The mean of the measured magnetic field strength in the B_x and B_z components versus the x position along the conduit are shown in figure 3.10. The error bars in the plots shows the bounds for which 95% of the data over 30 scans falls using the method shown in section 3.3.1.

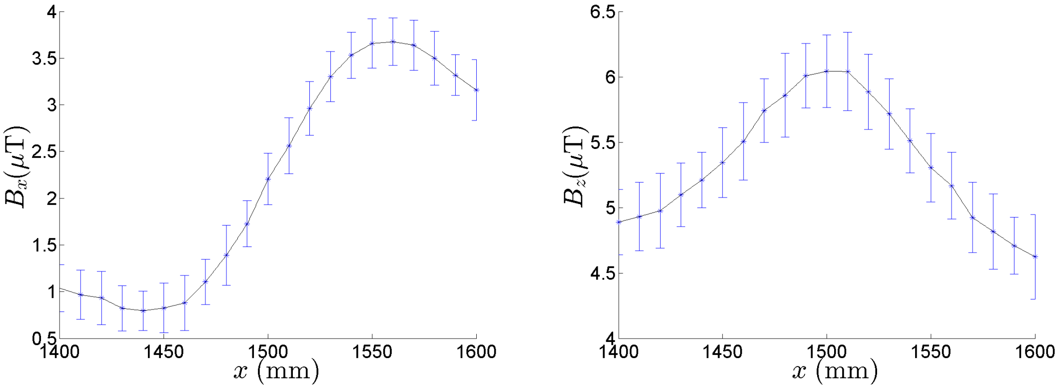

(a) Mean value of the x component magnetic field gradient, B_x, over a data sample size, N, of 30 in the range $x =$ 1400 - 1600 mm in steps in x of 10 mm. With error bars representing the 95% limits $B_{95} = \bar{B} \pm 1.96\sigma$.

(b) Mean value of the z component of the magnetic field gradient, B_z, over a data sample size, N, of 30 in the range $x =$ 1400 - 1600 mm in steps in x of 10 mm. With error bars representing the 95% limits $B_{95} = \bar{B} \pm 1.96\sigma$.

Figure 3.10: Mean value of the x, in a, and z , in b components of the magnetic field gradient, B_x and B_z, over a data sample size, N, of 30 in the range $x =$ 1400 - 1600 mm in steps in x of 10 mm. With error bars representing the 95% limits $B_{95} = \bar{B} \pm 1.96\sigma$.

To verify that the distribution of values for each point is a normal distribution a histogram of the deviation, $D_i = B_i - \bar{B}$ for each data point was plotted. The histograms for B_x and B_z are shown in figure 3.11. The histograms also show a normal distribution, this was generated using the values of the mean of the deviation $\bar{D}$, the 95% bounds, B_{95}, and scaled to the area of the curve equal to 630, the total number of data points. On the histograms the mean for each deviation $\bar{D}$ is marked as a dashed red line and the 95% bounds, $\bar{B} \pm B_{95}$, marked as dashed green lines.

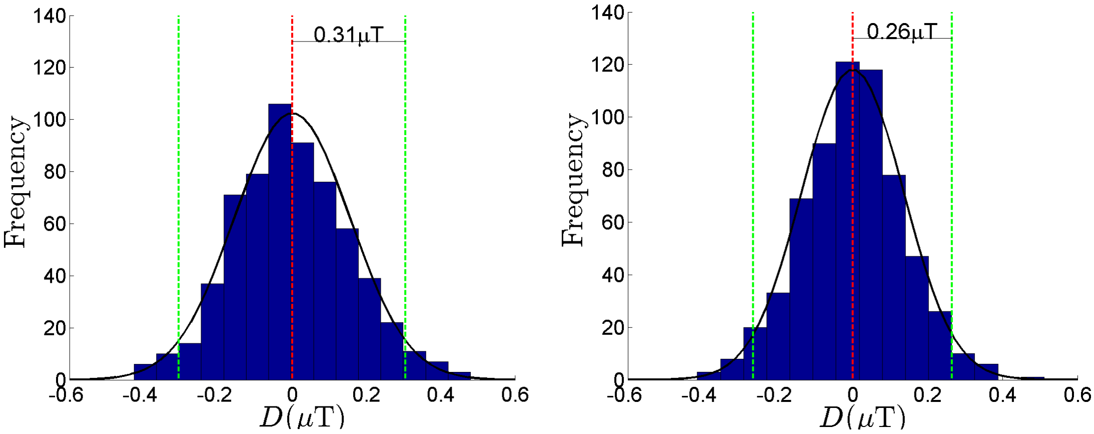

(a) Histogram showing the distribution of the deviation in the x component over 30 scans. The normal distribution calculated using the mean, standard deviation and sample size is plotted in black. The mean of the deviation is marked with a red dashed line and the 95% bounds marked with green dashed lines.

(b) Histogram showing the distribution of the deviation in the z component over 30 scans. The normal distribution calculated using the mean, standard deviation and sample size is plotted in black. The mean of the deviation is marked with a red dashed line and the 95% bounds marked with green dashed lines.

Figure 3.11: Histograms showing the distribution of the deviation from the mean of the magnetic field gradient components over 30 scans between $x = 1400$ - 1600 mm in steps of 10 mm. The normal distribution for the mean of the deviation, the standard deviation of the data and the number of data points in the distribution. The mean of the deviation, is marked with a red dashed line and the 95% bounds, $\bar{B} \pm B_{95}$, marked with green dashed lines.

3.3.3 Analysis of data repeatability

To test the data presented in the histograms in section 3.10a follows a normal distribution the Shapiro-Wilk test can be used [134]. The Shapiro-Wilk test tests if a set of data comes from a normally distributed population, this can be performed on data sets of $N \leq 2000$ [135]. The test produces a W value which has a range $0 \leq W \leq 1$, as the data tends towards a normal distribution the W value tends towards 1 [136]. For each N a W value threshold for which the data is considered to have a normal distribution can be calculated. The W value is calculated using equation 3.5.

$$W = \frac{(\sum_{i=1}^{N} a_i B_i)^2}{\sum_{i=1}^{N}(B_i - \bar{B})^2} \tag{3.5}$$

Where:

W is the W value for the data,

N is the number of data points,

a_i is the i_{th} linear unbiased coefficient,

B_i is the i_{th} data point, and

$\bar{B}$ is the mean of the data points.

The W value threshold for each sample size, N can also be found in a look up table, for $N = 630$ this is 0.985. The calculated W value for the x and z co-ordinates are 0.998 and 0.997 respectively. This shows a high level of normality in the collected data. As the data forms a normal distribution the equations for CI_{95} in section 3.3.1 can be considered to be valid for values of $N < 30$ [132].

The mean of the 95% bounds in B_x and B_z are 0.31μT and 0.26μT respectively. These show a high level of repeatability in the experimental set up and give good confidence in the data gathered in the laboratory. This allows a reduction in the number of repeat measurements in scans on the full length conduits, reducing the time taken to conduct an experiment. This reduction in time reduces the possibility of environmental effects changing over the scan time introducing further errors.

This high level of repeatability increases confidence in the results gathered from buried gas pipelines where the magnetic data can only be practically gathered once due to the long survey distances.

3.3.4 Discussion of data repeatability

The repeatability of an experiment is a measure of the variability of data gathered on the same equipment, by the same user, on the same subject in a short period of time. Repeatability is important to characterise for an experiment, a high level of repeatability gives confidence in the data collected as this suggests the data gathered is not expected to vary greatly between experiments. A low level of repeatability would indicate an inaccuracy in the data that would require further investigations to characterise in order to give confidence in the data [137].

The repeatability of the experimental equipment and methodology was characterised by repeating a scan of a known feature from a cut 1″ mild steel conduit 30 times at a height of 50 mm. The 30 repeated scans were used to calculate a mean and standard deviation for each of the points measured in the magnetic field. The 95% bounds typically used to state repeatability were calculated using the standard deviation. This data gives levels of repeatability of 0.31 μT and 0.26 μT for the calculated B_x and B_z components of the magnetic field strength respectively. This shows a high level of repeatability in the gathered laboratory data.

The variance of the data gathered in each scan from the calculated mean shows a normal distribution about the mean. This allows the error in the data to be characterised from smaller data sets, as for $N < 30$ the methods used to calculate the errors are only valid for data sets which are expected to be a normal distribution.

The experiment was carried out for only a narrow set of factors, a single 1″ mild steel conduit with a height above the array of 50 mm. The values of repeatability will vary with conduit size, height above the conduit and magnitude of the field from the cut. The values of repeatability calculated for this specific case are therefore not applicable to other experimental configurations. These experiments verified that the distribution of the errors in the data is expected to be a normal distribution around the mean. This allows the repeatability limits to be estimated for the different experimental configurations from a smaller number of repeated data sets.

In this work only the repeatability has been assessed. The reproducibility, where the experiment has been carried out on different equipment or by a different user, of the experimental data has not been investigated. Characterising the reproducibility of this data in future investigations would give further insight into the validity of data gathered in the laboratory.

The repeatability of the experimental set-up and methodology has been evaluated for 30 scans of a cut in a 1″ diameter mild steel conduit at a height of 50 mm. This shows a high level of repeatability with 95% bounds of ~ 0.3 μT in the magnetic gradient. The error in the data gathered shows a normal distribution about the mean. This allows for a smaller number of repeated scans in further experiments to calculate the 95% bounds, as the error is expected to be in a normal distribution about the mean.

3.4 Conclusion

The laboratory set-up used to conduct the experiments on mild steel conduits as pipe simulants has been described. This consists of a Bartington Mag649 connected to a scanning arm which allows the magnetometer to be moved in a two-dimensional plane above the test subject using stepper motors. A stand to hold the test sample in position is attached to the scanning stand to hold the sample steady relative to the magnetometer origin.

The conduit pipes used in these experiments have been described. Four conduit sizes were used for this, these had nominal diameters of 1/2″, 3/4″, 1″ and 1 1/2″. The actual physical dimensions and material properties have been given for these. These conduits have been chosen due to ease of availability, ease of cutting, similar material properties to field pipes and they have a seam weld.

The repeatability of magnetic data gathered on a conduit using the laboratory set-up has been assessed. The system shows a high level of repeatability giving 95% bounds of 0.31 μT and 0.26 μT in the B_x and B_z components respectively for 30 scans on a cut 1″ conduit. The variation from the mean for this data shows a normal distribution, allowing repeated data sets of $N < 30$ to be gathered and assessed in further experiments as the data is expected to give a normal distribution about the mean.

Chapter 4

Visualisation of vector fields

4.1 Introduction

The data gathered in the laboratory is gathered in three orthogonal components of the magnetic field strength in a three-dimensional grid of points. Visualisation is the art of displaying scientific data so that the underlying patterns can be interpreted quickly and accurately by a non-expert end user. Visualisation is capable of relaying a large quantity of information to a user that would be meaningless if presented as a simple list of values [138]. Visualisation of a vector field must communicate both a direction and magnitude of the vectors in the field to the viewer however there is no natural representation for visualising three-dimensional vector fields [139].

Using an algorithm to analyse the data from the magnetic array can lead to features that do not conform to the pre-programmed algorithm's detection parameters being ignored. The data can be presented using a visualisation technique to allow the user to identify anomalies in the data for further investigation which an algorithm may overlook. Finding a visualisation technique that can effectively represent the gathered vector field data could lead to improvements in anomaly location and make finding non-standard anomalies easier for the end user.

Visualisation methods are separated into two categories direct and indirect methods. Direct vector visualisation methods represent the magnitude and direction of the field at discrete points within the field. Indirect visualisation methods on the other hand show the physical effects of the vector field requiring the user's inference of the local vector field [140].

Scientific computer visualisation of data sets is a relatively new field, first formulated as a discipline in its own right in 1987 [141]. Since then many techniques for visualisation of scientific data have been proposed. Techniques that have been used to represent vector fields include [139][142]:

- hedgehog plots,
- streamlines, and
- convolution textures.

Hedgehog plots use arrows to represent the vector field at discrete points, showing the shape of the field at discrete points to allow the user to interpret the full field [143]. Streamlines plot the path a theoretical particle injected into the vector field would take, this allows the underlying flow of the vector field to be interpreted by the user [144]. Linear integral convolution (LIC) produces a texture using the vector field to convolve a white noise image producing a texture which shows the shape of the vector field [142].

Visualisation of a vector field to maximise the information of the vector field shape and magnitude scalar field conveyed to the user can increase the ability of the end user to find features in the data. This is not currently used in large stand-off magnetometry, an algorithm is instead used to locate the features detected with the magnetometer. A visualisation technique could be implemented to supplement this algorithm leading to the identification of additional anomalies for further investigation.

The visualisation techniques have been considered and assessed for use in presenting the data gathered in the laboratory. These were also considered for how they could be incorporated into the analysis of the field pipeline survey data.

4.2 Visualisation of vector fields

4.2.1 Hedgehog plots

A hedgehog plot is a method of visualisation that shows line segments at discrete grid positions throughout the field indicating the direction of the vector field at these points. These line segments can be scaled in length to show the magnitude of the vector and have an icon such as an arrow to denote the vector direction [139].

Hedgehog plots show the field direction and magnitude at discrete points in the field. The data points in the field must be spaced far enough apart to prevent the line segments from overlapping as this will obscure information about the field for the user and make the plot unreadable at too high a data density. Spacing these points too far apart however could lead to small anomalies in the field being missed due to the surrounding line segments not being affected by the anomaly.

The different directions and lengths of the arrows through the vector field in a hedgehog plot can lead to optical illusions, these illusions distort the user's ability to distinguish both the point at which the field is being represented and the length of the arrows. This effect can be avoided by normalising the length of the line segments then applying a colour map to represent the magnitude of the field, instead of scaling the lengths of the arrows to represent the magnitude.

The extra level of abstraction created by adding colour map can however make it difficult for the user to visualise the vector field shape. Hedgehog plots using arrows to represent a two-dimensional vector field described by $\vec{v} = x^2\hat{\imath} + y^2\hat{\jmath}$ are shown in figure 4.1.

The problem of creating optical illusions is particularly visible in figure 4.1a. The arrows in the figure are spaced at regular cartesian positions in the field. Due to the shape of the field and changing arrow lengths, the positions of the arrows appear to lie on a curve, misleading the user as to the position of the vector field points sampled. In figure 4.1b with arrows of the same length, the cartesian positions of the arrows are easier to decipher. In figure 4.1b the shape of the vector at small magnitudes is also easier for the end user to see than in figure 4.1a. This is due to the arrows in the length scaled plot being small at small magnitudes whereas the colour map version have equal length arrows. In the colour map hedgehog plot, it is however harder for the end user to visualise the shape of the field than in the arrow length scaled version due to the combination of two different forms of information presented.

The problem of overlapping points and difficulty distinguishing the directions of the arrows is further exacerbated when the plot extended to three dimensions. Three-dimensional hedgehog plots are difficult for viewers to discern where each point is in the space and how the arrow is oriented [145]. A three-dimensional hedgehog plot for a vector field described by $\vec{v} = x^2\hat{\imath} + y^2\hat{\jmath} + z^2\hat{k}$ is shown in figure 4.2.

In figure 4.2 it can be seen that when expanded to three dimensions it becomes difficult for the user to determine the direction or magnitude of the vector field, making these three-dimensional plots useful in only a limited number of cases.

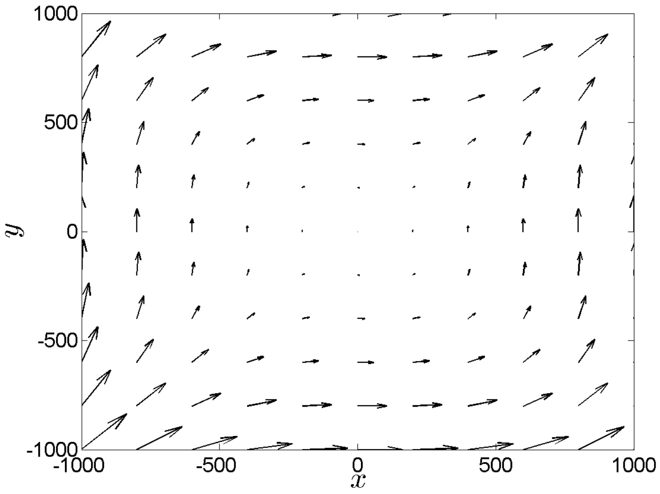

(a) Hedgehog plot with arrows representing the direction of the vector field at discrete points in the field. The arrow lengths are scaled to represent the magnitude of the vector at these points in the vector field described by $\vec{v} = x^2\hat{\imath} + y^2\hat{\jmath}$.

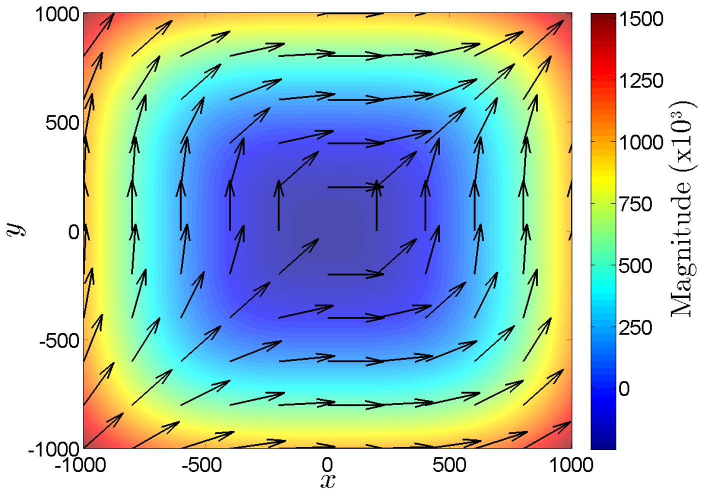

(b) Hedgehog plot with arrows of equal length representing the direction of the vector field at discrete points in the field. The magnitude of the vector field is represented with a colour map in the vector field described by $\vec{v} = x^2\hat{\imath} + y^2\hat{\jmath}$.

Figure 4.1: Hedgehog plots with arrows representing the direction of the vector field at discrete points in the vector field described by $\vec{v} = x^2\hat{\imath} + y^2\hat{\jmath}$. The magnitude of the vector field is represented by scaled arrow lengths shown in subfigure a, and with an applied background colour map shown in subfigure b.

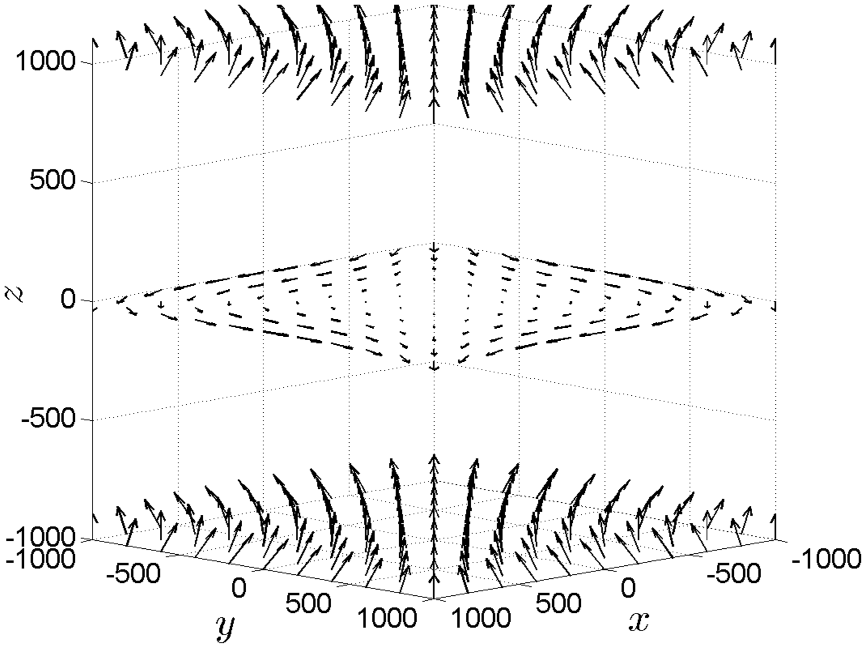

Figure 4.2: Three-dimensional hedgehog plot using arrows to represent the direction of the vector at discrete points in a vector field described by $\vec{v} = x^2\hat{\imath} + y^2\hat{\jmath} + z^2\hat{k}$. The arrow lengths are scaled to represent the magnitude of the vector field at these points in the vector field.

4.2.2 Streamline plots

A streamline plot traces the path that a theoretical particle injected into the field at a defined position would take as it moves through the field. These are generated by stepwise integration through the field [144]. The position of the particle at Δt is given by [146]:

$$x(t + \Delta t) = \int_{t}^{t+\Delta t} v_0(x(t))dt \tag{4.1}$$

where:

x is the particle position,

t is the time,

Δt is the time step, and

v_0 is the vector field.

Particle positions are calculated at each time step as they move through the field and a curve fitted to the positions to produce a trace. This is then repeated for multiple particles injected at different positions to build up a picture of the vector field flow. Due to the particle time step positions not necessarily ending at a position with gridded data, interpolation of the data between these positions is required [139].

A streamline plot does not represent the magnitude of the field, another method is therefore required to represent the magnitude of the vector field. This can be done by imposing a colour map on the background to represent the magnitude. The magnitude can also be shown by marking the particle position at the end of each time step with bigger distances travelled in the time step showing greater magnitude. Figure 4.3a shows a streamline plot for a vector field described by $\vec{v} = x^2\hat{\imath} + y^2\hat{\jmath}$ with no magnitude information. Figure 4.3b shows the streamline for the same vector field with a colour map imposed on the background to show the vector field magnitude.

In figure 4.3a the field shape is well represented with local and global features easily visible, however there is no magnitude information given. In figure 4.3b

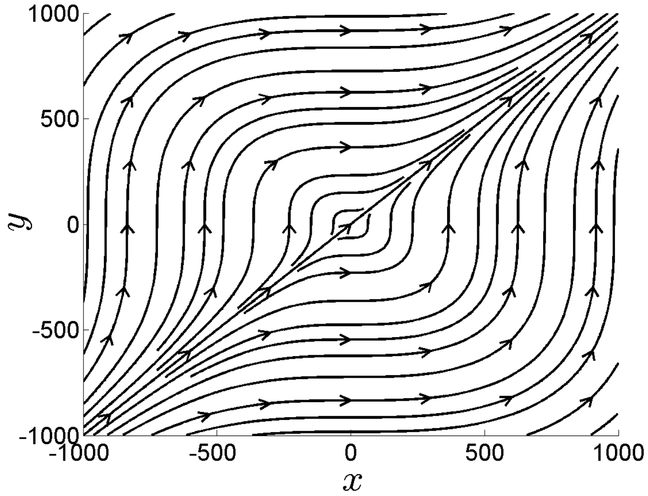

(a) Streamlines representing the shape of the vector field described by $\vec{v} = x^2\hat{\imath} + y^2\hat{\jmath}$. There is no representation of the magnitude of the field shown.

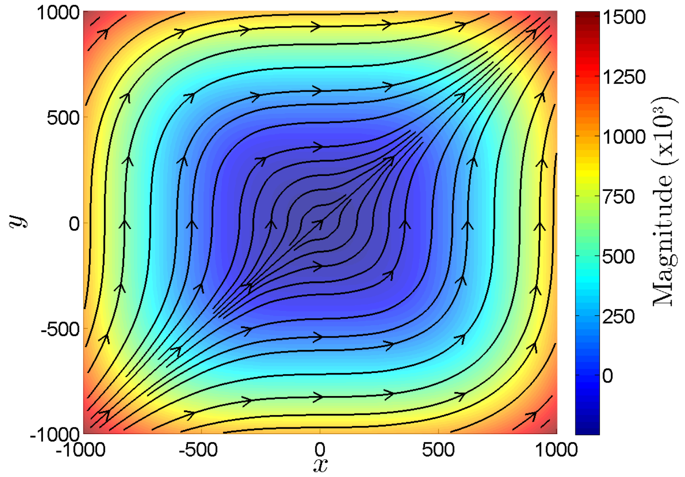

(b) Streamlines representing the shape if the vector field described by $\vec{v} = x^2\hat{\imath} + y^2\hat{\jmath}$. A colour map has been imposed on the background to represent the magnitude of the field.

Figure 4.3: Streamlines showing the paths that theoretical particles injected into the field would take for a vector field described by $\vec{v} = x^2\hat{\imath} + y^2\hat{\jmath}$ to show the vector field shape. Subfigure a has no representation of the magnitude of the field while subfigure b has a colour map imposed on the background to represent the magnitude of the field.

the magnitude is represented by an imposed colour map. This colour map makes reading the vector field flow and direction more difficult by reducing the contrast of the streamline to the background.

Streamline plots can be used to show two-dimensional planar slices through a three-dimensional vector plot by showing slices though the data on a three-dimensional axis. These slices must be carefully chosen to avoid missing important information or causing them to overlap on the plot meaning information from slices further back is obscured. The slice plots have the same problems as two-dimensional stream slices in that they do not show the magnitude of the vector without the colour map. In the three-dimensional axis case the addition of a colour map increases the possibility of overlapping information. Examples of slices for the vector field $\vec{v} = x^2\hat{\imath} + y^2\hat{\jmath} + z^2\hat{k}$ are shown in figure 4.4a without a colour map and figure 4.4b with the colour map added.

Figures 4.4a showing streamlines to show the path theoretical particles would travel through the vector field. The streamlines in three dimensions represent the shape and flow of the vector field in the slices chosen. These are easily read by the user and give a good impression of the shape and flow of the vector field, there is however no magnitude information. Figure 4.4b shows the same slices through the same vector field as subfigure 4.4a with a colour map imposed in the background to show the magnitude of the field in the slices. This colour map allows the user to assess the magnitude of the vector field in the slices, however the colour map obscures the ease of picking out the vector field shape from the streamlines.

4.2.3 Linear integral convolution

Image convolution is used commonly in image processing to carry out tasks such as edge detection, smoothing and enhancing. This involves calculating each pixel on the final image using the original image and a filter matrix. Unlike hedgehog and streamline plots linear integral convolution (LIC) produces a texture which is continuous and not discretised, this means that anomalies in the data set will not be missed by falling between cells. The texture can convey such a high density of detail that the end user will be overwhelmed and unable to identify anomalies.

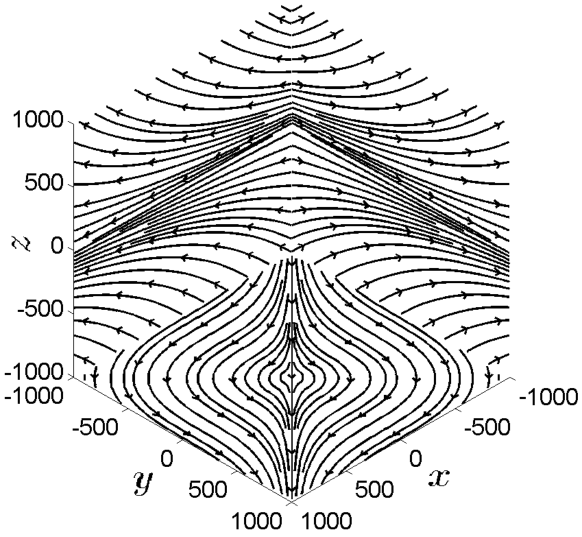

(a) Streamlines showing the paths that theoretical particles injected into the vector field would move through for a vector field described by $\vec{v} = x^2\hat{\imath} + y^2\hat{\jmath} + z^2\hat{k}$. These are shown in slices at x = -1000, y = 1000 and z = -1000 on a three-dimensional axis. These have no representation of the magnitude of the field in these slices.

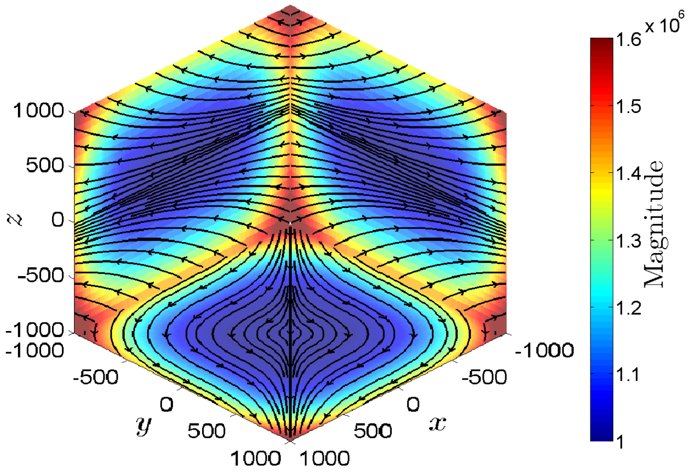

(b) Streamlines showing the paths that theoretical particles injected into the vector field would move through for a vector field described by $\vec{v} = x^2\hat{\imath} + y^2\hat{\jmath} + z^2\hat{k}$. These are shown in slices at x = -1000, y = 1000 and z = -1000 on a three-dimensional axis. These have a colour map imposed on the background of each slice to represent the magnitude of the field at these positions.

Figure 4.4: Streamlines showing the paths that theoretical particles injected into the vector field would move through for a vector field described by $\vec{v} = x^2\hat{\imath} + y^2\hat{\jmath} + z^2\hat{k}$. These are shown in slices at x = -1000, y = 1000 and z = -1000 on a three-dimensional axis. In subfigure a there is no representation of the magnitude of the field in these slices, while in subfigure b these have a colour map imposed on the background of each slice to represent the magnitude of the field at these positions.

The LICs generated in this work were created using an available Matlab toolbox [147]. As part of this work the toolbox was adapted to show axes for the positional information and an overlaid colour map to show the value of the magnitude of the vector field to the end user.

In LICs the output image is calculated as a convolution of the intensity values over the integral curves of the vector field [142]. The original image to which this convolution is applied is a randomised, white noise image. This allows the pixels in the original image to give the final image high contrast for the user while not introducing a secondary pattern that could be picked up by the user when no such pattern exists in the data [148].

In LIC the local behaviour of a vector is first approximated by calculating the streamline that starts at the centre of a pixel in both the positive and negative direction for a fixed distance, l. This pixel of focus is designated P_0 and has the centre co-ordinates $(x + 0.5, y + 0.5)$.

The streamline is calculated stepwise calculating the next pixel in the forwards direction, P_i from the pixel coordinates of the last step, P_{i-1} the vector direction at that pixel $v(P_{i-1})$ and the parametric distance along the vector field from P_{i-1} to the nearest cell edge, Δs_{i-1}. The equation is given by:

$$P_i = P_{i-1} + \frac{V(P_{i-1})}{||V(P_{i-1})||}\Delta s_{i-1} \tag{4.2}$$

The symmetry about a cell is required to be maintained to avoid misleading visualisation. The pixel path in the negative direction is similarly calculated stepwise with the equation:

$$P'_i = P'_{i-1} + \frac{V(P'_{i-1})}{||V(P'_{i-1})||}\Delta s'_{i-1} \tag{4.3}$$

Δs_{i-1} and $\Delta s'_{i-1}$ are always positive and are required to take the advected co-ordinates into the $i+1_{\mathrm{th}}$ cell taking the streamline segment out of the current cell. The next step is to integrate along these streamlines to produce a linear integral convolution matrix. For each continuous segment i an integral of a convolution kernel $k(w)$ is calculated using:

$$h_i = \int_{s_i}^{s_i+\Delta s_i} k(w)dw \tag{4.4}$$

where:

$s_0 \; = 0$ and

$s_i \; = s_{i-1} + \Delta s_{i-1}$

The entire LIC for an output pixel F'(x,y) is given by

$$F'(x,y) = \frac{(\sum_{i=0}^{l} F(P_i)h_i + \sum_{i=0}^{l'} F(P_i')h_i')}{(\sum_{i=o}^{l} h_i + \sum_{i=0}^{l'} h_i')} \tag{4.5}$$

where:

$F(P)$ is the input pixel corresponding to the vector at (P_x, P_y), and

$l = i$ such that $s_i \leq L < s_{(i+1)}$.

The numerator of this equation represents the line integral of the kernel multiplied by the input pixel field, while the denominator normalises the output pixel weight. LIC produces textures that show the vector field shape, but do not show the magnitude of the vector at each point. This can be added onto the plot by adding a colour map to the final image to show the magnitude at each point.

Figure 4.5a shows an LIC texture for a vector field defined by the equation $\vec{v} = x^2\hat{i} + y^2\hat{j}$, figure 4.5b shows an LIC texture for the same vector field with a colour map showing the magnitude of the vector field at each point.

In figure 4.5a the shape of the vector field is easy to see and covers the whole field rather than discrete sections as in hedgehog or streamline plots. This makes any anomalies easier for the user to pick out and reduces the chance of any anomalies being missed by the user of the visualisation method. In figure 4.5b the vector field shape as well as magnitude is shown, this allows the user to pick out both vector field shape and magnitude. The colour map makes it more difficult to pick out the fine vector shape over some colours by reducing the contrast in the texture. No polarity of vector field flow is represented in either figure 4.5a or 4.5b.

The LIC with a colour map visualisation technique presents the most information density to the end user of the techniques assessed in this chapter. These have the lowest probability of missing anomalies in the vector field data and present the easiest method of finding the anomalies to the end user.

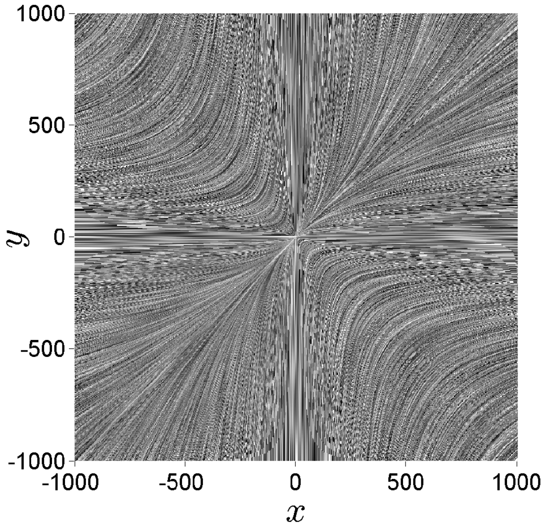

(a) Linear integral convolution texture generated to represent the vector field shape for the full vector field shape in the vector field described by $\vec{v} = x^2\hat{\imath} + y^2\hat{\jmath}$. The texture does not have any magnitude information presented in it.

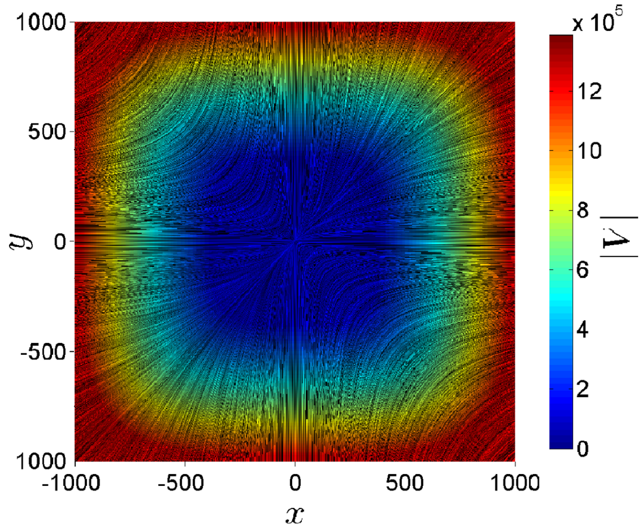

(b) Linear integral convolution texture generated to represent the vector field shape for the full vector field shape in the vector field described by $\vec{v} = x^2\hat{\imath} + y^2\hat{\jmath}$. The texture has a colour map imposed on it to show the magnitude of the vector field.

Figure 4.5: Linear integral convolution textures generated to represent the vector field shape for the vector field described by $\vec{v} = x^2\hat{\imath} + y^2\hat{\jmath}$. Subfigure a does not have any representation of the magnitude of the field, while subfigure b used a colour map imposed onto the texture to represent the magnitude of the vector field.

4.3 Visualisation of laboratory experiment data

To assess the visualisation techniques outlined in section 4.2, the three techniques were applied to laboratory experimental data presented in full in chapter 6. The laboratory data used was the data gathered in magnetometer scans of three permanent magnets, the full results and methodology for these scans are detailed later in this thesis, in section 6.3.

This data set was chosen for analysis of the visualisation techniques for analysis of the laboratory data as it has multiple anomalies throughout the field scanned. This allows for the visual assessment of the data by the user to find these while highlighting any problems with the method that would prevent the user from identifying these anomalies. The three visualisation techniques that have been assessed in this section are:

4.3.1 for hedgehog plots,

4.3.2 for streamlines, and

4.3.3 for LICs.

4.3.1 Hedgehog plots

Hedgehog plots have been generated for the magnetometry data from scans on three permanent magnets. Figure 4.6a shows the hedgehog plot for the data with the arrow length scaled by the magnitude of the vector field at that position. Figure 4.6b shows the hedgehog plot for the data with the arrow lengths normalised and a colour map applied to show the magnitude field for the data.

In the case with arrow length scaling shown in figure 4.6a the increased magnetic field magnitude in the range x = -100 – 100 mm can easily be seen. The zero-crossings (turning points) in the B_z component of the field at approximately x = -50 mm and in the B_x component at approximately x = 25 mm can be found, however this requires some interpretation on the part of the viewer to understand how these points are shown in these plots. The problem of optical illusions discussed in the hedgehog plot technique section 4.2.1 can be seen in the z co-ordinated where the arrows sit along lines of constant z but appear to be at different heights to each other, particularly in the high magnitude region x = -100 – 100 mm.

In the case with normalised arrow lengths and continuum colour map shown in figure 4.6b the increased magnetic field magnitude in the x = -100 – 100 mm range can easily be seen due to the contrasting colours between this region and the lower areas of magnitude in the field. The zero-crossings discussed for the arrow length scaling plot above can be seen though these still require interpretation by the user. The problem of optical illusions is less pronounced than in the arrow length scaling technique, however this is still present in the lines of constant height depending on if there is a positive or negative B_z component.

4.3.2 Streamline plots

Streamlines have been generated for the magnetometry data from three permanent magnets in the laboratory. Figure 4.7a shows a set of streamlines showing the path a theoretical particle injected into the field would take to show the shape and direction of the vector field, there is no representation of the magnitude field in this technique. Figure 4.7b shows these streamlines overlaid on a colour map which shows the magnitude of the field in this region.

In the case with only streamlines shown in figure 4.7a the zero-crossings are easily seen as turning points in the streamlines with limited interpretation from the user required. In the case with the colour map shown in figure 4.7b the streamlines are the same as in the case with no colour map so give the exact same information with the added information of the increased magnitude in the area x = -100 – 100 mm which was shown in the hedgehog plots shown in section 4.3.1.

4.3.3 Linear integral convolution

Linear integral convolution (LIC) textures have been generated for data from scans of three permanent magnets in the laboratory. Figure 4.8a shows the texture representing the magnetic field shape from the laboratory data, this texture has no representation of the magnitude of the field. Figure 4.8b shows the colour map for the magnetic field magnitude, this map only represents the magnitude with

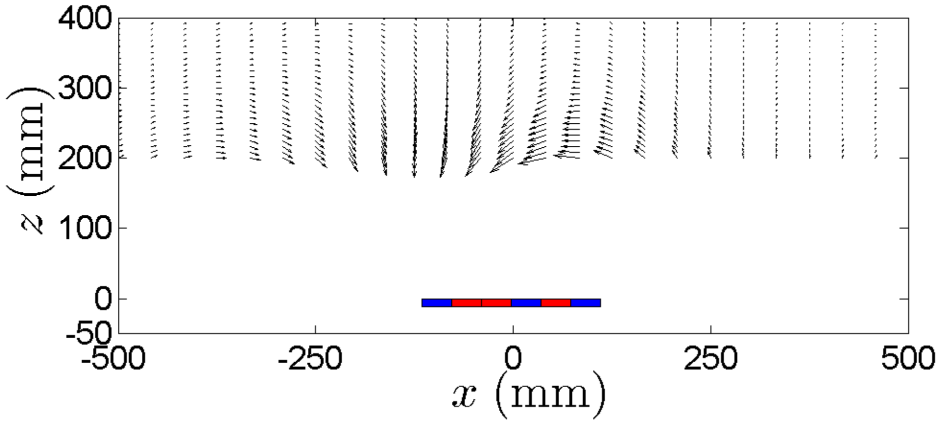

(a) Hedgehog plot showing the magnetic field from three magnets in the laboratory, the arrows show the direction of the arrows and the length of the arrows is scaled to represent the magnitude of the field.

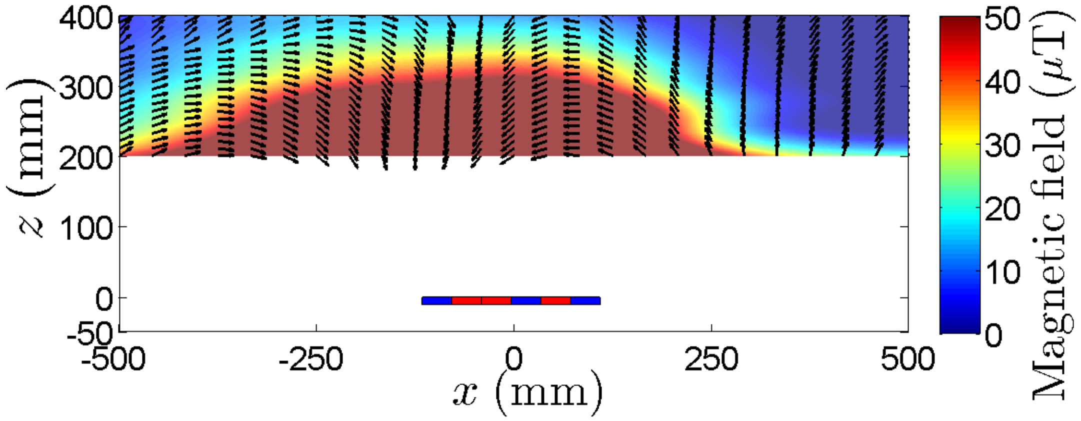

(b) Hedgehog plot showing the magnetic field from three magnets in the laboratory, the arrows show the direction of the arrows and the colour map to represents the magnitude of the field.

Figure 4.6: Hedgehog plots showing the magnetic field strength data from three magnets gathered in laboratory experiments. In both subfigure a and b the vector directions in the field are represented by arrows at discrete points through the field. In a the arrow lengths are scaled to represent the vector magnitude at these points, in b the magnitude of the vector field is represented as a continuum by a colour map.

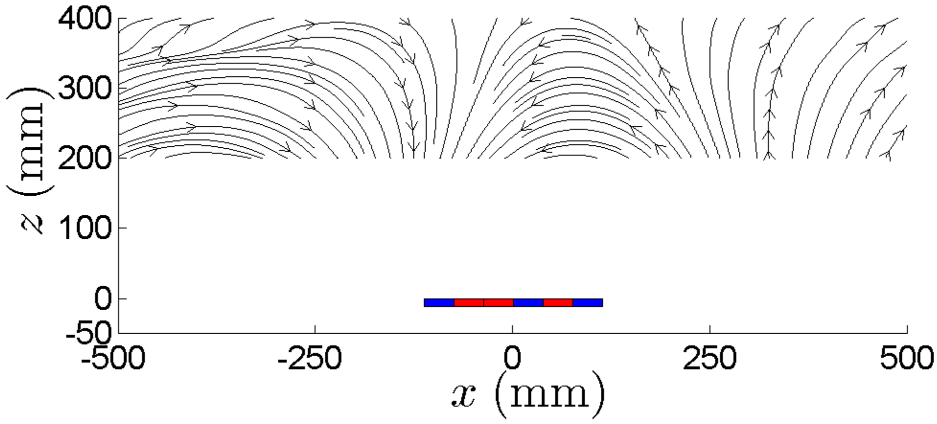

(a) Streamlines showing the magnetic field from three magnets in the laboratory, the lines represent the direction a theoretical north pole injected into the field would travel through to show the vector field shape, the magnitude of the vector field is not represented by this method.

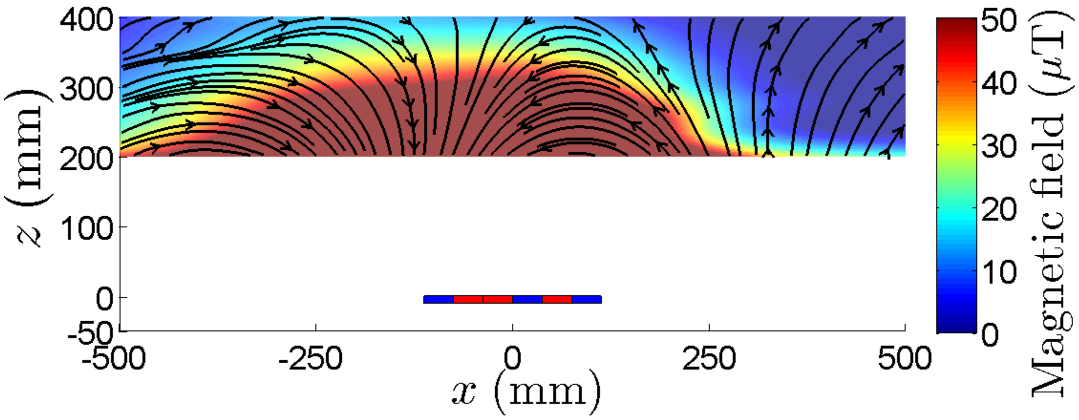

(b) Streamlines showing the magnetic field from three magnets in the laboratory, the lines represent the direction a theoretical north pole injected into the field would travel through to show the vector field shape, the magnitude of the vector field is represented by a colour map.

Figure 4.7: Streamlines showing the path a theoretical north pole injected into the magnetic field from three magnets measured in the laboratory, would take to represent the vector field shape. In subfigure a the magnitude of the vectors are not shown, in subfigure b the magnitude is represented by a colour map.

no vector field shape represented. Figure 4.8c shows the composite of figures 4.8a and 4.8b to represent the vector field shape and magnitude.

In figure 4.8a the zero-crossings are clearly identifiable as a feature in the field shape, these also highlight the angular deflection in the feature position discussed in chapter 6. These anomalies are not identifiable in figure 4.8b as there is no representation of the vector field, however the area of increased magnitude is easily visible. In the composite of the two, shown in figure 4.8c the crossings can be easily identified, the region of increased magnitude can help to interpret the peak and zero-crossing locations in the magnetic field.

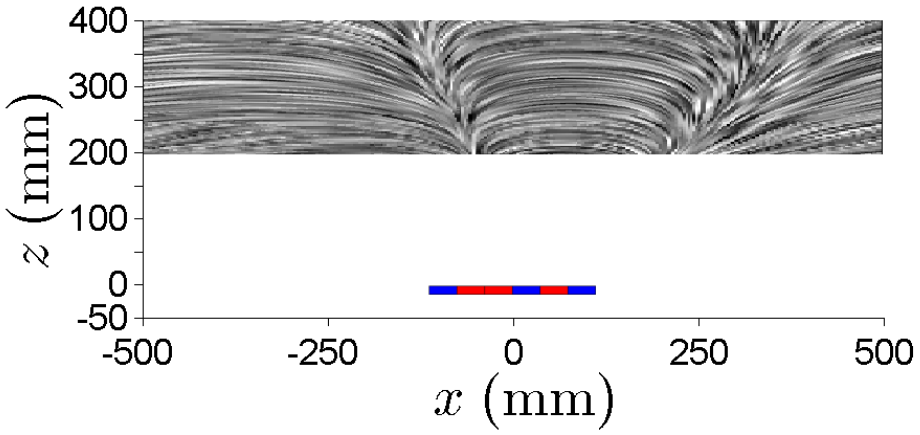

(a) Linear integral convolution texture of the magnetic field from three magnets measured in the laboratory representing the vector field shape.

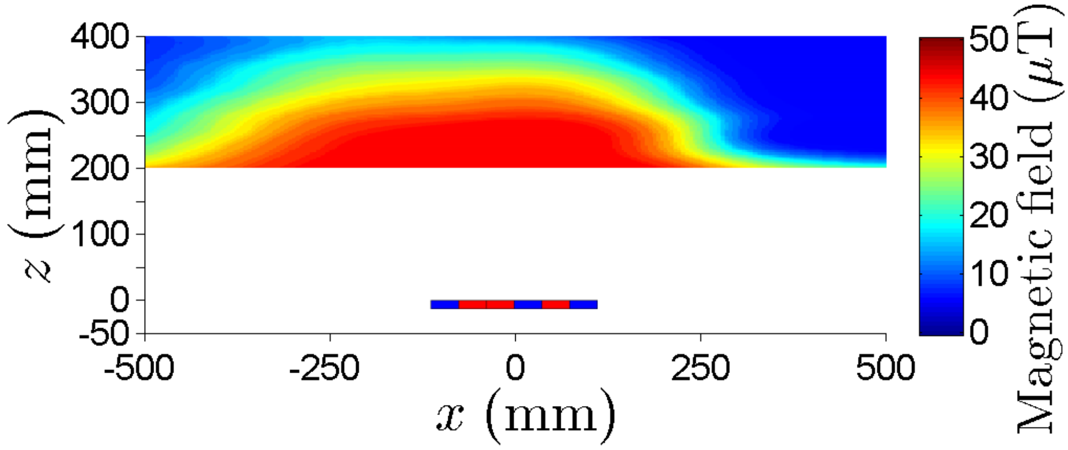

(b) Colour map of the magnetic field from three magnets measured in the laboratory representing the magnitude of the magnetic field.

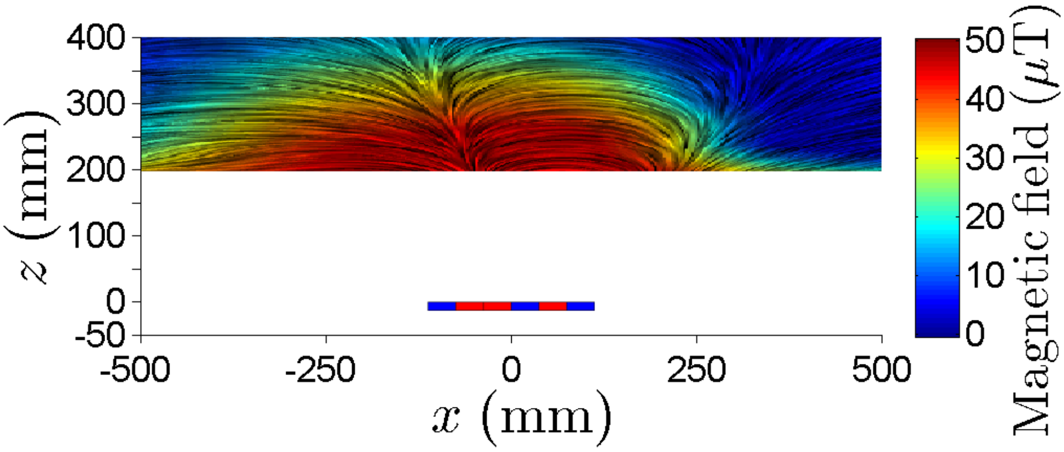

(c) Combined linear integral convolution texture and colour map representing the vector field shape and magnitude for the field from three magnets measured in the laboratory.

Figure 4.8: Figures showing the laboratory data gathered from three magnets: a linear integral convolution texture representing the magnetic field shape is shown in subfigure a, a colour map representing the magnitude of the magnetic field in subfigure b and the combination of both to represent the shape and magnitude of the field is shown in subfigure c.

Figure 4.9a Shows the LIC texture generated from the laboratory magnetic scan data from three permanent magnets to represent the vector field shape. A colour map has been applied to show the B_x component of the field. Figure 4.9b also shows the LIC texture generated from the laboratory magnetic field data representing the vector field shape, the colour map applied shows the B_z component of the field.

These figures show the shape of the vector field allowing the anomalies in the field shape, for example zero-crossings, to be easily identified. The individual component colour maps further identify the zero-crossings in each component as well as making the locations of peaks easily interpreted to the user.

To investigate the number of data points required to produce useful LIC textures the data gathered for the three magnets in the laboratory three LIC textures have been produced with different numbers of sample points in the z direction. The LIC textures for the three sample point case are shown in figure 4.10, these

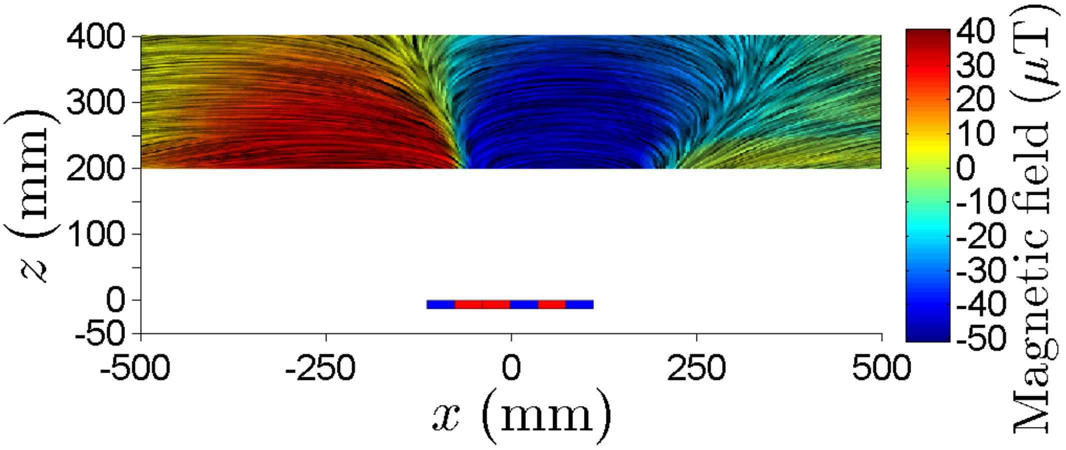

(a) Linear integral convolution texture of the magnetic field from three magnets in the laboratory representing the vector field shape. The colour map represents the x component of the magnetic field.

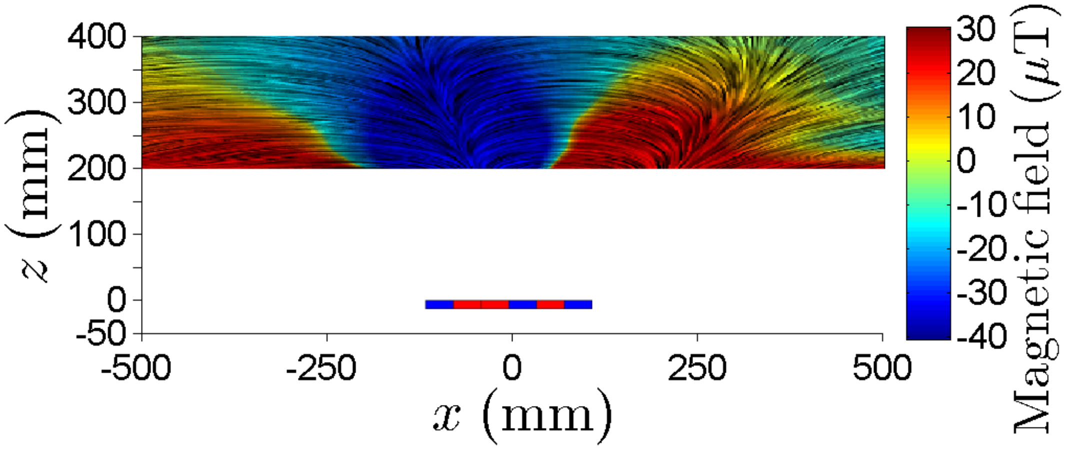

(b) Linear integral convolution texture of the magnetic field from three magnets in the laboratory representing the vector field shape. The colour map represents the z component of the magnetic field.

Figure 4.9: Linear integral convolution textures showing the vector field shape for the magnetic field measured in the laboratory from three magnets. The magnitude in the x and z components of the magnetic field are shown in subfigure a and b respectively.

have been produced using three evenly spaced data points in z in subfigure 4.10a, using five evenly spaced data points in z in subfigure 4.10b and nine evenly spaced data points in z in subfigure 4.10c.

In the three sample points example shown in figure 4.10a the texture generated to represent the vector field shape is hard to interpret as it is not well defined and shows little detail in the field. The magnitude colour map generated in this case does show the region of high magnitude, however this too is low resolution and shows the region $z > 300$ mm, $x <$ -300 mm as high magnitude while this region is relatively low magnitude on the laboratory data.

The five sample point LIC texture, shown in figure 4.10b shows a well defined representation of the vector field shape. This allows the user to pick out the anomalies in the field easier than in the three sample points example. The colour map representing the magnitude field has a greater resolution than that in the three sample point case. The region falsely shown as high magnitude in the three sample point example is correctly represented as relatively low magnitude in this case.

Figure 4.10c shows an LIC texture generated using nine sample points from the laboratory data, this shows the greatest definition in the vector field representation of the three examples. This makes accurate location of the anomalies easier to the end user. The colour map representing the magnitude of the field has the highest resolution of the three examples and gives the more accurate representation of the magnitude of the field at each region. The region shown incorrectly as high magnitude in the three sample point example is correctly represented as low magnitude and the colour map shows a greater region of variance between the high and low magnitude regions allowing the gradient to be interpreted easier by the end user giving a better impression of the magnetic field shape.

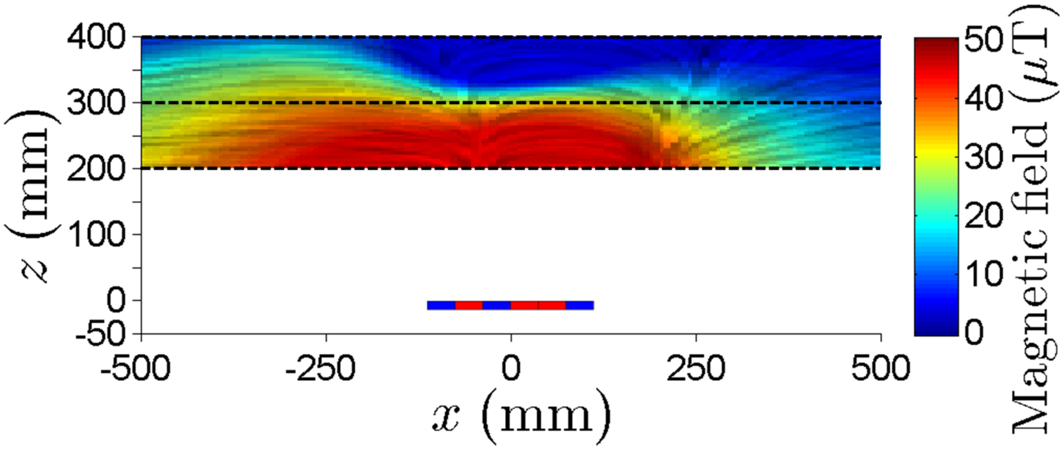

(a) Linear integral convolution texture for laboratory scan on three magnets created from the magnetometer data gathered from scans at three evenly spaced heights above the magnets shown with dashed black lines.

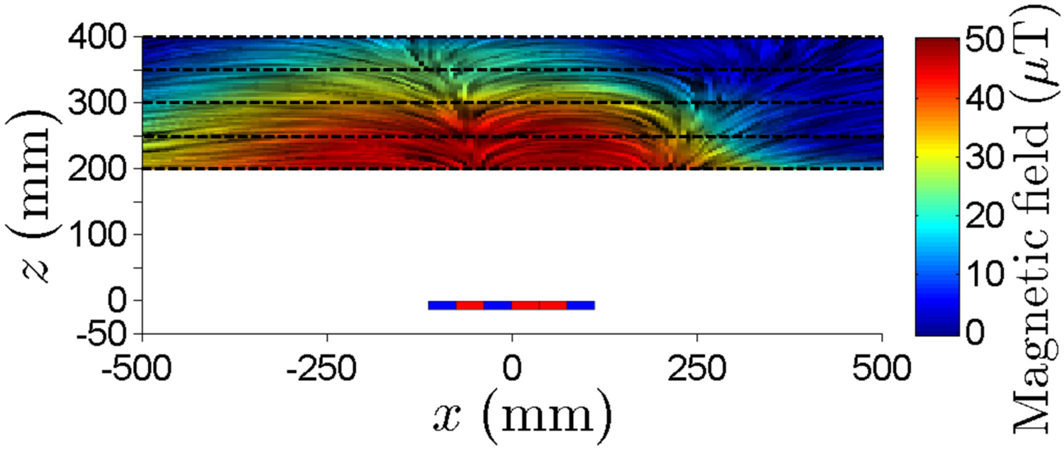

(b) Linear integral convolution texture for laboratory scan on three magnets created from the magnetometer data gathered from scans at five evenly spaced heights above the magnets shown with dashed black lines.

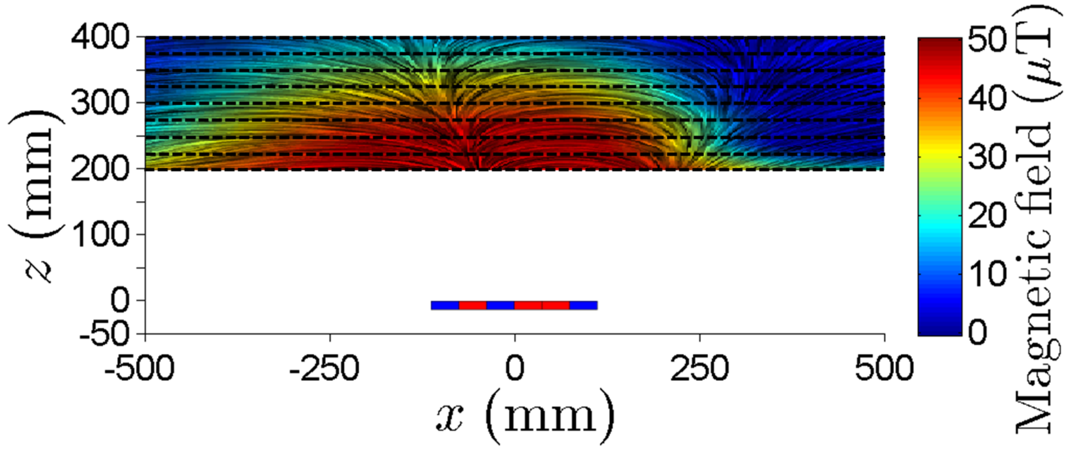

(c) Linear integral convolution texture for laboratory scan on three magnets created from the magnetometer data gathered from scans at nine evenly spaced heights above the magnets shown with dashed black lines.

Figure 4.10: Linear integral convolution textures for magnetic field strength data from three magnets in the laboratory. Subfigure 4.10a was created with data from three evenly spaced heights above the magnets. Subfigure 4.10b was created with data from five evenly spaced heights above the magnets. Subfigure 4.10c was created with data from nine evenly spaced heights above the magnets shown with dashed black lines.

4.4 Visualisation Discussion

Presenting vector field data, for example a magnetic field, to allow visual interpretation by an end user is difficult to achieve as both the vector field shape and the magnitude must be shown to give a complete picture. Previously contour and linear plot techniques have been used for magnetic data in NDT. Identifying and utilising a technique that presents both a vector field shape and magnitude field will allow for anomalies to be easier identified by a non-expert user. Vector field visualisation of the data gathered both in the laboratory and in pipeline surveys would supplement the use of algorithms that only search for specific anomaly categories, potentially identifying a greater range of anomalies in the gathered data.

In this section three visualisation techniques for vector fields have been assessed to display the magnetic field data gathered in the laboratory, these were:

- hedgehog plots,
- streamlines, and
- linear integral convolution (LIC) textures.

Hedgehog plots represent the vector field shape and direction at discrete points though the field using arrows. The magnitude is shown either by scaling the arrow lengths or by imposing a colour map in the background. These plots can suffer from optical illusions making it difficult for the user to pick out the position and direction of the arrows. These plots can only represent sparse data to prevent the arrows from overlapping each other, the arrows must also be carefully scaled to avoid this. Areas of low magnitude can make it difficult to view the arrow lengths and direction in the magnitude length scaled plot as the arrows become very small in these regions.

Streamlines show the lines that trace out the path that theoretical particles injected into the field would follow. This shows the field shape and direction of the vector field, a colour map can be added to these to represent the magnitude. The positions of the particle injection must be carefully chosen to avoid missing anomalies in the streamline plot. Due to the way the theoretical particle moves through the field in a time step, the position it ends in may not have any vector field information requiring interpolation of the field for this step. This can show an area where there is an anomaly as not having one due to this interpolation. Streamlines can display both sparse and dense data to represent the vector field for the end user.

A linear integral convolution (LIC) texture gives the greatest information density with no advanced interpretation required for an end user to understand the shape of the vector field measured. The addition of a colour map, as part of this work, increased the information conveyed from the figure by providing the user with the magnitude of the field together with the vector field shape from the texture. LIC textures present the greatest information density to the user of the visualisation techniques investigated in this work. LICs require more data points through the field to produce a meaningful texture and they do not represent the flow of the vector field.

The three techniques have been assessed for use in representing data from the laboratory for three permanent magnets. In the hedgehog plots the optical illusions inherent in these plots and the necessary sparse points plotted to prevent the arrows from overlapping, prevent these from giving a good representation of all the field information. The hedgehog plots allow the user to identify details such as zero-crossings in the components, however this require significant interpretation by the user to understand and locate these properly. In the streamlines for the laboratory data the anomalies can be seen as turning points in the streamlines. These have a lower interpretation requirement though do not give an immediately obvious relationship of how these anomalies vary with distance from the magnets.

In the LIC textures generated for the laboratory data it can be seen that a composite of the texture with a colour map is required to give a complete representation of the field, the anomalies can easily be identified and located in these. If the colour map is used to show the two components rather than the magnitude this makes identifying the peaks and zero-crossings easily identifiable to the end user. This technique also shows the direction of the field as it shows the components as positive or negative.

The number of points required to create an LIC texture was investigated. LIC textures were plotted for the field from the laboratory data for three, five and nine evenly spaced heights of sample points. The three sample point texture gives a poor representation of the vector field shape and represents the magnitude of the field incorrectly. The five sample point texture gives a good representation of the field from the laboratory showing sharp lines, this allows the position of anomalies in the field to be more precisely identified by the end user. The colour map representing the magnitude of the magnetic field is more accurate than the three sample point example, giving a greater resolution of the field magnitude. The texture produced using nine sample heights shows a sharp and easily interpreted texture giving easy identification of the anomalies and their locations. The colour map in the nine sample heights shows a high resolution of the magnetic field magnitude information making interpretation of the anomalies easier to an end user.

LIC textures have not previously been utilised in magnetic surveying to present the results from the survey. The addition of this technique combined with the colour map would allow the measured magnetic field data to be easily analysed by an end user. This would assist in finding anomalies in the measured field which may not be detected by an algorithm searching for specific, pre-programmed conditions. To use LIC textures in analysing the field measurements of an underground pipeline more than three sample points are required as three points do not replicate the field adequately for visual analysis. The addition of two extra magnetometers, one either side of the centre magnetometer, would give enough data points for a LIC texture representing the field to be produced.

As part of the work to create a visualisation technique suitable for the data gathered in this work an existing LIC Matlab toolbox [147] was used to produce the monochrome textures. This tool box was expanded on to incorporate a colour map to represent the magnitude of the field as anomalies in both vector field shape and magnitude can indicate a anomaly in the magnetic field.

Further techniques for both the laboratory and field data can be explored to visualise the vector field data. Gathering data from a magnetometer array with a greater number of magnetometers on the array would allow for the generation of the more advanced techniques, for example LIC textures in a strip above the pipeline to be generated. This gives a quick way for a user to identify anomalies in the magnetic field due to the pipeline.

The methods of visualisation presented in this section are used to present and analyse the data gathered in the laboratory experiments. To show the full magnetic field from a scan planar LIC textures have been used as these give the best density of useful information to the user. LIC textures could be used in the field to give a strip texture of the magnetic field from the pipeline above the pipe to give visual representations of the pipeline. This will however require more than three magnetometers in the array to give more data to create the textures. When used in tandem with the current detection algorithm this could increase the accuracy and usefulness of the system.

4.5 Conclusion

Three visualisation techniques have been assessed for the representation of vector field data to an end user. Hedgehog plots, streamlines and LIC textures have been considered. An LIC with a colour map give the best representation of a densely sampled field representing both the field shape and magnitude. The field survey array does not currently give dense enough data to produce LIC textures for the gathered data. The addition of magnetometers to the array to give denser data would allow a LIC to be produced for a strip above the pipe allowing users to easily find features in the field that could be missed by an analysis algorithm. The LIC texture visualisation method has been used to present and analyse the laboratory data in the next chapters.

Chapter 5

Optimum magnetometer separation in the scanning array

5.1 Introduction

Magnetic field data gathered from the survey array is used to calculate the magnetic gradient field to remove background fields to locate anomalies from the pipeline. The gradient calculated from the magnetic data from the survey is dependent on the separation of the magnetometers in the array. To increase the sensitivity of the field magnetometer array to the anomalies, the amplitude of the anomalies in the calculated gradient field should be maximised.

The magnetic field strength data from the magnetometers in the survey array is used to calculate the gradient field, $\Delta\Delta B$. The separation of the magnetometers effects the amplitude of the anomalies in the calculated gradient field, through measuring the field at different positions and taking into account the magnetometer separation in the gradient field calculation. Maximising the amplitude of the anomalies in the gradient field will increase the sensitivity to low amplitude anomalies and decrease the probability of anomalies in the field being missed.

The separation of the magnetometers in the field survey array has previously been considered only in the determination of the depth of the pipeline in the depth algorithm [120][22]. The optimum magnetometer separation has not previously been studied in relation to maximising the gradient field anomaly amplitude for increased detection sensitivity. This information would allow the survey magnetometry array to be tailored to the specific circumstances of a survey, to increase the reliability of the data gathered.

The aim of this chapter is to investigate how the separation of the magnetometers in the array effects the amplitude of the anomalies in the gradient field, calculated from an anomaly in the magnetic field from a cut in a conduit used as a pipe simulant. The first part of this investigation was to create features in the conduit to create representative anomalies in the gradient field, this was achieved by subjecting the conduits to the stress of cutting with a pipe cutter and characterising the anomaly in the gradient field. The next part of this investigation was to use this anomaly data to investigate how the separation of the magnetometers effects the amplitude of these anomalies.

5.2 Experimental methodology

The investigations detailed in this chapter were carried out using the experimental set-up described in chapter 3. In each experiment the conduit being scanned was placed onto the aluminium sample stand and the magnetometer positioned level with the centreline of the conduit. The magnetometer was moved in a plane radially outwards level with the centreline to give the xz plane, in the range along the conduit of $x = 900 - 2700$ mm and radially out from the conduit of $z = 25 - 400$ mm. The data in the plane was gathered in a cartesian grid with steps of $\Delta x = 20$ mm and $\Delta z = 25$ mm. With the x origin defined as the end of the conduit and the z origin defined as the centreline of the conduit. A scan was taken of the ambient magnetic field in the laboratory prior to the conduit being positioned, these were deducted from the scans for the LICs to give only the field from the conduit.

After the xz plane was scanned in this range the conduit was rotated anti-clockwise looking along the conduit in the positive x direction through $\Delta\Theta = 22.5°$, the scan was then repeated to give another radial plane for the conduit. This was repeated in the range $\Theta = 0 - 337.5°$. The origin of the rotation was defined as the seam weld of the conduit. This was repeated three times for each conduit to give an estimation of the 95% repeatability bounds. A schematic of the set-up for these conduit scans is shown in figure 5.1. The procedure for the experiments is shown as a flow chart in figure 5.2.

A scan was taken without the conduit present in the scanning plane, an LIC of this data is shown in figure 5.3.

5.3 Magnetic measurement of discontinuity in the susceptibility of a cut steel conduit

5.3.1 Experimental basis

To investigate the effects of the magnetometer separation on the amplitude of an anomaly in the gradient field due to a discontinuity in the susceptibility in a steel conduit, a feature in the pipe wall must first be created and assessed in

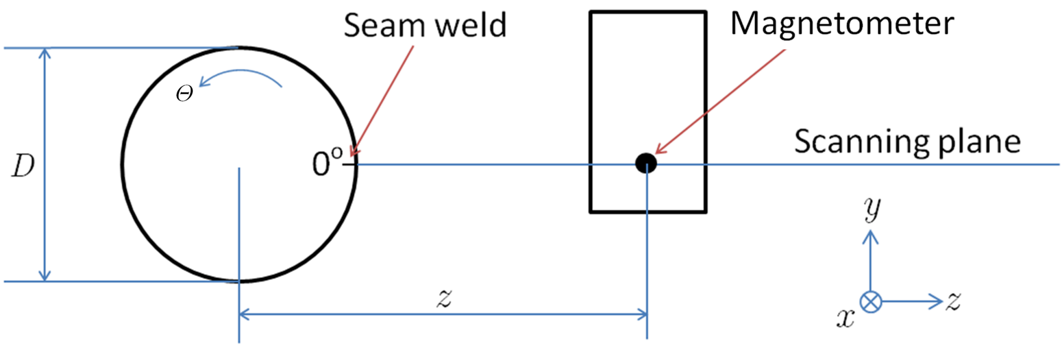

Figure 5.1: Schematic of the set-up used to scan the cut full length conduit in three dimensions. The B_x component being along the conduit and the B_z component radially outwards from the conduit.

the laboratory. This was created by stressing the conduit by cutting a full length of conduit using a standard pipe cutter. The burr created on the interior of the conduit by this cutting was removed using a blunt blade run around the inside of the conduit wall. This cutting created a stress region in the conduit wall and created a discontinuity in the permeability of the conduit wall.

The feature in the gradient field created by the cutting must give a good representation of an anomaly in the gradient field from a pipe in the field, to give validity to the effects of the magnetometer separation on the amplitude relationship found in the laboratory experiments. This validity is vital to the laboratory results being used to make recommendations for further development or adaptations of the current magnetometry survey array.

The conduits were cut and placed on the sample stand, in the laboratory set-up described in chapter 3. These were placed together in the orientation that they were prior to cutting with the seam welds aligned. The conduits were then scanned using the methodology detailed in section 5.2 above. Four different diameters of conduit were scanned, this was to assess the difference in the feature amplitude between the different sized conduits.

The expected form of the anomalies in the magnetic gradient from the discontinuity is calculated using the Wang defect model shown in section 2.4.4 from [116]. This is used to compare the scan results from the discontinuities measured

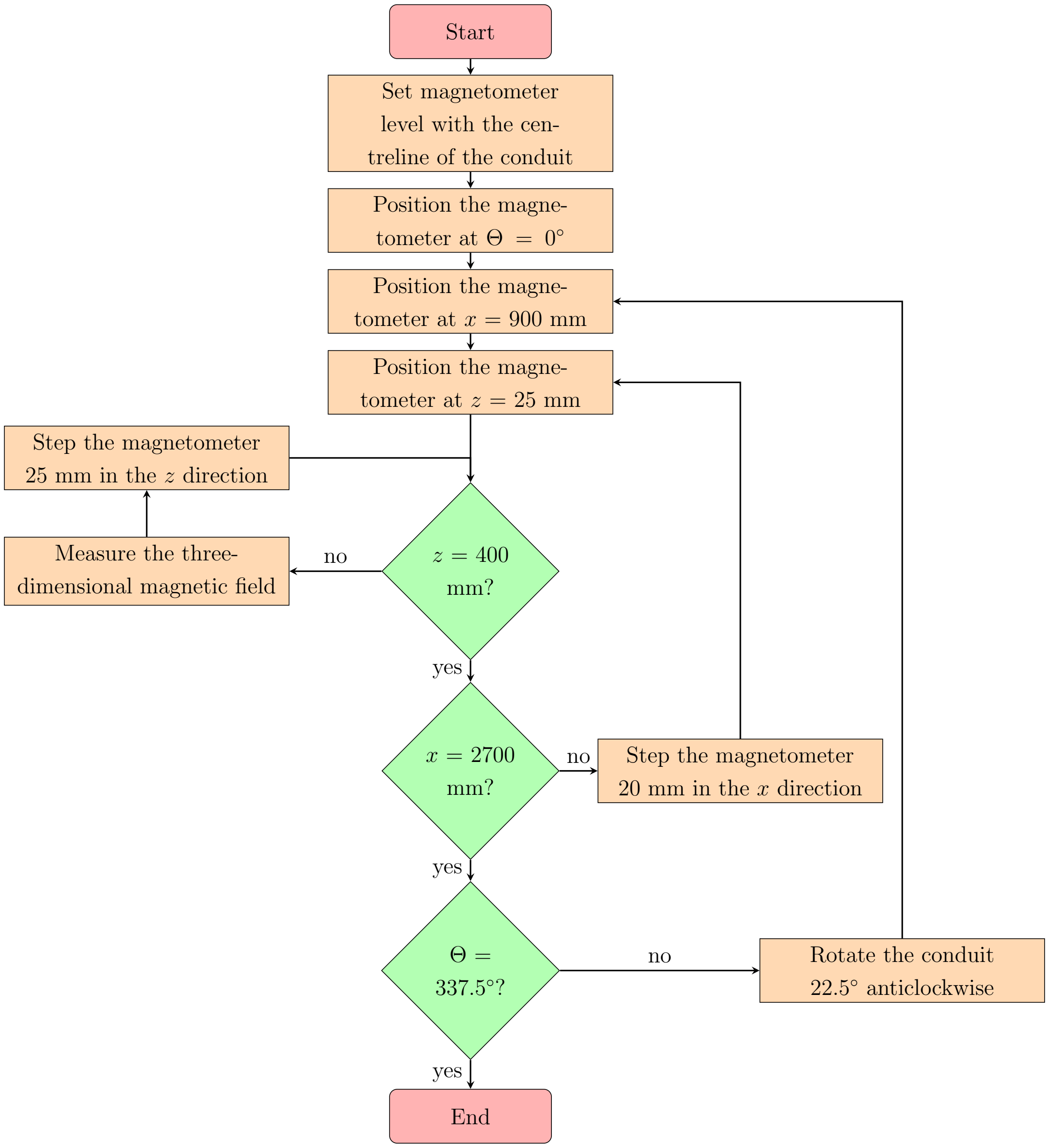

Figure 5.2: Flow chart showing the experimental procedure used to measure the three-dimensional magnetic field around a conduit in radial planes. The scan was repeated three times for each conduit to be able to determine the repeatability of the experiment.

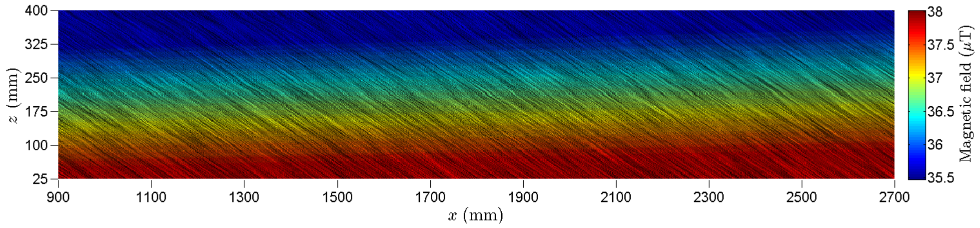

Figure 5.3: Linear integral convolution texture showing the magnetic field strength in the xz plane for the range $x = 900 - 2700$ mm, $z = 25 - 400$ mm in the scanning plane in the laboratory with no conduit present.

in the laboratory in these experiments to the theoretical magnetic field from a defect zone.

The anomaly from the gradient field from a discontinuity in the susceptibility caused by cutting the conduits has been assessed in order to verify the validity of these as a simulant for features measured in field surveys. This will give validity to the recommendations made from the results of the laboratory investigations for further development of the magnetometry survey array.

5.3.2 Results of magnetic scan on 1″ nominal diameter light grade steel conduit

5.3.2.1 LIC textures of 1″ nominal diameter steel conduit with manufactured discontinuity in the material susceptibility

For the xz radial plane scanned, at every other Θ in the scan an LIC texture has been created as described in section 4.2. These textures show the xz radial plane in the range $x = 900 - 2700$ mm and $z = 25 - 400$ mm at angles around the conduit spaced 45° apart in the range $\Theta = 0 - 315°$.

The LIC textures created with the data from the scans of the 1″ conduit with no created features or other processes carried out on it are shown in figure 5.4. The LIC textures for the 1″ conduit with a single cut are shown in figure 5.6 and the textures for the 1″ conduit with two cuts are shown in figure 5.7. The calculated gradient field for the uncut, one cut and two cut cases for the 1″ conduit in the $\Delta\Delta B_x$ and $\Delta\Delta B_z$ gradient fields are shown in figures 5.8, 5.9 and

5.10 respectively. These were calculated from a data point separation of 75 mm between the centre and outer magnetometers at a height above the centreline of 50 mm. The angle between the magnetometers was used to define the separation in the radial system to maintain a constant spacing relative to the centreline of the conduit for the different sizes of conduit.

Figure 5.4 was used to choose the appropriate position to cut the conduit to create the discontinuity in the susceptibility. In order to minimise the effects on the resulting field from variations in the initial field the first discontinuity in the susceptibility was made at a position in the conduit where the variation in the magnetic field from the conduit was at a minimum. The region with the lowest variation was determined by calculating the gradient of the magnitude scalar field using equation 5.1 [149]. The magnitude of the x and z components of the $\nabla|B|$ field are shown in figure 5.5a and figure 5.5b respectively for the xz plane at $\Theta = 0°$.

$$V = \nabla|B| = \frac{\partial|B|}{\partial x}\hat{\imath} + \frac{\partial|B|}{\partial y}\hat{\jmath} + \frac{\partial|B|}{\partial z}\hat{k} \tag{5.1}$$

Where:

V is the gradient vector field,

∇ is the vector differential operator, defined as $\frac{\partial}{\partial x}\hat{\imath} + \frac{\partial}{\partial y}\hat{\jmath} + \frac{\partial}{\partial z}\hat{k}$,

$\hat{\imath}$, $\hat{\jmath}$ **and** $\hat{k}$ are the unit vectors in the x, y and z directions respectively, and

$|B|$ is the magnitude of the magnetic field strength scalar field.

In figure 5.4 it can be seen that in the region $x = 900 - 1900$ mm the field is approximately uniformly radial as the texture in this region is approximately vertical. In the region $x = 2300 - 2700$ mm the field is approximately uniformly parallel to the conduit wall. In figures 5.5a and 5.5b it can be seen that in the regions $x = 900 - 1200$ mm and $x = 1600 - 2300$ mm there is a greater gradient in the x component than the surrounding values, indicating high variation in the magnitude of the magnetic field strength in these regions. The z component in regions $x = 1000 - 1300$ mm, $2000 - 2400$ mm and $2600 - 2700$ mm have large variation in magnetic field strength magnitude. Using this information, the

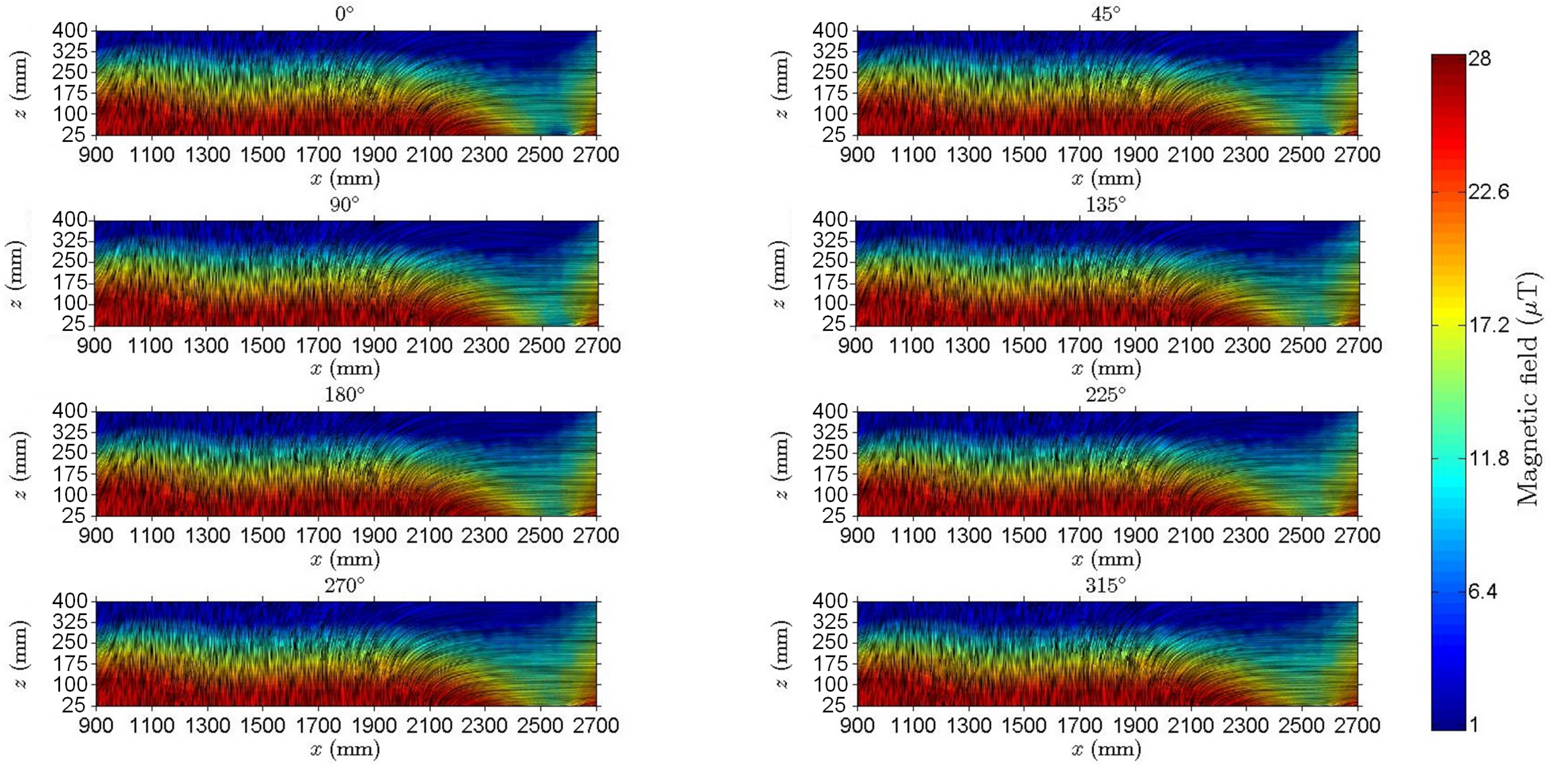

Figure 5.4: Linear integral convolution textures showing magnetic field strength in the xz plane for the range $x = 900 - 2700$ mm, $z = 25 - 400$ mm for each of the angles around the conduit $\Theta = 0 - -315°$ in 45° steps for an uncut 1″ nominal diameter steel conduit. The magnetic field strength magnitude is represented by a colour map for each case.

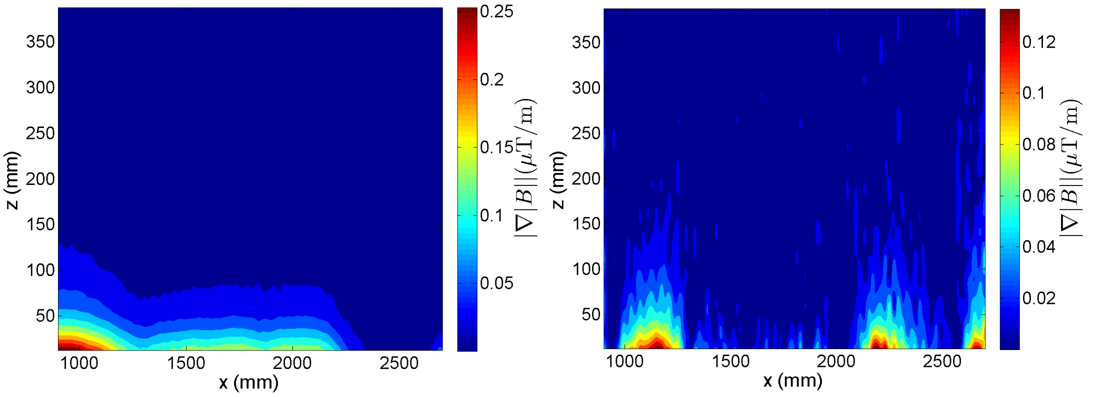

(a) Plot showing the magnitude of the x component of the $\nabla|B|$ field, for the magnetic field strength in the xz plane for a scan on an uncut 1″ conduit in the region $x = 900 - 2700$ mm, $z = 25 - 400$ mm at $\Theta = 0°$.

(b) Plot showing the magnitude of the z component of the $\nabla|B|$ field, for the magnetic field strength in the xz plane for a scan on an uncut 1″ conduit in the region $x = 900 - 2700$ mm, $z = 25 - 400$ mm at $\Theta = 0°$.

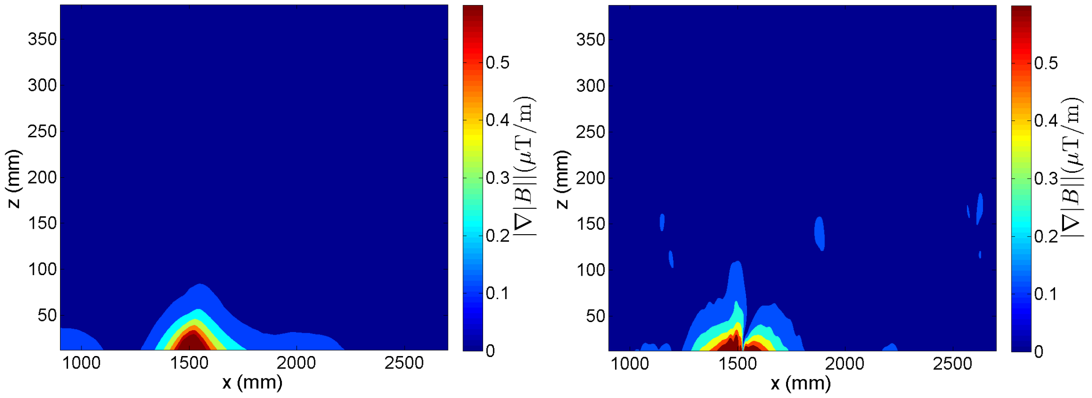

(c) Plot showing the magnitude of the x component of the$\nabla|B|$ field, for the magnetic field strength in the xz plane for a scan on a 1″ conduit cut at $x = 1500$ mm, in the region $x = 900 - 2700$ mm, $z = 25 - 400$ mm at $\Theta = 0°$.

(d) Plot showing the magnitude of the z component of the$\nabla|B|$ field, for the magnetic field strength in the xz plane for a scan on a 1″ conduit cut at $x = 1500$ mm, in the region $x = 900 - 2700$ mm, $z = 25 - 400$ mm at $\Theta = 0°$.

Figure 5.5: Plots representing the magnitude of the x and z component of the $\nabla|B|$ field component in a and b respectively, for the magnetic field strength in the xz plane for a scan on an uncut 1″ conduit and c and d respectively, for the magnetic field strength in the xz plane for a scan on a 1″ conduit cut at $x = 1500$ mm.

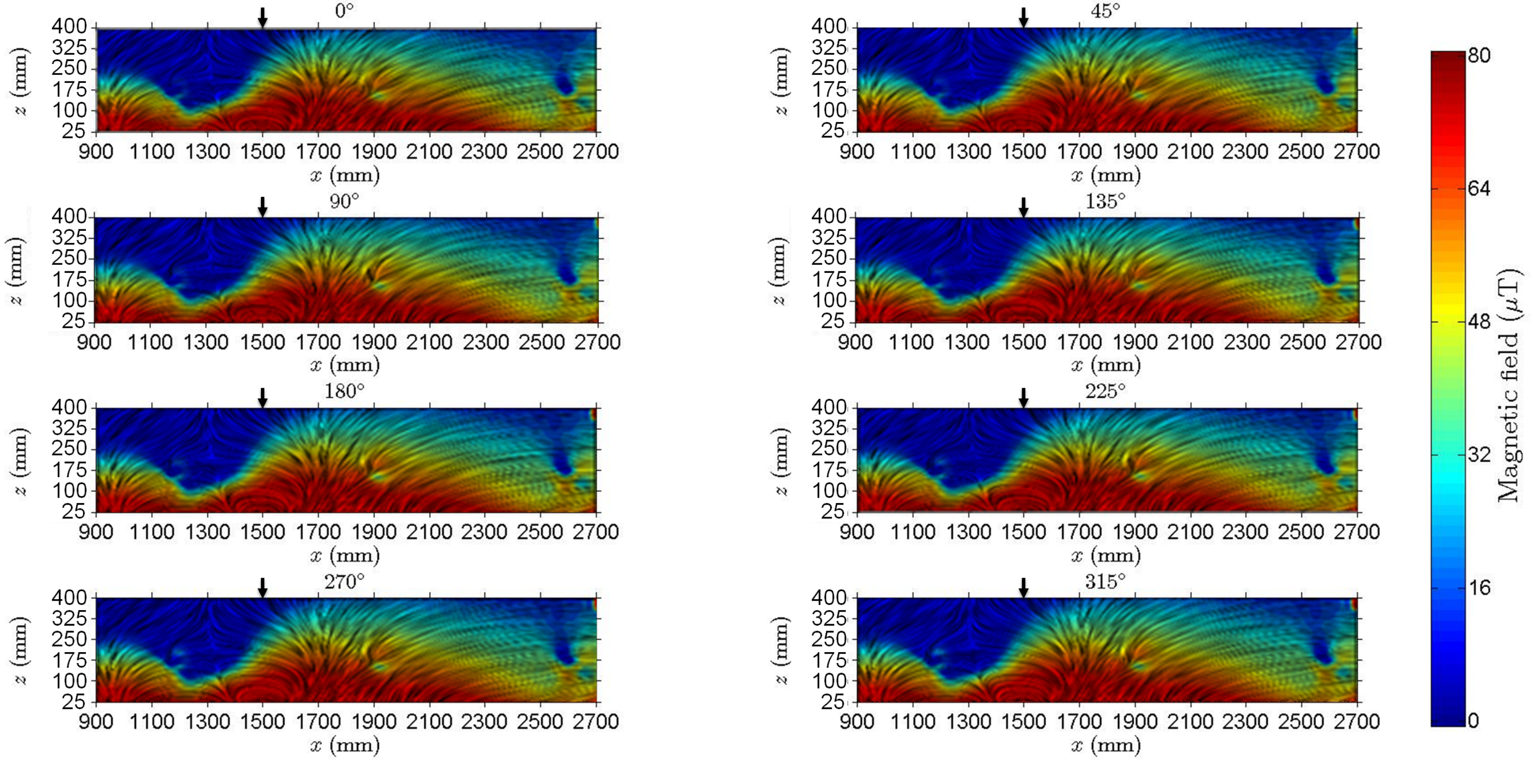

Figure 5.6: Linear integral convolution textures showing magnetic field strength in the xz plane for the range $x = 900 - 2700$ mm, $z = 25 - 400$ mm for each of the angles around the conduit $\Theta = 0 - -315°$ in 45° steps for a $1''$ nominal diameter steel conduit cut at $x = 1500$ mm, indicated by the black arrows. The magnetic field strength magnitude is represented by a colour map for each case.

regions $x = 1300 - 1600$ mm and $2400 - 2600$ mm are the best areas for the initial μ discontinuity to reduce the effects of features in the initial magnetic field. Due to the approximately uniform radial field in the region $x = 900 - 1900$ mm the position for the initial cut was chosen as $x = 1500$ mm.

The LICs for the xz planes in the range $x = 900 - 2700$ mm, $z = 25 - 400$ mm for each Θ in the range $\Theta = 0 - 315°$ for the $1''$ diameter conduit cut at $x = 1500$ mm are shown in figure 5.4. Using the same method as for figure 5.5a and 5.5b above, the gradient in the magnetic field strength for figure 5.6 was calculated. These are shown in figure 5.5c and figure 5.5d for x and z components of the $\nabla|B|$ field respectively.

In figures 5.5c and 5.5d it can be seen that in the region $x = 1350 - 1750$ mm there is a higher gradient in both the x and z components of the $\nabla|B|$ field indicating high variation in the magnitude of the magnetic field strength in these regions. In the regions $x = 900 - 1350$ mm and $1750 - 2700$ mm the value of $\nabla|B|$ field is small indicating small variation in the magnitude of the magnitude of the magnetic field.

In figure 5.6 it can be seen that the shape of the magnetic field strength in the regions $x = 900 - 1100$ mm and $2000 - 2700$ mm is unchanged from figure 5.4, though with an increased magnitude. Using this information, the position for the second discontinuity in the susceptibility was chosen as $x = 2500$ mm, this is due to the low variation in the field shape in this region, this also allowed investigation of the effects of the discontinuity in the susceptibility the parallel field in the region as opposed to the radial field in the region of the first discontinuity.

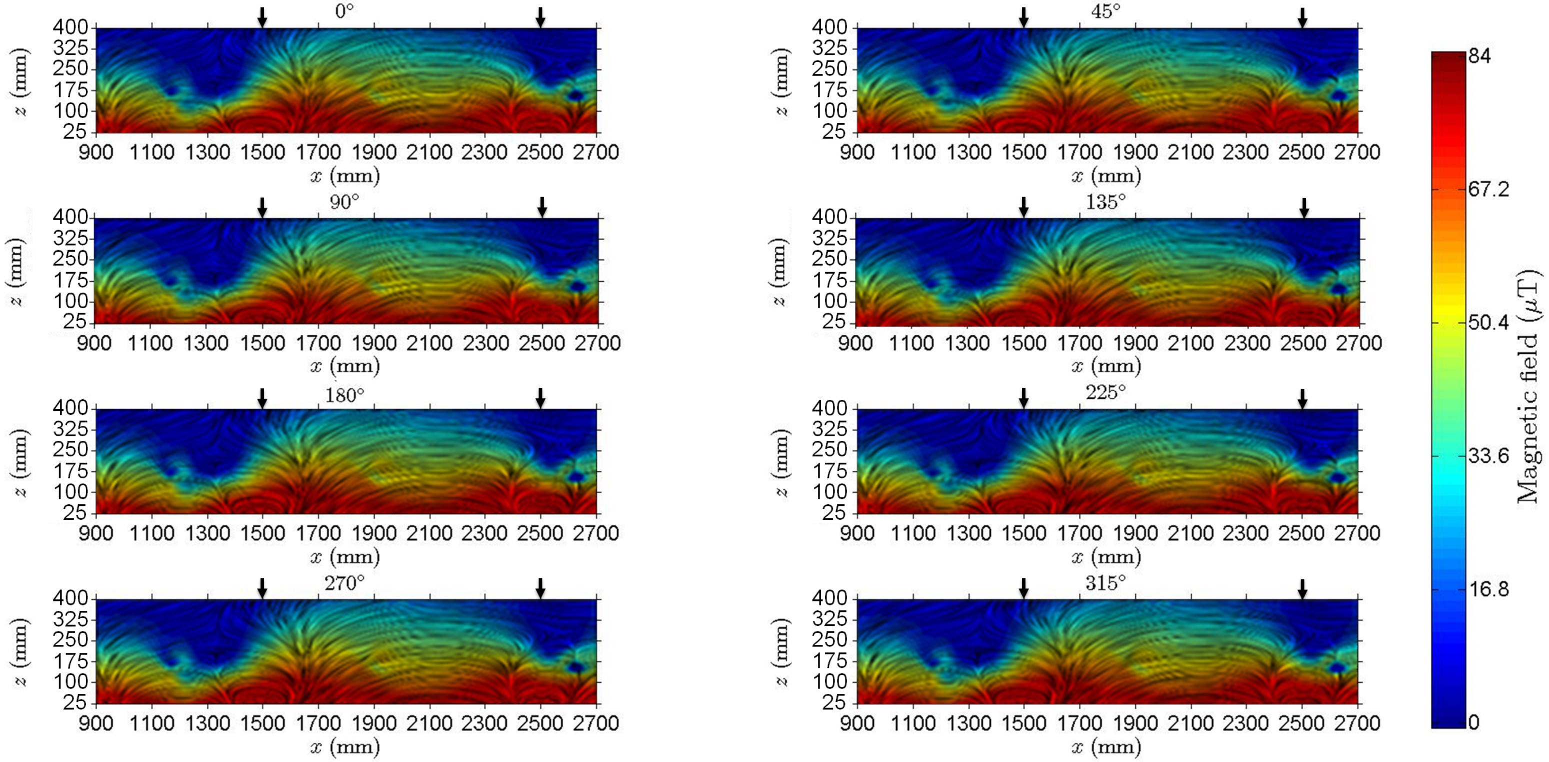

Figure 5.7: Linear integral convolution textures showing magnetic field strength in the xz plane for the range $x = 900 - 2700$ mm, $z = 25 - 400$ mm for each of the angles around the conduit $\Theta = 0 - 315°$ in 45° steps for a $1''$ nominal diameter steel conduit cut at $x = 1500$ mm and $x = 2500$ mm, indicated by the black arrows. The magnetic field strength magnitude is represented by a colour map for each case.

5.3.2.2 Magnetic gradient measurements along the centre of the $1''$ conduit

The calculated magnetic gradient fields 50 mm from the outer wall of the conduit as delivered with no manufactured defects in line with the centreline measured in the laboratory are shown in figure 5.8. The scans were repeated 3 times for each position and the error bars calculated for the 95% interval for the data. These show a low magnitude magnetic gradient field from the conduit with no obvious defect zone magnetic signatures.

The gradient fields for the same conduit after being cut using a pipe cutter at $x = 1500$ mm is shown in figure 5.9, this shows a clear peak in the x component and zero-crossing in the z component of the gradient field centred at the location of the cut, the magnitude of the peak in the field is approximately ten times greater than the maximum magnitude of the gradient field from the uncut conduit.

The gradient field calculated from the magnetometer scans of the same conduit with a second cut at $x = 2500$ mm are shown in figure 5.10, these show a second peak in x and zero-crossing in z centred at the location of the second cut with approximately the same amplitude as the first cut. The first cut shows the same amplitude in the gradient field before and after the second cut.

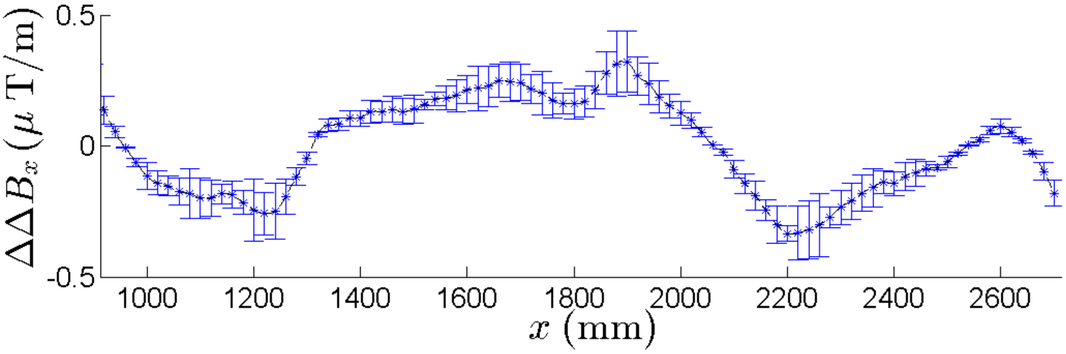

(a) Plot showing the $\Delta\Delta B_x$ component of the magnetic field for a 1″ diameter conduit, designated conduit 1, at a height from the conduit of $z = 50$ mm. The conduit was as delivered with no cuts or other processes carried out on it prior to the magnetic scan.

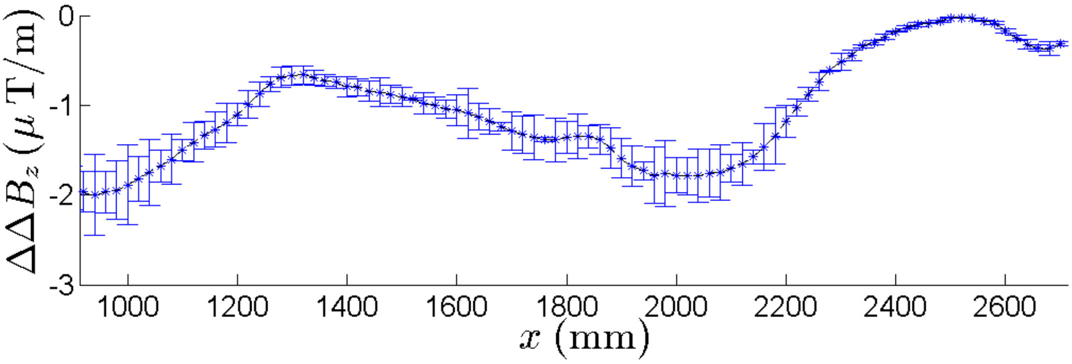

(b) Plot showing $\Delta\Delta B_z$ component of the magnetic field for a 1″ diameter conduit, designated conduit 1, at a height from the conduit of $z = 50$ mm. The conduit was as delivered with no cuts or other processes carried out on it prior to the magnetic scan.

Figure 5.8: Plots showing the $\Delta\Delta B_x$ and $\Delta\Delta B_z$ components of the magnetic gradient for a 1″ diameter conduit, designated conduit 1, at a height from the conduit of $z = 50$ mm. The conduit was as delivered with no cuts or other processes carried out on it prior to the magnetic scan.

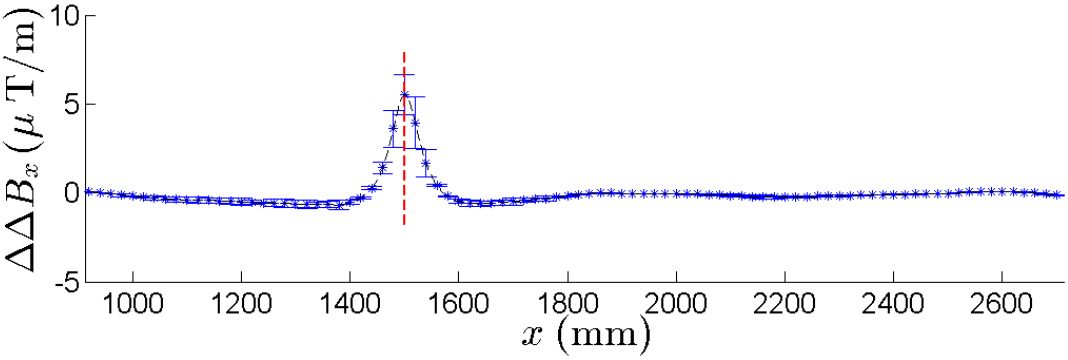

(a) Plot showing the $\Delta\Delta B_x$ component of the magnetic field for a 1″ diameter conduit, designated conduit 1, at a height from the conduit of z = 50 mm. The conduit has a single cut to produce a μ discontinuity, made using a pipe cutter at x = 1500 mm shown with a red dashed line.

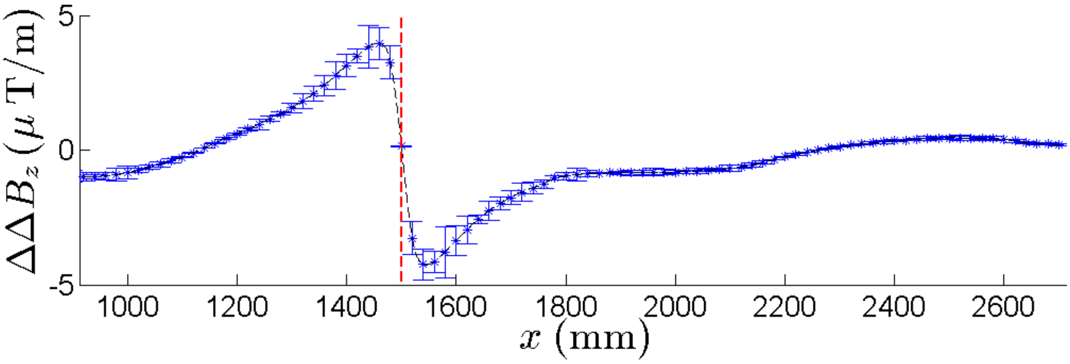

(b) Plot showing the $\Delta\Delta B_z$ component of the magnetic field for a 1″ diameter conduit, designated conduit 1, at a height from the conduit of z = 50 mm. The conduit has a single cut to produce a μ discontinuity, made using a pipe cutter at x = 1500 mm shown with a red dashed line.

Figure 5.9: Plots showing the $\Delta\Delta B_x$ and $\Delta\Delta B_z$ components of the magnetic field for a 1″ diameter conduit, designated conduit 1, at a height from the conduit of z = 50 mm. The conduit has a single cut to produce a μ discontinuity, made using a pipe cutter at x = 1500 mm shown with a red dashed line.

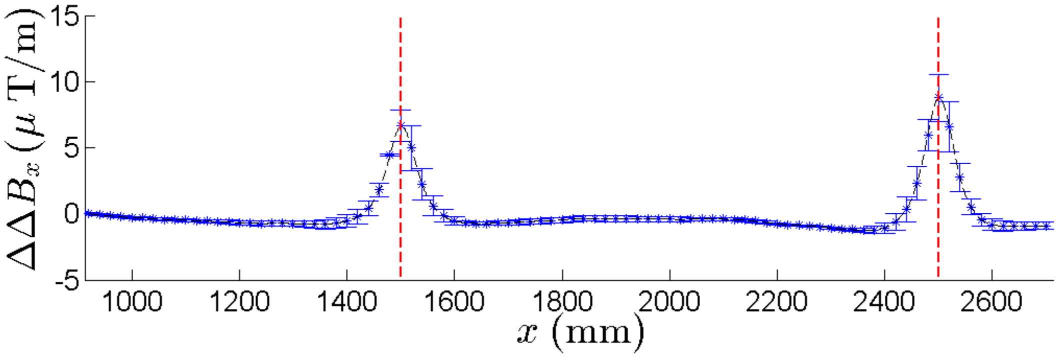

(a) Plot showing the $\Delta\Delta B_x$ component of the magnetic field for a 1″ diameter conduit, designated conduit 1, at a height from the conduit of $z = 50$ mm. The conduit has two cuts to produce μ discontinuities, made using a pipe cutter at $x =$ 1500 mm and $x = 2500$ mm shown with red dashed lines.

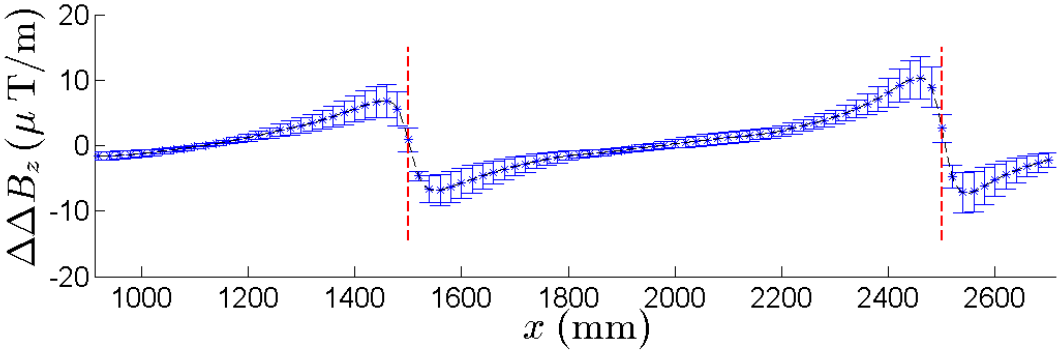

(b) Plot showing the $\Delta\Delta B_x$ component of the magnetic field for a 1″ diameter conduit, designated conduit 1, at a height from the conduit of $z = 50$ mm. The conduit has two cuts to produce μ discontinuities, made using a pipe cutter at $x =$ 1500 mm and $x = 2500$ mm shown with red dashed lines.

Figure 5.10: Plots showing the $\Delta\Delta B_x$ and $\Delta\Delta B_z$ components of the magnetic field for a 1″ diameter conduit, designated conduit 1, at a height from the conduit of $z = 50$ mm. The conduit has two cuts to produce μ discontinuities, made using a pipe cutter at $x = 1500$ mm and $x = 2500$ mm shown with red dashed lines.

5.3.2.3 Effects of cutting method on magnetisation

To investigate the effect on the magnetic field from the conduit from the cutting method, a 1″ diameter conduit was cut using a band saw to reduce heating effects on the conduit. The gradient field calculated from the magnetometer scans from a 1″ conduit with cuts at $x = 1500$ and 2500 mm made using a band saw are shown in figure 5.11. These scans were repeated three times each and these repeated scans were used to calculate the 95% confidence intervals for the magnetic gradient field. These are represented by the error bars in the plot.

These show peaks in x and zero-crossing in z centred at $x = 1500$ mm, the cut at $x = 2500$ mm shows a peak in the x component but does not have a zero-crossing in the z component. There is a characteristic double turning point in the gradient of the field at this point, this does not cross $\Delta\Delta B_z = 0$ as there is an offset field.

In the x component there is a zero-crossing at $x = 1300$ mm, this corresponds to a peak in the z component due to the clamping in the band saw for cutting. A similar feature can be seen at $x = 2650$ mm at the other clamping position in the cutting process. The z component of the magnetic gradient field has an increasing offset for positions with $x > 1800$ mm, this is due to a slight curvature in the conduit in this area.

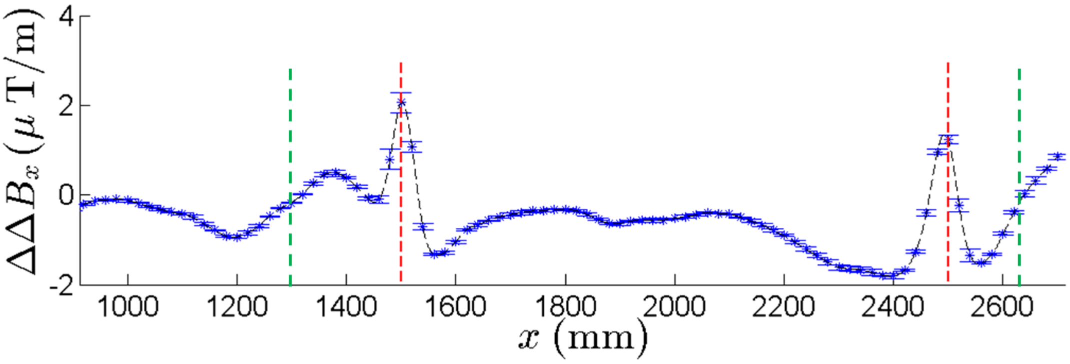

(a) Plot showing the $\Delta\Delta B_x$ component of the magnetic field for a 1″ diameter conduit, designated conduit 1, at a height from the conduit of $z = 50$ mm. The conduit has two cuts to produce μ discontinuities, made using a band saw at $x = 1500$ mm and $x = 2500$ mm shown with red dashed lines. The clamping positions during cutting are shown with green dashed lines.

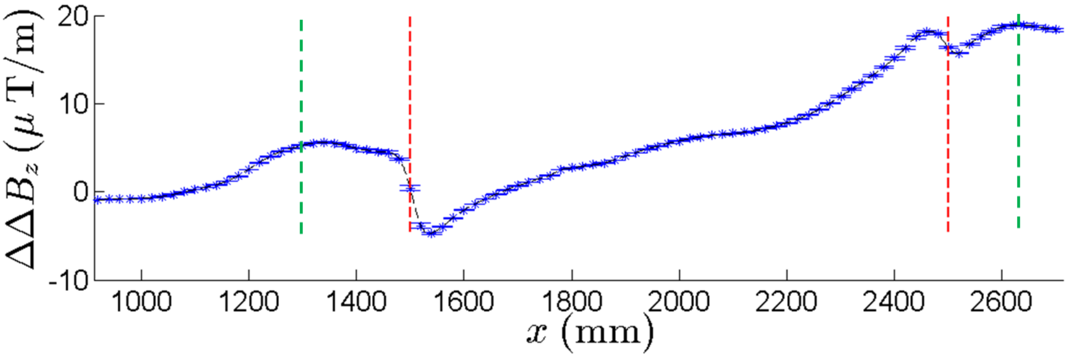

(b) Plot showing the $\Delta\Delta B_x$ component of the magnetic field for a 1″ diameter conduit, designated conduit 1, at a height from the conduit of $z = 50$ mm. The conduit has two cuts to produce μ discontinuities, made using a band saw at $x = 1500$ mm and $x = 2500$ mm shown with red dashed lines. The clamping positions during cutting are shown with green dashed lines.

Figure 5.11: Plots showing the $\Delta\Delta B_x$ and $\Delta\Delta B_z$ components of the magnetic field for a 1″ diameter conduit, designated conduit 1, at a height from the conduit of $z = 50$ mm. The conduit has two cuts to produce μ discontinuities, made using a band saw at $x = 1500$ mm and $x = 2500$ mm shown with red dashed lines. The clamping positions during cutting are shown with green dashed lines.

5.3.3 Results of magnetic scan on $^1/_2''$ nominal diameter heavy grade steel conduit

The gradient of the magnetic fields calculated from the magnetic field measured in the laboratory 50 mm from the outer pipe wall surface of a $^1/_2''$ conduit wall in line with the centreline are shown in figure 5.12 for the case with two cuts at $x =$ 1500 mm and $x = 2500$ mm. These scans were repeated three times and used to calculate the 95% confidence intervals, these are shown on the plot as error bars.

These show a peak in the x component and a zero-crossing in the z component of the magnetic gradient from the conduit centred at the cuts. The amplitude of the second cut anomaly is approximately twice that of the first cut anomaly in both cases. There is an anomaly shown as a zero-crossing in the x component and two negative peaks in the z component at $x = 2075$ mm, this was the position the conduit was clamped in the pipe vice to allow the cuts to be made. This clamping into the vice has subjected the conduit to a compressive stress in that region and so has caused an area of increased magnetisation through the Villari effect.

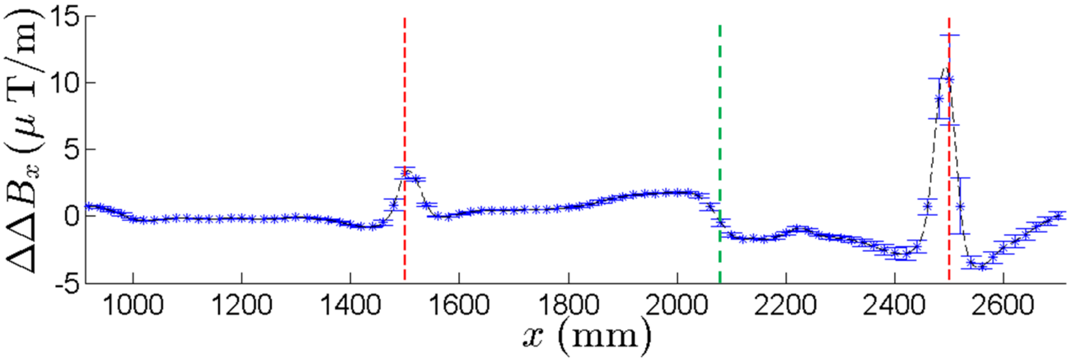

(a) Plot showing the $\Delta\Delta B_x$ component of the magnetic field for a 1/2″ diameter conduit, designated conduit 2, at a height from the conduit of $z = 50$ mm. The conduit has two cuts, to produce μ discontinuities, made using a pipe cutter at $x = 1500$ mm and $x = 2500$ mm shown with red dashed lines. The clamping position during cutting is shown with a green dashed line.

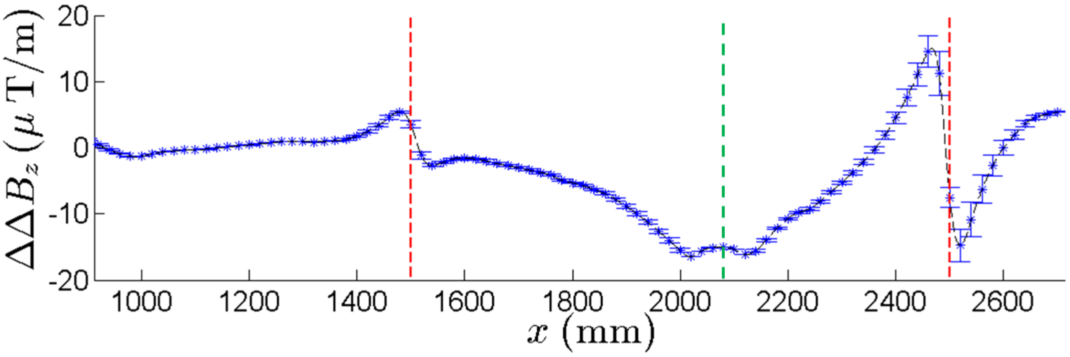

(b) Plot showing the $\Delta\Delta B_z$ component of the magnetic field for a 1/2″ diameter conduit, designated conduit 2, at a height from the conduit of $z = 50$ mm. The conduit has two cuts, to produce μ discontinuities, made using a pipe cutter at $x = 1500$ mm and $x = 2500$ mm shown with red dashed lines. The clamping position during cutting is shown with a green dashed line.

Figure 5.12: Plots showing the $\Delta\Delta B_x$ and $\Delta\Delta B_z$ components of the magnetic field for a 1/2″ diameter conduit, designated conduit 2, at a height from the conduit of $z = 50$ mm. The conduit has two cuts, to produce μ discontinuities, made using a pipe cutter at $x = 1500$ mm and $x = 2500$ mm shown with red dashed lines. The clamping position during cutting is shown with a green dashed line.

5.3.4 Results of magnetic scan on $^3/_4''$ nominal diameter heavy grade steel conduit

The magnetic gradient fields calculated from the magnetic field measured at 50 mm above the pipe wall outer surface in line with the centreline from a $^3/_4''$ conduit with two cuts at $x = 1500$ and 2500 mm, are shown in figure 5.13. These were scanned three times and the 95% confidence interval from the scans calculated, this is represented by the error bars in the plots.

The second cut anomaly shows the characteristic peak and zero-crossing centred on the cut, the first cut anomaly shows a peak in x but there is no corresponding zero-crossing in z though the characteristic waveform is present with an offset which prevents this from crossing the $\Delta\Delta B_z = 0$ line centred at the cut. The first cut anomaly shows a peak in x with approximately four times the amplitude of the second cut anomaly, however the peak to peak amplitude in the z in the first cut anomaly is only twice the amplitude of the second cut anomaly. There is another peak in the x component at approximately $x = 2100$ mm, this has a corresponding zero-crossing in the z component this is the location that the conduit was clamped into the pipe vice for cutting. This peak and zero-crossing is a result of the stress from this clamp due to the Villari effect. There is an increased gradient field in the z component of the magnetic field at $x < 1400$ mm this corresponds to a negative offset in the x component. This was found to be due to a deformation in the conduit as delivered which had caused a bend in the conduit increasing causing a defect zone.

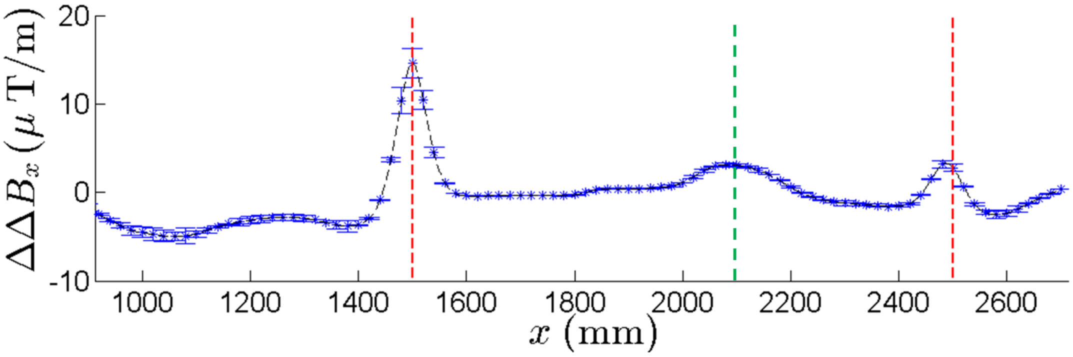

(a) Plot showing the $\Delta\Delta B_x$ component of the magnetic field for a $^3/_4''$ diameter conduit, designated conduit 1, at a height from the conduit of $z = 50$ mm. The conduit has two cuts, to produce μ discontinuities, made using a pipe cutter at $x = 1500$ mm and $x = 2500$ mm shown with red dashed lines. The clamping position during cutting is shown with a green dashed line.

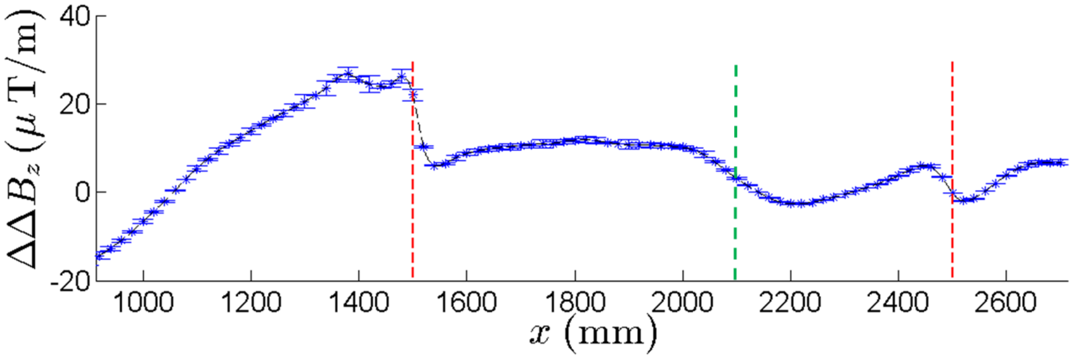

(b) Plot showing the $\Delta\Delta B_z$ component of the magnetic field for a $^3/_4''$ diameter conduit, designated conduit 1, at a height from the conduit of $z = 50$ mm. The conduit has two cuts, to produce μ discontinuities, made using a pipe cutter at $x = 1500$ mm and $x = 2500$ mm shown with red dashed lines. The clamping position during cutting is shown with a green dashed line.

Figure 5.13: Plots showing the $\Delta\Delta B_x$ and $\Delta\Delta B_z$ components of the magnetic field for a $^3/_4''$ diameter conduit, designated conduit 1, at a height from the conduit of $z = 50$ mm. The conduit has two cuts, to produce μ discontinuities, made using a pipe cutter at $x = 1500$ mm and $x = 2500$ mm shown with red dashed lines. The clamping position during cutting is shown with a green dashed line.

5.3.5 Results of magnetic scan on $1^1\!/_2''$ nominal diameter heavy grade steel conduit

The magnetic gradients calculated for a measured magnetic field 50 mm from the outer surface of the pipe wall, from a $1^1\!/_2''$ conduit cut at $x = 1500$ and 2500 mm are shown in figure 5.14. The scans were repeated three times and the 95% error bounds calculated, these are represented by the error bars.

These plots show the characteristic peak and zero-crossing in x and z respectively centred at the cuts. With the peak from the second cut anomaly having a slightly greater amplitude than that of the first cut anomaly. The x gradient field shows another peak at approximately $x = 1900$ mm, this is the location at which the conduit was clamped into the pipe vice for cutting and so experienced compressive stress in this region leading to a change in the magnetisation. A negative peak in the x component of the gradient field occurs at approximately $x = 1100$ mm, this coincides with a region of large gradient in the gradient field. There is another negative peak in x coinciding with an area of large gradient in the z component at approximately $x = 2300$ mm, these are due to a minor deviation from straight in the conduit.

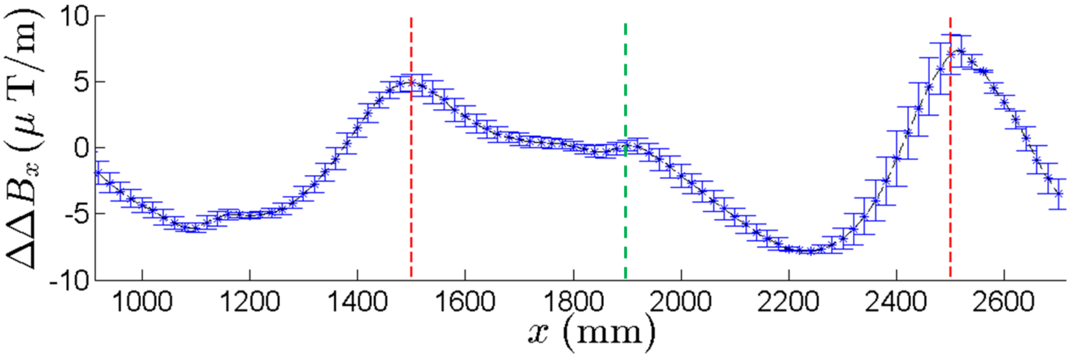

(a) Plot showing the $\Delta\Delta B_x$ component of the magnetic field for a 1½″ diameter conduit, designated conduit 2, at a height from the conduit of $z = 50$ mm. The conduit has two cuts, to produce μ discontinuities, made using a pipe cutter at $x =$ 1500 mm and $x = 2500$ mm shown with red dashed lines. The clamping position during cutting is shown with a green dashed line.

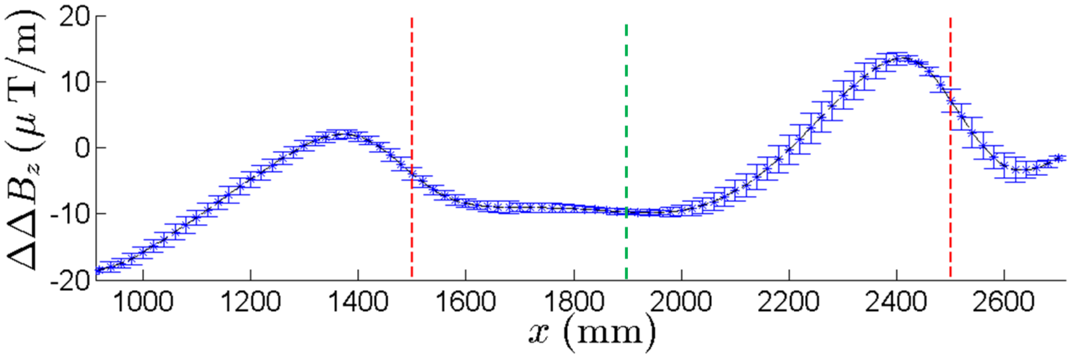

(b) Plot showing the $\Delta\Delta B_z$ component of the magnetic field for a 1½″ diameter conduit, designated conduit 2, at a height from the conduit of $z = 50$ mm. The conduit has two cuts, to produce μ discontinuities, made using a pipe cutter at $x =$ 1500 mm and $x = 2500$ mm shown with red dashed lines. The clamping position during cutting is shown with a green dashed line.

Figure 5.14: Plots showing the $\Delta\Delta B_x$ and $\Delta\Delta B_z$ components of the magnetic field for a 1½″ diameter conduit, designated conduit 2, at a height from the conduit of $z = 50$ mm. The conduit has two cuts, to produce μ discontinuities, made using a pipe cutter at $x = 1500$ mm and $x = 2500$ mm shown with red dashed lines. The clamping position during cutting is shown with a green dashed line.

5.3.6 Analysis of magnetic scans of cut steel conduits

Figure 5.15 show the gradient field data gathered in the laboratory with the predicted gradient field from the Wang defect model given in section 2.4.4 for a height above the defect of 50 mm, defect depth of 1.6 mm the same as wall thickness of the conduit and a defect width of 2 mm the thickness of the blade in the pipe cutter.

	1500 mm	2500 mm
x	0.973	0.973
z	0.992	0.998

Table 5.1: Table of the correlation co-efficients for the two cuts in the 1″ conduit against the Wang defect model of the cuts.

The correlation coefficients between the laboratory data for x and z components of the gradient field from the two cuts in the 1″ conduit and the Wang defect model for these cuts are shown in table 5.1. These show a high level of correlation between the laboratory data and the Wang defect model. This suggests that the magnetic gradient field measured from the conduit give a good representation of a defect. The 1″ conduit was analysed in this way as these light conduits have the nearest wall thickness to diameter ratio to natural gas pipelines used in the NTS with a wall thickness of 1.6 mm compared to 3.2 mm for the other sizes.

5.3.7 Discussion of cut steel conduit results

The relationship between the anomaly amplitude and the separation between the magnetometers in the array is currently unknown. Knowledge of this relationship can be used to optimise the array to give the magnetic anomalies the maximum amplitude in the magnetic gradient field increasing the sensitivity of the array to these anomalies. To be able to assess this relationship, representative defects must be created and measured in the laboratory for a range of magnetometer separations. These defects were created by cutting steel conduits using pipe cutters and the defects scanned with the magnetometer.

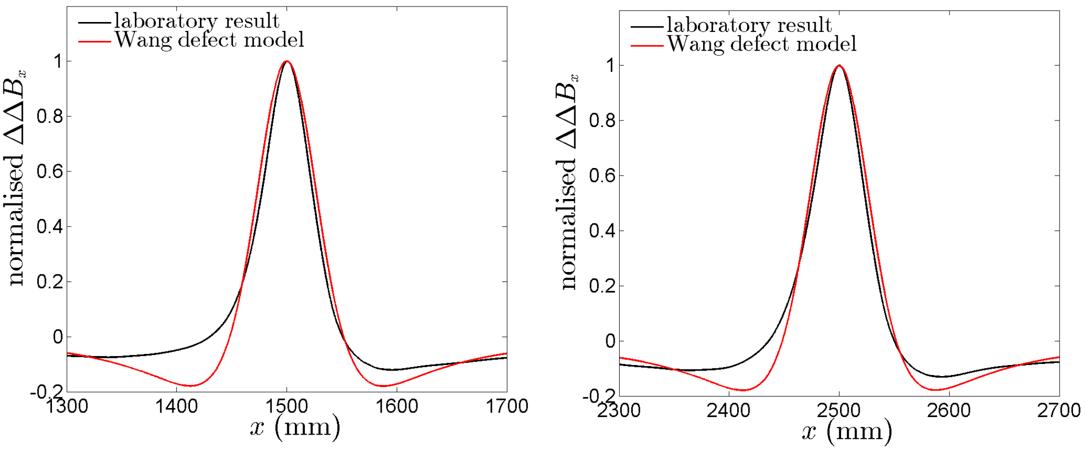

(a) Plot showing the normalised x component of the gradient field from the cut at $x = 1500$ mm in the 1″ measured in the laboratory and predicted by the Wang model.

(b) Plot showing the normalised x component of the gradient field from the cut at $x = 2500$ mm in the 1″ measured in the laboratory and predicted by the Wang model.

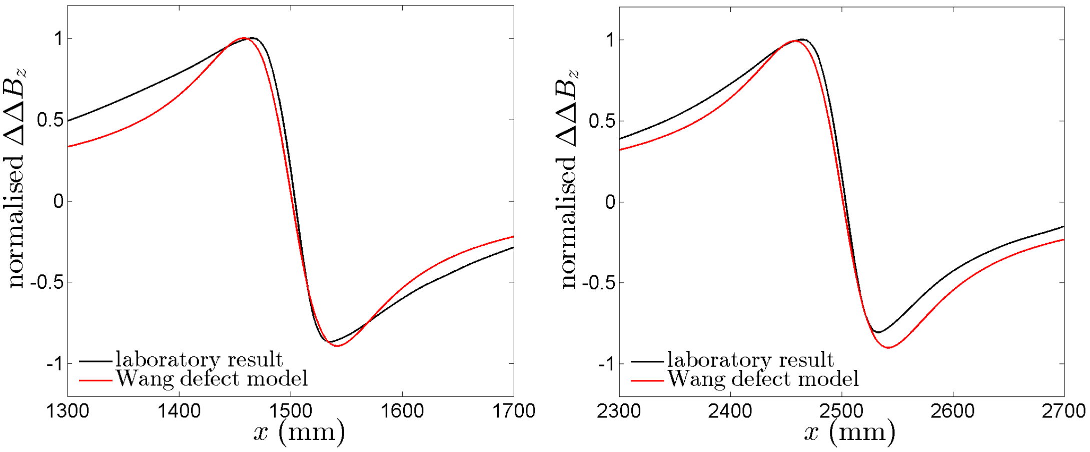

(c) Plot showing the normalised z component of the gradient field from the cut at $x = 1500$ mm in the 1″ measured in the laboratory and predicted by the Wang model.

(d) Plot showing the normalised z component of the gradient field from the cut at $x = 2500$ mm in the 1″ measured in the laboratory and predicted by the Wang model.

Figure 5.15: Plots showing the gradient field from the cuts in the 1″ conduit from the laboratory data and predicted by the Wang defect model.

In this study defects were created in different diameter conduit pipes by cutting them using a standard pipe cutter. These cuts were positioned by identifying the areas in the uncut conduit with the lowest variation to minimise the effects of the original state on the gradient field from the cuts in a $1''$ conduit. These positions were repeated in the other diameter conduits to maintain the position of the defects in each scan and to reduce any effects due to the distance from the conduit ends. These were each scanned with a magnetometer in the xz plane at different angles around the conduits to allow a three-dimensional magnetic field to be built up which can be used to calculate the gradient field.

The data from the scans on the conduits show a peak in the x component and a zero-crossing in the z component of the magnetic gradient field centred at the cuts, as predicted by the magnetised cylinder and Wang defect models. The magnetic gradient fields from the cut conduits show a high degree of correlation to the Wang defect model for the same dimensions, this shows that the cut conduits give a good representation of a defect for further analysis. These comparisons are shown in figure 5.15, with the correlation coefficients given in table 5.1.

The peaks and zero-crossings in the magnetic gradient field from the cuts show that the stress from the cutting created a magnetisation, this is the case for both the pipe cutter and band saw cutting methods. This anomaly in the magnetic gradient field from the cut regions show that the self magnetic flux leakage can be used to detect features in ferromagnetic materials such as pipelines, this can be used for non-destructive testing of the material.

The LICs from the conduits show a high degree of radial symmetry in the uncut, single cut and two cut cases. This is predicted by the pipe dipole model in which a pipe is considered to be a single dipole. When a ferromagnetic cylinder is considered with an axial magnetisation there is a radial component predicted by the diameter to length ratio of the cylinder. This radial field shows radial symmetry from the cylinder, as does the predicted axial field. This is confirmed by these results.

The heavy duty conduits were clamped into a pipe vice, this was in order to be able to cut these conduits using the pipe cutter. The vice was designed to not create any changed in the geometry of the pipe when it was held in position and was tightened only to the point where it was tight enough to prevent the conduit moving while it was being cut. The position at which the conduits were held in the vice is identifiable in the magnetic gradient fields as peaks and zero-crossing at the location of the clamp. This shows that the stress zone created by the clamping creates a change in the magnetisation in the conduit wall, verifying the ability of large stand-off magnetometry to detect stress concentration zones in a pipe wall.

In two of the conduits there are other anomalies in the magnetic gradient field besides the cuts and clamping points. These were found to be due to the conduits deviating very slightly from straight in these positions. This shows that the stress caused by bending causes a change in the magnetisation of the conduit wall and that this can be detected by large stand-off magnetometry.

These investigations were only completed on small conduits with a high wall curvature. Larger pipes used for transmission have a low wall curvature and so could give a different magnetic gradient field signal due to the defect being on an approximately flat plane as opposed to around a curve in the smaller diameter conduits.

The defects in the conduits in these investigations were full wall depth defects which went completely around the conduits, this is different to a defect in a pipe wall which do not go completely through the wall of the pipe and are not fully radial on the pipe wall. The stress created by the defect is due to the cutter rather than the pressure in the pipe and is built up quickly rather than slow corrosion progression over a number of years. These factors could lead to a difference in the anomaly in the magnetic gradient field detected by the large stand-off magnetometry.

The cuts made in the conduits give a magnetic gradient field that shows a high level of correlation with that predicted by the Wang defect model, this suggests that the cuts are a good approximation to defects in a pipe wall. All the sizes of conduits investigated give a peak and zero-crossing centred on the location of the cut in the conduit consistent with the model of self magnetic flux leakage from these stress zones. The pipe cutter generates stress in the conduit wall as it cuts the pipe, creating the stress concentration zone that is detected by the large stand-off magnetometry.

This shows that these cuts created in the conduit walls are representative of a defect in a pipe wall and can be used to assess the effect of the separation of the magnetometers on the amplitude of the anomalies in the magnetic gradient field.

5.4 Optimum magnetometer separation in the magnetometer array

To investigate the effect that the magnetometer separation in the magnetometer array has on the amplitude of the anomaly in the gradient field, the scans of the features created by cutting the conduits in section 5.3 were analysed for different data points for the outer magnetometer positions.

The relationship between the magnetometer separation and the amplitude in the feature of the magnetic gradient field is important in informing further development of the magnetometer survey array to increase the sensitivity of the instrument. This knowledge will also inform the configuration of the survey magnetometer array for each different circumstance.

The relationship between the magnetometer separation and the amplitude of the anomalies in the calculated gradient field has not previously been investigated for the array. A separation of 0.5 m is currently used in field surveys for all circumstances, improvements in this separation could increase the sensitivity of the system in detecting features in pipelines.

The magnetic gradient field is calculated using equation 5.3.

$$\Delta\vec{B}_{12} = \frac{\left(\vec{B}_1 - \vec{B}_2\right)}{S} \qquad \Delta\vec{B}_{23} = \frac{\left(\vec{B}_2 - \vec{B}_3\right)}{S} \tag{5.2}$$

$$\Delta\Delta\vec{B} = \Delta\vec{B}_{12} - \Delta\vec{B}_{23} \tag{5.3}$$

Where:

$\vec{B}_1$, $\vec{B}_2$ and $\vec{B}_3$ are the three-dimensional magnetic field strengths from the magnetometers as numbered in figure 2.19,

S is the separation between magnetometers,

$\Delta\vec{B}_{12}$ **and** $\Delta\vec{B}_{23}$ are the three-dimensional gradients across the two magnetometers indicated by the subscripts and,

$\Delta\Delta\vec{B}$ is the three-dimensional gradient field used in the survey analysis.

5.4.1 Methodology for determining the optimum magnetometer separation

To determine the optimum separation between the magnetometers in the magnetometry array, the magnetic gradient field for the cut conduit sections was calculated for different separations of the magnetometers. To measure how the separation affects the amplitude of the anomaly in the gradient field, first the method of measuring the amplitude must be defined. The amplitude of the peaks $\Delta\Delta B(x^{peak})$ and $\Delta\Delta B(z-z)$ were measured as shown in figures 5.16a and 5.16b respectively. These amplitudes were taken for each magnetometer separation in the scanning array, these amplitudes were normalised to allow comparisons between the different conduit sizes and magnetic fields.

To calculate the anomaly amplitude defined in figure 5.16 for different magnetometer separations the magnetic field data for different points was used for the outer magnetometer data. The angle between the centre and outer magnetometers at the pipe was used to specify the separation, this method removes the potential scaling factors from the different conduit diameters and also takes into account the height of the magnetometer from the centreline of the conduit. A schematic for this is shown in figure 5.17.

The angle between the magnetometers in the array was varied and the separation between the magnetometers at the pipe centreline calculated using equation 5.4 [150].

$$S = z\tan(\theta) \tag{5.4}$$

Where:

S is the separation between the inner and outer magnetometers,

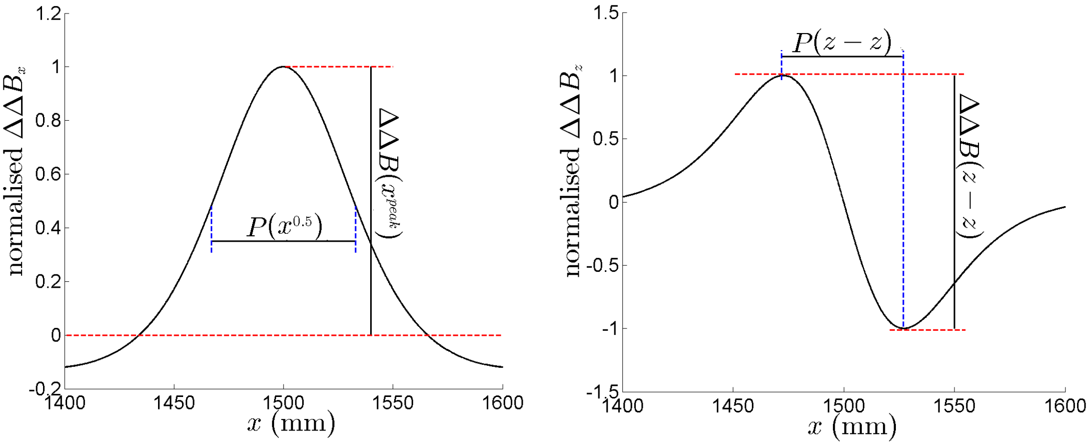

(a) Shape of the normalised peak in the $\Delta\Delta B_x$ component of the magnetic field calculated from the Wang model showing the peak amplitude, $\Delta\Delta B(x^{peak})$ and full width at half max, $P(x^{0.5})$.

(b) Shape of the normalised zero-crossing in the $\Delta\Delta B_z$ component of the magnetic field calculated the Wang model showing the amplitude, $\Delta\Delta B(z-z)$ and peak to peak width, $P(z-z)$.

Figure 5.16: Plots representing the normalised $\Delta\Delta B_x$ and $\Delta\Delta B_z$ components of the magnetic field calculated from the Wang defect model. Defining the properties of the plots: the $\Delta\Delta B_x$ peak amplitude, $\Delta\Delta B(x^{peak})$, the $\Delta\Delta B_x$ full width at half max, $P(x^{0.5})$, the $\Delta\Delta B_z$ crossing amplitude $\Delta\Delta B(z-z)$ and the $\Delta\Delta B_z$ peak to peak width, $P(z-z)$.

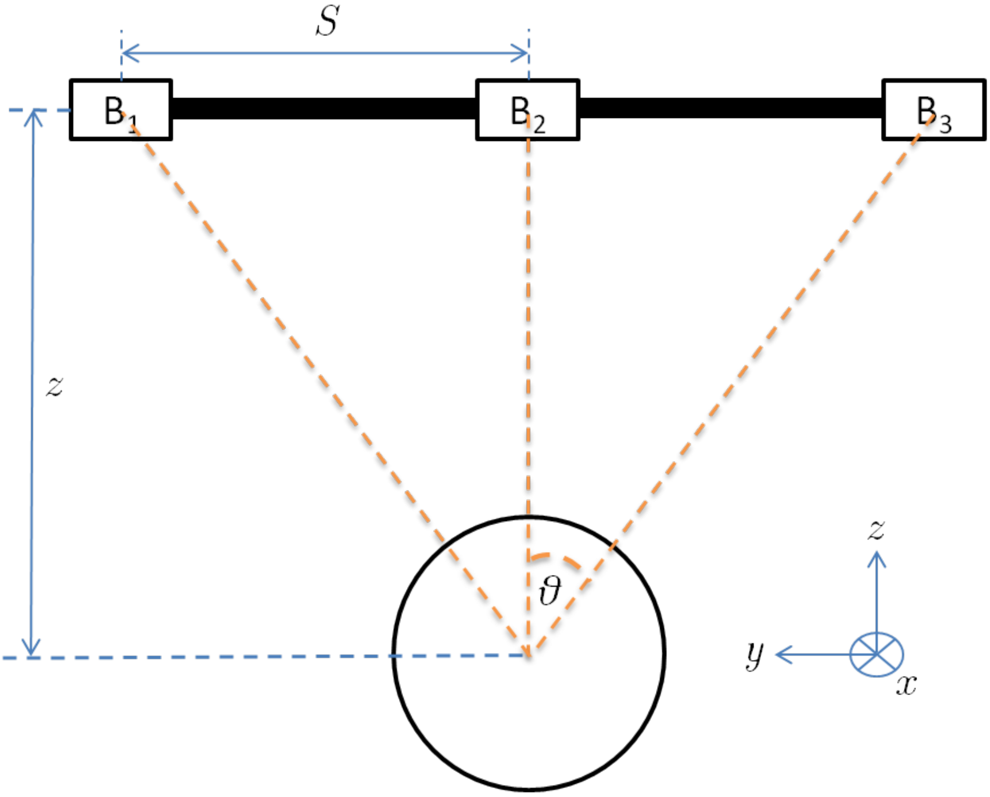

Figure 5.17: Figure showing the pipe and array defining the height, z, array separation, s, and magnetometer angle, Θ.

z is the height of the centre magnetometer from the centreline of the pipe, and

θ is the angle between the inner and outer magnetometer at the centreline of the pipe.

The current survey array is typically used at a height above the pipe centreline of 2 – 4 m, this gives an angle of separation range of 14 – 7° for the current separation of 0.5 m.

5.4.2 Laboratory magnetometer separation results

The amplitude of the anomalies in the gradient field in the x and z components were calculated for angles between the magnetometers in the range $\theta = 5 - 35°$, these were normalised for comparison between the anomalies. These were calculated for heights above the centreline of the conduit of $z = 50 - 300$ mm for conduits with nominal diameters of $^1/_2''$, $^3/_4''$, $1''$ and $1^1/_2''$. The relationship between the angle and the normalised amplitude for the different heights and conduit diameters are shown in figure 5.18.

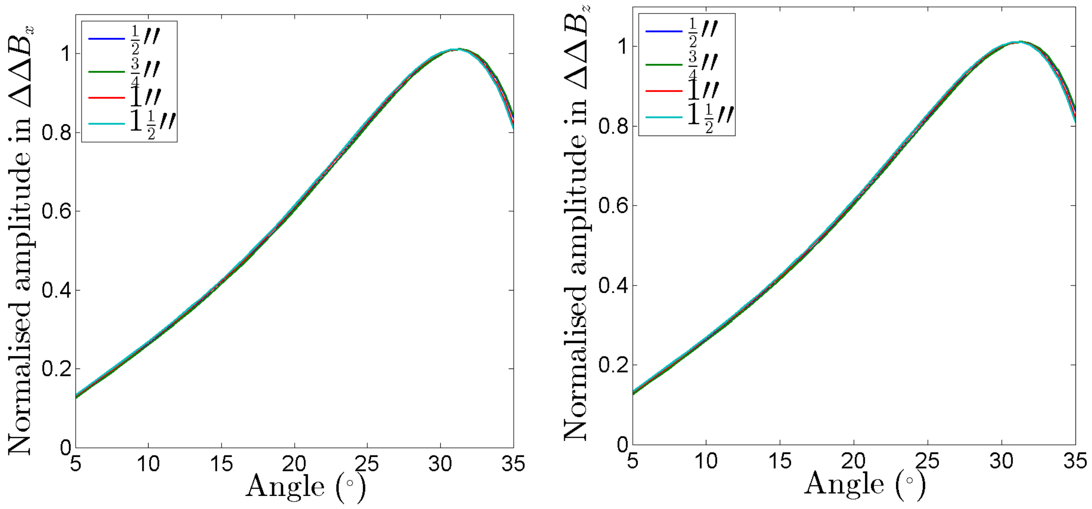

(a) Plot showing the normalised amplitude of the peak in $\Delta\Delta B_x$ from a cut conduit for different angles of the magnetometer array at an array height z = 50 mm.

(b) Plot showing the normalised amplitude of the peak in $\Delta\Delta B_z$ from a cut conduit for different angles of the magnetometer array at an array height z = 50 mm.

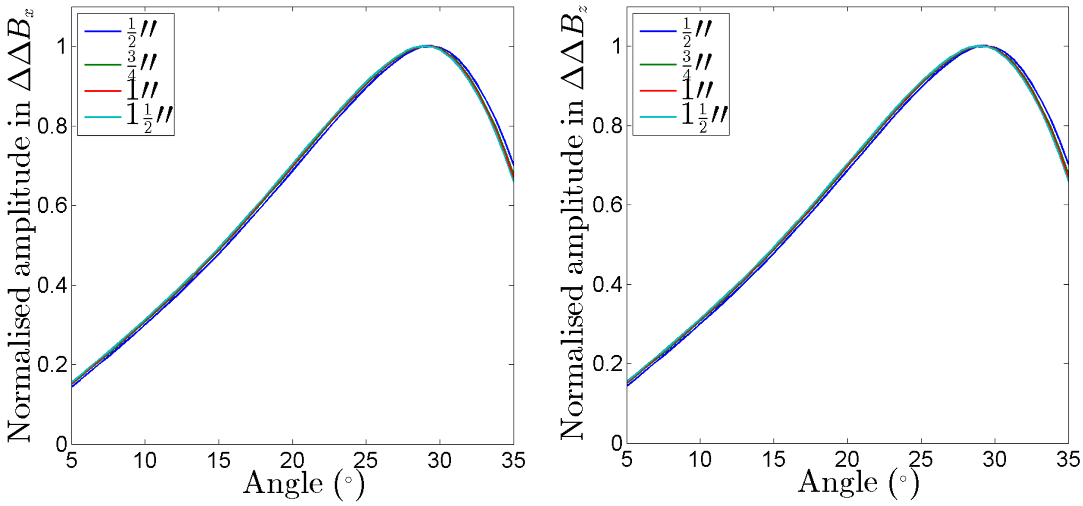

(c) Plot showing the normalised amplitude of the peak in $\Delta\Delta B_x$ from a cut conduit for different angles of the magnetometer array at an array height z = 100 mm.

(d) Plot showing the normalised amplitude of the peak in $\Delta\Delta B_z$ from a cut conduit for different angles of the magnetometer array at an array height z = 100 mm.

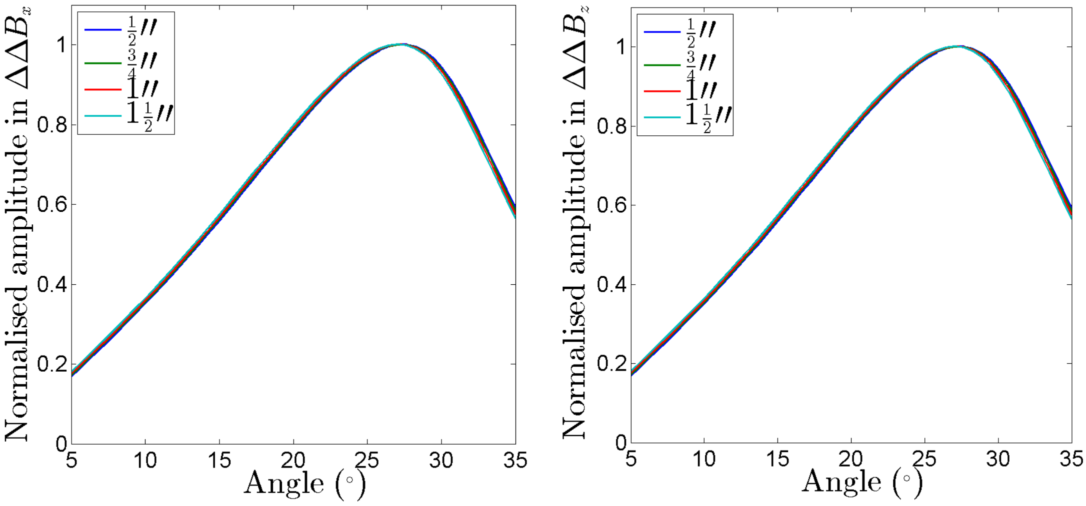

(e) Plot showing the normalised amplitude of the peak in $\Delta\Delta B_x$ from a cut conduit for different angles of the magnetometer array at an array height z = 150 mm.

(f) Plot showing the normalised amplitude of the peak in $\Delta\Delta B_z$ from a cut conduit for different angles of the magnetometer array at an array height z = 150 mm.

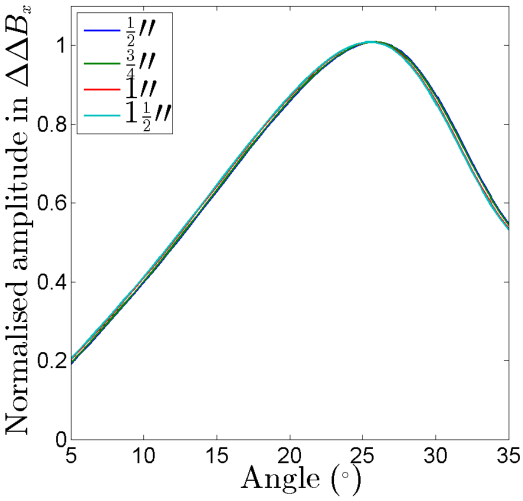

(g) Plot showing the normalised amplitude of the peak in $\Delta\Delta B_x$ from a cut conduit for different angles of the magnetometer array at an array height z = 200 mm.

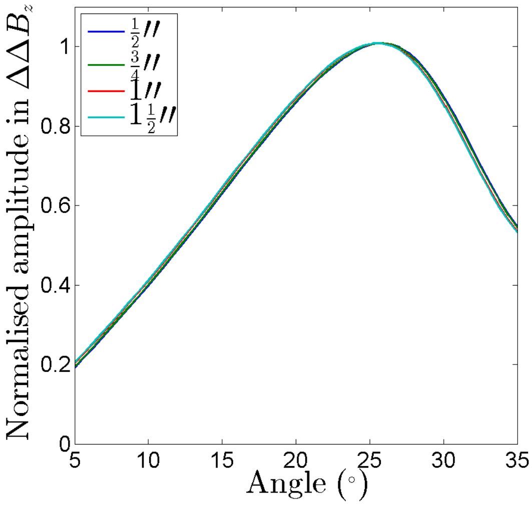

(h) Plot showing the normalised amplitude of the peak in $\Delta\Delta B_z$ from a cut conduit for different angles of the magnetometer array at an array height z = 200 mm.

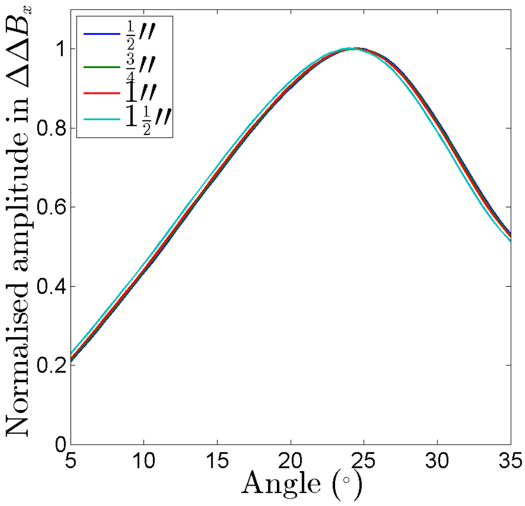

(i) Plot showing the normalised amplitude of the peak in $\Delta\Delta B_x$ from a cut conduit for different angles of the magnetometer array at an array height z = 250 mm.

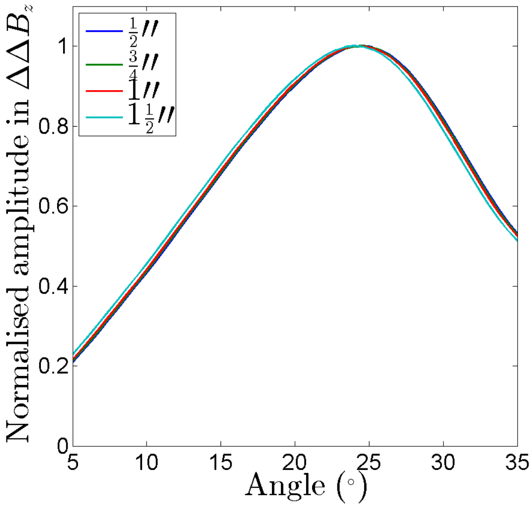

(j) Plot showing the normalised amplitude of the peak in $\Delta\Delta B_z$ from a cut conduit for different angles of the magnetometer array at an array height z = 250 mm.

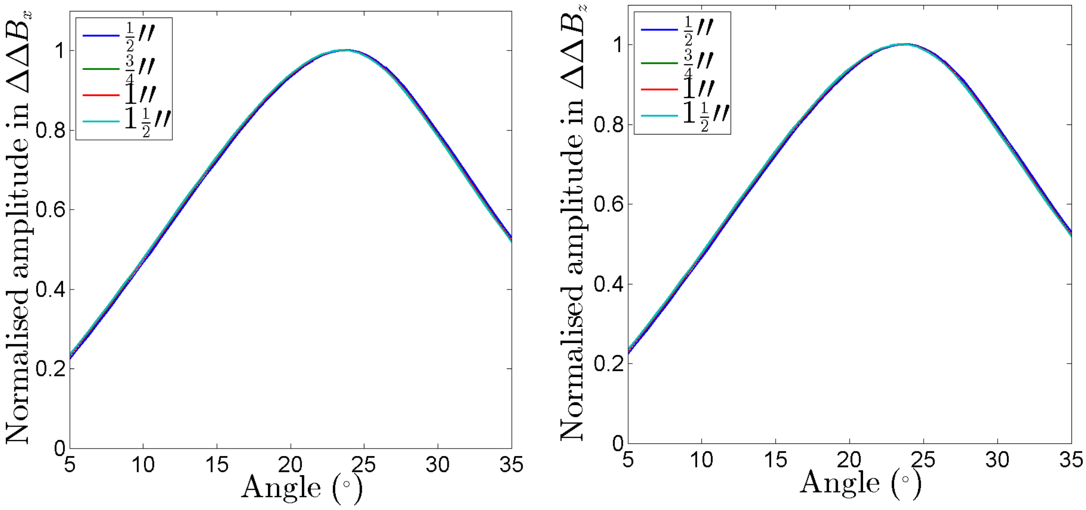

(k) Plot showing the normalised amplitude of the peak in $\Delta\Delta B_x$ from a cut conduit for different angles of the magnetometer array at an array height z = 300 mm.

(l) Plot showing the normalised amplitude of the peak in $\Delta\Delta B_z$ from a cut conduit for different angles of the magnetometer array at an array height $z = 300$ mm.

Figure 5.18: Plots showing the normalised peak amplitudes in the $\Delta\Delta B_x$ and $\Delta\Delta B_z$ components of the magnetic field against the array angle from the centreline of the conduit, θ, for conduits with diameter $^1/_2''$, $^3/_4''$, $1''$ and $1^1/_2''$. At array heights, z, of: 50 mm in a and b, 100 mm in c and d, 150 mm in e, f, 200 mm in g and h, 250 mm in i and j and 300 mm in k and l.

5.4.3 Laboratory magnetometer separation analysis

Surfaces showing how the normalised peak amplitude of an anomaly in the x and z components of the gradient field, from a feature in a $1''$ conduit varies with the angle between the magnetometers and the height above the centreline of the conduit are shown in figure 5.19. Contour plots with a colour map to represent 5% bins of the normalised peak amplitude in the x and z components of the gradient field, from a feature in a $1''$ conduit against the magnetometer angle and the height above the centreline of the conduit, are shown in figure 5.20.

The surfaces shown in figure 5.19 and colour maps in figure 5.20 show that as the magnetometers are moved further away from the conduit the angle tends towards less variation with distance. The colour maps in figure 5.20 show the peak at an angle of approximately 33° which tends towards a value of 23° at 300 mm.

Figure 5.21 shows the laboratory results for a $1''$ cut conduit in the laboratory with the values calculated from the magnetised cylinder model shown in section 2.3.2 and the Wang defect model shown in section 2.4.4. Both the laboratory data and the Wang defect model have their peaks at approximately 23° while the magnetised cylinder model gives a peak at an angle of approximately 23.5° in both the x and z component of the gradient field.

The magnetised cylinder versus angle relationship shows a greater peak amplitude at 5° than the other models but has a lower gradient than the laboratory data or Wang model. The magnetised cylinder model also has a lower gradient as the angle increases past the peak, this relationship after the peak is similar to the Wang defect model but both give a greater peak amplitude than is measured in the laboratory for angles greater than the peak angle. The Wang model versus angle relationship has the same peak as the laboratory data though with a larger gradient and greater curvature of the line before the angle of the peak. The correlation coefficients of the two models and the laboratory data for the x and z components of the gradient field are shown in table 5.2.

	Magnetised cylinder	Wang defect	Laboratory data	
Magnetised cylinder	–	0.97	0.96	x
Wang defect	0.97	–	0.97	
Laboratory data	0.96	0.98	–	
	z			

Table 5.2: Table of the correlation coefficients between the magnetised cylinder and Wang defect models and the laboratory data in the x and z components of the magnetic gradient.

The plots in figure 5.19 and correlation coefficients in table 5.2 show that the expanded Wang model and hollow magnetised cylinder model match with what is seen in the laboratory data. These give the same peak and shape of the relationship, though both overestimate the peak amplitude at angles greater than the angle which gives the peak amplitude. These provide further evidence that the relationship observed in the laboratory is accurate.

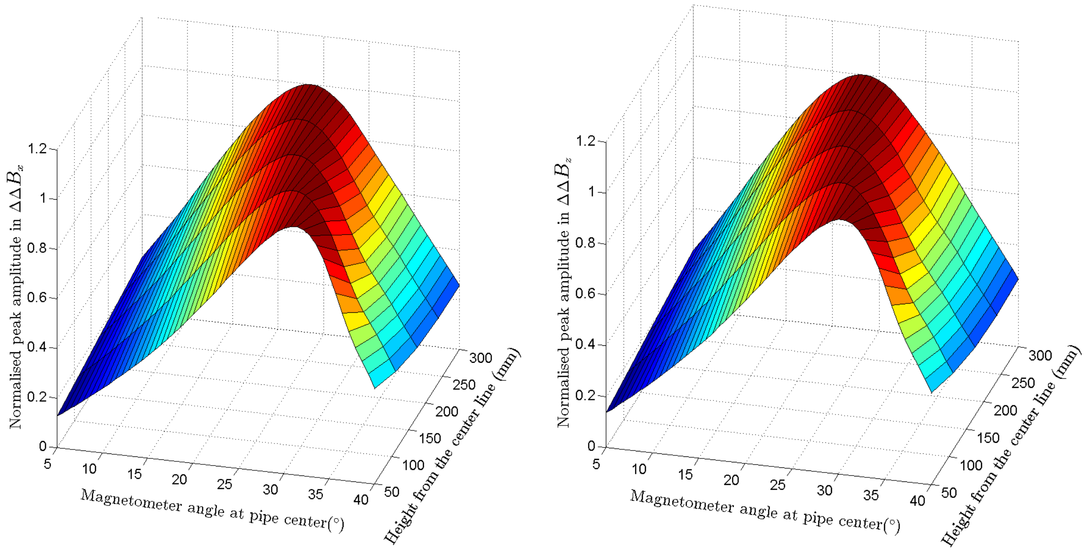

(a) Surface plot showing the normalised peak amplitudes in the $\Delta\Delta B_x$ component of the magnetic field from a 1″ diameter conduit, for a range of angles to the outer magnetometer for a range of heights from the centreline of the conduit.

(b) Surface plot showing the normalised peak amplitudes in the $\Delta\Delta B_z$ component of the magnetic field from a 1″ diameter conduit, for a range of angles to the outer magnetometer for a range of heights from the centreline of the conduit.

Figure 5.19: Plots showing the normalised peak amplitudes in the $\Delta\Delta B_x$ and $\Delta\Delta B_z$ component of the magnetic field from a 1″ diameter conduit, for a range of angles to the outer magnetometer for a range of heights from the centreline of the conduit.

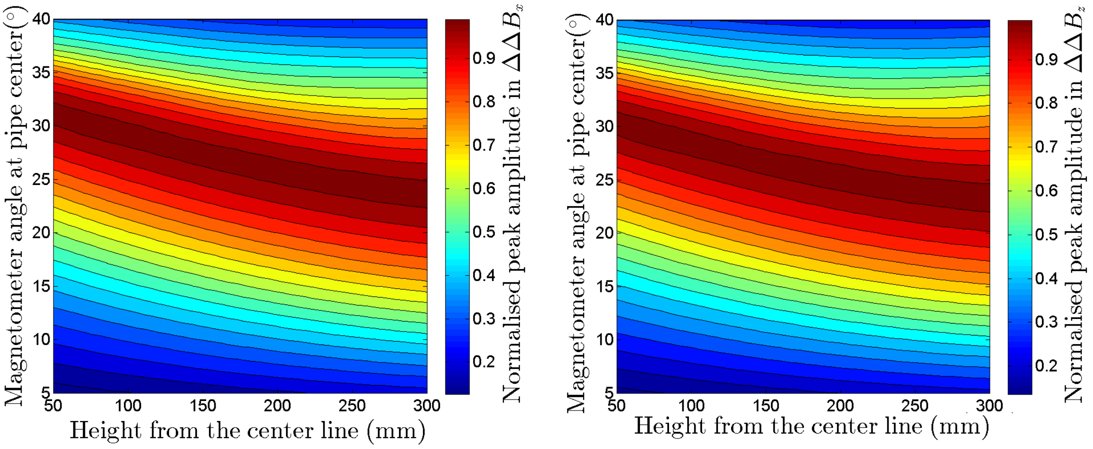

(a) Plot showing the peak amplitude in the $\Delta\Delta B_x$ component of the magnetic field versus the magnetometer angle for different heights above the conduit centreline in bins of 5% of maximum amplitude.

(b) Plot showing the peak amplitude in the $\Delta\Delta B_z$ component of the magnetic field versus the magnetometer angle for different heights above the conduit centreline in bins of 5% of maximum amplitude.

Figure 5.20: Plot showing the peak amplitude in the $\Delta\Delta B_x$ and $\Delta\Delta B_z$ components of the magnetic field versus the magnetometer angle for different heights above the conduit centreline in bins of 5% of maximum amplitude.

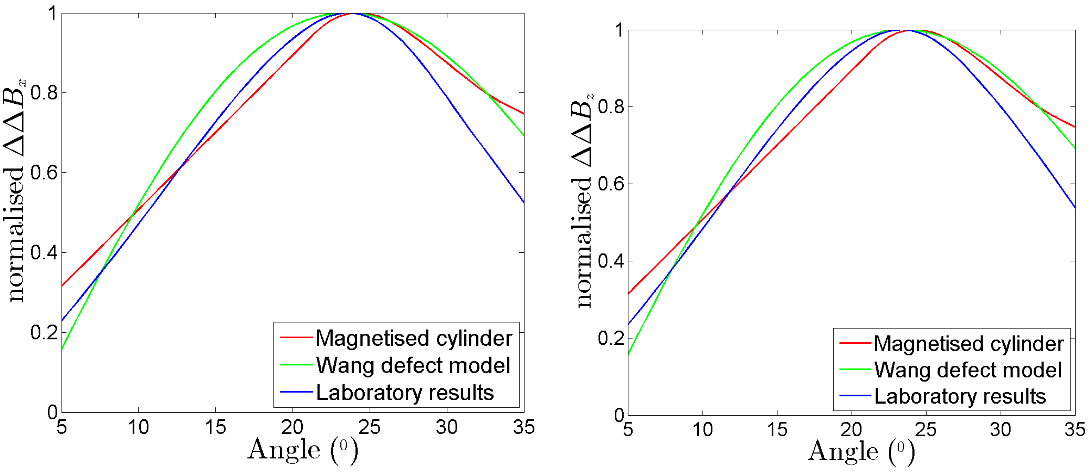

(a) Plot showing the normalised amplitude of the peak in $\Delta\Delta B_x$ calculated for the magnetised cylinder model, Wang defect model, and the data from the laboratory experiment on a cut conduit, versus different angles of the magnetometer array.

(b) Plot showing the normalised amplitude of the peak in $\Delta\Delta B_z$ calculated for the magnetised cylinder model, Wang defect model, and the data from the laboratory experiment on a cut conduit, versus different angles of the magnetometer array.

Figure 5.21: Plots showing the normalised amplitude of the peak in $\Delta\Delta B_x$ and $\Delta\Delta B_z$ calculated for the magnetised cylinder model, Wang model, and the data from the laboratory experiment on a cut conduit, versus different angles of the magnetometer array.

5.4.4 Laboratory magnetometer separation discussion

The magnetometry survey array uses three magnetometers separated laterally to calculate the magnetic gradient field from the magnetic field strengths measured at the three points. The effect of the separation of the magnetometers on the amplitude of a feature in the gradient field calculated from a cut conduit has not previously been evaluated. Identification of the relationship between the feature amplitude and the magnetometer separation will allow the survey array to be further developed to maximise the gradient field amplitude calculated from the array. Maximising the amplitude in the gradient field from the feature will increase the probability of detection of these features.

For all four diameters of conduit scanned, the maximum amplitude of the feature in the $\Delta\Delta B$ field is achieved at approximately the same angle for the same magnetometer height above the conduit centreline. For different magnetometer heights above the centreline this peak angle decreases as the height increases. These results show no relationship between the diameter of the conduit and the angle that gives the maximum feature amplitude. For a height above the centreline of 50 mm the peak amplitude is achieved at approximately 32°, this tends to a value of 23° at 300 mm. The trend as the height above the centreline increases stabilises to a value of approximately 23°.

The relationship between the outer magnetometer angle and the feature amplitude shows a linear increase from the origin to the peak and the same gradient decrease after the peak. This allows an envelope to be defined for which the array will give feature amplitudes greater than a percentage of the maximum amplitude. This accounts for the fact that the height above the pipe centreline in the field is not fixed and can vary, meaning a fixed magnetometer angle will not give optimum readings for a full pipeline survey.

The relationship between the magnetometer separation angle and the peak amplitude from the 300 mm height laboratory results has been compared to the same scenario in the Wang defect model and the axially magnetised cylinder model. The Wang model and laboratory results show the same peak angle while the magnetised cylinder model has a greater peak angle. The Wang defect model and magnetised cylinder model predict a decrease in the amplitude with deviation from the peak angle lower than the laboratory results. These models and the laboratory results all give correlation coefficients > 0.95 showing that both of the models and the laboratory results agree.

The current magnetometry survey array has a magnetometer separation of 0.5 m, in a survey the typical height above the centreline is 2 – 4 m, this gives an angle range of 14 – 7°. Taking the 300 mm amplitude to angle relationship as the relationship for these as the amplitude trend with height above the array levels out at approximately this height, this gives a normalised amplitude range of 0.3 – 0.75. The peak separation for the magnetometers in this case is 0.85 – 1.7 m. Increasing the separation of the magnetometers to 0.75 m would give a normalised amplitude range of 0.5 – 0.9, increasing the separation to 1 m would give normalised peak amplitudes in the range 0.75 – 1.

Increasing the separation of the magnetometers in the magnetometry survey array will give a greater amplitude of the anomalies in the magnetic gradient field. Increasing the separation of the magnetometers will increase the width of the magnetometry array making it more difficult to manoeuvre. This would also increase the walking noise in the signal from the operator carrying the survey array, where the array deviates from perfectly level along the array length causing one outer magnetometer to drop and the other to rise. Increasing the array to a separation of 0.75 m would give a normalised amplitude increase of 0.15 – 0.2, the inclusion of further magnetometers between the outer and centre magnetometer could be used to correct for the additional noise from the increase in width.

The Wang model expansion to a three-dimensional system in order to calculate the gradient field shows good agreement with the laboratory data and magnetised cylinder showing that this expansion is valid for the defect in a ferromagnetic material to calculate the gradient field from the magnetic field.

The results from these laboratory experiments have only been taken for features due to cuts in small diameter conduits in the laboratory. The pipelines in the field are typically a much larger diameter and scanned from a greater height above the pipe centreline. While the peak angle tends towards 23° this has not been tested for larger heights above the pipe or greater diameter pipes. A future investigation in this area could be conducted to investigate this relationship for typical pipe diameters and heights to ensure this relationship still holds.

The effect of the magnetometry separation on the amplitude of the anomaly in the magnetic gradient field from a pipe feature has been investigated. This has been done for laboratory data from scans on conduits that have been cut to create a discontinuity and compared to the relationship from two models, the magnetised cylinder and Wang defect models. These give angles for the magnetometers of the peak amplitude for the features in the magnetic gradient field of 32 – 23° with increasing height above the centreline, this relationship stabilises at approximately 23°. For a typical height above the centreline in the field of 2 – 4 m this gives a separation of 0.85 – 1.7 m.

5.5 Conclusion

The relationship between the separation of the magnetometers in the magnetometry array and the amplitude of the anomalies in the magnetic gradient field has been investigated in the laboratory.

This investigation involved four different diameter conduits with discontinuities created by cutting the conduits, these were then scanned in the laboratory. Each conduit was scanned for xz planes around the conduit to give a three-dimensional radial magnetic field, this was used to calculate the magnetic gradient field from the conduits.

The calculated magnetic gradient field from the scans show a peak in the x component and zero-crossing in the z component. These anomalies in the magnetic gradient field match with the shape of the anomaly predicted by the Wang defect model, this verifies that these discontinuities are a good representation of defect zones in a ferromagnetic material. To investigate the optimum separation of the magnetometers the amplitude of the anomalies in the magnetic gradient field were considered for different angular separations between the centre and outer magnetometers at the pipe centreline.

The relationship between the angular separation and the amplitude of the gradient field anomalies is approximately linearly increasing from small angles then gives a parabolic peak and decreases linearly after the peak region. The peak occurs at 32° at a distance from the centreline of the conduit of 50 mm and decreases to 23° at 300 mm, the relationship between the height above the centreline of the conduit and the peak angle flattens towards a value of 23° with increasing height.

The relationship between the angle and the amplitude in the anomaly in the gradient field from a defect measured in the laboratory has a high level of correlation with the relationships calculated from the magnetised cylinder and Wang defect models giving validity to this result.

Chapter 6

Laboratory experiments on pipe section simulants

6.1 Introduction

The magnetometry survey array is used to find anomalies in the magnetic field from defect features in gas pipeline walls for non-interference inspection. To determine the positional accuracy of the detection system magnetic dipoles were used to simulate pipe section dipoles, AlNiCo magnets and magnetised steel conduit sections were used. These simulants were scanned in the laboratory and the magnetic field strength measured to compare the position of the detected anomalies in the magnetic field to the known positions of the dipoles at different heights above the simulant.

The relationship between the detected anomaly in the magnetic field and the defect feature can be used to improve locational accuracy of detections for the magnetometry array. Pipe features detected in pigging operations are related to their nearest weld, therefore detecting the weld position accurately will allow these features to be located more accurately. This will allow excavations to be precisely located and smaller in scale, reducing the disruption and cost of any repairs required to the detected features.

The pipeline dipole model treats each pipe section in the pipeline as a dipole along the centreline of the pipe, these are randomly oriented with respect to each other [82]. Previous simulation work on the field from a pipeline made of a series of dipoles, shows a field leakage from the joints between dipole sections. The field from these regions is deflected along the pipeline from the joint depending on the combination of dipoles further along the pipline [121].

The pipe dipole model assumes that each pipe section is a strong permanent magnet and that the joint between each section is a small region of magnetisation that is differently magnetised to the section either side of it. This has not previously been verified in laboratory experiments for a combination of dipoles.

The investigations in this section have been conducted on simulant pipelines built from axially magnetised dipoles to determine if the pipeline dipole model will produce a magnetic anomaly at each joint as predicted in the dipole simulations. This investigation assessed the locational accuracy of using the anomaly in the magnetic field to project back to the pipeline to predict the location of the feature, in order to improve the accuracy of the magnetometry survey array.

6.2 Experimental methodology

The laboratory set-up used for these experiments is described in chapter 3. Before any scans were taken of the simulants, a scan of the background field in the laboratory from the equipment, electronics and construction of the building was taken. This was used to deduct the background from the scans of the simulants. This was done rather than using the gradient method used in chapter 5. In the case of different heights above the simulants the change in angle of the outer measurement positions would create a variance as shown in chapter 5 if the magnetometer measurement positions were kept constant. In the case where the angles were kept constant there would be a variance due to the laboratory environment being magnetically noisier on small scales than those encountered in the field.

For the AlNiCo magnet experiments, the magnets were placed on an aluminium frame and held in position using stainless steel bolts at either end, the magnets were placed touching with no gap between them. A schematic diagram of this set-up is shown in figure 6.1.

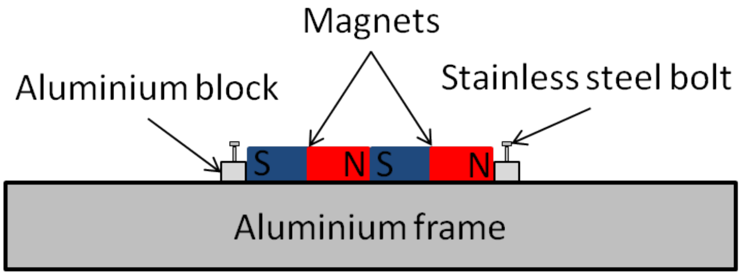

Figure 6.1: Diagram showing two cuboid AlNiCo magnets on the aluminium frame held in place with stainless steel bolts to prevent movement during the scan.

The one and two magnet cases were scanned directly above the centreline of the magnets in the range x = -200 – 200 mm in steps of Δx = 5 mm, with the centre of the simulants positioned at x = 0 mm. The three magnet case was scanned in the range x = -500 – 500 mm in steps of Δx = 10 mm with the centre of the simulants positioned at x = 0 mm. All of the magnet cases were scanned at heights above the top surface of the magnets of z = 200 – 400 mm in steps of Δz = 25 mm. z = 200 mm was the closest the magnetometer could approach the magnets without saturating.

The scans were repeated three times for each magnet to allow for the measurement repeatability to be calculated as shown in section 3.3.1, the background room scans were subtracted from the magnetic field strength data gathered. This was then used for the analysis of the positional accuracy of anomaly detection.

For the cut conduit section experiments, three lengths of conduit 250 mm long were cut from a 1″ diameter mild steel conduit using a standard pipe cutter. These were magnetised using an AlNiCo magnet which was stroked along the surface of the conduit at a constant speed aligned with the seam weld of the conduit, then placed onto an aluminium frame to hold them in position.

To test the induced magnetisation from this technique a 400 mm long mild steel rod with a diameter of 10 mm was first scanned and then magnetised in this way four times, being scanned after each magnetisation. The rod was placed on the frame and scanned along the centreline of the rod after each magnetisation in the region x = -300 – 300 mm with the rod centred at x = 0 mm in steps of Δx = 10 mm at a height above the rod of z = 200 mm. The three conduits were individually scanned in the region x = -200 – 200 mm with the conduit centred at x = 0 mm, these were then placed in various configurations of two and three conduits. The two conduit cases were scanned in the region x = -300 – 300 mm with conduits centred at x = 0 mm and the three conduit cases were scanned in the region x = -400 – 400 mm with the conduits centred at x = 0 mm. All cases were scanned at heights above the conduit surface of z = 50 – 300 mm in steps of Δz = 25 mm.

Each configuration was scanned three times for each to allow for the measurement repeatability to be calculated as shown in section 3.3.1 and the background room scans were subtracted from the magnetic field strength data gathered. This was then used for the analysis of the positional accuracy of the anomaly detection.

6.3 Magnetic field measurements using AlNiCo magnets to represent pipe section dipoles

6.3.1 Experimental basis

For verification of the magnetic field shape and magnetic field strength plots AlNiCo permanent magnets with marked poles were used to simulate pipe sections as dipoles. A diagram of a magnet used with its dimensions is shown in figure 6.2.

These magnets were chosen as they have marked poles allowing known combinations and orientations to be created repeatable. These permanent magnets were also readily available, relatively weak permanent magnets allowing for the magnetometer to be approached closer to the magnets without saturating the magnetometer. The magnets were mounted onto an aluminium frame using stainless steel bolts to hold them in position. The magnets were held together with no gap between them.

6.3.2 AlNiCo magnet dipole results

The magnetic field strength in the B_x and B_z directions for a single AlNiCo magnet aligned SN in the positive x direction at a height of $z = 200$ mm along the centreline of the magnet are shown in figure 6.3. A linear integral convolution (LIC) texture representing the magnetic field shape and magnitude for a single AlNiCo magnet aligned SN in the positive x direction in the range $z = 200 - 400$ mm above the centre of the magnet is shown in figure 6.4.

The magnetic field strength in the B_x and B_z directions for two AlNiCo magnets aligned SN-SN in the positive x direction at a height of $z = 200$ mm along the centreline of the magnet are shown in figure 6.5. An LIC texture representing the magnetic field shape and magnitude for two AlNiCo magnets aligned SN-SN in the positive x direction in the range $z = 200 - 400$ mm above the centre of the magnet is shown in figure 6.6.

The magnetic field strength in the x and z directions for two AlNiCo magnets aligned SN-NS in the positive x direction at a height of $z = 200$ mm along the centreline of the magnet are shown in figure 6.7. An LIC texture representing the magnetic field shape and magnitude for two AlNiCo magnets aligned SN-NS in the positive x direction in the range $z = 200 - 400$ mm above the centre of the magnet is shown in figure 6.8.

The magnetic field strength in the x and z directions for three AlNiCo magnets aligned SN-SN-NS in the positive x direction at a height of $z = 200$ mm along the centreline of the magnet are shown in figure 6.9. An LIC texture representing the magnetic field shape and magnitude for the three AlNiCo magnets aligned SN-SN-NS in the positive x direction in the range $z = 200 - 400$ mm above the centre of the magnet is shown in figure 6.10.

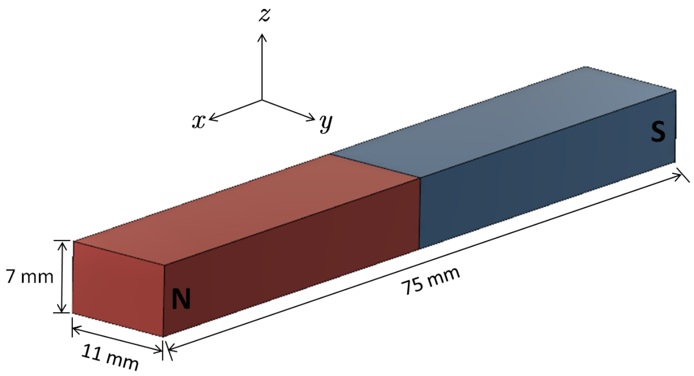

Figure 6.2: Diagram showing the direction of the axes and dimensions of the AlNiCo magnets used in the experiments as dipole pipe section simulants.

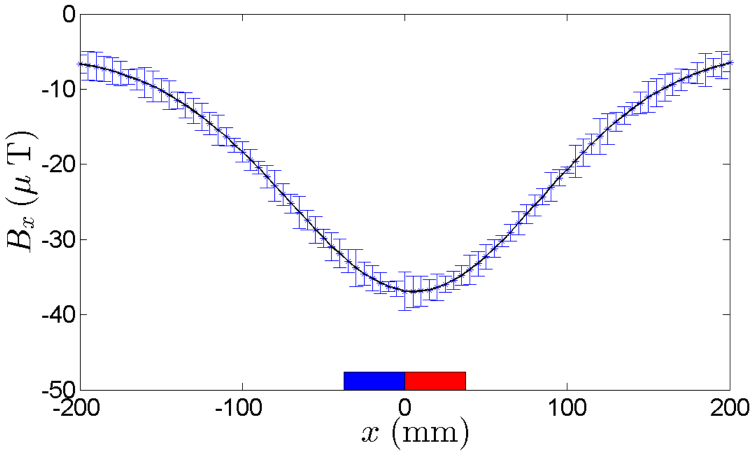

(a) Plot showing the B_x component of the magnetic field strength from an AlNiCo magnet with a length of 75 mm, centred at $x = 0$ mm aligned with its north pole in the positive x direction at a height from the top of the magnet of $z = 200$ mm. The magnet's position in the x direction is shown by coloured rectangles, with blue representing the south pole and red representing the north pole.

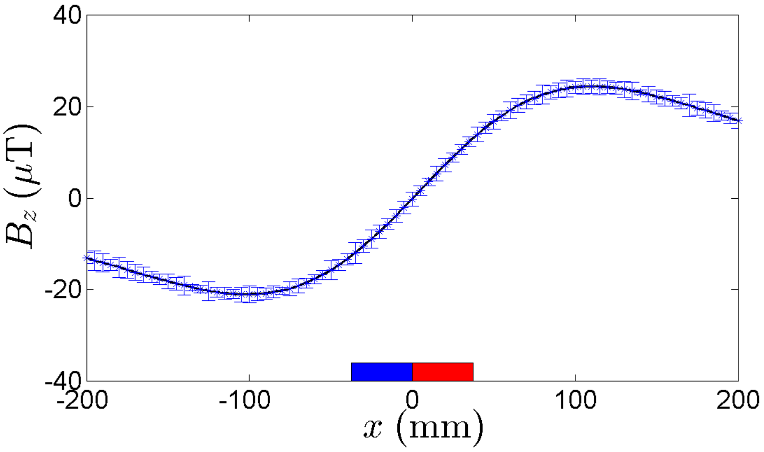

(b) Plot showing the B_z component of the magnetic field strength from an AlNiCo magnet with a length of 75 mm, centred at $x = 0$ mm aligned with its north pole in the positive x direction at a height from the top of the magnet of $z = 200$ mm. The magnet's position in the x direction is shown by coloured rectangles, with blue representing the south pole and red representing the north pole.

Figure 6.3: Plots showing the B_x and B_z components of the magnetic field strength in a and b respectively from an AlNiCo magnet with a length of 75 mm, centred at $x = 0$ mm aligned with its north pole in the positive x direction at a height from the top of the magnet of $z = 200$ mm. In each the magnet's position in the x direction is shown by coloured rectangles, with blue representing the south pole and red representing the north pole.

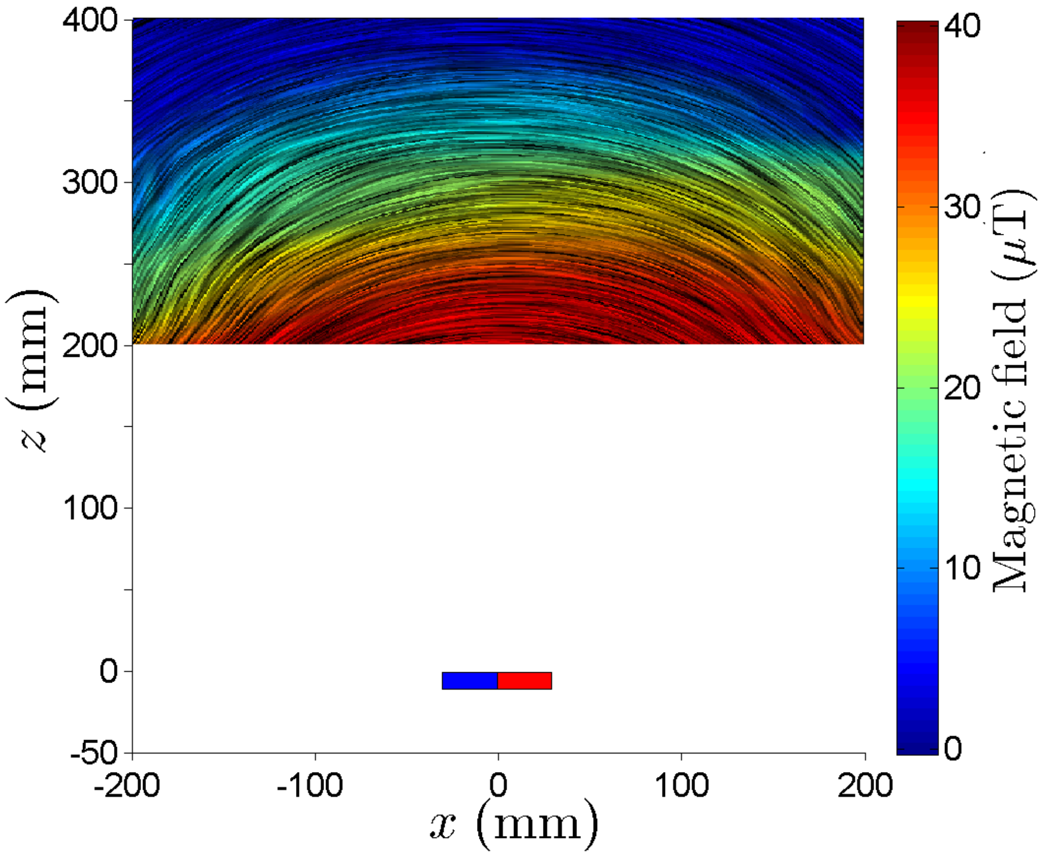

Figure 6.4: Linear integral convolution texture showing the magnetic field from an AlNiCo magnet centred at $x = 0$ mm for heights from the top of the magnet $z = 200$ - 400 mm. No data is shown for $z < 200$ mm as the magnet strength saturated the magnetometer below this level. The magnet's position is shown by coloured rectangles, with blue representing the south pole and red representing the north pole.

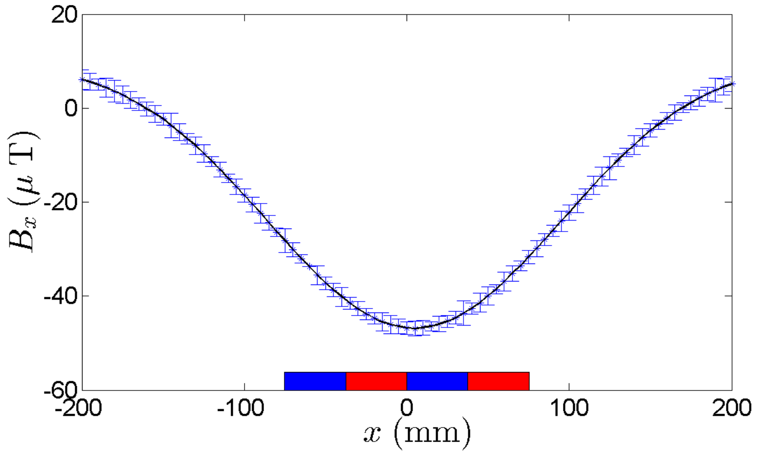

(a) Plot showing the B_x component of the magnetic field strength from two AlNiCo magnets, each with a length of 75 mm, arranged SN-SN centred at $x = 0$ mm at a height from the top of the magnets of $z = 200$ mm. The magnets' positions in the x direction are shown by coloured rectangles, with blue representing the south pole and red representing the north pole.

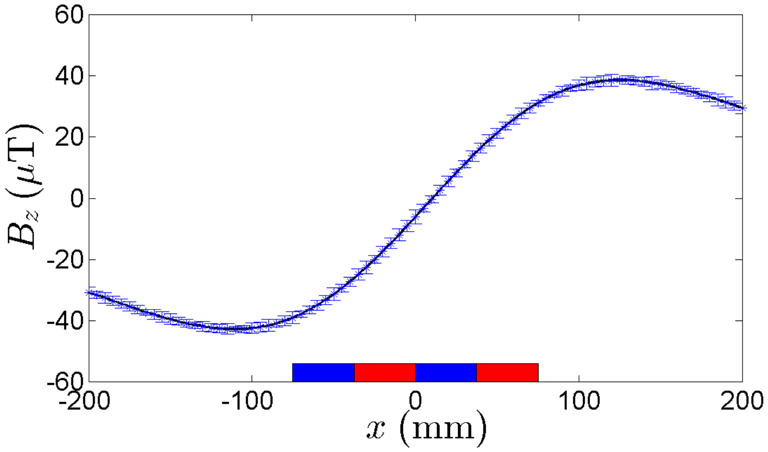

(b) Plot showing the B_z component of the magnetic field strength from two AlNiCo magnets, each with a length of 75 mm, arranged SN-SN centred at $x = 0$ mm at a height from the top of the magnets of $z = 0$ mm. The magnets' positions in the x direction are shown by coloured rectangles, with blue representing the south pole and red representing the north pole.

Figure 6.5: Plot showing the B_x and B_z components of the magnetic field strength in a and b respectively from two cuboid AlNiCo magnets, each with a length of 75 mm, arranged SN-SN centred at $x = 0$ mm at a height from the top of the magnets of $z = 200$ mm. In each the magnets' positions in the x direction are shown by coloured rectangles, with blue representing the south pole and red representing the north pole.

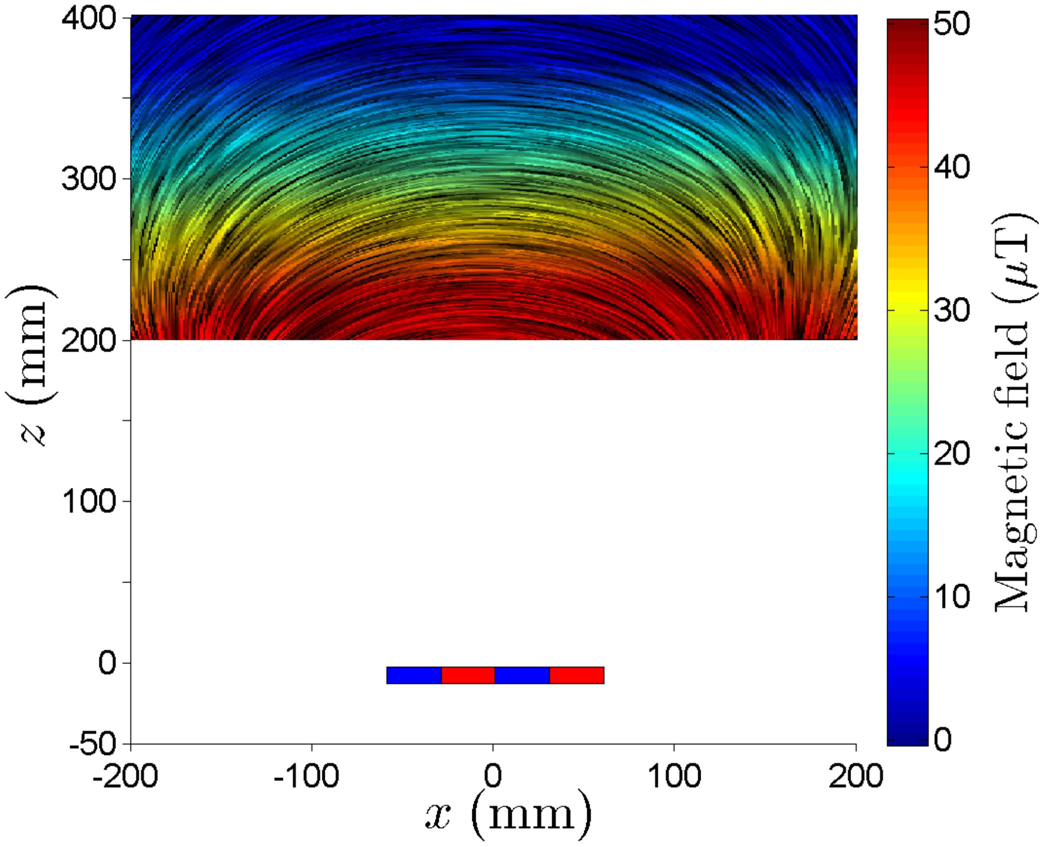

Figure 6.6: Linear integral convolution texture showing the magnetic field from two cuboid AlNiCo magnets arranged SN-SN centred at $x = 0$ mm for heights from the top of the magnet $z = 200$ - 400 mm. No data is shown for $z < 200$ mm as the magnet strength saturated the magnetometer below this level. The magnets' positions are shown by coloured rectangles, with blue representing the south pole and red representing the north pole.

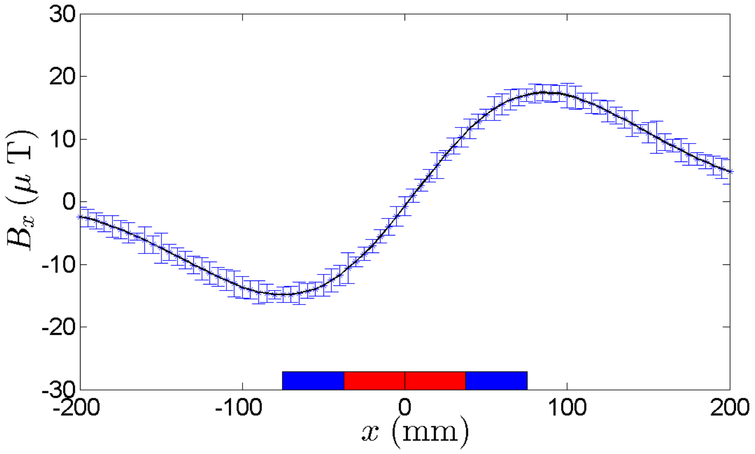

(a) Plot showing the B_x component of the magnetic field strength from two AlNiCo magnets, each with a length of 75 mm, arranged SN-NS centred at $x = 0$ mm at a height from the top of the magnets of $z = 200$ mm. The magnets' positions in the x direction are shown by coloured rectangles, with blue representing the south pole and red representing the north pole.

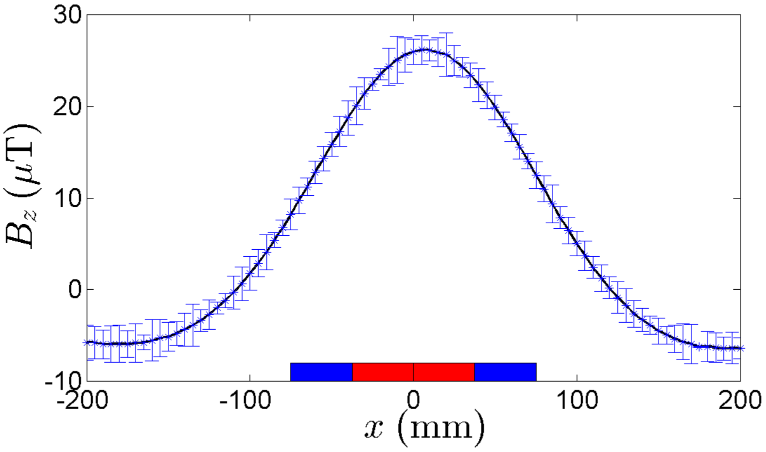

(b) Plot showing the B_z component of the magnetic field strength from two AlNiCo magnets, each with a length of 75 mm, arranged SN-NS centred at $x = 0$ mm at a height from the top of the magnets of $z = 200$ mm. The magnets' positions in the x direction are shown by coloured rectangles, with blue representing the south pole and red representing the north pole.

Figure 6.7: Plot showing the B_x and B_z components of the magnetic field strength in a and b respectively from two AlNiCo magnets, each with a length of 75 mm, arranged SN-NS centred at $x = 0$ mm at a height from the top of the magnets of $z = 200$ mm. In each the magnets' positions in the x direction are shown by coloured rectangles, with blue representing the south pole and red representing the north pole.

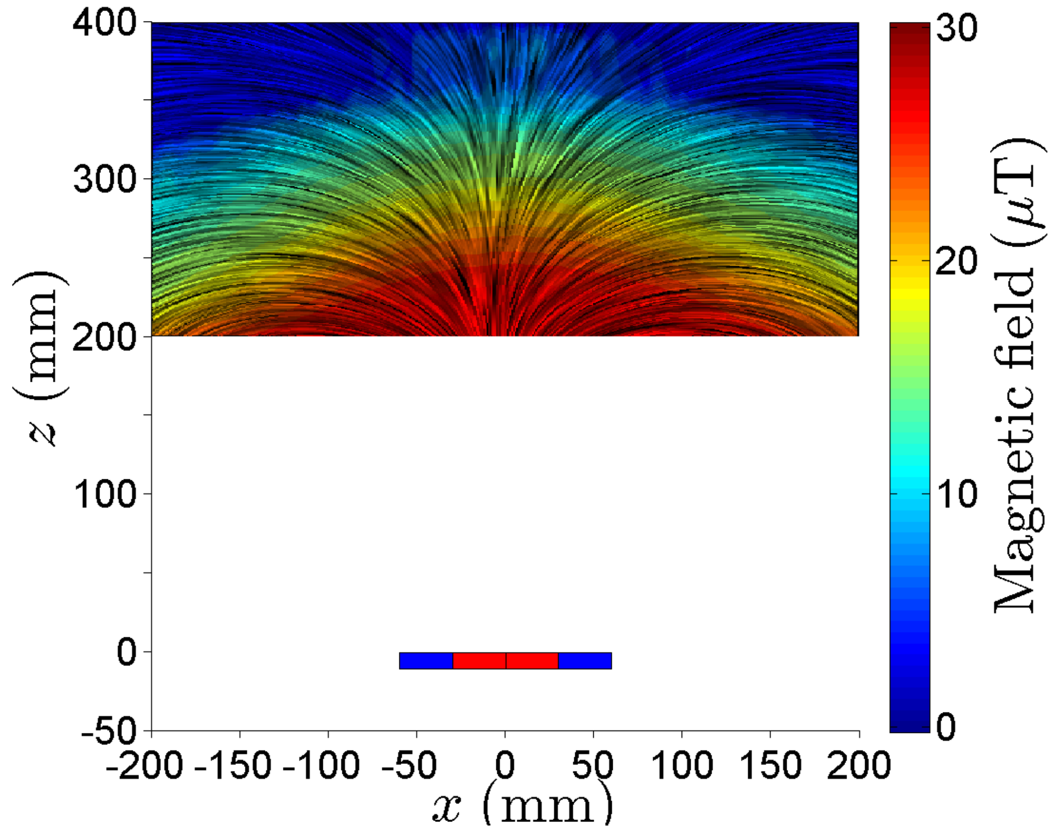

Figure 6.8: Linear integral convolution texture showing the magnetic field from two AlNiCo magnets arranged SN-NS centred at $x = 0$ mm for heights from the top of the magnet $z = 200$ - 400 mm. No data is shown for $z < 200$ mm as the magnet strength saturated the magnetometer below this level. The magnets' positions are shown by coloured rectangles, with blue representing the south pole and red representing the north pole.

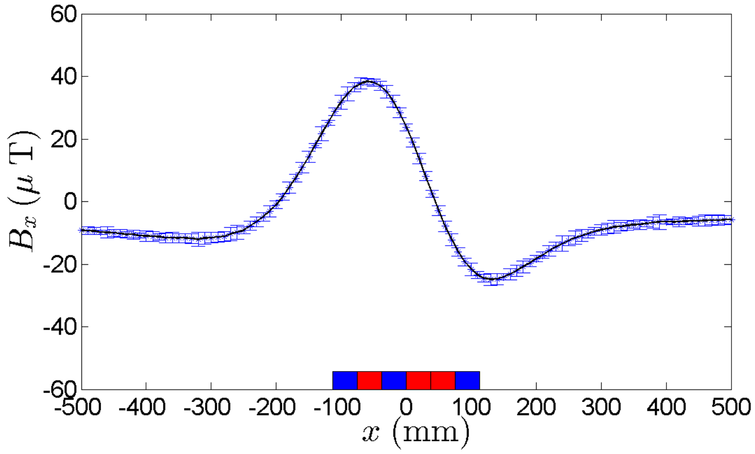

(a) Plot showing the B_x component of the magnetic field strength from three AlNiCo magnets, each with a length of 75 mm, arranged SN-SN-NS centred at $x = 0$ mm at a height from the top of the magnets of $z = 200$ mm. The magnets' positions in the x direction are shown by coloured rectangles, with blue representing the south pole and red representing the north pole.

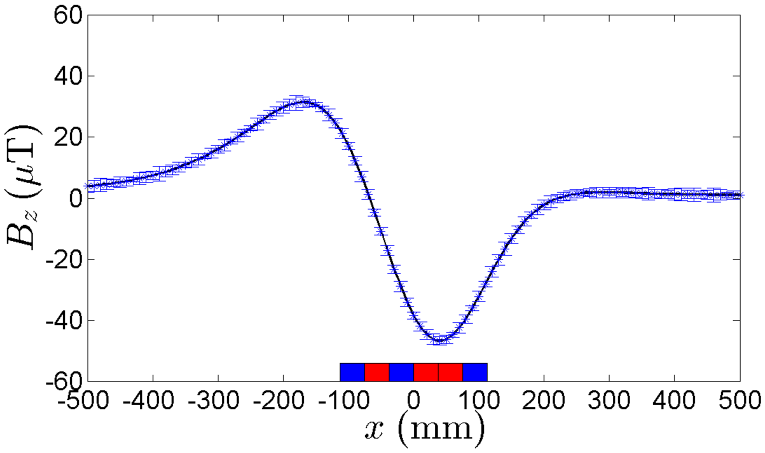

(b) Plot showing the B_z component of the magnetic field strength from three AlNiCo magnets, each with a length of 75 mm, arranged SN-SN-NS centred at $x = 0$ mm at a height from the top of the magnets of $z = 200$ mm. The magnets' positions in the x direction are shown by coloured rectangles, with blue representing the south pole and red representing the north pole.

Figure 6.9: Plot showing the B_x and B_z components of the magnetic field strength in a and b respectively from three AlNiCo magnets, each with a length of 75 mm, arranged SN-SN-NS centred at $x = 0$ mm at a height from the top of the magnets of $z = 200$ mm. In each the magnets' positions in the x direction are shown by coloured rectangles, with blue representing the south pole and red representing the north pole.

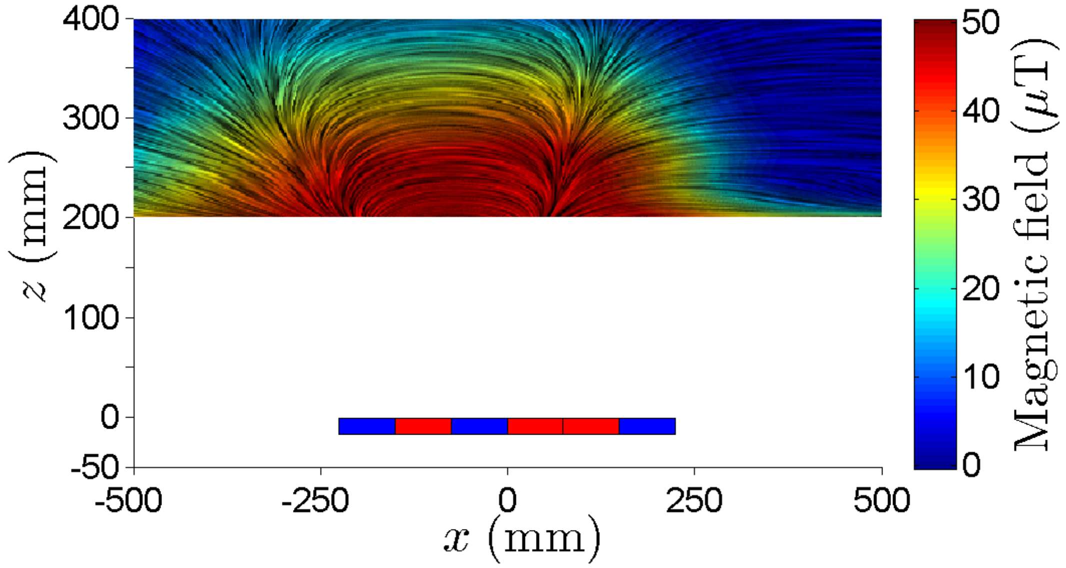

Figure 6.10: Linear integral convolution texture showing the magnetic field from three AlNiCo magnets arranged SN-SN-NS centred at $x = 0$ mm for heights from the top of the magnets $z = 200$ - 400 mm. No data is shown for $z < 200$ mm as the magnet strength saturated the magnetometer below this level. The magnets' positions are shown by coloured rectangles, with blue representing the south pole and red representing the north pole.

6.3.3 AlNiCo magnet dipole analysis

The peaks and zero-crossings in the magnetic field strength in the B_x and B_z components for the four AlNiCo magnet alignment cases given in subsection 6.3.2, SN, SN-SN, SN-NN and SN-SN-NS, in the x direction for each z position in the results were located and plotted. The locations of the peaks and zero-crossings were taken by polynomial interpolation between three data points either side of the feature to give a more accurate position when these fell between two data points. These are shown in figure 6.11 for the single magnet SN case, in figure 6.12 for the two magnet SN-SN case, in figure 6.13 for the two magnet SN-NS case and in figure 6.14 for the three magnet SN-SN-NS case.

The single magnet case shown in figure 6.11 shows that the peak in B_x and zero-crossing in B_z extrapolate to the centre of the magnet, while the peaks in B_z extrapolate back to the ends of the magnet, in this case there are no zero-crossings in B_x. The features pointing back to the centre of the magnet appear at approximately the same x position in all heights, this means that projecting directly down from the detected feature will give an accurate position for the centre of the magnet. The features for the edges of the magnet are further offset as the distance from the magnet increases. This means that projecting directly down from these detected features in the magnetic field strength will give an error in the position of the ends of the magnet.

In the case where two magnets are arranged SN-SN, shown in figure 6.12, the peaks in B_x and the zero-crossings in B_z extrapolate back to the centre of the two magnets as in the single magnet case. The zero-crossings in B_x and peaks in B_z extrapolate to the joint between the magnets, this is also as in the single magnet case. The features that point to the joint between the magnets have approximately the same x position and so the projection directly down from these features would correctly position the feature. The features that project back to the centre of the magnets however have higher deflections in the x direction with increasing distance from the magnets, this will cause increasing error in the position of the magnets if projected directly downwards from the detected feature. For accurate positioning of the feature multiple points at multiple heights must be found and projected back.

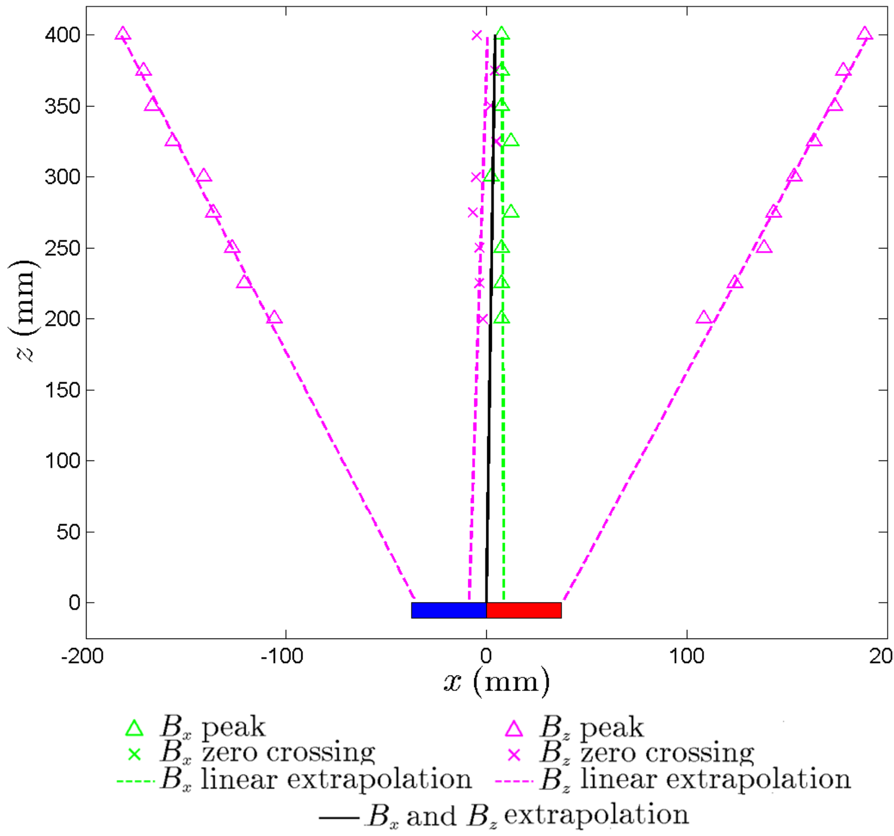

Figure 6.11: Plot showing the positions of the peaks and zero-crossings in the B_x and B_z components of magnetic field strength for an AlNiCo magnet centred at $x = 0$ mm, aligned in the SN direction in the positive x direction for heights from the magnet of $z = 200$ - 400 mm. With linear extrapolations plotted back to the position on the magnet for the peaks, zero-crossings and average of both. The magnet is represented in position by coloured rectangles with the south pole represented in blue and the north pole represented in red.

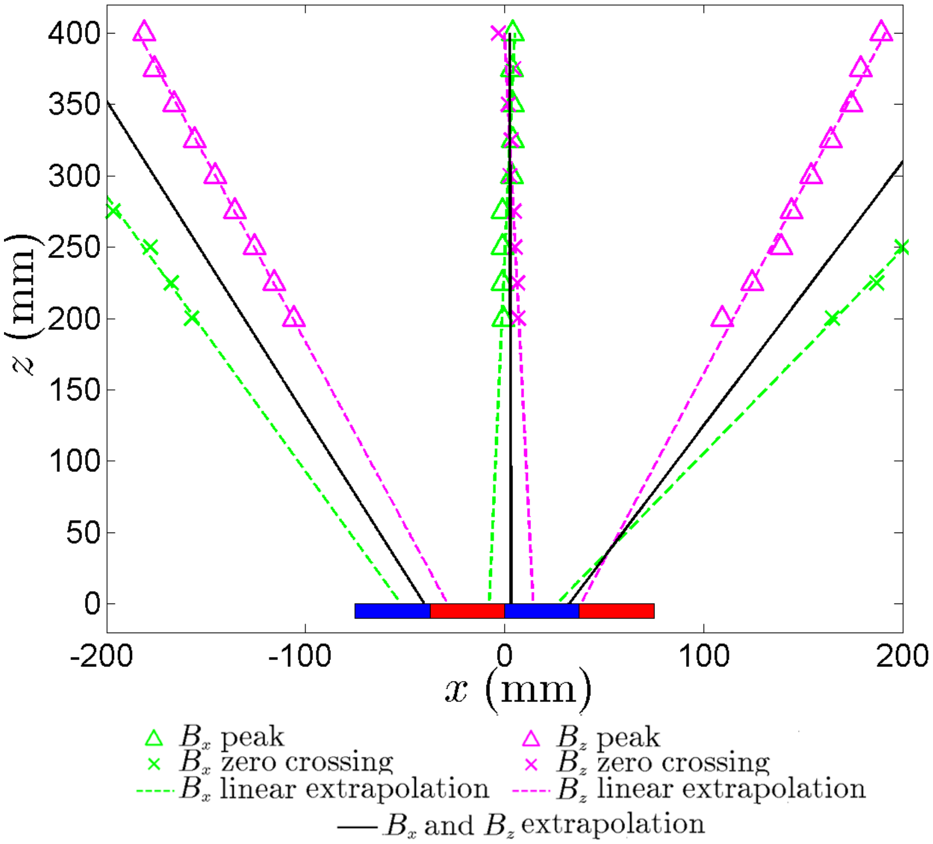

Figure 6.12: Plot showing the positions of the peaks and zero-crossings in the x and z components of magnetic field strength for two AlNiCo magnets centred at $x = 0$ mm, aligned in the SN-SN direction in the positive x direction for heights from the magnets of $z = 200$ - 400 mm. With linear extrapolations plotted back to the position on the magnets for the peaks, zero-crossings and average of both. The magnets are represented in position by coloured rectangles with the south pole represented in blue and the north pole represented in red.

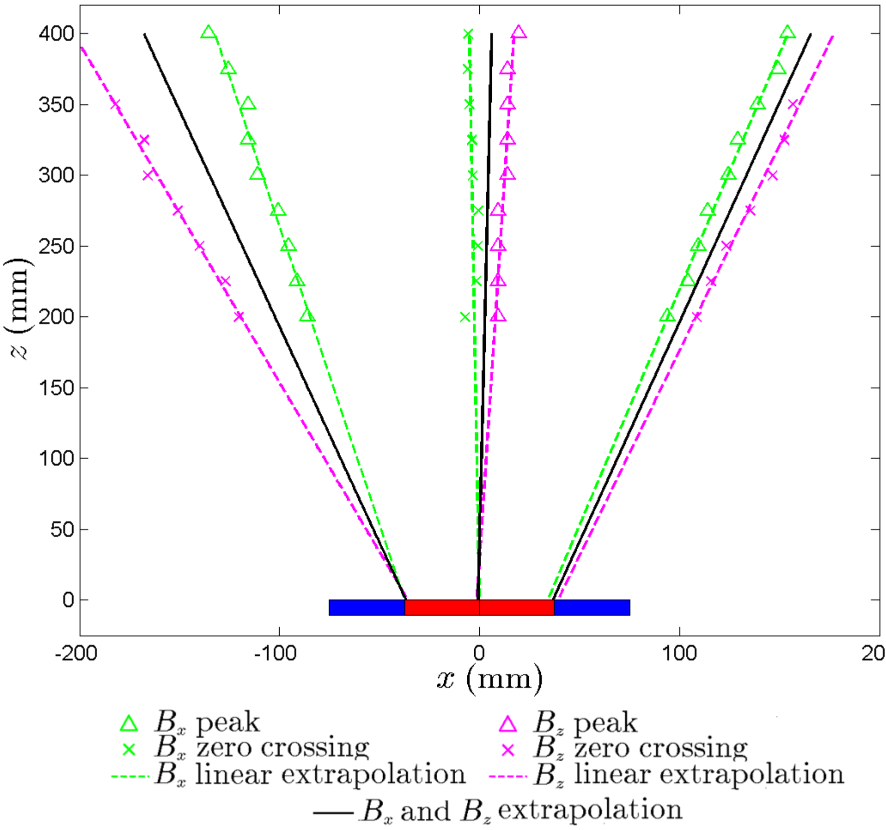

Figure 6.13: Plot showing the positions of the peaks and zero-crossings in the B_x and B_z components of magnetic field strength for two AlNiCo magnets centred at $x = 0$ mm, aligned in the SN-NS direction in the positive x direction for heights from the magnets of $z = 200$ - 400 mm. With linear extrapolations plotted back to the position on the magnets for the peaks, zero-crossings and average of both. The magnets are represented in position by coloured rectangles with the south pole represented in blue and the north pole represented in red.

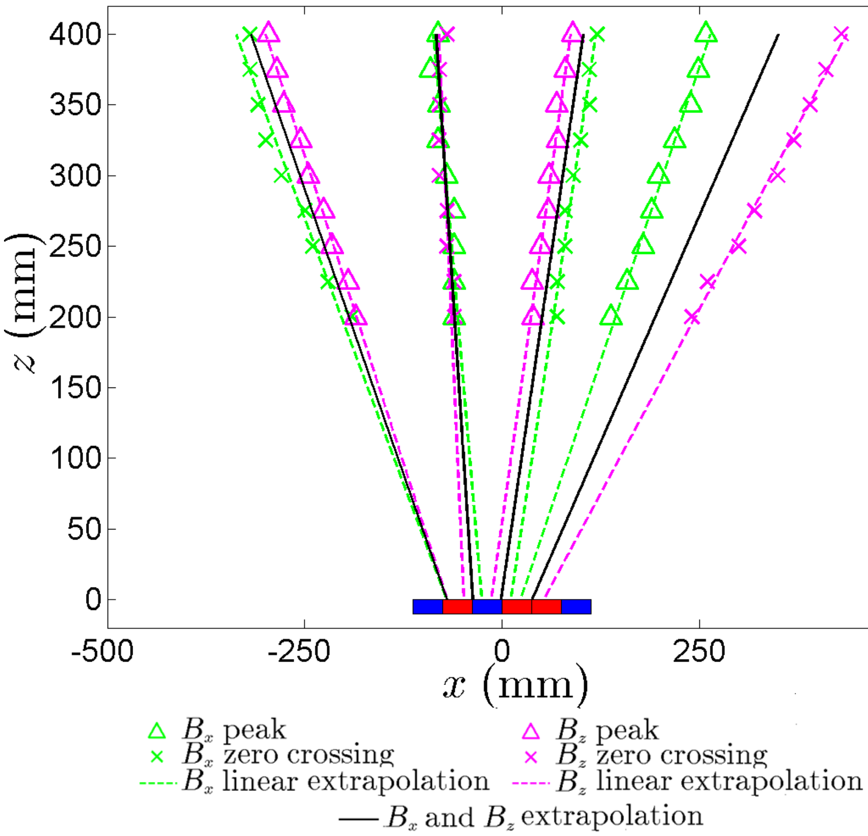

Figure 6.14: Plot showing the positions of the peaks and zero-crossings in the B_x and B_z components of magnetic field strength for three AlNiCo magnets centred at $x = 0$ mm, aligned in the SN-SN-NS direction in the positive x direction for heights from the magnets of $z = 200$ - 400 mm. With linear extrapolations plotted back to the position on the magnets for the peaks, zero-crossings and average of both. The magnets are represented in position by coloured rectangles with the south pole represented in blue and the north pole represented in red.

In the two magnet case arranged SN-NS, shown in figure 6.13, the zero-crossings in B_x and peaks in B_z extrapolate back to the joint between the magnets. This is the opposite of the case where the magnets are aligned as in SN-SN. The peaks in B_x and zero-crossings in B_z extrapolate to the centres of the magnets, this is also the opposite to the SN-SN case. The points that project back to the joints between the magnets have approximately the same x position for each height above the magnets and so projecting downwards from these features will give an accurate position of the magnets. The points that project to the centre of the magnets however have a greater deflection from the centre position with increasing height above the magnets. Projecting directly downwards from these features would give an error in the position of the magnets, taking multiple heights and projecting between them would be required to accurately project back to the centre of the magnets.

In the three magnet case, arranged SN-SN-NS, shown in figure 6.14 the peaks in the B_x and zero-crossings in B_z extrapolate back to the joints between the magnets. In this case the feature in the magnetic field strength is the same for both a N-S joint and a N-N joint. This is different from the S-N and N-N joints in the two magnet cases which have their peaks and zero-crossings in the opposite component to each other, this suggests that in the case with multiple joints the joints will be detectable with the same features. The zero-crossings in the B_x and the peaks in the B_z extrapolate back to the centres of two of the magnets, this is the same as in the SN-SN case.

The average angle of the deflection of the extrapolation from normal to the magnets for the four cases presented in this section is 16° with a maximum angle of 32° .

6.4 Short length magnetised steel conduit

6.4.1 Experimental basis

In the AlNiCo magnet cases, solid cuboid permanent magnets were used to simulate pipe section dipoles. To use the correct geometry in simulating the pipe section dipoles hollow steel cylinders were used, these were short sections of steel conduit 250 mm in length.

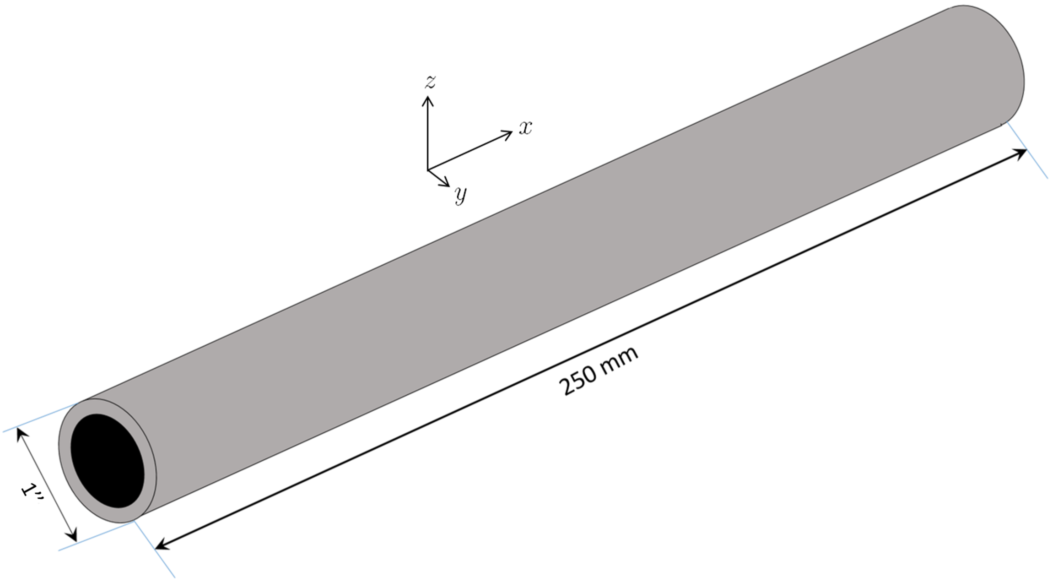

Figure 6.15: Diagram showing the axes and dimensions of the conduit used for the experiments on magnetised conduit sections. The conduits used have a length of 250 mm and diameter of 1″ and were magnetised using one of the AlNiCo magnets used in section 6.3.2.

6.4.1.1 Magnetisation of a steel rod

To assess the magnetisation method for the magnetisation of the conduit sections a steel rod was scanned, then magnetised with an AlNiCo magnet, the type used in section 6.3 and scanned between each magnetisation.

The magnetisation was induced in the rod by placing the north pole of the AlNiCo magnet against one end of the rod and pulling it along the outside surface of the rod at a constant speed until it passed the other end of the rod. Subsequent magnetisations were repeated pushing the magnet in the same direction along the rod at approximately the same speed. A magnetic scan was completed after each pass with the magnet, the resulting B_x and B_z component of magnetic field strength from each scan, including the initial state of the rod, are shown in figure 6.16.

The results from the magnetisation of the rod show that the initial magnetisation of the rod is removed by the first stroke with the magnet. These also show that the change in the magnetisation produced by the first stroke is the largest, with subsequent strokes reinforcing the magnetisation from the first stroke tending towards a saturation value. This indicated that a single stroke with a magnet on the conduit will be sufficient to induce a dipole in the conduit that ignores the initial conditions of the conduit.

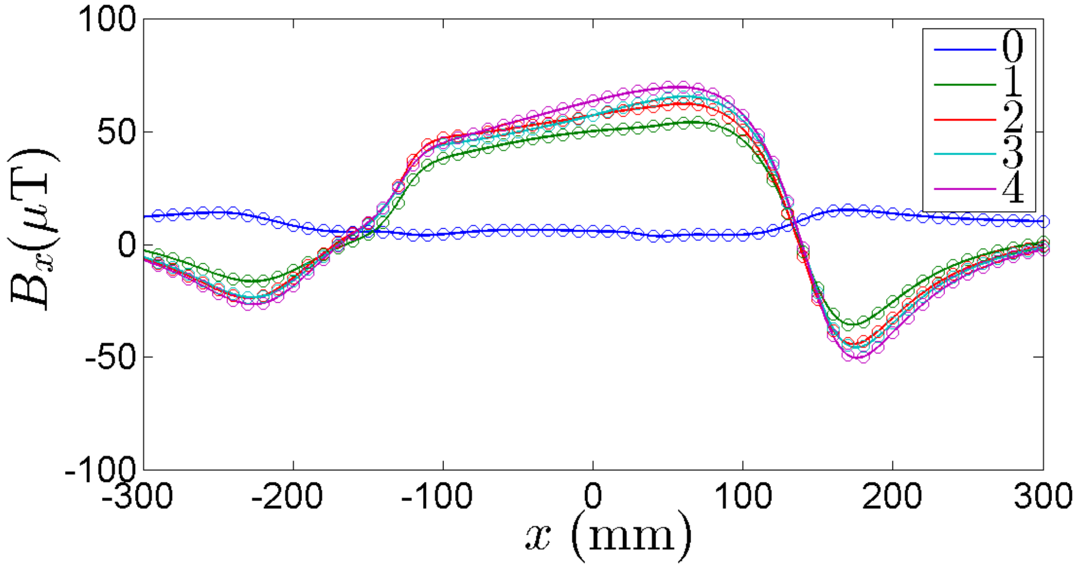

(a) Plot showing the B_x component of the magnetic field strength from the steel rod after strokes with an AlNiCo magnet at a height above the rod of $z = 200$ mm. The legend shows the cumulative number of strokes with the magnet before each scan.

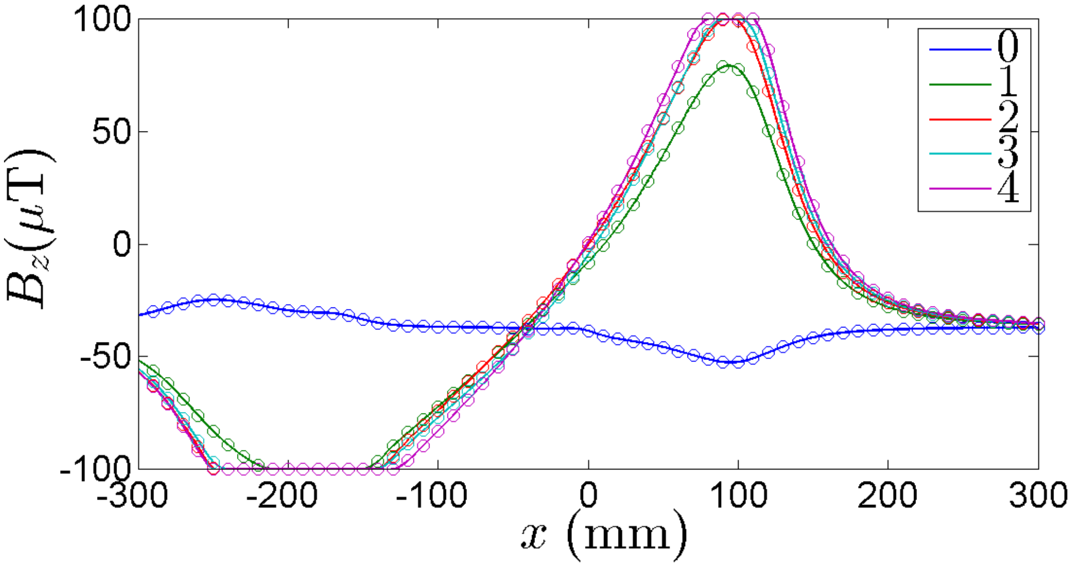

(b) Plot showing the B_z component of the magnetic field strength from the steel rod after strokes with an AlNiCo magnet at a height above the rod of $z = 200$ mm. The legend shows the cumulative number of strokes with the magnet before each scan.

Figure 6.16: Plots showing the B_x and B_z components of the magnetic field strength in subfigure a and b respectively from the steel rod after strokes with an AlNiCo magnet at a height above the rod of $z = 200$ mm. The legend shows the cumulative number of strokes with the magnet before each scan.

6.4.2 Steel conduit dipole results

6.4.2.1 Individual magnetised steel conduit results

The three magnetised conduits were scanned to find the magnetic field strength for each conduit section after magnetisation. These were designated conduit 1, 2 and 3 arbitrarily in the order they were scanned in order to identify which are used in the different configurations investigated in subsection 6.4.2.2.

Linear integral convolution textures representing the magnetic vector field shape and magnitude for each conduit section were also produced for the xz plane above the centreline of the conduit aligned above the seam weld. These are shown for conduit 1 in figure 6.18, for conduit 2 in figure 6.20 and for conduit 3 in figure 6.22.

The x and z components of the magnetic field strength are shown for each section at a height above the top of the conduit of $z = 50$ mm. These are shown for conduit 1 in figures 6.17 for the x and z components, for conduit 2 in figures 6.19 for the x and z components and for conduit 3 in figures 6.21 for the x and z components.

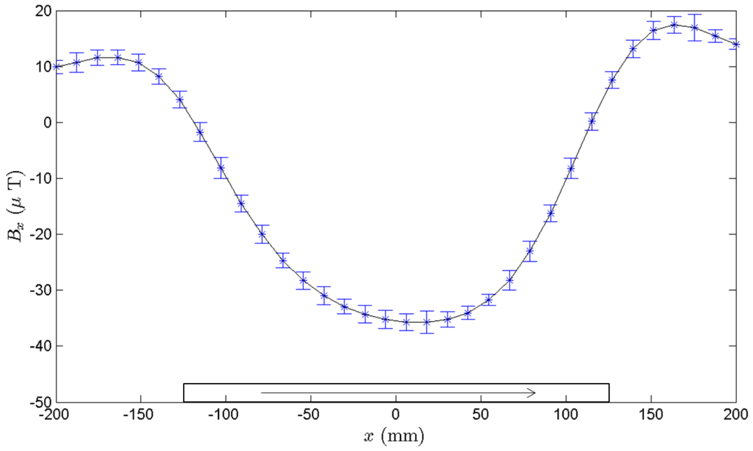

(a) Plot showing the B_x component of magnetic field strength from a 250 mm long, 1″ diameter magnetised conduit section (designated conduit 1) centred at $x = 0$ mm at a height $z = 50$ mm above the top of the conduit. The position of the conduit in the x direction is shown by the rectangle, with the arrow showing the direction of magnetisation of the conduit.

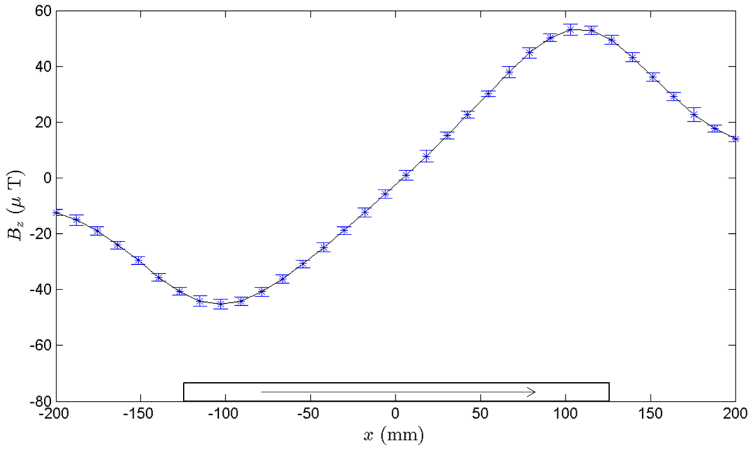

(b) Plot showing the B_z component of magnetic field strength from a 250 mm long, 1″ diameter magnetised conduit section (designated conduit 1) centred at $x = 0$ mm at a height $z = 50$ mm above the top of the conduit. The position of the conduit in the x direction is shown by the rectangle, with the arrow showing the direction of magnetisation of the conduit.

Figure 6.17: Plots showing the B_x and B_z components of magnetic field strength in a and b respectively from a 250 mm long, 1″ diameter magnetised conduit section (designated conduit 1) centred at $x = 0$ mm at a height $z = 50$ mm above the top of the conduit. The position of the conduit in the x direction is shown by the rectangle, with the arrow showing the direction of magnetisation of the conduit.

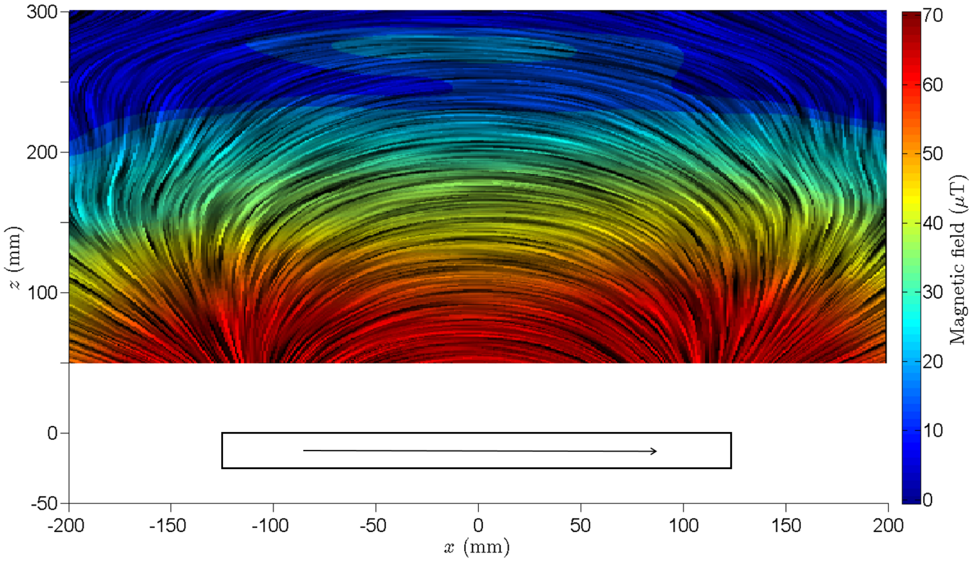

Figure 6.18: Linear integral convolution texture showing the magnetic field from a 250 mm long, 1″ magnetised conduit (designated conduit 1) centred at $x = 0$ mm for heights from the top of the conduit $z = 50$ - 300 mm. The position of the conduit is shown by a rectangle, with an arrow showing the direction of the magnetisation.

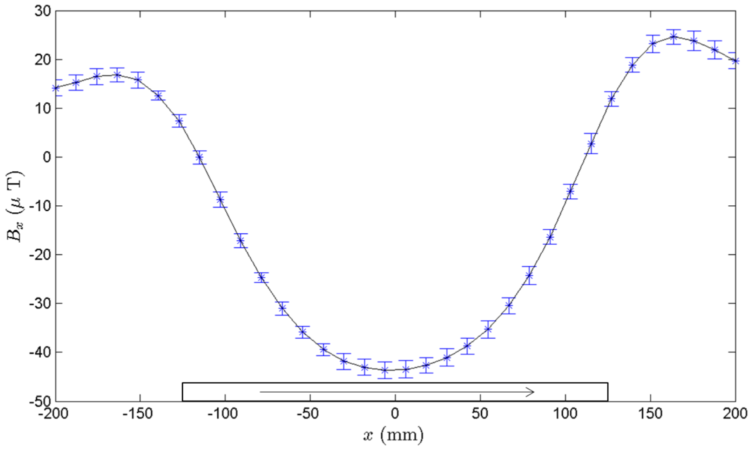

(a) Plot showing the B_x component of magnetic field strength from a 250 mm long, 1″ diameter magnetised conduit section (designated conduit 2) centred at $x = 0$ mm at a height $z = 50$ mm above the top of the conduit. The position of the conduit in the x direction is shown by the rectangle, with the arrow showing the direction of magnetisation of the conduit.

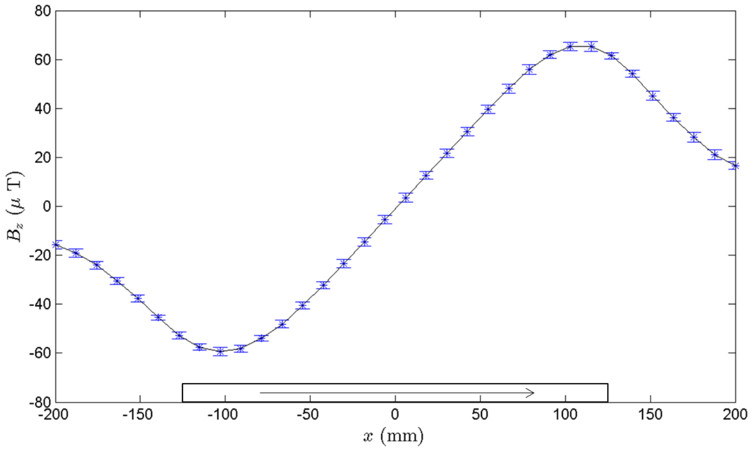

(b) Plot showing the B_z component of magnetic field strength from a 250 mm long, 1″ diameter magnetised conduit section (designated conduit 2) centred at $x = 0$ mm at a height $z = 50$ mm above the top of the conduit. The position of the conduit in the x direction is shown by the rectangle, with the arrow showing the direction of magnetisation of the conduit.

Figure 6.19: Plots showing the B_x and B_z components of magnetic field strength in a and b respectively from a 250 mm long, 1″ diameter magnetised conduit section (designated conduit 2) centred at $x = 0$ mm at a height $z = 50$ mm above the top of the conduit. The position of the conduit in the x direction is shown by the rectangle, with the arrow showing the direction of magnetisation of the conduit.

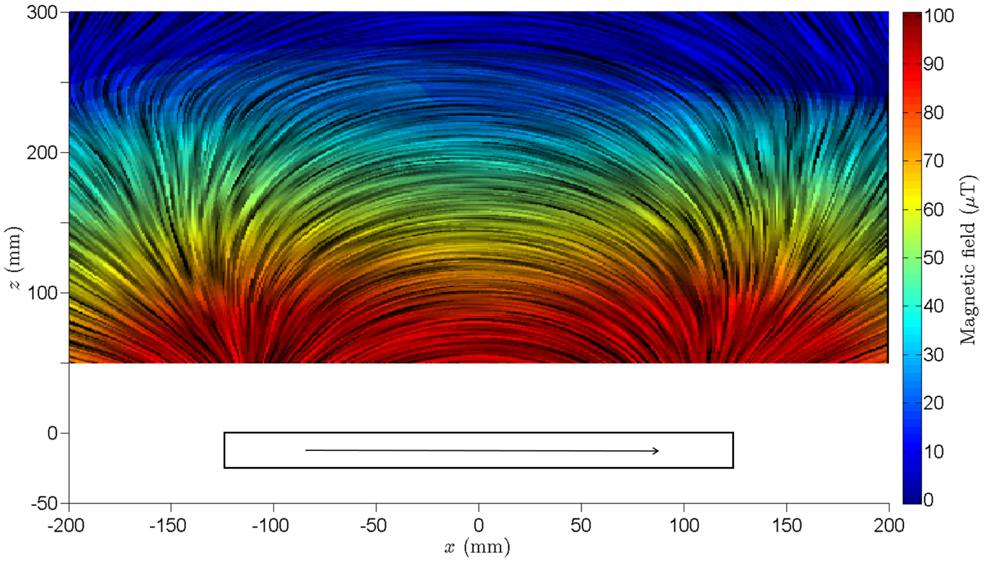

Figure 6.20: Linear integral convolution texture showing the magnetic field from a 250 mm long, 1″ magnetised conduit (designated conduit 2) centred at $x = 0$ mm for heights from the top of the conduit $z = 50$ - 300 mm. The position of the conduit is shown by a rectangle, with an arrow showing the direction of the magnetisation.

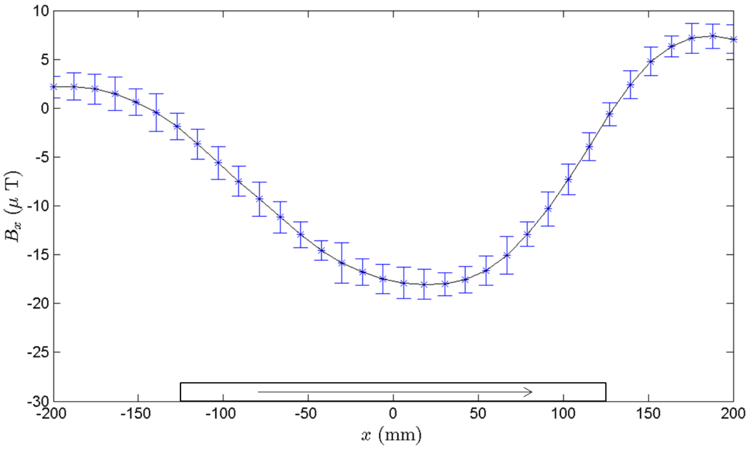

(a) Plot showing the B_x component of magnetic field strength from a 250 mm long, 1″ diameter magnetised conduit section (designated conduit 3) centred at $x = 0$ mm at a height $z = 50$ mm above the top of the conduit. The position of the conduit in the x direction is shown by the rectangle, with the arrow showing the direction of magnetisation of the conduit.

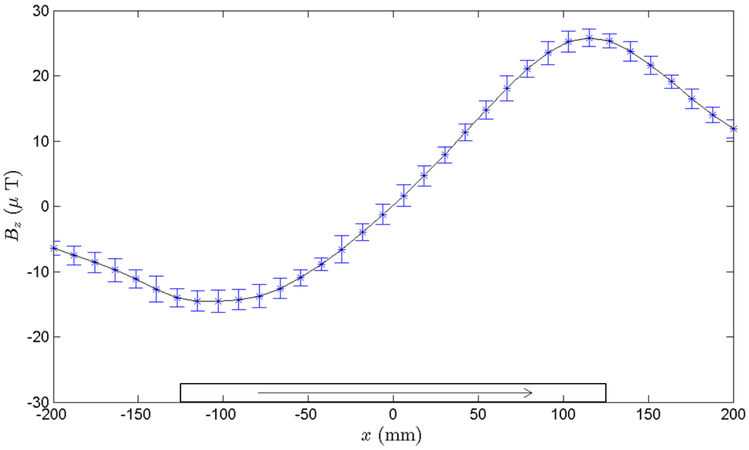

(b) Plot showing the B_z component of magnetic field strength from a 250 mm long, 1″ diameter magnetised conduit section (designated conduit 3) centred at $x = 0$ mm at a height $z = 50$ mm above the top of the conduit. The position of the conduit in the x direction is shown by the rectangle, with the arrow showing the direction of magnetisation of the conduit.

Figure 6.21: Plots showing the B_x and B_z components of magnetic field strength in a and b respectively from a 250 mm long, 1″ diameter magnetised conduit section (designated conduit 3) centred at $x = 0$ mm at a height $z = 50$ mm above the top of the conduit. The position of the conduit in the x direction is shown by the rectangle, with the arrow showing the direction of magnetisation of the conduit.

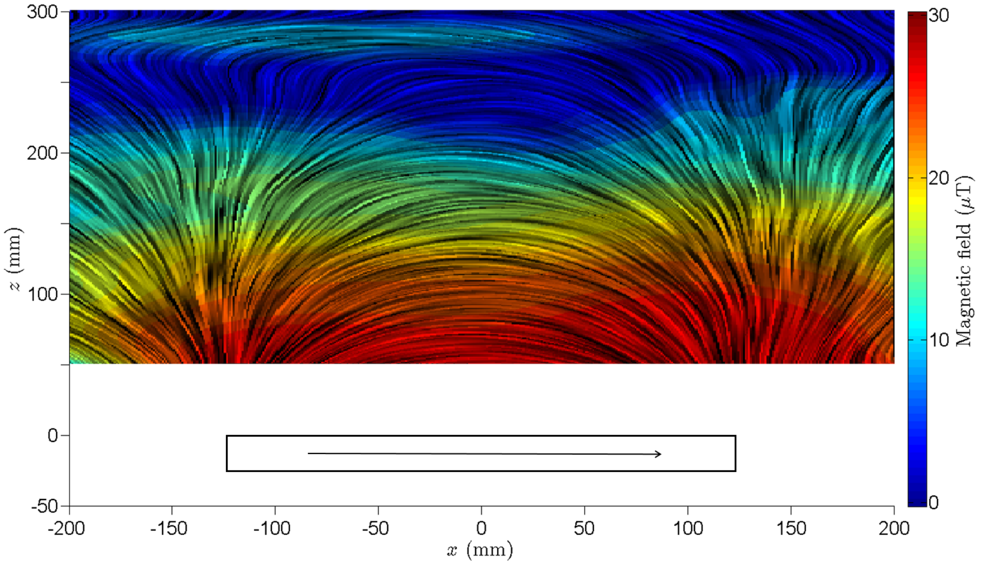

Figure 6.22: Linear integral convolution texture showing the magnetic field from a 250 mm long, 1″ magnetised conduit (designated conduit 3) centred at $x = 0$ mm for heights from the top of the conduit $z = 50$ - 300 mm. The position of the conduit is shown by a rectangle, with an arrow showing the direction of the magnetisation.

6.4.2.2 Multiple magnetised steel conduit configurations results

Using the three conduits scanned in subsection 6.4.2.1 in different configurations allows the investigation of different arrangements of dipoles as in the AlNiCo magnet case in section 6.3.2. This allows measurements to be gathered closer to the surface of the conduit with the magnetometer without saturating it due to the lower levels of magnetisation induced in the conduits.

The configurations presented below are two conduits with aligned directions of magnetisation, two conduits with opposite directions of magnetisation, three conduits all with aligned directions of magnetisation and three conduits with the end conduit being aligned opposite to the other two conduits' direction of magnetisation.

Figure 6.23 show the B_x and B_z components of magnetic field strength for a height above the surface of the conduit of $z = 50$ mm, for conduits 1 and 2 arranged with their direction of magnetisation both pointing in the positive x direction. Figure 6.26 shows the LIC texture representing the magnetic vector field and magnitude for this case for heights above the conduits of $z = 50 - 300$ mm.

Figure 6.25 show the B_x and B_z components of magnetic field strength for a height above the surface of the conduit of $z = 50$ mm, for conduits 1 arranged with its direction of magnetisation both pointing in the positive x direction and conduit 2 arranged with its direction of magnetisation pointing in the negative x direction. Figure 6.24 shows the LIC texture representing the magnetic vector field and magnitude for this case for heights above the conduits of $z = 50 - 300$ mm.

Figure 6.27 show the B_x and B_z components of magnetic field strength for a height above the surface of the conduit of $z = 50$ mm, for conduits 1, 2 and 3 arranged with their direction of magnetisation all three pointing in the positive x direction. Figure 6.28 shows the LIC texture representing the magnetic vector field and magnitude for this case for heights above the conduit of $z = 50 - 300$ mm.

Figure 6.29 show the B_x and B_z components of magnetic field strength for a height above the surface of the conduit of $z = 50$ mm, for conduits 1, 2 and

3 arranged with conduit 1 and 2's direction of magnetisation both pointing in the positive x direction and conduit 3's direction of magnetisation pointing in the negative x direction. Figure 6.30 shows the LIC texture representing the magnetic vector field and magnitude for this case for heights above the conduit of $z = 50 - 300$ mm.

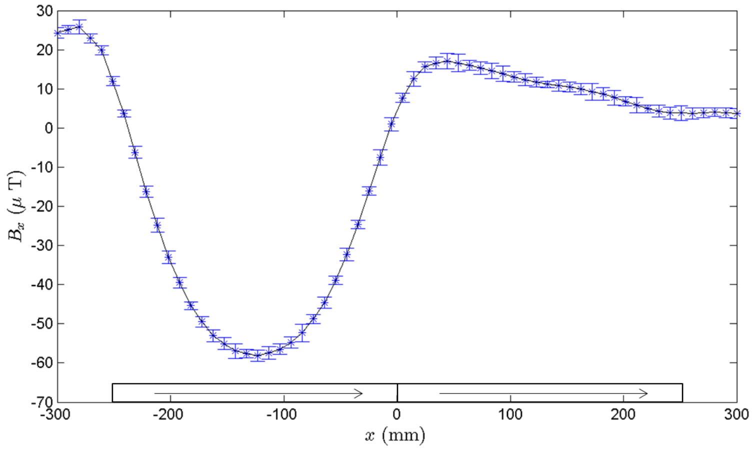

(a) Plot showing the B_x component of magnetic field strength from two 250 mm long, 1″ diameter magnetised conduit sections (conduit 1 and 2) centred at $x = 0$ mm at a height $z = 50$ mm above the top of the conduits with their magnetisation directions aligned. The positions of the conduits in the x direction are shown by the rectangles, with the arrows showing the direction of magnetisation of the conduits.

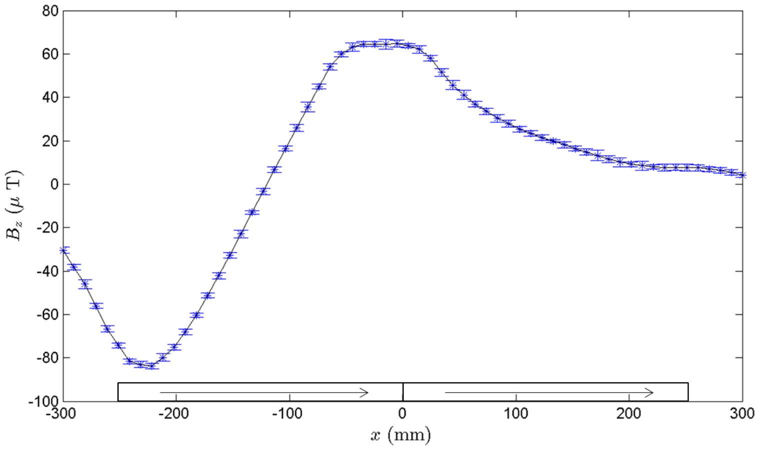

(b) Plot showing the B_z component of magnetic field strength from two 250 mm long, 1″ diameter magnetised conduit sections (conduit 1 and 2) centred at $x = 0$ mm at a height $z = 50$ mm above the top of the conduits with their magnetisation directions aligned. The positions of the conduits in the x direction are shown by the rectangles, with the arrows showing the direction of magnetisation of the conduits.

Figure 6.23: Plots showing the B_x and B_z components of magnetic field strength in a and b respectively from two 250 mm long, 1″ diameter magnetised conduit sections (conduit 1 and 2) centred at $x = 0$ mm at a height $z = 50$ mm above the top of the conduits with their magnetisation directions aligned. The positions of the conduit in the x direction are shown by the rectangles, with the arrows showing the direction of magnetisation of the conduits.

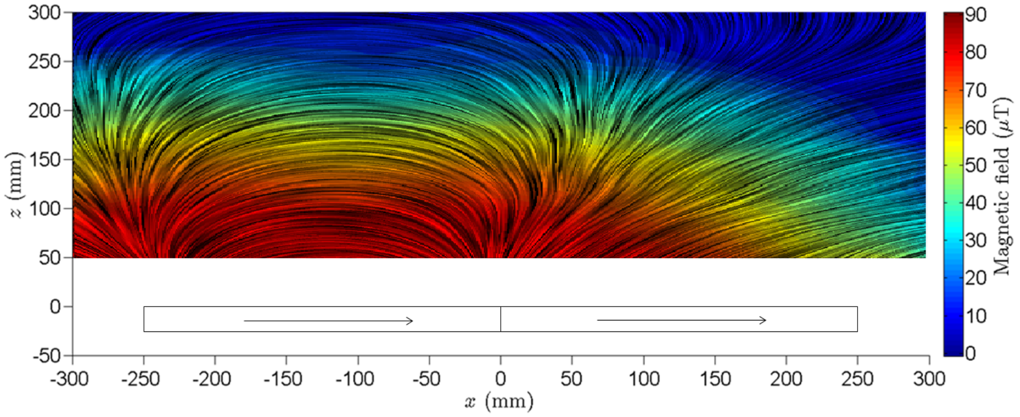

Figure 6.24: Linear integral convolution texture showing the magnetic field from two 250 mm long, 1″ magnetised conduits (conduits 1 and 2) centred at $x = 0$ mm for heights from the top of the conduits $z = 50 - 300$ mm with their magnetisation directions aligned. The positions of the conduits are shown by rectangles, with arrows showing the directions of the magnetisation.

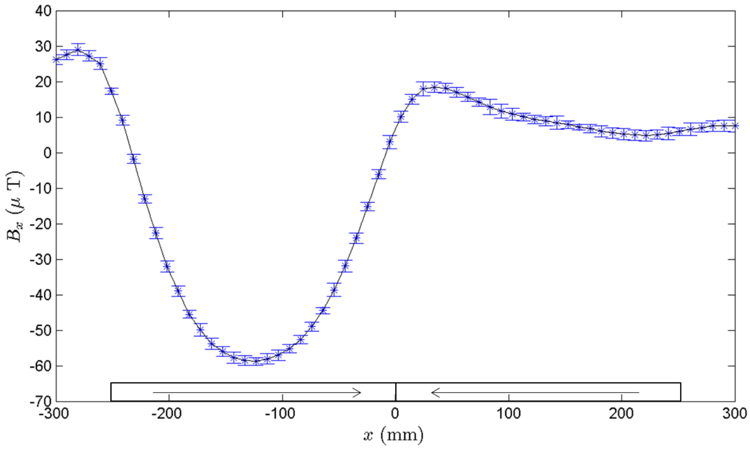

(a) Plot showing the B_x component of magnetic field strength from two 250 mm long, 1″ diameter magnetised conduit sections (conduit 1 and 2) centred at $x = 0$ mm at a height $z = 50$ mm above the top of the conduits with their magnetisation directions in opposition. The positions of the conduits in the x direction are shown by the rectangles, with the arrows showing the direction of magnetisation of the conduits.

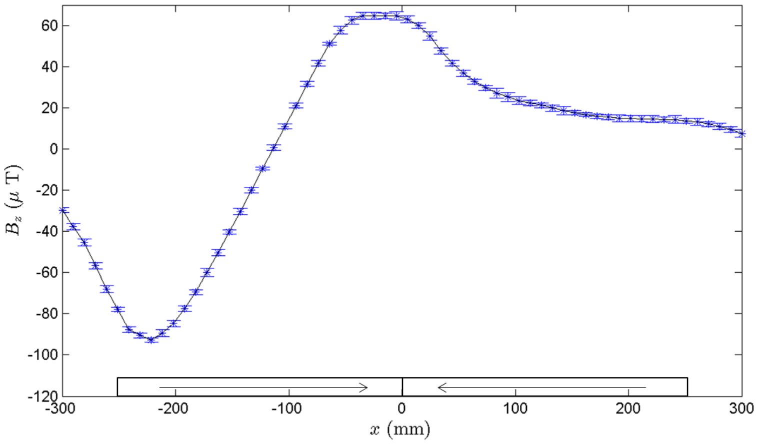

(b) Plot showing the B_z component of magnetic field strength from two 250 mm long, 1″ diameter magnetised conduit sections (conduit 1 and 2) centred at $x = 0$ mm at a height $z = 50$ mm above the top of the conduits with their magnetisation directions in opposition. The positions of the conduits in the x direction are shown by the rectangles, with the arrows showing the direction of magnetisation of the conduits.

Figure 6.25: Plots showing the B_x and B_z components of magnetic field strength in a and b respectively from two 250 mm long, 1″ diameter magnetised conduit sections (conduit 1 and 2) centred at $x = 0$ mm at a height $z = 50$ mm above the top of the conduits with their magnetisation directions in opposition. The positions of the conduits in the x direction are shown by the rectangles, with the arrows showing the direction of magnetisation of the conduits.

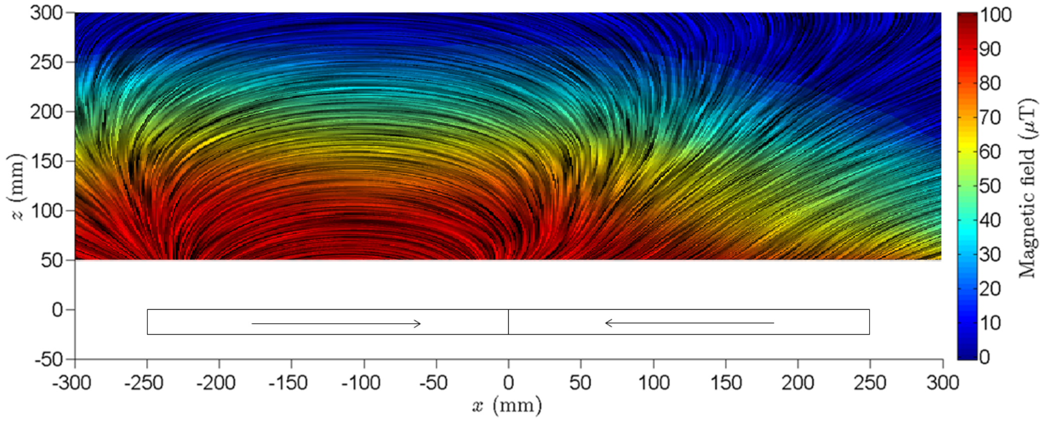

Figure 6.26: Linear integral convolution texture showing the magnetic field from two 250 mm long, 1″ magnetised conduits (conduits 1 and 2) centred at $x = 0$ mm for heights from the top of the conduits $z = 50 - 300$ mm with their magnetisation directions in opposition. The positions of the conduits are shown by rectangles, with arrows showing the directions of the magnetisation.

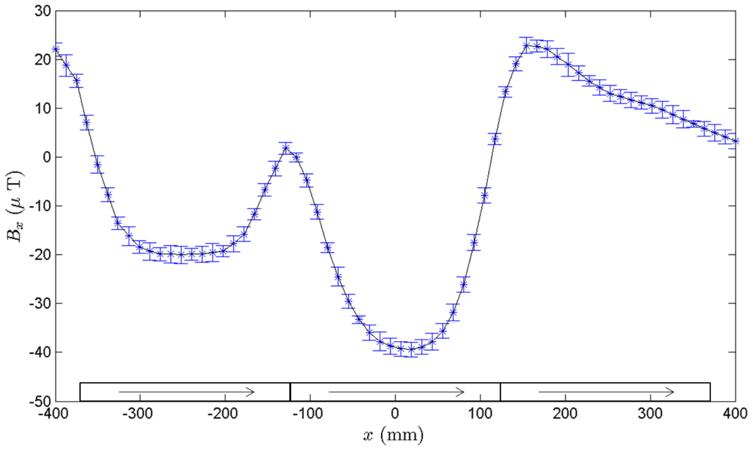

(a) Plot showing the B_x component of magnetic field strength from three 250 mm long, 1″ diameter magnetised conduit sections (conduit 1, 2 and 3) centred at $x = 0$ mm at a height $z = 50$ mm above the top of the conduits. The positions of the conduits in the x direction are shown by the rectangles, with the arrows showing the direction of magnetisation of the conduits.

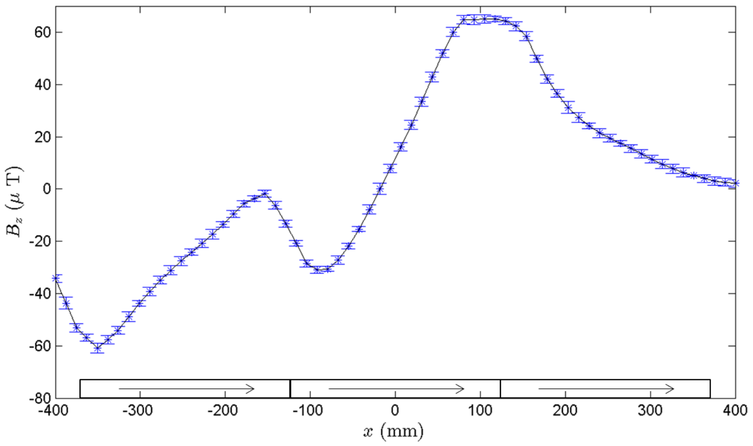

(b) Plot showing the B_z component of magnetic field strength from three 250 mm long, 1″ diameter magnetised conduit sections (conduit 1, 2 and 3) centred at $x = 0$ mm at a height $z = 50$ mm above the top of the conduits. The positions of the conduits in the x direction are shown by the rectangles, with the arrows showing the direction of magnetisation of the conduits

Figure 6.27: Plots showing the B_x and B_z components of magnetic field strength in a and b respectively from three 250 mm long, 1″ diameter magnetised conduit sections (conduit 1, 2 and 3) centred at $x = 0$ mm at a height $z = 50$ mm above the top of the conduits with their magnetisation directions in opposition. The positions of the conduits in the x direction are shown by the rectangles, with the arrows showing the direction of magnetisation of the conduits.

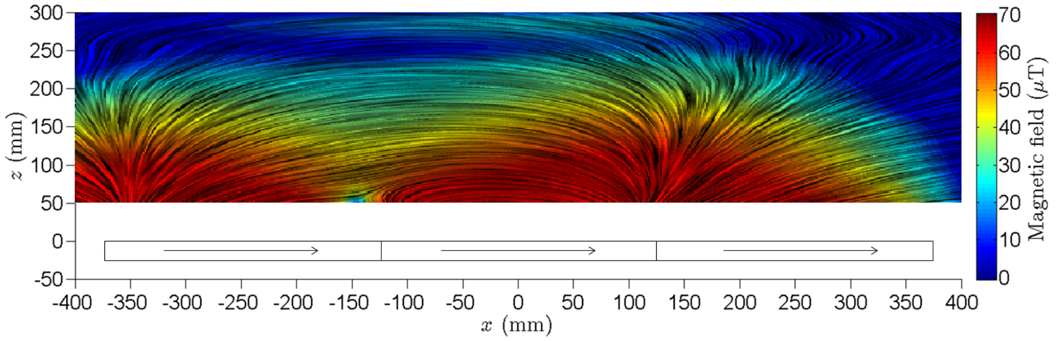

Figure 6.28: Linear integral convolution texture showing the magnetic field from three 250 mm long, 1″ magnetised conduits (conduits 1, 2 and 3) centred at $x = 0$ mm for heights from the top of the conduits $z = 50 - 300$ mm. The positions of the conduits are shown by rectangles with arrows showing the directions of the magnetisation.

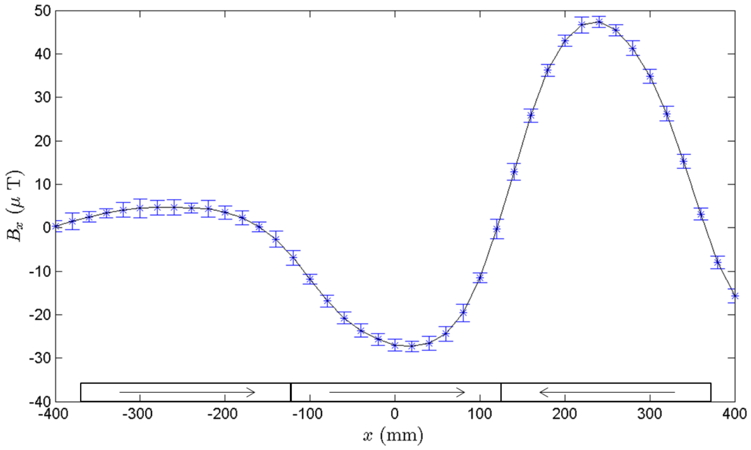

(a) Plot showing the B_x component of magnetic field strength from three 250 mm long, 1″ diameter magnetised conduit sections (conduit 1, 2 and 3) centred at $x = 0$ mm at a height $z = 50$ mm above the top of the conduits. The positions of the conduits in the x direction are shown by the rectangles, with the arrows showing the direction of magnetisation of the conduits.

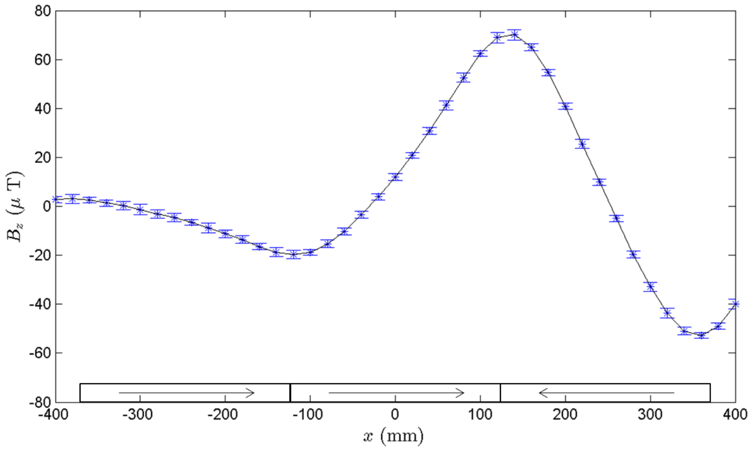

(b) Plot showing the B_z component of magnetic field strength from three 250 mm long, 1″ diameter magnetised conduit sections (conduit 1, 2 and 3) centred at $x = 0$ mm at a height $z = 50$ mm above the top of the conduits. The positions of the conduits in the x direction are shown by the rectangles, with the arrows showing the direction of magnetisation of the conduits

Figure 6.29: Plots showing the B_x and B_z components of magnetic field strength in a and b respectively from three 250 mm long, 1″ diameter magnetised conduit sections (conduit 1, 2 and 3) centred at $x = 0$ mm at a height $z = 50$ mm above the top of the conduits with their magnetisation directions in opposition. The positions of the conduits in the x direction are shown by the rectangles, with the arrows showing the direction of magnetisation of the conduits.

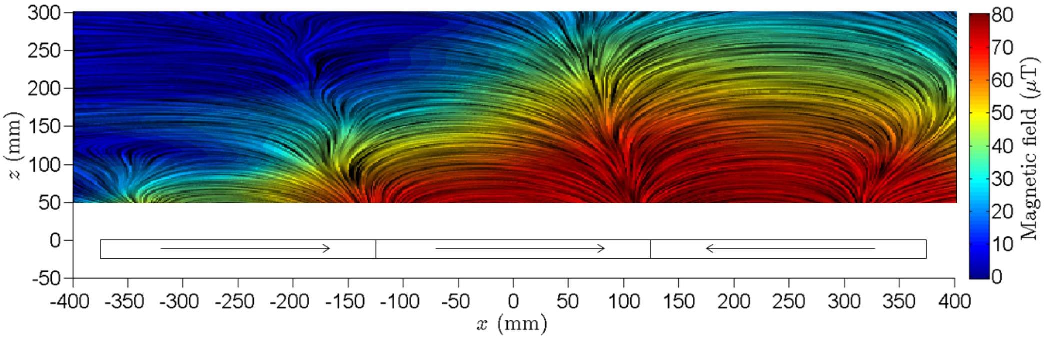

Figure 6.30: Linear integral convolution texture showing the magnetic field from three 250 mm long, 1″ magnetised conduits (conduits 1, 2 and 3) centred at $x = 0$ mm for heights from the top of the conduits $z = 50 - 300$ mm. The positions of the conduits are linear integral convolution shown by rectangles, with arrows showing the directions of the magnetisation.

6.4.3 Steel conduit dipole analysis

6.4.3.1 Individual magnetised steel conduit analysis

To analyse the magnetised conduit results, the locations of the peaks and zero-crossings in the x direction for each z for the B_x and B_z components of magnetic field strength were found. The locations of the peaks and zero-crossings were found by polynomial interpolation between three data points either side of the anomaly to give a more accurate position when these fell between two data points. These were plotted on a set of axes with a linear best fit plotted and extrapolated back to $z = 0$ mm, the surface of the conduit, for each. Each peak was paired with a zero-crossing in the other component of the magnetic field strength and a linear best fit plotted for these, this was also extrapolated to $z = 0$ mm, the surface of the conduit, for each.

The peak, zero-crossing and extrapolated lines for conduit 1, 2 and 3 are shown in figures 6.31, 6.32 and 6.33 respectively. These show that the peaks in the B_x and zero-crossings in B_z project back to the centre of the magnetised conduit section. This corresponds to the results in the AlNiCo magnet case shown in figure 6.11. For the zero-crossings in B_x and peaks in B_z these project approximately $25 - 50$ mm towards the centre from the ends of the magnetised conduit section. This differs from the AlNiCo magnet cases shown in figure 6.11 where these point to the ends of the magnets.

In the single conduit sections the anomalies in the magnetic field strength for the centre have approximately the same x position for the different heights whereas the anomalies in the magnetic field strength that project towards the edges of the conduit sections have increasing deflection with increasing height. This indicates that as in the magnet cases in section 6.4.3.1 projecting directly down from any detected anomalies in the magnetic field strength will give an error in the positions of the ends of the conduit sections. This further shows that anomalies must be detected at multiple heights in order to accurately project back to the features in the conduit sections.

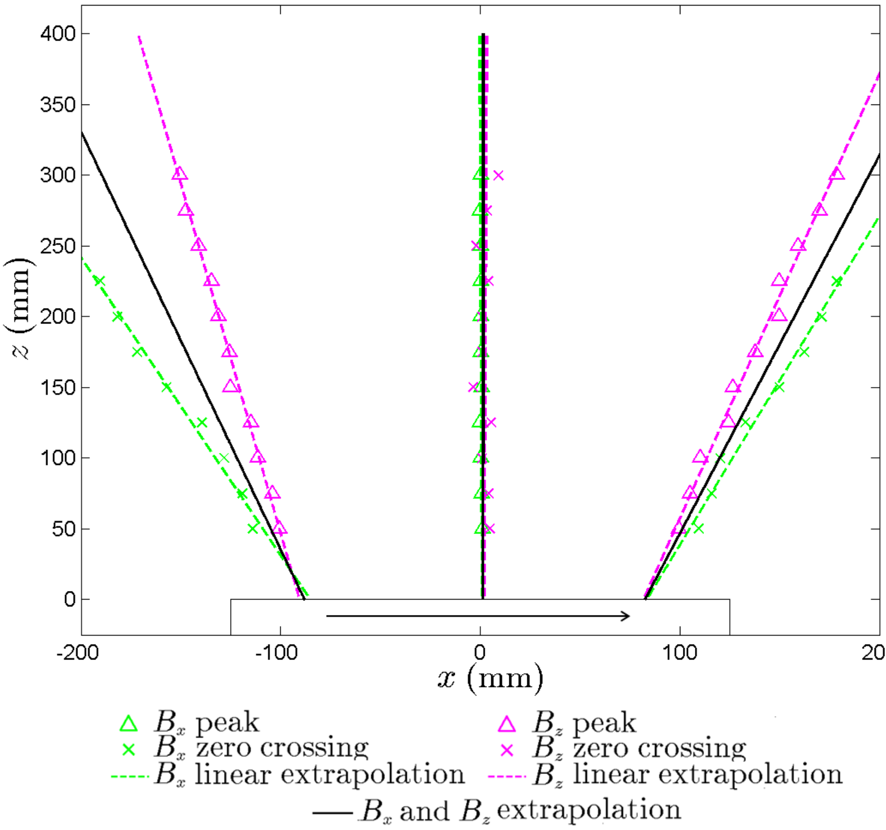

Figure 6.31: Plot showing the positions of the peaks and zero-crossings in the B_x and B_z components of magnetic field strength for a 250 mm long, 1 $''$ diameter magnetised conduit, designated conduit 1, centred at $x = 0$ mm for heights from the conduit of $z = 50 - 300$ mm. With linear extrapolations plotted back to the position on the conduit for the peaks, zero-crossings and average of both. The conduit is represented in position by a rectangle, with the arrow representing the magnetisation direction.

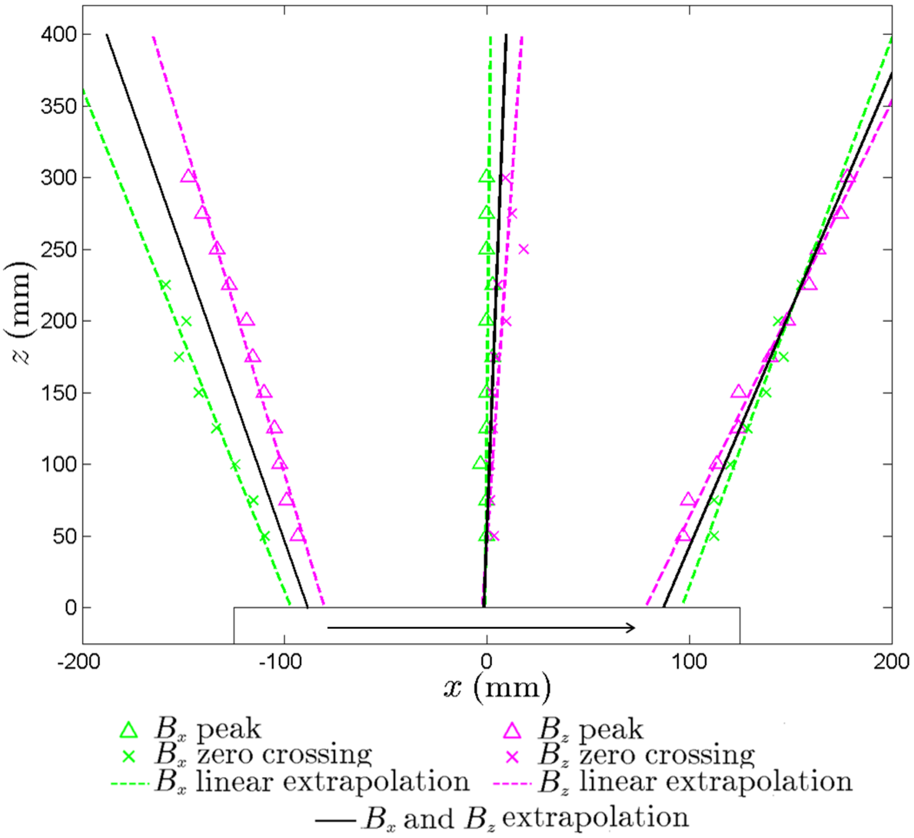

Figure 6.32: Plot showing the positions of the peaks and zero-crossings in the B_x and B_z components of magnetic field strength for a 250 mm long, 1 $''$ diameter magnetised conduit, designated conduit 2, centred at $x = 0$ mm for heights from the conduit of $z = 50 - 300$ mm. With linear extrapolations plotted back to the position on the conduit for the peaks, zero-crossings and average of both. The conduit is represented in position by a rectangle, with the arrow representing the magnetisation direction.

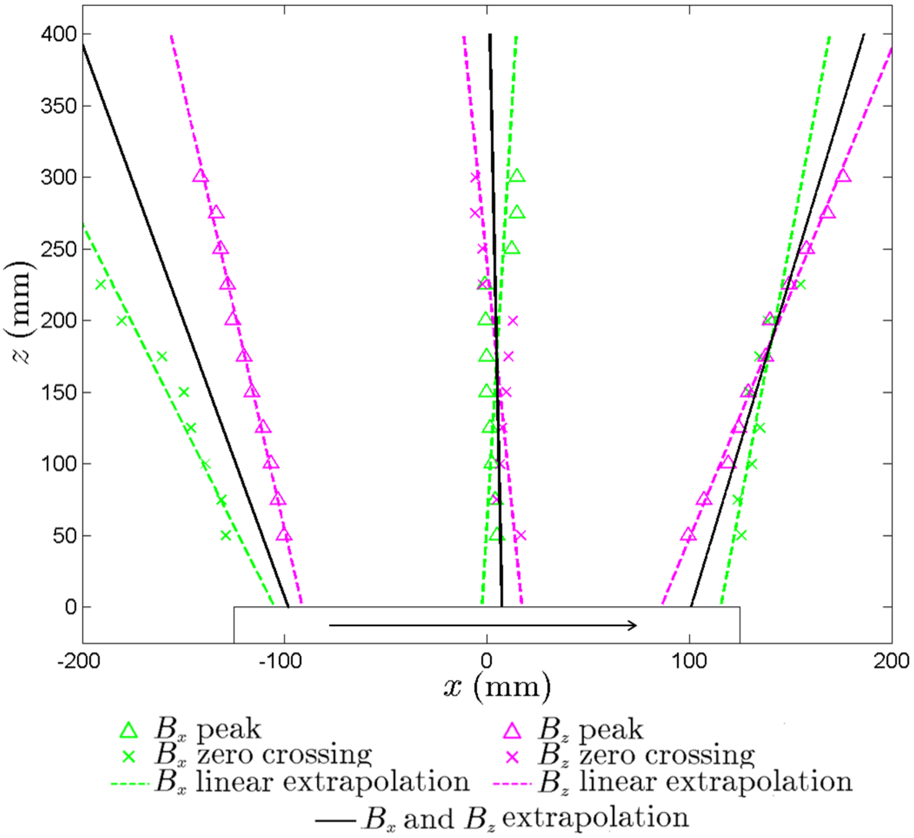

Figure 6.33: Plot showing the positions of the peaks and zero-crossings in the B_x and B_z components of magnetic field strength for a 250 mm long, 1 $''$ diameter magnetised conduit, designated conduit 3, centred at $x = 0$ mm for heights from the conduit of $z = 50 - 300$ mm. With linear extrapolations plotted back to the position on the conduit for the peaks, zero-crossings and average of both. The conduit is represented in position by a rectangle, with the arrow representing the magnetisation direction.

6.4.3.2 Multiple magnetised steel conduit configurations analysis

For the multiple conduit cases given in section 6.4.2.2 the locations in x of the peaks and zero-crossings in the magnetic field strength for each z measured were found and plotted in the same way as for the single conduit cases given in section 6.4.3.1.

The peak and zero-crossing locations in each are shown in figure 6.34 for the two conduit aligned magnetisation case and in figure 6.35 for the opposite magnetisation case. The peaks and zero-crossings for the three conduit case are shown in figure 6.36 for the all three aligned case and figure 6.37 for two aligned and the end conduit in opposition.

The cases with two conduit sections, those with aligned magnetisation and opposite magnetisation are shown in figures 6.34 and 6.35 respectively. In both cases the peak in the B_x and zero-crossing in B_z project back to the centre of left most conduit, conduit 1 from the single conduit case, as in the single conduit cases. The zero-crossings in B_x and peaks in B_z project back to the same position, in from the edges of the conduit section towards the centre, on the left most conduit as in the single conduit cases. In both of the two conduit cases there are a set of peaks in B_x with no corresponding zero-crossings in B_z these project to approximately $25 - 50$ mm from the edge of the right most conduit in the aligned case and to the joint in the opposite case.

In all cases the anomalies in the magnetic field strength deflect further from the area on the conduit sections with increased height from the section. This indicates that as in the single conduit and AlNiCo magnet cases projecting directly down to the conduit from the anomaly in the magnetic field will give inaccuracies in the position of the section of the conduit responsible for the anomaly. In these cases scans at multiple heights are required to accurately project to the conduit sections.

The three conduit cases in section 6.4.3.2, the case with all conduit magnetisations aligned and the case with the end conduit opposite to the other two are presented in figures 6.36 and 6.37 respectively.

In the case where all three conduit magnetisations are aligned it can be seen that the zero-crossings in B_x and peaks in B_z project back to the ends of the

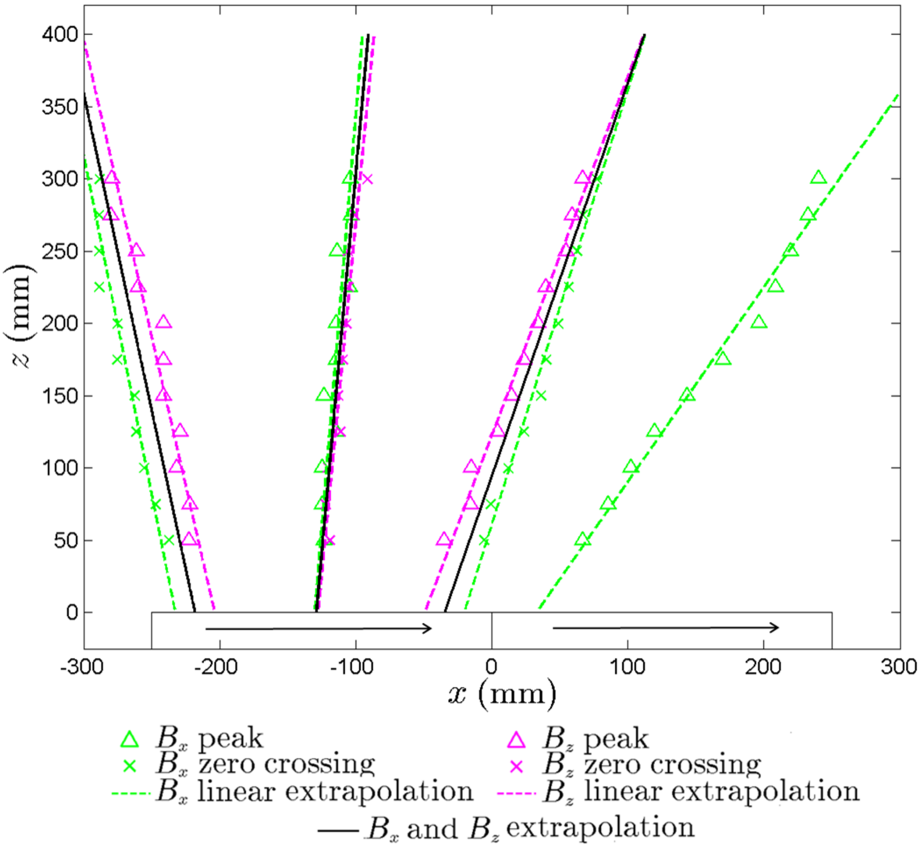

Figure 6.34: Plot showing the positions of the peaks and zero-crossings in the B_x and B_z components of magnetic field strength for two 250 mm long, 1″ diameter magnetised conduits centred at $x = 0$ mm at heights from the conduits of $z = 50 - 300$ mm. With linear extrapolations plotted back to the position on the magnet for the peaks, zero-crossings and average of one component's peak with the corresponding other component's zero-crossing. The conduits are represented in position by rectangles, with the arrow representing the magnetisation direction.

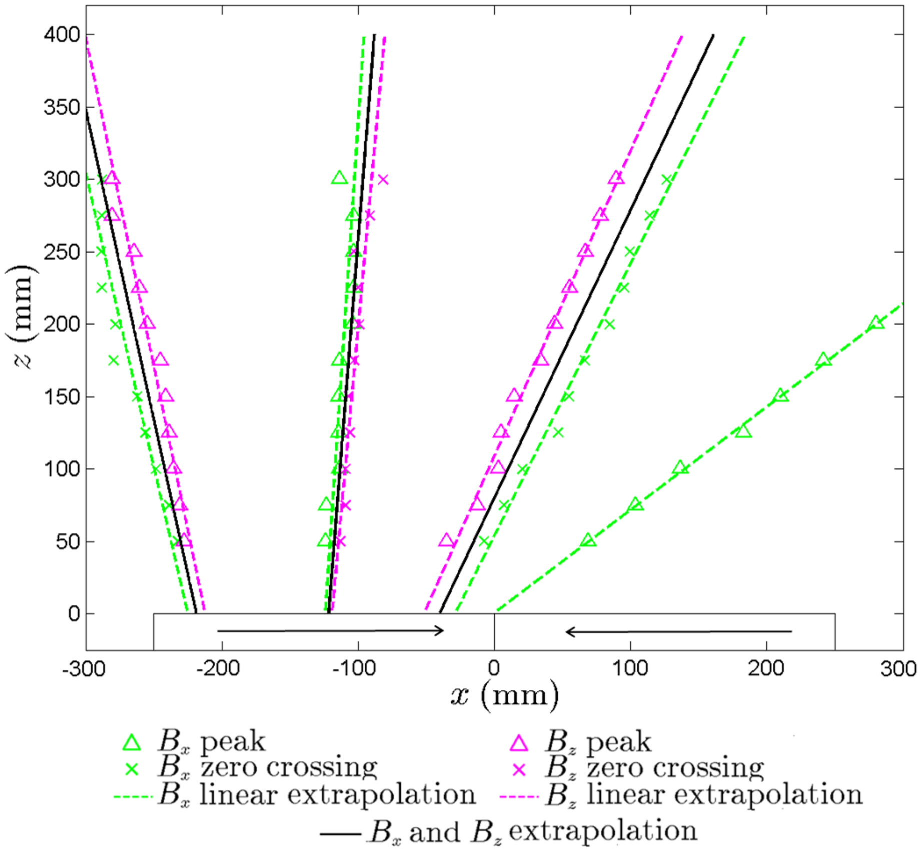

Figure 6.35: Plot showing the positions of the peaks and zero-crossings in the B_x and B_z components of magnetic field strength for two 250 mm long, 1″ diameter magnetised conduits centred at $x = 0$ mm at heights from the conduits of $z = 50 - 300$ mm. With linear extrapolations plotted back to the position on the magnet for the peaks, zero-crossings and average of one component's peak with the corresponding other component's zero-crossing. The conduits are represented in position by rectangles, with the arrow representing the magnetisation direction.

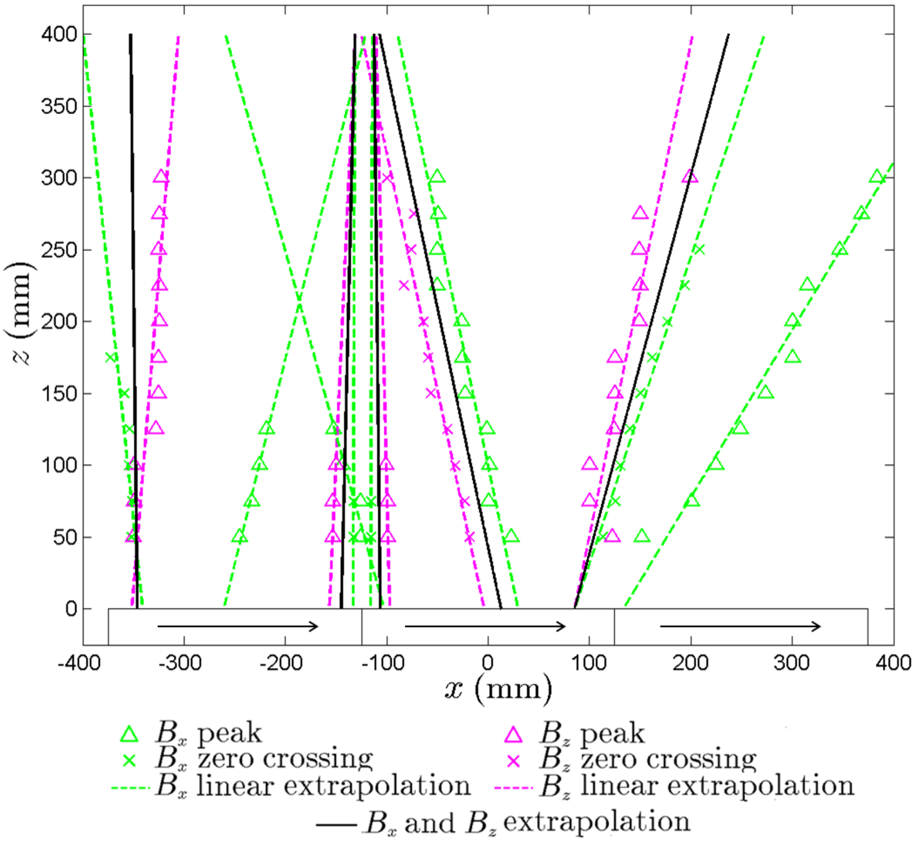

Figure 6.36: Plot showing the positions of the peaks and zero-crossings in the B_x and B_z components of magnetic field strength for three 250 mm long, 1″ diameter magnetised conduits centred at $x = 0$ mm at heights from the conduits of $z = 50 - 300$ mm. With linear extrapolations plotted back to the position on the magnet for the peaks, zero-crossings and average of one component's peak with the corresponding other component's zero-crossing. The conduits are represented in position by rectangles, with the arrow representing the magnetisation direction.

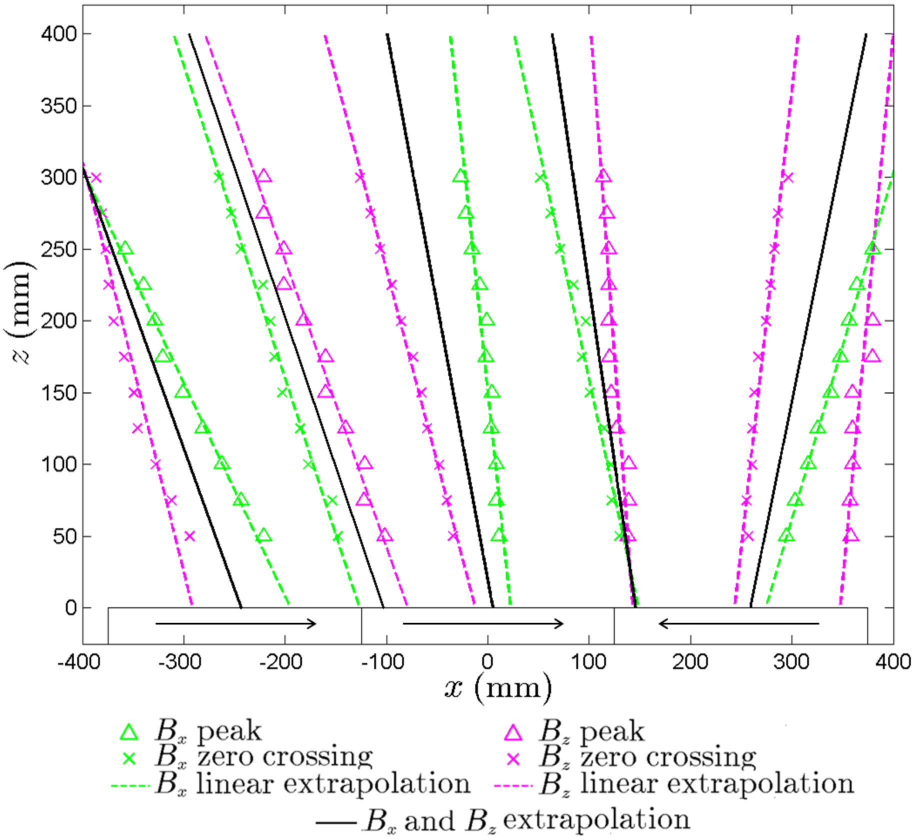

Figure 6.37: Plot showing the positions of the peaks and zero-crossings in the B_x and B_z components of magnetic field strength for three 250 mm long, $1''$ diameter magnetised conduits centred at $x = 0$ mm at heights from the conduits of $z = 50 - 300$ mm. With linear extrapolations plotted back to the position on the magnet for the peaks, zero-crossings and average of one component's peak with the corresponding other component's zero-crossing. The conduits are represented in position by rectangles, with the arrow representing the magnetisation direction.

left most two conduits. The peaks in B_x that have corresponding zero-crossings in B_z project back to the centre of the middle conduit. There are three sets of peaks in B_x with no corresponding zero-crossing in B_z, one set points back to the centre of the left most conduit section, the other two project back to the left ends of the second and third conduit section. There are no anomalies related to the centre or to the right end of the right most conduit.

When the right most conduit is rotated to have its direction of magnetisation in opposition to the direction of magnetisation of the other two conduits, the peaks in B_x and zero-crossings in B_z project back to the centre of the conduits, while the zero-crossings in B_x and peaks in B_z project to the ends of the conduits. The peaks in B_z that project to the right end of the third conduit do not have a corresponding zero-crossing in B_x. There are no anomalies in the magnetic field strength for the left end of the first conduit, the right end of the first conduit and the right end of the second conduit.

In both of the three conduit section cases the anomalies in the magnetic field strength deflect with increasing height and so projecting directly down from any detected anomalies will introduce a positional error. To correct this positional error the magnetic field strength at multiple heights must be measured. Rotating the third conduit section changes the projection angle on all of the magnetic field strength anomalies, indicating that a change in the direction of one pipeline section can alter the anomalies at distant sections. As the orientation of the pipe sections in a pipeline is unknown it is necessary to measure multiple heights above the pipeline as these angles cannot be predicted. This backs up the conclusion from the AlNiCo magnet case that measurement of multiple heights in the field will increase positional accuracy on the pipeline from detected anomalies.

6.5 Discussion

The location of features on pipelines is important to identify in order to reduce the disruption and cost of any repair work the feature necessitates. The method of projecting to the features from detected anomalies in the magnetic field greatly effects the accuracy of location of the feature in the pipe wall. This method has not been previously investigated. Currently projection directly down from the magnetometry array is used to give the position of the feature in the pipe wall. Investigation of the projection method could be used to improve the feature accuracy from the location of the anomaly in the magnetic field.

Magnetometer scans of AlNiCo magnets used to represent pipe sections in the pipeline were completed to assess the magnetic field from a pipeline of dipole sections. Due to the magnetometer measurement range the magnetic field close to this simulant pipeline could not be measured. To allow for closer approach and to give the correct geometry of the pipe sections, short magnetised sections of conduit were used as pipe section simulants.

The scans on the AlNiCo magnets show that a co-located peak and zero-crossing in opposite components of the magnetic field can be detected. In the single magnet case these relate to the centre of the magnet with peaks in B_z indicating the ends of the magnet. In the multiple magnet cases these anomalies relate to the joints between the magnets and the centre of the dipoles. The scans on the magnetised conduits show the same pattern of peaks and zero-crossings as in the AlNiCo magnet case with the edge detections deflecting in from the edge of the conduits.

The co-located peaks and zero-crossings in the components of the magnetic fields that indicate an anomaly in the magnetic field at different heights above the simulated pipeline were analysed, this was related to the positions of the features at the simulant pipeline. This analysis shows that the current model of projecting directly down from the detected anomaly is incorrect and will introduce an error into the projected feature location. The anomalies in the magnetic field show a deflection from vertically above the pipeline simulant, these deflections increase the inaccuracy in the location of the feature as the distance from the simulant pipeline is increased.

The deflections in the anomalies can be seen to be linear, this shows that measuring the magnetic field at different heights above the pipeline will allow for the angle of deflection to be measured and coupled with the distance information used to project accurately to the feature causing the anomaly. This deflection fits with the previous simulations that show a pipeline constructed of dipole sections [82][121].

This shows that to improve the accuracy of locating the features on the pipeline from the magnetic field more than one height measurement in the magnetometry array is needed. Due to the linear nature of the offsets, two layers of magnetometry array could accomplish this positional improvement, however more layers will further increase the accuracy by accounting for errors in any one of the individual measurements. This is demonstrated in the peaks in B_z at $x =$ 50 – 150 mm in the three aligned magnetised conduit case shown in figure 6.36. The peak at $z = 50$ mm is offset compared to the linear fit and if taken with the peak at $z = 75$ mm would give a line which is deflecting at an angle of -35° from a line normal to the pipe wall. Taking all the detected peaks in B_z gives an angle from a line normal to the pipe wall of 12.5°, which is deflecting in the opposite direction from normal to the case with just the $z = 50$ mm and $z = 75$ mm peaks.

A greater distance between these additional magnetometry layers would give a greater angular resolution, these are due to the magnetic field only being measured at discrete points through the field. This is demonstrated in the opposite aligned two conduit case shown in figure 6.35, for the zero-crossings in B_z in the range x = -100 – -150 mm. In this case taking the zero-crossings detected at $z = 75$ mm and $z = 100$ mm or at $z = 125$ mm and $z = 150$ mm would give a projection directly downwards from the detected zero-crossings but taking the zero-crossings at $z = 50$ mm and $z = 100$ mm or at $z = 125$ mm and $z = 175$ mm would give an angle from normal to the pipe of 5.7° as shown in the plot.

A separation between the layers that is too large however will reduce the signal strength at the higher layers due to increased distance between the layer and the pipeline. This could lead to anomalies being missed in the higher layers, meaning only one height is measured as in the single layer array and so giving no improvements. This is demonstrated in the three aligned magnetised conduits case shown in figure 6.36. In this case the peaks in B_x in the range x = -200 – -300 mm, where in the layers above $z = 125$ mm no peak is detected in the magnetic field at these points.

The mean of the deflection angles for both the AlNiCo magnet and magnetised conduit examples presented in this chapter is 16°. The maximum deflection angles identified are 32° in the magnet cases and 34° in the magnetised conduit cases.

For a typical magnetometry survey array height above the centreline of the pipe of 2 – 4 m on a typical pipeline diameter of $36''$ this gives an average deflection of 0.45 – 1.04 m and a maximum deflection of 0.96 – 2.21 m in the magnet case and 1.04 – 2.39 m in the magnetised conduit case. Determining and correcting for these angles could improve the feature locational accuracy by up to the values of 2.39 m determined from this laboratory data.

These investigations were carried out on small magnets and conduits at a closer proximity than in the field surveys, while the deflection in the location of the anomalies in the magnetic field is linear at this scale it is not necessarily linear at larger scales. These investigations assume the pipe section dipole model is correct as the simulated pipelines in both cases had imposed dipoles. The simulated pipelines scanned were short total length, not welded and open ended, these could all effect the pipeline magnetic field, the anomaly locations and the deflections of the features.

The relationship between the location of the anomaly in the magnetic field and the feature in the pipeline has been investigated in the laboratory using AlNiCo magnets and magnetised conduit sections to simulate pipe sections in a pipeline. The laboratory results show a linear deflection in the location of the anomaly with increasing distance from the pipeline. The current model of projecting directly down to the pipeline from the detected anomaly gives an incorrect feature location due to this deflection. This error in the feature location can be corrected by using multiple layers of magnetometry arrays to measure the anomaly at different heights above the pipeline to measure the deflection and use this to project back to the feature accurately.

6.6 Conclusion

Scans on AlNiCo magnets and magnetised steel conduit sections have been completed at varying heights to simulate pipe section dipoles in the field. These scans show that in both cases using peaks and zero-crossings in the B_x and B_z components of magnetic field strength does detect the features of the dipole at the object being scanned.

In the case of a single AlNiCo magnets the centre and edges of the dipole can be detected above the magnet, when this is increased to multiple magnets the centres and joints between the magnets can be detected in this way. When plotting the multiple layers above the magnet it can be seen that these anomalies are deflected from being on a line normal to the surface of the magnet. These results suggest that inferring the position of the cause of the anomaly in the magnetic field strength as being directly down from the magnetometer array when this anomaly is detected is incorrect. This will produce positional inaccuracies which will increase with distance from the dipole. Extra layers of magnetic field strength information are therefore required to correct for these deflections in the magnetic field strength anomalies.

When this is expanded to magnetised steel conduit sections to allow for closer measurement with the magnetometer, it can again be seen that magnetic anomalies can be detected for the centre and in from the edges of the magnetised conduits. When the different layers are plotted it can again be seen that these deflections are present in the magnetic field strength anomalies, further reinforcing the case for using multiple layers of magnetometers to accurately project back from the detected anomaly to the feature at the pipe position.

These results show that multiple layers of magnetometers would increase the positional accuracy of pipe features from detected magnetic field anomalies. The linear nature of the deflection suggests that two layers would be sufficient to overcome this effect, however any errors in either of the magnetometry layers could increase the inaccuracy of position by giving an incorrect deflection. The chance of this incorrect deflection is reduced with increasing layers, however these would increase the weight, cost and power requirements of the magnetometer array. The greater the height of layer the better the angular resolution that will be given for these offsets due to the measurements along the pipe being discrete points. Too large a separation however, will cause the higher layers to fail to detect the anomalies due to the increased distance from the source of the magnetic field.

A further study using the array to measure the magnetic field from a known pipeline in the field at different heights is required to determine the size of this deflection in gas pipelines and to optimise the distance between these layers for increasing the positional accuracy of detected features.

Chapter 7

Conclusion

This project was set out to explore the use of large stand-off magnetometry for non-invasive inspection of buried natural gas steel pipelines, with a focus on the survey array tool used to conduct these inspections. Non-invasive techniques for inspection of gas pipelines are required to supplement current techniques to prevent interruptions in the gas supply from a failure of the pipeline.

Natural gas is a major component of the UK's energy usage, this gas is transported using a pipeline network. The main national network of these pipelines is known as the national transmission system which was constructed in the 1960s. As the pipelines have aged the major cause of incidents resulting in an unplanned release have gas has been corrosion in the pipe wall. Corrosion is a defect that progresses with time until the pipe wall is no longer able to contain the pressure within the pipe and an unplanned release of gas occurs. These incidents can be prevented by timely detection of the corrosion and action taken to repair the pipe wall. Another major cause of these incidents is due to external interference such as the pipeline being struck by an excavator during construction work, these can be prevented by maintaining accurate maps of the pipeline location and prompt inspection of the pipeline following a reported strike. Pipeline incidents can have major consequences such as loss of life, property damage, interruption of gas supply and reputational damage to the pipeline operator. In-line inspection is used to inspect pipelines using a tool known as a pig, this in-line inspection carries risks to the pipeline and operators. Furthermore not all pipelines are piggable indicating a need for complimentary inspection techniques for gas pipelines. Large stand-off magnetometry detects the self magnetic flux leakage from the defect in the material, this is one such prospective inspection technique. The large stand-off magnetometry survey tools used for these inspections were developed at the University of Leeds in collaboration with Speir Hunter. The magnetometry survey tools have been deployed for non-invasive inspections of pipelines since 2012 by Speir Hunter. The magnetometry survey array is described in section 2.5.

The objectives and questions which were considered in this project were:

Objective 1: To investigate the presentation of the magnetometry survey data to improve anomaly location by a user.

How can the data from the magnetometry survey be presented in a way which maximises the ability of the user to pick out anomalies in the magnetometry data with minimal interpretation required?

Objective 2: To investigate if there is an optimum magnetometer separation in the survey array and determine the anomaly to separation relationship.

How does the magnetometer separation effect the sensitivity of the magnetometry survey array through the relationship between this magnetometer separation and the amplitude of the anomalies in the magnetic field and what is this relationship?

Objective 3: To investigate the locational relationship between the magnetic anomalies and pipeline features and how this affects the accuracy of feature location.

How does a detected anomaly in the magnetic field relate to the location of the feature in the pipeline and how can this feature locational accuracy be improved?

Objective 4: To use the data gathered in the laboratory to provide recommendations for future development on the large stand-off magnetometry survey array.

What improvements to the magnetometry survey array does this research suggest should be implemented to improve the detection and location of pipeline features to increase the usefulness of large stand-off magnetometry as a complimentary non-invasive technique for pipeline inspection?

The investigations in this research were conducted in the laboratory using a stepper motor positioned magnetometer to gather three-dimensional magnetic field strength data from simulants.

The results of this research are presented in full in their individual chapters. This section presents a brief account of these findings to answer each of the research questions outlines above.

Objective 1: is investigated in chapter 4.

To investigate how the magnetometry data can best be presented to the end user to allow anomalies in the magnetic field to be easily identified. Three methods of visualising the vector field data gathered from the magnetometers in the magnetometry survey array were considered. A convolution method known as linear integral convolution (LIC) which convolves a white noise image to represent the vector field with an imposed colour map to show the magnitude of the field was found to be able to represent the vector field in an easily understandable way and give a high anomaly resolution.

Objective 2: is investigated in chapter 5.

To investigate the effect of the separation between the centre and outer magnetometers in the magnetometry array on the amplitude of the anomaly in the magnetic gradient field. Pipe features were created by cutting a range of different diameter steel conduit using a pipe cutter. These features were scanned in the laboratory to gather the magnetic anomaly data from the cuts in the conduits. This magnetic data was compared to theoretical models for defects in ferromagnetic materials to verify these laboratory observations match with the expected magnetic field from these features. These showed a high level of correlation with the theoretical model.

The gathered magnetic data was used to calculate the magnetic gradient field for the anomaly for different separations between the magnetometers. The separation of the magnetometers was considered in terms of the angle between them at the pipe centreline. The relationship between the amplitude of the anomalies in the gradient field shows a linear increase in the amplitude of the anomalies in the gradient field rising to a peak before decreasing linearly with increasing angle between the magnetometers. This peak is at an angle of 33° at a height above the conduit centreline of 50 mm and an angle of 23° at a height above the centreline of the conduit of 300 mm. The relationship between the angle which gives the peak amplitude of the anomaly in the magnetic gradient field flattens out as the height above the centreline increases, this tends towards a value of 23°. This relationship shows a high level of correlation between the laboratory data and two different theoretical models of the magnetic anomalies from these defects.

Objective 3: is investigated in chapter 6.

Experiments were conducted to investigate the relationship between the location of the anomaly in the detected magnetic field and the feature in the pipe wall. In these experiments pipelines were represented by pipeline simulants, these were considered as a series of axially aligned dipoles as in the pipe dipole model. Two different dipoles were considered, AlNiCo magnets and short lengths of magnetised conduit.

The pipeline simulants made up of magnets show that pairs of peaks and zero-crossings can be related to the centres of the magnets and the joint between the magnets. These anomalies in the magnetic field however are deflected along the pipeline by different angles, these had an average angular deflection of 16° and a maximum deflection of 32°. In the pipeline simulants made up of magnetised conduit sections the anomalies project back to the centre of the conduits and the joints between the conduit sections. These conduit section simulant pipelines show an average angular deflection of 16° with a maximum deflection of 34°. These deflections show a linear projection from the anomaly location to the feature at the pipeline simulant.

Objective 4: is synthesised from the results gathered in the first three objectives.

The investigations to fulfil the first three objectives of the project were used to make recommendations for the future development of the magnetometry survey array.

For the production of meaningful linear integral convolution textures from the magnetometry survey data must be a minimum of five data points wide. This would require the addition of two magnetometers in-line with the magnetometry array in the survey tools. These additional magnetometers would allow for an LIC texture to be generated for the strip traced out by the magnetometry array above the pipeline. When viewed this could allow additional anomalies to be identified which would not found by an algorithm with set detection parameters.

The investigation into the effect of the magnetometer separation on the amplitude of the anomaly in the magnetic gradient has identified an optimum angular separation of 23° between the centre and outer magnetometer at the pipe centreline. The current magnetometry survey array has a separation of 0.5 m and during a survey is typically used at a height of 2 – 4 m above the pipe centreline. This gives an angular separation in the survey tools of 14 – 7° giving a normalised amplitude range of 0.3 – 0.75 of the peak amplitude. To give the peak amplitude in the magnetic gradient anomaly a magnetometer separation of 0.85 – 1.7 m would be required to give the optimum angle of 23° for a height above the centreline of the pipe of 2 – 4 m. This increase in array width could increase the sensitivity of the magnetometry tools, however this increase in width will reduce the manoeuvrability of the array and increase the effects of the operator walking with the survey array not keeping the magnetometry array section perfectly level.

The investigation into the locational relationship between the detected anomaly in the magnetic field and the feature in the pipeline has identified a deflection from vertical in the locations of the anomalies at different heights above the pipeline. This deflection has an average angle of 16° and a maximum angle of 34°, for the typical survey height above the pipeline of 2 – 4 m, on a typical pipe size of 36″. This gives an average locational inaccuracy of 0.45 – 1.04 m and a maximum locational inaccuracy of 1.04 – 2.39 m depending on the height above the pipeline. The addition of extra layers of magnetometers in the survey tool would allow the deflection angle be determined, this information can then be used to correct for deflection in the location the anomaly from the magnetic field compared to the feature on the pipeline. The deflection of the anomalies with the height above the pipeline shows a linear relationship, this would allow the deflection angle to be determined from two magnetometry layers, however additional layers will further increase the accuracy of determining this angle.

The laboratory investigation on the cut conduits shows that the feature in the pipe creates an anomaly in the magnetic field. This is detectable as a co-located peak and zero-crossing in magnitude of the longitudinal and radial magnetic fields as predicted in the magnetic flux leakage defect model [79]. This detected field does not use any additional magnetising fields to create the flux leakage, this conforms to the self magnetic flux leakage model [103].

The wave form of the anomalies from the cuts in the 1″ conduit show a high level of correlation with the Wang defect model which models a defect zone of dislocated magnetic charges [116]. The survey tool uses a magnetometry array of three magnetometers which are used to calculate the magnetic gradient field, the Wang defect model is only given for a two-dimensional scenario, this has been expanded in this investigation to give a model for the magnetic gradient field from a defect. These calculated gradient fields from the expanded Wang defect model show a high level of correlation with the results from the laboratory. The relationship between the angular separation between the magnetometers and the anomaly amplitude calculated from the laboratory data were compared to the expanded Wang defect model and the model for an axially magnetised cylinder [83]. These show a high level of correlation suggesting these models are valid for these circumstances.

In the pipeline simulant investigations there is an anomaly related to the joints between the pipe section simulants, this confirms the observation of regularly spaced peaks in the magnetic field above a pipeline corresponding to the weld positions [8]. The deflections in the anomalies detected from the pipeline simulants confirms the magnetic field from modelled pipelines made from a series of pipeline dipoles [82].

Future research into the large stand-off magnetometry system can be conducted to compliment the research conclusions from this project, this should focus on replicating the findings from the laboratory in this project to buried gas pipelines. This project gives three hypothesis that can be tested in future research these are:

a. that a magnetic data set of at least five data points wide can be used to generate LIC textures which can improve identification of anomalies in the magnetic field from a pipeline.

b. that there is an optimum angular separation of the magnetometers in the magnetometry array that maximises the amplitude of the anomaly in the magnetic gradient field, and that this angle is approximately 23°.

c. that there is a deflection along the pipe in the location of the anomaly in the magnetic field from a pipeline feature, and that this has an average deflection from normal of 16°.

These hypothesis can be tested by measuring the magnetic field in a three-dimensional volume above pipelines with known feature locations.

This data can be used to generate LIC textures along the surveyed area to test hypothesis **a**, these textures can be inspected to identify the anomalies in the magnetic field. Any expected anomalies that are missed can be investigated to improve the data presentation. Any anomalies beyond what is expected from the pipeline features can be explored to find if these are a false identification or from an unknown feature in the pipe.

To test hypothesis **b** the magnetometry data from the known pipeline can be used to calculate the magnetic gradient field for different magnetometer positions either side of the pipeline. The amplitudes of the anomalies in the magnetic gradient field from the pipeline features can be determined for each of the positions considered in this data, to give the relationship of the anomaly amplitude to the angular separation of the magnetometers. This can be repeated for multiple heights above the pipeline to confirm that the angle that gives the maximum amplitude in the magnetic gradient anomalies is approximately 23°, as hypothesised from these laboratory results. If the angle that gives the maximum amplitude is approximately 23° this confirms the relationship between this angle and the height above the pipe centreline from the laboratory results. If the angles measured in this way do not confirm the relationship determined in the laboratory this data can be used in conjunction with the laboratory data to further investigate this relationship.

The deflections of the anomalies along the pipeline from the features can be calculated from this three-dimensional magnetic field data to test hypothesis **c**. The anomaly positions for multiple features at multiple heights can be considered. This anomaly location information can be linearly interpolated between different heights to compare the projected feature location to the actual pipeline feature location. If this shows a linear projection to the pipeline feature position this will confirm the hypothesis, if a different projection relationship is determined in this work then this can be used to improve the feature location accuracy in the survey array.

This project has provided recommendations for the future development of the large stand-off magnetometry system based on experiments conducted in the laboratory environment, these studies however have a number of limitations which must be considered.

The investigations conducted in the laboratory were conducted on small scale conduit pipes which were stressed by cutting rather than pressure, this caused a compressive rather than expansive stress in the material which will create a different magnetisation according to prior published research into the Villari effect [10]. The conduits used in the lab were an order of magnitude smaller diameter than typical pipelines in the national transmission system with a greater wall thickness to pipe diameter ratio and were scanned at a much closer distance than would be achieved in a non-invasive magnetometry survey. These conduits were not of the same alloy as the pipelines used in the field.

These laboratory experiments, despite these limitations, can be considered valid for informing further development of the system for non-invasive inspection of gas pipelines in the national transmission system. These conduits have the same geometry as gas pipelines with a seam weld, they are constructed from an alloy with a Young's modulus of 268 GPa versus a Young's modulus of 290 GPa for gas pipelines. The magnetic field measured from the conduits conform to the theory for magnetic fields from gas pipelines, therefore giving confidence in these results.

This project has focussed on informing future development of the large stand-off magnetometry survey array tools to compliment in-line inspection and to provide an inspection technique that is capable of meeting the gap in pipeline inspection in cases when the pipe is not suitable for in-line inspection. Using laboratory experiments methods of presenting the magnetometry data, the relationship between the magnetometer separation and the sensitivity of the array and the relationship between the detected anomalies in the magnetic field and the feature at the pipeline have been explored.

The recommendations from this project for the future development of the magnetometry survey array are to use a magnetometry survey system with multiple magnetometer array layers, each with a centre magnetometer to the furthest outer magnetometer of 0.75 m, comprising a minimum of five magnetometers in each array.

References

[1] European Gas pipeline Incident data Group, “10th Report of the European Gas Pipeline Incident Data Group (period 1970 – 2016),” 2018. xi, 4, 6

[2] Alberta Energy and Utilities Board, “Pipeline Performance in Alberta 1980-1997,” 1998. xi, 5, 8

[3] Alberta Energy and Utilities Board, “Pipeline Performance in Alberta 1990-2005,” 2007. xi, 5, 8

[4] Alberta Energy and Utilities Board, “Report 2013-B: Pipeline Performance in Alberta1990-2012,” 2013. xi, 5, 8

[5] National Transportation Safety Board, “Natural Gas Pipeline Rupture and Fire Near Carlsbad, New Mexico August 19, 2000,” 2003. xii, 12, 13, 14, 15

[6] National Transportation Safety Board, “Pacific Gas and Electric Company Natural Gas Transmission Pipeline Rupture and Fire San Bruno, California September 9, 2010,” 2011. xii, xiii, 17, 18, 20

[7] National Transportation Safety Board, “Columbia Gas Transmission Corporation Pipeline Rupture Sissonville, West Virginia December 11, 2012,” 2014. xiii, 20, 22

[8] W. T. Sowerbutts, “The use of Geophysical Methods to Locate Joints in Underground Metal Pipelines,” *Quarterly Journal of Engineering Geology*, vol. 21, pp. 273–281, 1988. xiii, 31, 32, 223

[9] E. D. Torre, *Magnetic hysteresis*. IEEE press, 1999. xiv, 34

[10] D. Atherton and D. Jiles, "Effects of stress on magnetization," *NDT International*, pp. 15–19, 1986. xiv, 33, 35, 225

[11] J. Blitz, *Electrical and Magnetic Methods of Non-destructive Testing*. Chapman and Hall, 1991. xiv, 47

[12] S. Paeper, B. Brown, and T. Beuker, "Inline Inspection of Dents and Corrosion Using "High Quality" Multi-Purpose Smart-Pig Inspection Data," *Proceedings of IPC 2006 6th International Pipeline Conference*, 2002. xv, 49

[13] D. Jiles, *Introduction to Magnetism and Magnetic Materials, Third Edition*. Taylor & Francis group, 2016. xxxiii, 38

[14] Rosen, "Rogeo Xyz Service In-line Precision Pipeline Route Mapping And Strain Assessment," tech. rep., Rosen, 2017. xxxiii, 50

[15] British Standards Institution, "BS EN 10255:2004: Non-alloy steel tubes suitable for welding and threading. Technical delivery conditions," tech. rep., BSI, 2004. xxxiii, 72

[16] Amperican Petrolium Institute, "API specifications 5L Specification for Line Pipe," tech. rep., Amperican Petrolium Institute, 2002. xxxiii, 72

[17] American Society of Mechanical Engineers, "ASME/ANSI B36.10/19 Carbon, Alloy and Stainless Steel Pipes - Dimensions." xxxiii, 76

[18] International Energy Agency, "Golden Rules for a Golden Age of Gas," tech. rep., International Energy Agency, 2012. 2

[19] Y. D. Jo and B. J. Ahn, "Analysis of hazard areas associated with high-pressure natural-gas pipelines," *Journal of loss prevention in the process industries*, vol. 15, no. 3, pp. 179–188, 2002. 2

[20] G. Hiltscher, W. Mühlthaler, and J. Smits, *Industrial Pigging Technology*. Wiley-VCH, 2003. 2, 47, 48

[21] S. Freear, B. Varcoe, D. M. J. Cowell, S. G. H. Staples, and C. Vo, “Patent WO2013\128212 - Fault Detection For Pipelines,” 2013. 2, 59

[22] S. Freear, C. Vo, B. Varcoe, D. M. J. Cowell, S. G. H. Staples, and C. L. Cookson, “Patent WO2018\046947 - Pipeline Mapping System,” 2018. 2, 59, 116

[23] National Grid, “Annual Report and Accounts,” tech. rep., National Grid, 2011. 2

[24] C. Mitchell, J. Sweet, and T. Jackson, “A study of leakage from the UK natural gas distribution system,” *Energy Policy*, vol. 18, no. 9, pp. 809–818, 1990. 2

[25] Energy networks association, “Gas network innovation strategy,” tech. rep., Gas innovation and governance group, 2018. 2, 3

[26] Office for national statistics, “UK Energy statistics, Q1 2018,” tech. rep., Department for business, energy and industrial strategy, 2018. 3

[27] Committee in Climate Change, “Next steps from UK heat policy,” tech. rep., Committee in Climate Change, 2016. 3

[28] National Grid, “Shareholder Information,” tech. rep., National Grid, 2009. 3

[29] DECC and Ofgem, “Statutory Security of supply report,” tech. rep., Department for business, energy and industrial strategy, 2017. 3

[30] J. Stern, “UK gas security: time to get serious,” *Energy policy*, vol. 32, pp. 1967–1979, 2004. 3

[31] A. Stirling, “What is energy security? Uncertainties, dynamics, strategies,” *presentation to conference Energy security: What do we know, and what should be done*, 2009. 3

[32] T. I. Williams, *A history of the British gas industry.* Oxford University Press, 1981. 3

[33] S. Arapostathis, "Natural gas network development in the uk (1960-2010)," tech. rep., UK Energy Research Centre, 2011. 3

[34] P. E. Dodds and W. McDowall, "The future of the UK gas network," *Energy Policy*, vol. 60, p. 3, 2013. 3

[35] House of Lords Select Committee, "Energy Supply: How Secure Are We? 14th Report Session 2001–02, HL Paper 82," tech. rep., House of Lords Select Committee, 2002. 3

[36] J. Skea, M. Chaudry, and X. Wang, "The role of gas infrastructure in promoting UK energy security," *Energy Policy*, vol. 43, pp. 202–213, 2012. 3

[37] H. Wang and I. J. Duncan, "Likelihood, causes, and consequences of focused leakage and rupture of U.S. natural gas transmission pipelines," *Journal of Loss Prevention in the Process Industries*, vol. 30, pp. 177–187, 2014. 4

[38] D. Furchtgott-Roth, "Pipelines are safest for transportation of oil and gas," *Manhattan Institute for Policy Research*, 2013. 4

[39] Standing Senate Committee on Energy, the Environment and Natural Resources, "A study of the safe transport of hydrocarbons by pipelines, tankers and railcars in Canada," tech. rep., Standing Senate Committee on Energy, the Environment and Natural Resources, 2013. 4

[40] H. Dossier, "Gas Pipeline Explosion at Ghislenghien, Belgium," *Hazards Intelligence*, 2005. 9

[41] French Ministry for Sustainable Development DGPR/SRT/BARPI, "Rupture and Ignition of a Gas Pipeline 30 July 2004, Ghislenghien, Belgium.," 2009. 11

[42] N. E. V. Loey, R. van de Schoot, and A. W. Faber, "Post-traumatic Stress Symptoms After Exposure to Two Fire Disasters: Comparative Study," *PLoS One*, 2012. 11

[43] Fluxys, "Fluxys Rapport Financier Semestriel 2011," 2011. 12

[44] P. W. Parfomak, “Keeping Americas Pipelines Safe and Secure. Key Issues for Congress,” tech. rep., Congressional Research Service, 2010. 12

[45] United States Department of Justice, “El Paso Natural Gas to Pay $15.5 Million Penalty and Perform Comprehensive Reforms to Pipeline System,” 2007. 15

[46] Independent Review Panel San Bruno Explosion, “Report of the Independent Review Panel San Bruno Explosion,” tech. rep., California Public Utilities Commission, 2011. 15

[47] Public Utilities Commission of the State of California, “Modified Presiding Officer’s Decision Regarding Alleged Violations by Pacific Gas and Electric Company in Connection With the San Bruno Explosion and Fire,” 2015. 17

[48] J. Sullivan, “PG&E Sentenced for San Bruno Blast,” *Risk Management*, vol. 64, no. 2, 2017. 19

[49] W. J. Hinze, R. R. B. Von Frese, and A. H. Saad, *Gravity and Magnetic Exploration*. Cambridge University Press, 2013. 30, 31

[50] J. F. W. Bowles, R. A. Howie, D. J. Vaughan, and J. Zussman, *Rock-Forming Minerals Non-Silicates Oxides, Hydroxides and Sulphides*. The Geological Society Publishing House, 2011. 30

[51] W. Lowrie, *Fundamentals of Geophysics*. Cambridge university Press, 2007. 30

[52] Z. Gongliang, “Wujing Zongyao,” 1040. 30

[53] J. Needham, *Science and Civilisation in China: Volume 4, Physics and Physical Technology, Part 1, Physics*. Cambridge University Press, 1962. 30

[54] J. Vardalas, “History Lesson The Magnetic Compass,” *IEEE Tech History*, 2013. 30

[55] H. Carlborg, “Om Gruvkompasser, Malmletning och Kompassgångare,” *Sancte Örjens Gille Stockholm*, 1963. 30

[56] Bookstrom, “Magmatic features of iron ores of the Kiruna type in Chile and Sweden; ore textures and magnetite geochemistry,” *Economic Geology*, 1994. 30

[57] D. M. McCann, P. D. Jackson, and M. G. Culshaw, “The Use of Geophysical Surveying Methods in the Detection of Natural Cavities and Mineshafts,” *Quarterly Journal of Engineering Geology and Hydrogeology*, vol. 20, pp. 59–73, 1987. 31

[58] M. Marchetti, L. Cafarella, D. Di Mauro, and A. Zirizzotti, “Ground Magnetometric Surveys and Integrated Geophysical Methods for Solid Buried Waste Detection: A Case Study,” *Annals of Geophysics*, vol. 45, no. 3/4, pp. 563–573, 2002. 31

[59] S. D. Billings, “Discrimination and Classification of Buried Unexploded Ordnance Using Magnetometry,” *IEEE Transactions on Geoscience and Remote Sensing*, vol. 42, no. 6, pp. 1241–1251, 2004. 31

[60] J. C. Wynn, “A review of geophysical methods used in archaeology,” *Geoarchaeology: An International Journal*, vol. 1, no. 3, pp. 245–257, 1986. 31

[61] M. Aitken, “Magnetic Prospecting: An Interim Assessment,” *Antiquity*, vol. 33, no. 131, pp. 205–208, 1959. 31

[62] M. Dabas and A. Tabbagh, “Magnetic prospecting,” *Archaeological Method and Theory: An Encyclopedia*, pp. 335–339, 2000. 31

[63] W. T. C. Sowerbutts, “A Magnetic Method to Locate Joints in Buried Metal Pipelines,” *Geophysics Journal International*, vol. 85, no. 1, p. 248, 1986. 31

[64] S. Breiner, “Applications Manual for Portable Magnetometers,” *Geometrics*, 1973. 31

[65] S. P. Gay, "The Effects of Cathodically Protected Pipelines on Aeromagnetic surveys," *Applied Geophysics*, vol. 51, no. 8, pp. 1671–1684, 1986. 32

[66] P. Weiss, "L'hypothèse du champ molèculaire et la propriètè ferromagnètique," *J. Phys. Theor. Appl.*, 1907. 32

[67] R. Lanza and A. Meloni, *The Earth's Magnetism: An Introduction for Geologists*. Springer, 2006. 32

[68] J. Joule, "On a New Class of Magnetic Forces," *Ann. Electr. Magn. Chem*, vol. 8, pp. 219–224, 1842. 32

[69] R. M. Bozorth, *Ferromagnetism*. Wiley, 1951. 32

[70] E. W. Lee, "Magnetostiction and Magnetomechanical Effects," *Rep. Prog. Phys.*, pp. 184–229, 1955. 33

[71] E. Villari, "Change of magnetization by tension and by electric current," *Annual Review of Physical Chemistry*, vol. 128, pp. 87–122, 1865. 33

[72] R. M. Bozorth and H. J. Williams, "Effect of Small Stresses on Magnetic Properties," *Reviews of Modern Physics*, vol. 17, no. 1, pp. 72–80, 1945. 33

[73] L. N. Mulay, *Magnetic susceptibility*. Interscience Publishers, 1963. 33

[74] G. Bertotti, *Hysteresis in magnetism for physicists, material scientists and engineers*. Academic press, 1998. 33

[75] D. C. Jiles and D. L. Atherton, "Theory of ferromagnetic hysteresis (invited)," *Journal of Applied Physics*, vol. 55, no. 6, pp. 2115–2120, 1984. 33

[76] D. Atherton and D. Jiles, "Effects of stress on magnetisation of steel," *IEEE Transactions on Magnetics*, vol. 19, no. 2021, 1983. 36

[77] L. Li, *Stress effects on ferromagnetic materials: investigation of stainless steel and nickel*. PhD thesis, Iowa State University, 2004. 36

[78] D. C. Jiles, "Theory of the magnetomechanical effect," *J. Phys. D. App. Phys.*, vol. 28, pp. 1537–1546, 1995. 36

[79] D. C. Jiles, "Review of Magnetic Methods for Non-destructive Evaluation," *NDT International*, vol. 21, no. 5, pp. 311–319, 1988. 36, 47, 223

[80] D. C. Jiles, "Review of magnetic methods for nondestructive evaluation (Part 2)," *NDT International*, vol. 23, no. 2, pp. 93–92, 1990. 36, 47

[81] D. X. Chen, E. Pardo, and A. Sanchez, "Fluxmetric and magnetometric demagnetizing factors for cylinders," *Journal of Magnetism and Magnetic Materials*, vol. 306, pp. 135–146, 2006. 36

[82] S. G. H. Staples, B. T. H. Varcoe, C. Vo, D. Cowell, C. Cookson, and S. Freear, "Bar magnet model for large stand-off magnetometry," , 2017. 36, 162, 212, 223

[83] A. J. Petruska and J. J. Abbott, "Optimal Permanent-Magnet Geometries for Dipole Field Approximation," *IEEE Transactions on Magnetics*, vol. 49, no. 2, pp. 811–819, 2013. 36, 223

[84] J. A. Osborn, "Demagnetizing Factors of the General Ellipsoid," *Phys. Rev.*, vol. 67, pp. 351–357, 1945. 37

[85] J. M. D. Coey, *Rare-earth Iron Permanent Magnets.* Oxford University Press, 1996. 37

[86] D. X. Chen, J. A. Brug, and G. R. B., "Demagnetizing factors for cylinders," *IEEE transactions on magnetics*, vol. 27, no. 4, pp. 3601–3619, 1991. 37

[87] M. Beleggia, M. De Graef, Y. T. Millev, D. A. Goode, and G. Rowlands, "Demagnetisation factors for elliptic cylinders," *J. phys. D: Appl. Phys.*, vol. 38, pp. 333–3342, 2005. 37

[88] A. Aharoni, *Introduction to the Theory of Ferromagnetism*, ch. Another Energy Term, pp. 109–133. Oxford University Press, 1996. 37

[89] H. Zijlstra, *Experimental Methods in Magnetism: Measurement of Magnetic Quantities*. North-Holland Pub. Co., 1967. 38

[90] K. Umashankar, *Introduction to Engineering Electromagnetic Fields*. World Scientific Publishing Co. Pte. LTD., 1989. 38

[91] J. D. Jackson, *Classical Electrodynamics (2nd ed.)*. John Wiley & Sons, Inc., 1975. 40

[92] D. J. Griffiths, *Introduction to Electrodynamics*. Pearson Higher Ed., 2014. 40

[93] E. T. Whittaker and G. N. Watson, *A Course of Modern Analysis*. Cambridge University Press, 1962. 40

[94] T. L. Chow, *Introduction to Electromagnetic Theory: A Modern Perspective*, ch. 4. Magnetostatics, pp. 129–170. Jones and Bartlett, 2006. 42

[95] M. L. Nayyar, *Piping Handbook*. McGraw-Hill, Inc., 1999. 44

[96] R. E. Beissner, G. A. Matzkanin, and C. M. Teller, "NDE applications of magnetic leakage field methods," 1980. 47

[97] D. Woodley, "The origin of intelligent pigs," *Pipelines International*, pp. 26–28, 2011. 47

[98] F. Förster, "On the Way From the" Know-How" to the" Know-Why" in the Magnetic Leakage Field Method of Nondestructive Testing. I.," *Materials Evaluation*, vol. 43, no. 10, pp. 1154–1155, 1985. 47

[99] F. Förster, "On the way from the'know-how' to the'know-why' in the magnetic leakage field method of nondestructive testing. II.," *Materials Evaluation*, vol. 43, p. 1398, 1985. 47

[100] N. Zatsepin and V. Shcherbinin, "Calculation of the magnetostatic field of surface defects," *Defektoskopiya*, no. 5, pp. 50–59, 1966. 48

[101] S. M. Dutta, F. H. Ghorbel, and R. K. Stanley, "Dipole Modeling of Magnetic Flux Leakage," *IEEE transactions on magnetics*, 2009. 48

[102] S. M. Dutta, F. H. Ghorbel, and R. K. Stanley, "Simulation and Analysis of 3-D Magnetic Flux Leakage," *IEEE Transactions on Magnetics*, vol. 45, no. 4, pp. 1966–1972, 2009. 48

[103] A. A. Dubov, "The metal magnetic memory method," *FSUE "Izvestiya"*, vol. 256, 2011. 48, 223

[104] A. A. Dubov, "Principle features of metal magnetic memory method and inspection tools as compared to known magnetic NDT methods," *Cinde Journal*, vol. 27, no. 3, p. 16, 2006. 48

[105] S. G. H. Staples, C. Vo, D. M. J. Cowell, S. Freear, C. Ives, and B. T. H. Varcoe, "Solving the Inverse Problem of Magnetisation-Stress Resolution," *Journal of Applied Physics*, vol. 113, no. 13, 2013. 48, 51, 68

[106] H. A. Kishawy and H. A. Gabbar, "Review of pipeline integrity management practices," *International Journal of Pressure Vessels and Piping*, vol. 87, no. 7, pp. 373 – 380, 2010. 48

[107] R. L. Wade and J. R. Adams, "An Integrated Approach For Pipeline Fitness For Purpose Determination Using Corrosion and Geometry Pipeline Pig Inspection Systems," *Pipetech, Pattaya.*, 1995. 50

[108] G. Fung, W. P. Backhaus, S. McDaniel, and M. Erdogmus, "To Pig or Not to Pig: The Marlin Experience With Stuck Pig," tech. rep., Pipeline Research LTD, 2006. 50

[109] M. Weber, S. Arnrich, E. Willik, and R. Lessig, "Death by a cleaning pig - an unusual accident at work," *Archiv fur kriminologie*, 2004. 50

[110] A. A. Dubov, "A study of metal properties using the method of magnetic memory," *Metal science and heat treatment*, vol. 39, no. 9, pp. 401–405, 1997. 51

[111] IIW International Institute of Welding, "24497 Non-destructive testing: Metal magnetic memory," tech. rep., International Organisation for Standards, 2007. 51

[112] A. A. Dubov, "Physical base of the method of metal magnetic memory," *AMAS course on non-destructive testing of materials NTM 02 - Warsaw 2002*, 2002. 51

[113] S. Bao, M. Fu, S. Hu, Y. Gu, and H. Lou, "A review of the metal megnatic memory technique," *Proceedings of the ASME 2016 35th International Conference on Ocean, Offshore and Arctic Engineering OMAE2016*, 2016. 51

[114] M. Roskosz, A. Rusin, and J. Katowicz, "The metal magnetic memory method in the diagnostics of power machinery," *Achievements in materials and manufacturing engineering*, vol. 43, no. 1, pp. 362–370, 2010. 51

[115] L. Luming, H. Songling, W. Xiaofeng, S. Keren, and W. Su, "Magnetic field abnormality caused by welding residual stress," *Journal of Magnetism and Magnetic Materials*, vol. 261, pp. 385–391, 2003. 51

[116] Z. D. Wang, K. Yao, B. Deng, and K. Q. Ding, "Quantitative study of metal magnetic memory signal versus local stress concentration," *NDT&E International*, vol. 43, no. 6, pp. 513–518, 2010. 51, 118, 223

[117] Z. D. Wang, K. Yao, B. Deng, and K. Q. Ding, "Theoretical Studies of Metal Magnetic Memory Technique on Magnetic Fuxleakage Signals," *NDT&E International*, vol. 43, pp. 354–359, 2010. 51, 54

[118] Y. M. Shnir, *Magnetic Monopoles.* Springer, 2005. 52

[119] Topcon, "GR-5 with Vanguard Technology - Advanced GNSS Reciever," 2011. 64

[120] C. K. Vo, *Detection of Stress Concentration Zones in Ferrous Materical using Stand-off Magnetometry.* PhD thesis, School of Electronic and Electrical Engineering, University of Leeds, 2015. 68, 116

[121] S. G. H. Staples, *Using the Villari Effect to Detect Anomalies in Steel Materials.* PhD thesis, Department of Physics and Astronomy, University of Leeds, 2017. 68, 74, 162, 212

[122] Z. Li, R. Jarvis, P. B. Nagy, S. Dixon, and P. Cawley, “Experimental and simulation methods to study the Magnetic Tomography Method (MTM) for pipe defect detection,” *NDT & E International*, vol. 92, pp. 59–66, 2017. 68

[123] Z. Li, S. Dixon, P. Cawley, R. Jarvis, P. B. Nagy, and S. Cabeza, “Experimental studies of the magneto-mechanical memory (MMM) technique using permanently installed magnetic sensor arrays,” *NDT&E International*, vol. 92, pp. 136–148, 2017. 68

[124] Bartington Instruments Limited, “Mag648 & Mag649 Low Power Three-Axis Magnetic Field Sensors data sheet.” 69

[125] British Standards Institution, “BS EN 61386: Specification for steel conduit and fittings with metric threads of ISO form for electrical installations. Steel conduit, bends and couplers,” tech. rep., BSI, 1970. 72

[126] J. X. Wang, *What Every Engineer Should Know About Decision Making Under Uncertainty*. Marcel Dekker, 2002. 73, 80

[127] ISO/TC 69/SC 6 Technical Committee, “ISO 5725-1:1994(en) Accuracy (trueness and precision) of measurement methods and results,” tech. rep., International Organisation for Standards, 1994. 76

[128] J. M. Bland and D. G. Altman, “Statistical Methods For Assessing Agreement Between Two Methods Of Clinical Measurement,” *The Lancet*, vol. 327, no. 8476, pp. 307–310, 1986. 76, 77

[129] M. M. Shoukri and C. A. Pause, *Statistical Methods for Health Sciences*. CRC Press, 1999. 77

[130] J. Medhi, *Statistical Methods: An Introductory Text*. New Age international LTD., 1992. 77

[131] J. Gurland and R. C. Tripathi, “A Simple Approximation for Unbiased Estimation of the Standard Deviation,” *The American Statistician*, vol. 25, no. 4, pp. 30–32, 1971. 77

[132] J. Gosling, *Introductory Statistics*, ch. 4, pp. 55–72. Pascal Press, 1995. 77, 83

[133] T. Raylov and G. A. Marcoulides, *Basic Statistics an Introduction With R*, ch. 6.1.2 Sampling Distribution, pp. 83–87. Rowman & LittleField Publishers INC., 2013. 78

[134] N. L. Johnson, "Systems of Frequency Curves Generated by Methods of Translation," *Biometrika*, vol. 36, no. 1, p. 1, 1949. 83

[135] J. P. Royston, "An Extension of Shapiro and Wilk's W Test for Normality to Large Samples," *Journal of the Royal Statistical Society (Applied Statistics)*, vol. 31, no. 2, pp. 115–124, 1982. 83

[136] S. S. Shapiro and M. B. Wilk, "An analysis of variance test for normality (complete samples)," *Biometrika*, vol. 52, no. 3/4, pp. 591–611, 1965. 83

[137] J. M. Bland and D. G. Altman, "Measuring Agreement in Method Comparison Studies," *Statistical Methods in Medical Research*, no. 8, pp. 135–160, 1999. 84

[138] D. H. Laidlaw, R. M. Kirby, C. D. Jackson, J. S. Davidson, T. S. Miller, M. da Silva, W. H. Warren, and M. J. Tarr, "Comparing 2D Vector Field Visualization Methods: A User Study," *IEEE transactions on visualization and computer graphics*, vol. 11, no. 1, pp. 59–69, 2005. 88

[139] F. H. Post and J. J. van Wijk, "Visual Representation of Vector Fields – Recent Developments and Research Directions," *Contribution to the book of the ONR Workshop on Data Visualization*, 1993. 88, 89, 93

[140] R. B. Haber, "Visualization Techniques for Engineering Mechanics," *Computing Systems in Engineering*, vol. 1, no. 1, pp. 37–50, 1990. 88

[141] C. Johnson, "Top Scientific Visualisation Research Problems," *Visualisation Viewpoints*, 2004. 88

[142] B. Cabral and L. Leedom, "Imaging Vector Fields Using Line Integral Convolution," *Computer Graphics (SIGGRAPH 93 Proceedings)*, 1993. 88, 89, 97

[143] V. R. Klassen and S. J. Harrington, "Shadowed hedgehogs: A Technique for Visualizing 2D slices of 3D vector fields," in *Proceedings of the 2nd conference on Visualization '91*, 1991. 89

[144] J. P. Hultquist, "Interactive Numerical Flow Visualization Using Stream Surfaces," *Computing Systems in Engineering*, vol. 1, no. 2–4, pp. 349–353, 1990. 89, 93

[145] L. Hesselink, F. H. Post, and J. J. van Wijk, "Research Issues in Vector and Tensor Field Visualization," *IEEE Computer Graphics and Applications*, pp. 76–79, 1994. 90

[146] W. J. Schroeder and K. M. Martin, *Visualization Handbook: Overview of Visualization*, ch. 1, pp. 19–20. Elsevier-Butterworth Heinemann, 2005. 93

[147] N. B. Shamlo, "Matlab Toolbox For High Resolution Vector Field Visualization With Application in Improving the Understanding of Crack Propagation Mechanisms ," Master's thesis, San Diego State University, 2005. 97, 112

[148] R. Wegenkittl, E. Groller, and W. Purgathofer, "Animating Flow Fields: Rendering of Oriented Line Integral Convolution," *Proceedings of IEEE Conference on Computer Animation 1997*, 1997. 97

[149] P. C. Matthews, *Vector Calculus*, ch. Gradient, Divergence and Curl, pp. 45–65. Springer-Verlag London, 1998. 121

[150] B. D. Hymers, *A Treatise on Trigonometry and on Trigonometrical Tables and Logarithms*. Cambridge, 1841. 144